THESIS / THÈSE

DOCTOR OF SCIENCES

New porous functional materials for photo and electrochemical devices

Esperanca Garcia, Diogo Miguel

Award date:
2022

Awarding institution:
University of Namur
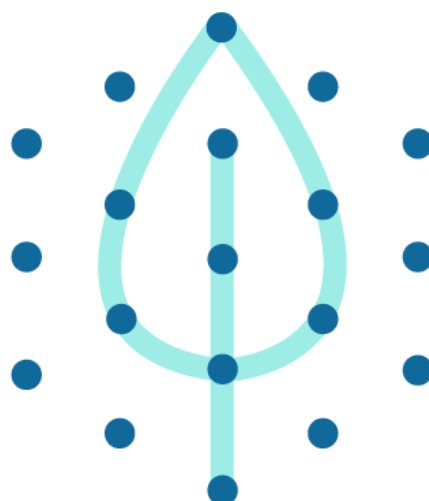Université de Pau et des Pays de l'Adour

Link to publication

escaled

European School on Artificial Leaf: Electrodes and Devices

New porous functional materials for photo and electrochemical devices

October 2018 - November 2022

Diogo M. E. Garcia

Cotutelle: Doctorate in Chemistry (Université de Pau et des Pays de l'Adour)
Doctorate in Chemical Sciences (Université de Namur)

Supervisors: Dr. Stéphanie Reynaud, CNRS permanent Researcher, Institut des Sciences Analytiques et de Physico-Chimie pour l'Environnement et les Matériaux, France

Prof. Bao-Lian Su, Laboratoire de Chimie des Matériaux Inorganiques (CMI), Full Professor at Université de Namur, Belgium

Co-supervisor: Dr. Claudia Custódia Simão Delgado, Pos-Doc, Head of Printed Sensors and Actuators research group, Department Functional Printing & Embedded Devices, Eurecat, Barcelona

Jury (President) Prof. Catherine Michaux, chemistry department Université de Namur, Belgium

New porous functional materials for photo and electrochemical devices

"Intelligence is the ability to adapt to change."
Stephen Hawking

ACKNOWLEDGMENTS

I would like to express my gratitude to Stéphanie Reynaud for having me as her student and welcoming me to the polymers' chemistry world. Thank you for all your support and dedication during my time in Pau and, especially, after I left and until today.

I would like to extend my sincere thanks to Prof. Su for the opportunity to be part of his research group in Namur as a student, without him, this Ph.D. would not be possible.

I would like to offer my thanks to Claudia Delgado for her support and supervision during these years and, specifically during my time in Mataró. Obrigado pela confiança e apoio desde a minha primeira passagem pela Eurecat até hoje, incentivando-me sempre a perseguir e atingir os meus objetivos. Obrigado por me desafiares e deixares dar largas à imaginação. Obrigado, como em 2018, pelos momentos em Barcelona, pelas boas conversas, pelos almoços e jantares.

I am grateful to Marc Fontecave for receiving me for a secondment in his research team in Paris. I must also express my gratitude to Yun for her support and all the techniques and concepts I learned from her during those three months. Your dedication brought up my interest in organic chemistry and synthesis, which I thought to be inexistent before.

To Laurent Billon, thank you for eSCALED. Thank you also for all the nice discussions. I deeply appreciate the way you communicate your scientific work no matter the background of your audience, it truly inspires me, as well as your initiative of going a step further, merging exact and human sciences in research.

I extend my thanks to Laia Francesch, the "mother of all ESRs". I cannot find enough words to express how grateful I feel for your support during all this time. It was a pleasure to meet you and to share such nice moments with you. Thank you for your support with all the administrative challenges throughout these years. I have to thank you for our nice conversations, sharing ideas and perspectives about a broad range of topics: life in general, technology, politics, research and science, career planning, traveling, our cultures, the latest movie from Quentin Tarantino, or revisiting our favorite rock bands.

To all eSCALED ESRs, thank you for the nice moments we shared, starting from the day we met for the first time in Tarragona. We haven't achieved our Nobel prize, not yet, but we did a great job, individually and together.

To Antoine and Pierre, thank you for your support and patience to clarify my doubts about the polymers' world and for the nice discussions that led us to achieve, together, such nice results.

I offer my thanks also to Paul for hosting me in Eurecat once again and allowing me to be part of his team. I must acknowledge the support of the FPED unit, in particular the members of team PSA who have received me and always made me feel part of them, comfortable, safe, and confident that I would achieve my goals.

Não posso deixar de agradecer à Sónia Pereira e Prof. Isabel que ainda durante a licenciatura e mestrado, respetivamente, estimularam o meu gosto pela investigação que me trouxe até ao dia de hoje.

Agradeço aos meus avós, que tanto contribuíram para ser o homem que sou hoje, por, desde sempre, me terem incentivado a perseguir os meus sonhos e ambições, por serem um exemplo de resiliência e dedicação.

Aos meus pais, obrigado por me terem dado liberdade para crescer e descobrir. Obrigado por, em conjunto, me terem feito quem sou hoje. Obrigado pelo carinho, apoio e proteção e por me inspirarem e motivarem a perseguir os meus objetivos, sempre.

Ao meu irmão Paulinho, obrigado por todo o apoio, por me abrir os horizontes e por estar presente, sempre. À Diana; Gonçalo e Matilde, que não tenham medo de voar, sair da caixa, seguir os vossos sonhos, que eu possa caminhar convosco, sempre.

À Constança, pelo companheirismo, pela presença constante, pela amizade, pela confiança, pelo apoio em todos os momentos, pela compreensão e paciência, por crescermos juntos, pelas loucuras e viagens inesperadas, obrigado.

À Nuxa, pelas conversas que duram horas e horas, pelas largas reflexões e trocas de ideias nos mais diversos temas, por estar presente e acompanhar o meu crescimento desde sempre, obrigado.

A toda a minha família, obrigado por serem como são, pela união e pelo amor.

Saeed, I am so grateful for having the chance to know you. Thank you for all the moments we shared, for the support, and our nice and long conversations. You have opened my mind and strongly contributed to my personal development during these years. Thank you for everything, golabi!

Eleftheria and Javi, thank you for all our coffees, meals, and beers, deep talks, the collective support, for the moments we shared. Thank you for the good times we spent.

À Carolina; ao Tomás; à Beatriz e ao Miguel, obrigado pela amizade e por se manterem presentes, ainda que à distância.

Alex, Hisham, Ahmed, Laura, Tik, Sandrine, Tiago, Mari Carmen, Fatima, and Lucile, thank you all for the nice moments we shared in Pau. Thank you for making me feel part of you. We will hopefully meet again in the future.

Benjamin, Quentin, Alexandra, Anthony, Ayrton, and Alessandra, thank you for all the support and friendship in Namur, I was lucky to find you. Thank you for the beers after work, the cappuccinos and cheesecakes at Coffee & More, you have made 2020 easier.

To those who somehow contributed to my scientific, technical and personal development during these years for years, thank you.

LIST OF ABBREVIATIONS

Abbreviation	Definition
4-pp	Four-Point Probe
ACN	Acetonitrile
ATRP	Atom transfer radical polymerization
CA	Chronoamperometry
CDCl$_3$	Deuterochloroform
CE	Counter electrode
CHCA	Alpha-cyano-4-hydroxy-cinnamic acid
CNT	Carbon nanotube
CO$_2$RR	Carbon dioxide reduction reaction
CRP	Controlled/living radical polymerization
CV	Cyclic voltammetry
DCCi	Dicyclohexylcarbodiimide
DCM	Dichloromethane
DIPEA	N,N-Diisopropylethylamine
DLS	Dynamic light scattering
DMF	Dimethylformamide
DMSO	Dimethyl sulfoxide
DSC	Differential scanning calorimetry
ECSA	Electrochemical active surface area
EDS	Energy dispersive spectroscopy
EMB	Emeraldine base
EMS	Emeraldine salt
FESEM	Field emission scanning electron microscopy
GDE	Gas diffusion electrode
GDL	Gas diffusion layer
HATU	1-[Bis(dimethylamino)methylene]-1H-1,2,3-triazolo[4,5-b]pyridinium 3-Oxide Hexafluorophosphate
HC	Honeycomb
HER	Hydrogen evolution reaction
HIPS	High impact poly(styrene)
ICP	Intrinsic conducting polymer
LEB	Leucoemeraldine base
MALDI-TOF	Matrix-assisted laser desorption/ionization – time-of-flight mass spectrometry
MBM	Methyl methacrylate-nbutyl acrylate-methyl methacrylate
MEA	Membrane electrode assembly
MeOH	Methanol
MOF	Metal-organic framework
MWCNT	Multi-wall carbon nanotubes
NHS	N-Hydroxysuccinimide
NMP	N-Methyl-2-pyrrolidone
NMR	Nuclear magnetic resonance
OCP	Open circuit potential
OER	Oxygen evolution reaction
PANI	Poly(aniline)
PEM	Proton exchange membrane
PET	Poly(ethylene terephthalate)
PGMEA	Propylene glycol methyl ether acetate
PHEMA	Poly(hydroxymethyl methacrylate)
PMDETA	N,N,N′,N′,N″-pentamethyldiethylenetriamine
PMMA	Poly(methyl methacrylate)
Pt/C	Platinum on graphitized carbon

| Abbreviation	Definition
PVC	Poly(vinyl chloride)
RE	Reference electrode
RhB	Rhodamine B
RHE	Reversible hydrogen electrode
SBM	Styrene-butadiene-methyl methacrylate
SBS	Styrene-butadiene-styrene
SEC	Size exclusion chromatography
SEM	Scanning electron microscopy
SPE	Screen-printed electrode
TANI	Tetra-aniline
TEM	Transmission electron microscopy
TGA	Thermo gravimetric analysis
THF	Tetrahydrofuran
TLC	Thin-layer chromatography
WE	Working electrode
XRD	X-ray powder diffraction
ZIF	Zeolitic imidazolate framework

INDEX

GENERAL

INTRODUCTION

GENERAL INTRODUCTION

Over recent years, the evolution of society and industry throughout the world has led to an increase in global energy demand and consumption. Nowadays, the anthropogenic demand for energy depends on limited sources of fossil fuels. However, the constant and increasing release of carbon dioxide (CO_2) and other Greenhouse Gases (GHG) since the industrial revolution has resulted in climate change.[1] The anthropogenic climate change is estimated to be translated into global warming of 1.5 °C, or higher, between 2021 and 2040. Although in 2020, during the imposition of strong emergency measures, due to COVID-19 spread out, the emissions of CO_2 and GHG were below the levels of 2019, this short reduction was not enough to attenuate the temperature rise of 1.5 °C. Several reports have stated that GHG emissions must be reduced to half by 2030 and to net-zero CO_2, *i.e.*, full decarbonization, by 2050 to increase the chances of limiting global warming to the 1.5 °C rises, compared to pre-industrial levels, to meet the 1.5 °C Paris Agreement.[2–6] So far, The Gambia was the only country to take actions considered fully compatible with the 1.5 °C Paris Agreement.[7]

In 2019, the European Commission presented the European Green Deal for the European Union (EU). The elements of this Green Deal are presented in Figure I-1 and include, not only, the EU's strategy to meet the United Nations' agenda for 2030, but also proposes the mobilization of the industry to a circular economy, re-thinks the construction and renovation of buildings in a resource-efficient way and the preservation of ecosystems and biodiversity.
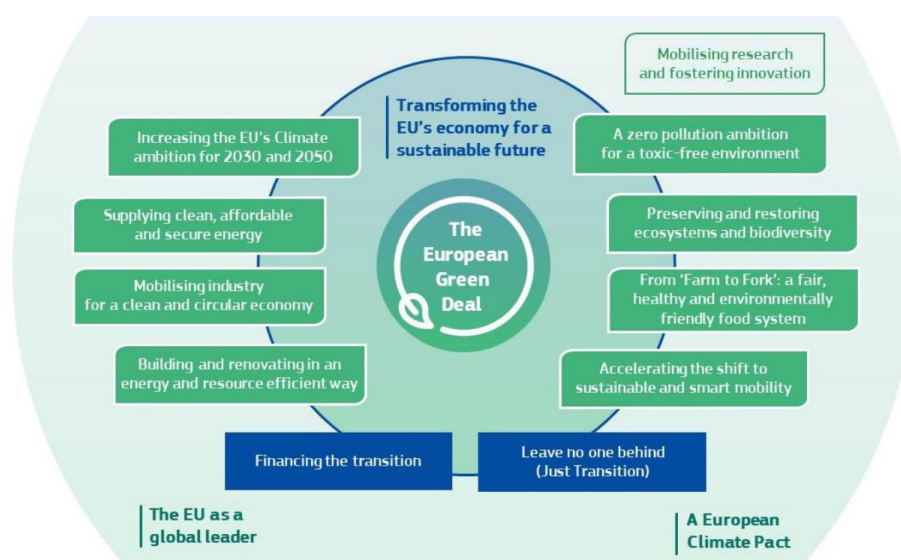
Figure I-1 – The elements of the European Green Deal. From[8]

Moreover, it also proposes an environmentally friendly, healthy, and fair food system. These means aim to reach the EU's carbon neutrality by 2050.[8] In 2020, the Commission committed to increasing

the EU's GHG reductions to at least 50 % towards 55 % by 2030 through an integrated hydrogen-based energy system.[9,10]

In this context, this thesis was performed under the frame of the eSCALED (European SChool on Artificial Leaf: Electrodes and Devices) project, a contribution to the structure of early-stage research training at the European level and strengthening European innovation capacity to elaborate an artificial leaf device as a response to climate change. Like a leaf in nature, eSCALED proposes to elaborate an artificial photosynthesis device capable of harvesting solar energy and storing it as molecules (solar fuels). The proposed device should combine a solar cell with a bio-inspired electrochemical stack where H_2O oxidation and H^+/CO_2 reduction are performed in microporous electrodes, mimicking the chloroplasts of a plant. Apart from promoting inter and multi-disciplinary research and formation on biological/biochemical, inorganic and soft matter, device engineering, and innovation, eSCALED targets the use of easy, cheap, and up-scalable processes based on organic and earth-abundant materials.

The works described in this thesis focus on the synthesis, characterization, and up-scaling of microporous polymer electrodes decorated with heterogeneous H^+/CO_2 reduction catalysts as a contribution to the eSCALED demonstrator devices. For this purpose, we worked on an innovative cathode architecture in a multi-disciplinary approach, merging the fields of polymers' chemistry and physical chemistry, hierarchically porous organic and inorganic materials, molecular catalysis, and printed electronics.

The manuscript is organized into five chapters:

CHAPTER I: titled "Context and state of the art" are dedicated to the state of the art, including a brief overview of the context and the economic and environmental issues that the society must face in terms of energy needs. The concepts of water electrolysis and artificial photosynthesis are outlined. This chapter reports then the necessary knowledge to get into Chapters II and III; Chapter IV and Chapter V, *i.e.*, the basics of the controlled radical polymerization and conducting polymers; the properties of zinc oxide and printed electronics, respectively. At the end of this chapter, the strategies followed within this thesis work are presented.

CHAPTER II: titled "Synthesis of a processable conducting material: block copolymer strategy" is dedicated to structured organic materials. It starts with the description of the elaboration of the conducting block copolymer containing (i) an insulating block of either polystyrene or copolymer of polystyrene and polyacrylate chosen to optimize the physical properties of the final material. (ii) a conducting part based on polyaniline. The process has been developed to optimize the control of the polymer size and functionality, the film-forming properties, and the final conductivity. The chapter ends with the preparation of structured materials following a breath figure methodology and their electrochemical characterization.

CHAPTER III: titled "Preparation of bipyridine-TANI based catalyst for H^+/CO_2 reduction" develops the synthesis of bipyridine (bpy) based catalyst for CO_2 electrochemical reduction.

Conducting block obtained within Chapter II is coupled to a bipyridine to benefit from its interaction with the electroactive block. Three different strategies for the coupling reaction between TANI and bipyridine are proposed and developed.

CHAPTER IV: titled "Synthesis of ZIF-8 templated macro-microporous zinc oxide and its photocatalytic activity" is dedicated to the elaboration of porous 3D-ordered material obtained from zeolitic imidazolate framework-8 (ZIF-8) and its application in photocatalysis. It starts with the synthesis of an innovative MOF-templated semiconducting material with tetrakaidecahedron porous structures. This material aims to fulfill the need for hierarchically porous structures as catalyst supports. The investigation and optimization of the synthesis protocol are developed, and a practical use case of such material is demonstrated for the photodecomposition of an organic pollutant. The works reported were developed at the facilities of the CMI group at the Université de Namur.

CHAPTER V: titled "Integration of printed electrodes in devices for green hydrogen production through water electrolysis" investigates the preparation of printed cathodes and membrane electrode assembly (MEA) devices for hydrogen generation. In this study we propose, for the first time, the use of screen-printed electrodes (SPEs) as the cathode in such devices. SPEs with different designs and working areas prepared from carbon-based commercially available printing pastes provide sufficient electron conductivity to promote the hydrogen evolution reaction (HER) in neutral pH buffered solution. The electrochemical performance of the SPEs with different designs is described by chronoamperometric tests in different electrolyzer cell configurations: H-cell, flow cell, and proton exchange MEA.

This thesis manuscript ends with a general conclusion and perspectives.

CHAPTER I

Context and state of the art

CHAPTER I: **CONTEXT AND STATE OF THE ART**

I.1. CONTEXT AND MOTIVATION

I.1.1. HYDROGEN GENERATION: CURRENT STATE AND FUTURE PERSPECTIVES

Energy obtained from renewable sources is crucial to decreasing the consumption of fossil fuel-derived energy, hence reducing CO_2 and GHG emissions.[11] In 2019, renewable sources contributed 13.5 % of the world's energy production, while fossil fuels represented 81.2 % of it. However, in the EU, in that same year, renewables represented 36.4 % of the produced energy. Within renewables, wind and hydropower correspond to 38.0 and 34.3 % of the overall electricity capacity in the EU, respectively, while solar photovoltaic stands for only 26.9 %.[12] It is expected that within the next years, and strongly endorsed by the European Green Deal, renewable energy sources such as solar and wind energy will dominate the energy system along with hydrogen as an energy carrier and other solar fuels.[13–17] However, the intermittent and variable nature of the given renewables appears as a challenge when shifting to a hydrogen-based economy.[18–21]

Hydrogen (H) is the most abundant, lightest, and simplest element in the universe. At standard conditions, hydrogen is a colorless, odorless, and flammable gas of diatomic molecules (H_2). However, in nature, and due to its reactivity, hydrogen only exists when coupled to other elements, hence, it needs to be obtained through different methods and from different sources.[22,23] H_2 is a versatile energy carrier and can be seasonally stored (long-term storage). Moreover, H_2 can

be distributed cost-effectively, since the infrastructures used nowadays for natural gas transmission and distribution may be suitable for H_2 with minimal or even without any modification.[24] Furthermore, when used as a fuel and due to its carbon-free composition, H_2 produces harmless products and no CO_2 or GHG are emitted.

It was estimated that of the 60 million tons of H_2 produced per year, 96 % derive directly from reforming or gasification of fossil fuels, namely, natural gas (49 %); hydrocarbons in the liquid state (29 %), and coal (18 %).[25,26] In fact, these processes make a significant contribution to global warming due to their inherent CO_2 and GHC emissions. For instance, steam reforming of methane (SMR) and coal gasification, which are, yet, the primary technologies for H_2 production, have a CO_2 emission factor of 8.9 kg CO_2/kg H_2 and 29.33 kg CO_2/kg H_2.[27,28] H_2 obtained through water electrolysis, still, represents only 4 % of worldwide H_2 production.[29] Nowadays, a color prefix is used to describe the H_2 produced from different methods as presented in Table I-1.
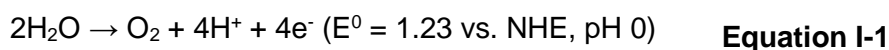
Table I-1 – Hydrogen color spectrum.

Terminology	Technology	Feedstock/power source	Greenhouse gas footprint
Green		Renewable	Minimal
Pink/purple/red	Wates electrolysis	Nuclear	Minimal
Yellow		Grid/mixed	Medium
Blue	Steam-methane reforming or gasification+ CCUS	Natural gas	Low
Turquoise	Methane pyrolysis	Natural gas	Solid black carbon
Grey	Steam-methane reforming	Natural gas	Medium
Brown	Gasification	Brown coal	High
Black		Black coal	High

"Grey" stands for the hydrogen produced from hydrocarbon reformation processes such as SMR, auto thermal reforming of natural gas, or partial oxidation of heavy oil or coal (some groups reported the H_2 produced from gasification of coal as "black" or "brown" H_2, depending on the type of coal used). Grey hydrogen is not suitable for the net-zero emissions path due to its substantial CO_2 emissions. However, if a carbon capture, usage, and storage system (CCUS) is coupled to SMR or autothermal reforming the hydrogen produced is given the prefix "blue". Even if the retrofitting of the existing infrastructures by coupling CCUS may involve high investments, blue hydrogen fits the net-zero and hydrogen plan since the combination with CCUS significantly reduces toxic emissions. "Turquoise" hydrogen is produced from natural gas as feedstock without any CO_2 emission through

the process of pyrolysis. Despite the absence of gaseous emissions, the solid carbon black is produced, however, the latter can be easily stored, contrary to CO_2, and has its market already established. Finally, the most wanted technology for a net-zero scenario is the H_2 produced from water electrolysis. Different authors in the literature have sub-divided the electrolysis-derived H_2 into green, yellow, and pink/purple/red hydrogen, depending on the power source used. The first, green hydrogen, many times reported as "renewable hydrogen", is produced from renewable power sources such as hydro, wind, or solar. Yellow hydrogen uses the grid or grid + renewable mixed system as an electricity provider. Lastly, red, purple, or pink (there is no consensus in literature) hydrogen uses nuclear energy as a source of electricity. The later and green hydrogen is considered the only GHG "clean" option, while the GHG footprint of yellow hydrogen may oscillate, depending on the source of electricity in use. However, currently, green hydrogen is still more expensive than grey hydrogen.[1,18,24,30–33] Yet, life cycle assessment (LCA) should be performed more precisely for each technology, under its specific working conditions and considering the manufacturing of each component. Hence, LCA studies play a significant role in informing the real GHG emissions, economical costs, and social footprint of H_2 production to clarify decision-making processes toward climate change mitigation and the United Nations' Sustainable Development Goals.[34–41]

I.1.2. WATER ELECTROLYSIS: CONCEPT TECHNOLOGIES

Water electrolysis has the potential to store the electricity provided by renewable sources in chemical bonds, through water splitting, generating H_2. The water oxidation to evolve oxygen at the positively charged electrode (anode) and the anode and the reduction reaction to evolving hydrogen at the negatively charged electrode (cathode) constitute the two half-cell reactions of the electrochemical water splitting process and are given in Equation I-1 and Equation I-2[42,43], respectively:

$$2H_2O \rightarrow O_2 + 4H^+ + 4e^- \ (E^0 = 1.23 \text{ vs. NHE, pH 0})$$ **Equation I-1**

$$4H^+ + 4e^- \rightarrow 2H_2 \ (E^0 = 0 \text{ vs. NHE})$$ **Equation I-2**

The H_2 chemical bonds, used as an energy carrier, can be reverted to regenerate electricity in fuel cells. Thus, power to a gas system combining electrolyzer and fuel cells, as exemplified in Figure I-1, is of great interest in the energy transition in establishing a hydrogen-based energy system.[44–47]
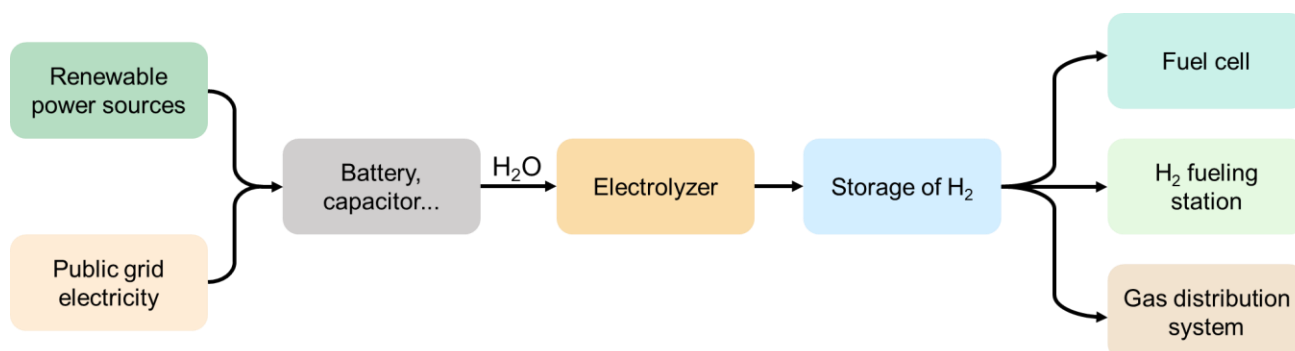
Figure I-1 – Components of power to gas system containing electrolyzer and fuel cells. Adapted from[45].

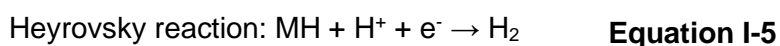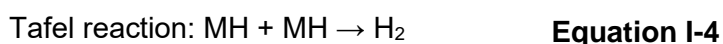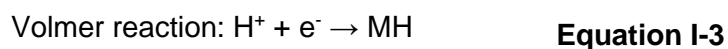In fuel cells, the working mechanism is based on the oxygen reduction reaction (ORR) and hydrogen oxidation reaction (HOR), which are the exact reverse half-cell reactions in the electrolyzers, the oxygen evolution reaction (OER), and the hydrogen evolution reaction (HER).[48–50]

The hydrogen evolution reaction (HER), studied in this work, can be described by three reactions:

$$\text{Volmer reaction: } H^+ + e^- \rightarrow MH \qquad \textbf{Equation I-3}$$

$$\text{Tafel reaction: } MH + MH \rightarrow H_2 \qquad \textbf{Equation I-4}$$

$$\text{Heyrovsky reaction: } MH + H^+ + e^- \rightarrow H_2 \qquad \textbf{Equation I-5}$$

The Volmer reaction (Equation I-3) consists of the combination of the H^+ adsorbed with the electrons provided by the external circuit. The Tafel reaction (Equation I-4) represents the direct combination of two adsorbed hydrogen atoms consequently forming H_2. Finally, the third, *i.e.*, the Heyrovsky reaction (Equation I-5) describes the combination of the electrons provided by the external circuit, the adsorbed hydrogen atom formed at the Tafel reaction, and one hydrogen ion also adsorbed at the electrode's surface.[51] Figure I-2 illustrates the three reactions describing the HER mechanism.
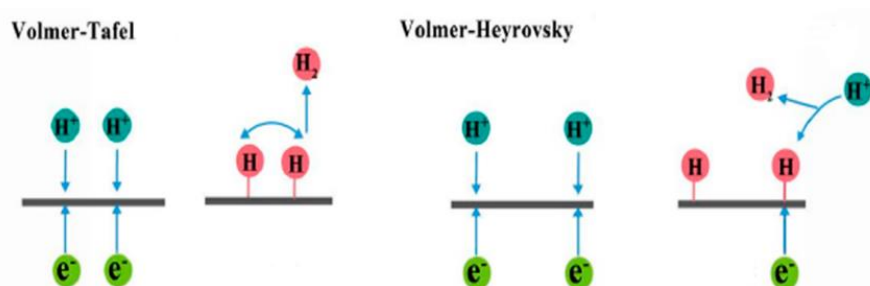
Figure I-2 – Illustrative representation of the reactions involved in the hydrogen evolution mechanism. Adapted from [51].

Three main types of electrolysis methods can be distinguished: alkaline water electrolysis (AWE); solid oxide electrolysis (SOE) and proton exchange membrane (PEM) water electrolysis. Figure I-3 presents schematic representations of the three technologies and the respective working mechanisms are given in Table I-2.
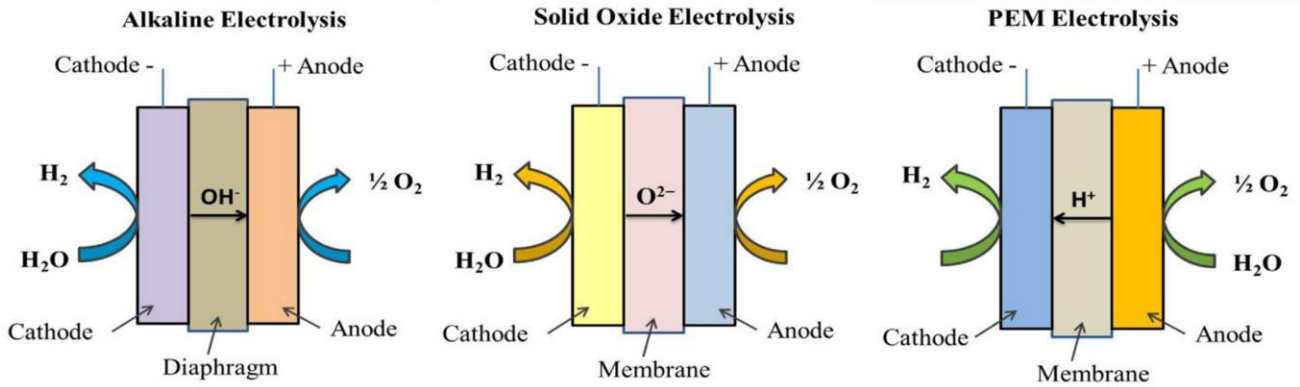
Figure I-3 – Schematic illustrations of AWE, SOE, and PEM electrolysis. Adapted from [52].

Table I-2 – Working mechanisms of the different water electrolysis technologies.

Technology	Mechanism	
Alkaline	Anode: $2OH^- \rightarrow H_2O + \frac{1}{2}O_2 + 2e^-$	**Equation I-6**
	Cathode: $2H_2O + 2e^- \rightarrow H_2 + 2OH^-$	**Equation I-7**
	Cell: $H_2O \rightarrow H_2 + \frac{1}{2}O_2$	**Equation I-8**
Solid oxide	Anode: $O^{2-} \rightarrow \frac{1}{2}O_2 + 2e^-$	**Equation I-9**
	Cathode: $2H_2O + 2e^- \rightarrow H_2 + O^{2-}$	**Equation I-10**
	Cell: $H_2O \rightarrow H_2 + \frac{1}{2}O_2$	**Equation I-11**
PEM	Anode: $H_2O \rightarrow 2H^+ + \frac{1}{2}O_2 + 2e^-$	**Equation I-12**
	Cathode: $2H^+ + 2e^- \rightarrow H_2$	**Equation I-13**
	Cell: $2H_2O + 2e^- \rightarrow H_2 + \frac{1}{2}O_2$	**Equation I-14**

Water electrolysis through microbial electrolysis cells (MEC) has been reported in the literature too, however, it won't be detailed in the present review. Alkaline electrolysis is the most matured technology in water electrolysis since it was reported for the first time in 1789 and it's already in a commercialization stage in the megawatt range. This technology operates at low temperatures, between 60 and 80 °C, under high pH conditions where aqueous solutions of KOH and/or NaOH are used as a reactant. In such a system, the electrodes are separated by an asbestos-porous diaphragm and the electrodes are typically from nickel and/or iron-based materials. Its working mechanism (Equation I-8) starts with two reactant molecules being reduced at the cathode and producing one H_2 molecule and two hydroxyl ions (OH^-) (Equation I-7). The first product is then removed from the cathode surface, while the two OH^- migrate through the diaphragm to the anode due to the electric field imposed. At the anode, the O_2 molecules are then produced and released (Equation I-6). SOE, first introduced in the 1980s, has attracted the attention of the research community due to its high efficiency while producing ultra-pure H_2. This device uses O^{2-} conductors, usually yttria and zirconia solid oxides, operate at high temperatures (500 – 850 °C) and high pressure and uses the steam form of water (Equation I-9, Equation I-10, and Equation I-11). Finally, water electrolysis through PEM technology was first developed by General Electric in 1966 as an alternative to AWE.[53] As in PEM fuel cells, PEM water electrolyzers use solid polymeric membranes as the electrolyte, usually, these are polysulfonated or phosphorated polymers with high proton

conductivity.[54] In PEM water electrolysis, water is oxidized at the anode, producing O_2, protons (H^+), and electrons (e^-) (Equation I-12). The electrons are conducted to the cathode by the external electric circuit, while the protons cross the membrane from the anode to the cathode. At the cathode, the protons are reduced by the electrons to produce H_2 (Equation I-13). In PEM, the applied potential, temperature, electrocatalysts' properties, and membrane resistance determine the H_2O splitting reaction rate.[29,45,52,55–57]

Table I-3 summarizes and compares some advantages and disadvantages associated with each technology.

Table I-3 – Water electrolysis technologies: advantages and disadvantages.

| Technology	Advantages	Disadvantages
Alkaline	Most highly developed and maturated. H_2 production up to the megawatt range. Non-noble catalysts. Long-term stability. Cheapest.	Safety concerning its corrosive liquid reactant. Cross-diffusion of product gases through the diaphragm. Low purity of H_2 produced. Low partial load range. Limited current density. Low operating pressure.
Solid oxide	High efficiency (up to 100 %). Operates under high pressure. non-noble catalysts.	Brittle ceramics limit their durability. Bulk system design. Low development – lab stage.
PEM	Simple and compact design. High purity of H_2 produced (up to 99.99%). High current density. Fast response. Gas cross-diffusion is avoided by the membrane.	Safety concerning its acidic corrosive environment. Limited lifetime of the membrane. High costs due to noble-metal catalysts and expensive membranes. High water purity is required.

Alkaline water electrolysis is, currently, the most developed technology and the cheapest available on the market. Moreover, its long-term stability in some power-to-gas facilities has already been demonstrated. The SOE technology is still primitive, *i.e.*, at a laboratory demonstration scale, and is the least developed compared to PEM and AWE. Furthermore, the bulk design and durability of its brittle ceramic components are seen as the major drawbacks of this technology. Notwithstanding, the high efficiency reported (up to 100%) under high-pressure operational conditions is seen as the major advantage supporting this technology. PEM water electrolysis is expected by some authors to be dominant in the market by 2030.[58] Electrolysis of water through PEM has the advantages of the simplicity and compact design of the device, performance at current densities and great purity of H_2 obtained, not requiring further purification steps. Moreover, PEM devices present a fast response, which is suitable for the combination with intermittent and fluctuating power sources such as wind and solar. Having a solid membrane between the electrodes, the cross-diffusion of the gaseous products is avoided, which could not be avoided in the AWE cells due to the inherent porosity of the diaphragm. As AWE, PEM water electrolysis occurs at a low temperature too, however higher efficiencies and power density were reported for PEM technology. Nowadays, PEM water electrolysis is the most expensive technology due to the high costs of the membrane and the rare

noble-metal catalysts used (Ru or Ir at the anode and Pt or Pd at the cathode). Furthermore, the membrane's lifetime is limited and compromises the long-term usage of the cell.[29,59–63]

Today, most of the research efforts on PEM electrolysis focus on reducing costs and assembly complexity to allow the scale-up of the device through more sophisticated manufacturing processes.[64] The costs of PEM water electrolysis could be reduced with the replacement of the current benchmarking noble-metal catalysts (Pt or Pd) for HER with non-precious metals (such as MoS_x-based catalysts) or using Ir-based alloys for the OER.[65–74][75–80] Another approach is to maximize the dispersion of the noble catalysts by using catalyst supports with a high surface area.[51,81–85] Furthermore, decreasing the catalyst loading on the electrodes without sacrificing the cell's performance would also promote cost reduction. Currently, the catalyst loadings in the cathode and anode side are $0.5 - 1$ mg/cm^2 and around 2 mg/cm^2, respectively. Studies regarding the structure, porosity, design, and manufacturing of other components such as current collectors and electrolyzers have been performed to optimize the overall cell performance and decrease costs.[86–91] As mentioned before, the need for high-purity water is a major drawback due to the high cost of the purification processes and the lack of pure water in nature, hence, studies have been performed on the design of electrocatalysts for seawater splitting.[92]

## I.1.3. ARTIFICIAL PHOTOSYNTHESIS

Beyond the use of renewable power sources for the production of hydrogen as an energy carrier and, therefore, a fuel, artificial photosynthesis (APS) is seen as one possible way to solve the problems of global warming. The concept of APS intends to mimic natural photosynthesis processes, bringing together photo collection (light process), energy conversion, and CO_2 capture (dark processes).[93] The vast majority of stored energy on Earth is a product of natural photosynthesis.[94] In nature, the water is converted into molecular oxygen, while CO_2 is converted through the carbon dioxide reduction reaction (CO_2RR) into carbohydrates or other carbon-rich products (Equation I-15).

$$xCO_2 + yH^+ \rightarrow C_xH_yO_z^-$$ **Equation I-15**
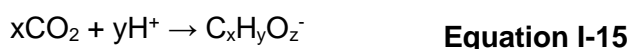
Photosynthesis is the largest and most efficient method for solar energy harvesting and conversion, therefore, artificial photosynthesis, and solar-driven CO_2RR, appear as appealing methods to store energy converted from the Sun; reduce atmospheric CO_2, and produce valuable chemicals.[95–99] The path towards efficient, long term and cost-effective APS systems require the development of ingenious reactor designs; catalysts with high turnover; efficient solar cells, and high throughput manufacturing processes.[100] Hence, the scientific community and policy makers must put their efforts together towards the development of green hydrogen technologies (described in section I.1.1.) and APS.

I.1.4. eSCALED PROJECT

The European School on Artificial Leaf: Electrodes and Devices, or eSCALED, focuses on the elaboration of an artificial leaf as a response to climate change, the accumulation of carbon dioxide in the atmosphere, and the emerging search for renewable and carbon-neutral energy technologies. Like a leaf in nature, eSCALED proposes to produce an artificial photosynthesis device, an "artificial leaf" capable of converting solar energy, H_2O, and CO_2 into "solar fuels" or commodities for chemistry in a stable and storable chemical form. The proposed eSCALED device combines a solar cell with a bio-inspired electrochemical stack where H_2O oxidation and H^+/CO_2 reduction are performed in microporous electrodes, mimicking the chloroplasts of a plant. Figure I-4 presents the proposed photoelectrochemical device, *i.e.*, an artificial leaf to perform artificial photosynthesis.
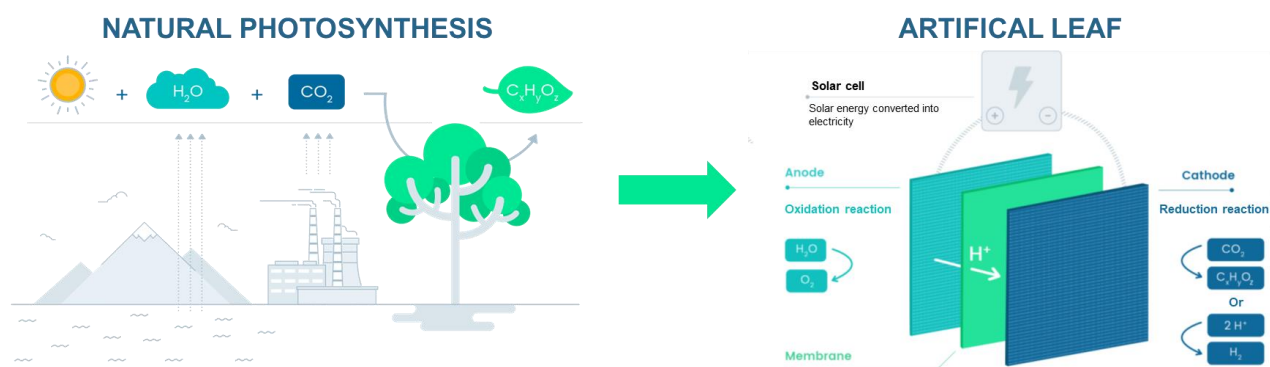
Figure I-4 – eSCALED's proposed artificial leaf architecture. Visit http://escaled-project.eu/ for more details.

Apart from promoting inter and multidisciplinary research and formation on biological/biochemical, inorganic, and soft matter, device engineering, and innovation, eSCALED targets the use of easy, cheap, and high throughput manufacturing processes, such as printing, based on organic and earth-abundant materials.

I.1.5. SCOPE OF MY WORK WITHIN eSCALED

Herein we describe the research work performed within early-stage researcher (ESR) training program 10 within the frame of the eSCALED Project. ESR 10 contributes to the eSCALED's artificial leaf device developing a cathode focused on the synthesis, characterization, and up-scaling of microporous polymer electrodes decorated with heterogeneous CO_2 and/or proton reduction catalyst. Therefore, to meet the needs of eSCALED and to converge with the expertise of the involved training institutions, the strategy to be followed should be defined according to the following assumptions:

- At the Institut des Sciences Analytiques et de Physico-Chimie pour l'Environnement et les Matériaux (IPREM), part of Université de Pau et des Pays de l'Adour (UPPA) in Pau (France),

the polymer-based electrodes will be developed, profiting from the expertise of the polymers' research group.

- The required microporosity will be studied with the expertise of the Laboratoire de Chimie des Matériaux Inorganiques (CMI), part of Université de Namur (Namur, Belgium), in the synthesis and development of porous materials for catalysis, based on zinc oxide.

- A secondment at the Laboratoire de Chimie des Processus Biologiques at the Collège de France (Paris, France) will be dedicated to studying the integration of the H^+ and/or CO_2 reduction heterogeneous catalysts into the microporous polymer electrodes.

- Finally, at the Functional Printing and Embedded Devices, part of Eurecat – Centre Tecnològic de Catalunya (Mataró, Spain), up-scalable and high throughput manufacturing processes, namely printing, will be employed for the deposition of the catalysts on large-area electron-conducting substrates.

I.2. STATE OF THE ART

To cope to develop microporous polymer electrodes decorated with heterogeneous H^+/CO_2 reduction catalysts as cathodes for eSCALED, the following requirements were identified:

- The polymer electrode must have mechanical compatibility with flexible substrates, such as proton exchange membranes.

- The polymer selected must be suitable for film formation and structuration.

- The polymer must be electron-conducting.

- The polymer should allow coupling (functionalization) with the catalysts or other functional groups for property tuning.

- Porous inorganic conducting or semiconducting materials as catalyst supports may be required for the heterogenization of the catalysts.

- The cathodes should be fabricated through up scalable and high-throughput manufacturing processes.

I.2.1. CONTROLLED RADICAL POLYMERIZATION FOR HETERO TELECHELIC POLYMERS

Controlled radical polymerization (CRP) has been established and developed over the last decades to overcome the limitations of free radical polymerization (FRP). The polymerization mechanism of FRP is given in Figure I-5.

INITIATION

$$I \rightarrow 2\,R\cdot$$

$$R\cdot + M \rightarrow RM\cdot$$

PROPAGATION

$$RM_1\cdot + M \rightarrow RM_2\cdot$$

$$RM_x\cdot + M \rightarrow RM_{x+1}\cdot$$

TERMINATION

Combination: $M_x\cdot + M_y\cdot \rightarrow M_{x+y}$

Disproportionation: $M_x\cdot + M_y\cdot \rightarrow M_x + M_y$
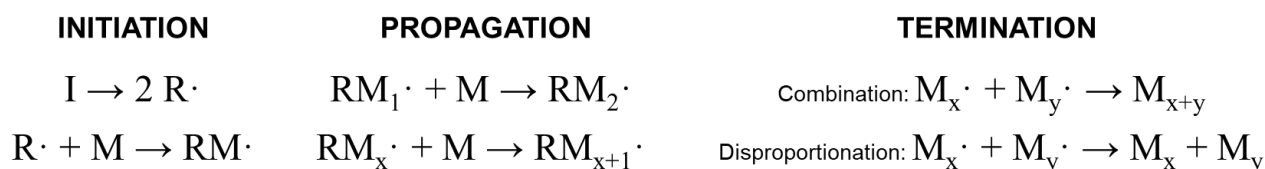
Figure I-5 – Steps of free radical polymerization.

FRP is initiated by the generation of active species, *i.e.*, free radicals (R·) from the decomposition of the initiator (I) which then react with the monomer and produce a new free radical (RM·). The polymer chains grow by successive addition of monomers until termination. This final step may occur by combination or disproportionation of the polymer chains at any time. In the first case, two growing chains (M_x·and M_y) react with each other and produce a single terminated, *i.e.*, non-reactive, polymer chain (M_{x+y}). Alternatively, by disproportionation, the two growing polymer chains interact via hydrogen abstraction, producing two polymer chains, one saturated and one unsaturated. [101] FRP is suitable for industrial scale since it does not require strict conditions for its polymerization process. However, in FRP the chain's termination rate prevails over the propagation, hence providing poor control of the molecular weight, end-functionality, molecular weight distribution, composition, and chain architecture.[102]
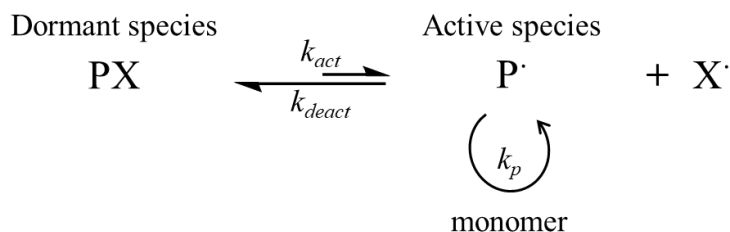
Controlled radical polymerizations (CRP) are the process of choice in macromolecular engineering, which has been expanding in the industry in recent years, to obtain functional polymers with well-defined architectures, predetermined molar masses, and low dispersity while keeping processing conditions close to the conventional process.[103]

Like classical radical polymerization, any controlled radical polymerization involves the initiation and propagation steps (k_p ~ 102-104 L.mol^{-1}.s^{-1}). However, for control to exist, the polymerization must make the irreversible termination reactions negligible. In the classical process, chain growth is irreversibly stopped during termination reactions by recombination and/or dismutation with very high rate constants (k_t ~ 108 L.mol^{-1}.s^{-1}). Controlling a radical polymerization is thus equivalent to promoting the propagation before any termination reaction according to Equation I-16:

$$\frac{v_p}{v_t} = \frac{k_p[P^{\bullet}][M]}{2k_t[P^{\bullet}]^2} \qquad \textbf{Equation I-16}$$

with [P] the concentration of growing chains (mol/L), [M] the concentration of monomer (mol/L), v_p, v_t, k_p, and k_t the velocities and constants of propagation and termination (L.mol^{-1}.s^{-1}), respectively.

The principle is then based on the use of a species reacting with the growing radical chains (P) by reversible and non-definitive terminations. An equilibrium shifted towards the so-called "dormant" species (PX) is established (Figure I-6). This equilibrium allows the lowering of the concentration of radicals in the medium and makes negligible irreversible termination reactions.
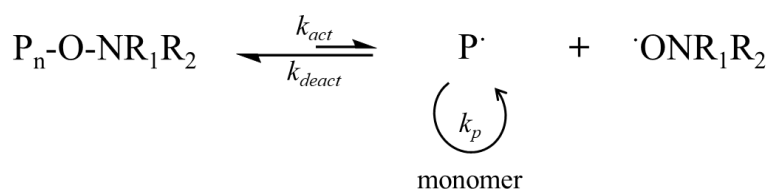
$$\text{Dormant species} \qquad\qquad \text{Active species}$$

$$\text{PX} \quad \xrightleftharpoons[k_{deact}]{k_{act}} \quad \text{P}^{\cdot} \quad + \quad \text{X}^{\cdot}$$

$$\left(\, k_p \,\right)$$

$$\text{monomer}$$

Figure I-6 – Equilibrium between dormant and active species during a controlled radical polymerization.

The control is also subject to rapid initiation before propagation. Thus, all the chains grow at the same speed and the exchanges between dormant species and active radical species are fast. Obtaining reactivatable macromolecular chains opens the way to the synthesis of structures not accessible by the classical radical polymerization process such as block copolymers obtained by chain extension.
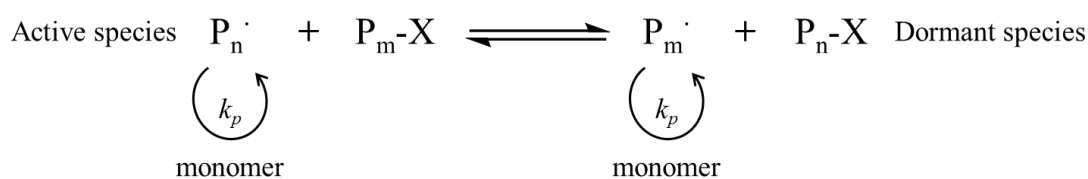
Three main CRP methods are usually distinguished in literature: stable nitroxide-controlled radical polymerization (NMP)[104], reversible addition-fragmentation chain transfer (RAFT)[105], and atom transfer radical polymerization (ATRP)[106].

- The first process, presented in Figure I-7, uses stable nitroxide radicals as counter radicals (X=R_1R_2NO- with R_1, R_2=alkyl, aryl, or forming a ring). The process is called NMP (nitroxide-mediated polymerization) or SFRP (stable free radical polymerization). It has its origins in the work of Gorges *et al.* in 1993 with the use of peroxide as an initiator and TEMPO as a nitroxyl radical for the polymerization of styrene.[107] Today, alkoxyamines (R_1R_2NOR) are preferred, and control is possible for styrene monomers, acrylate, and acrylamide in homogeneous and aqueous dispersed phases.

$$\text{P}_n\text{-O-NR}_1\text{R}_2 \quad \xrightleftharpoons[k_{deact}]{k_{act}} \quad \text{P}^{\cdot} \quad + \quad {}^{\cdot}\text{ONR}_1\text{R}_2$$

$$\left(\, k_p \,\right)$$

$$\text{monomer}$$

Figure I-7 – Equilibrium between dormant and active species during radical polymerization controlled by stable nitroxides (NMP).

- The second process, presented in Figure I-8, uses compounds carrying the thiocarbonylthio group (S=C-S) to control the polymerization. RAFT was described for the first time in described in 1995[108]. The growing chain $P_n{}^{\cdot}$ will add to a so-called dormant species, the chain P_m terminated by the RAFT agent, then generate an intermediate radical and release the growing chain $P_m{}^{\cdot}$ and the dormant species P_n bound to the RAFT agent. Propagation results in chain growth, and polymerization is controlled by establishing an equilibrium between dormant species and radical active species $P^{\cdot}$.

$$\text{Active species} \quad P_n{}^{\cdot} \quad + \quad P_m\text{-}X \quad \rightleftharpoons \quad P_m{}^{\cdot} \quad + \quad P_n\text{-}X \quad \text{Dormant species}$$

$$\left(k_p \right) \quad\quad\quad\quad\quad \left(k_p \right)$$

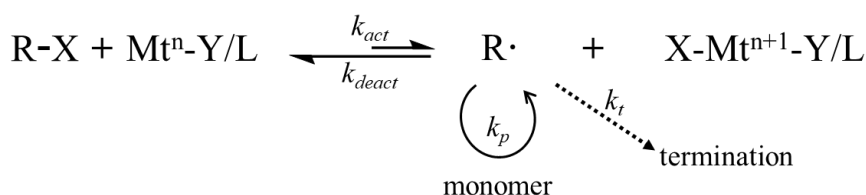$$\text{monomer} \quad\quad\quad\quad\quad \text{monomer}$$

Figure I-8 – Equilibrium between dormant and active species in RAFT.

- The third process, ATRP, uses transition metal complexes to establish active species/dormant species equilibrium. The origin of ATRP is attributed to the teams of Matyjaszewski *et al.*[109]17 and Sawamoto *et al.*[110] in 1995.

The mechanism of ATRP will be developed in the next section.

I.2.1.1. ATOM TRANSFER RADICAL POLYMERIZATION - ATRP

ATRP is a reversible redox process catalyzed by a transition metal complex (Mt^n-Y/L) generating radicals or active species. This complex consists of a transition metal (Mt^n) capable of expanding its coordination sphere and its oxidation number, usually a cuprous halide, a complexing (L), and a counterion able to form a covalent or ionic bond with the metal center. The homolytic cleavage of an alkyl halogen (R-X) generates one-electron oxidation (with a rate constant of activation k_{act}) of the metal complex (Mt^{n+1}-Y/L) and an organic radical R$\cdot$. Polymer chains grow by the addition of R$\cdot$ with the rate constant of propagation k_p. Termination reactions can also occur by coupling or disproportionation (k_t), however, it is very unlikely to happen in a well-controlled ATRP. The presence of the generated X-Mt^{n+1}-Y/L reversibly deactivates (k_{deact}) R$\cdot$ to form a halide-capped dormant polymer chain, minimizing the contribution of termination. The small contribution of terminated chains is accompanied by uniform growth of all the chains (narrow molecular weight distribution) due to the fast initiation and rapidly reversible deactivation. Figure I-9 illustrates a schematic of the ATRP mechanism.

$$\text{R-X} + Mt^n\text{-Y/L} \quad \underset{k_{deact}}{\overset{k_{act}}{\rightleftharpoons}} \quad \text{R}\cdot \quad + \quad \text{X-}Mt^{n+1}\text{-Y/L}$$

$$\left(k_p \right) \quad\quad\quad\quad k_t$$

$$\text{monomer} \quad\quad\quad \text{termination}$$

Figure I-9 – ATRP mechanism.

In summary, ATRP is a multicomponent system composed of a monomer, an initiator with a transferable (pseudo)halogen, a catalyst (a transition metal with a ligand) and can be carried in bulk, in solution, or an emulsion or suspension, *i.e.*, in a heterogeneous system.[106,109,111–116]

Through ATRP it is possible to synthesize hetero telechelic polymers, which are defined as polymeric molecules with functional groups at both end sides of the macromolecule backbone. They may have then the capacity to go into further reactions. Also, ATRP offers good control and uniform

growth of all polymer chains, which makes possible the tuning of chain length, *i.e.*, molecular weight (M_n). Moreover, through ATRP, after synthesis, the end-functionality of the polymer chain is preserved. These are key features for the present work to achieve low M_n polymers which can then be coupled to an electron-conducting block.[117]

I.2.2. CONDUCTING POLYMERS

As a class of materials, conducting polymers may be divided into two categories, the first give respect to polymers filled with additives having conducting properties, while the second defines the polymers which can propagate and generate charge carriers due to their backbone, they are called intrinsic conducting polymers.[118]

I.2.2.1. CATEGORY ONE: CONDUCTING COMPOSITE MATERIALS

In this case, the mixture of conducting materials such as carbon black, graphite powder, single or multi-walled carbon nanotubes (SWCNT or MWCNT, respectively), metal flakes, or fibers with polymer results in a conducting composite.[118] The conducting material improves the electrical conductivity while the polymeric matrix/binder promotes the mechanical strength and adhesion between particle/particle and particle/substrate. Poly(vinylidene fluoride) (PVDF), styrene-butadiene rubber (SBR), carboxymethyl cellulose (CMC), poly(methyl meth-acrylate) (PMMA), and poly(ethylene oxide) (PEO) are common polymer binders, accounting to 1 – 10 wt% of the solid content.[119]

In the present work, conducting composite materials with graphite powder as conducting filler were used to produce screen-printed electrodes. The use of such composite materials has been previously reported in the literature as suitable to produce reliable screen-printed working electrodes with suitable electron conductivity for electrochemical sensors.[120–122] Furthermore, graphite and carbon black/graphite screen-printing materials are considered to be commercially mature.[123]

I.2.2.2. CATEGORY TWO: INTRINSIC CONDUCTING POLYMERS

In 1978, the first intrinsic conducting polymer (ICP), polyacetylene, was discovered by Shirakawa.[124] The conductivity of such polymer was found to be improved by twelve orders of magnitude by oxidative doping.[125] ICPs merge the electric and optical properties characteristic of metals and semiconductors with the flexibility and easy manufacturing of polymers.[126] The electrical/electronic properties of such polymers are, in general, given by their π-conjugated systems, *i.e.*, a molecular structure of alternating single (σ) and double (π) bonds. Several ICPs have been investigated and reported, including polyacetylene; polypyrrole (PPy); poly(3,4-ethylene dioxythiophene) (PEDOT); polythiophene (PT), and polyaniline (PANI).[127,128]

Polyaniline (PANI), or poly(phenylinmineamine), is an ICP whose existence has been known since 1834 when Runge synthesized it for the first time. Due to its numerous possible applications

playing a conducting role in electronic devices, stability, and aniline's low cost, more and more studies have been focused on PANI.[129] PANI can be synthesized in two different ways, electrochemically or chemically. The chemical route is usually preferred when the polymer chain lengths are to be controlled.[130–134] It is composed of a mixture of reduced benzenoid and oxidized quinoid units, originating as a polymer with mixed oxidation states. Thus, PANI can exist in different forms due to its oxidation states. Figure I-10 presents the general molecular structure of PANI and its neutral three oxidation states.
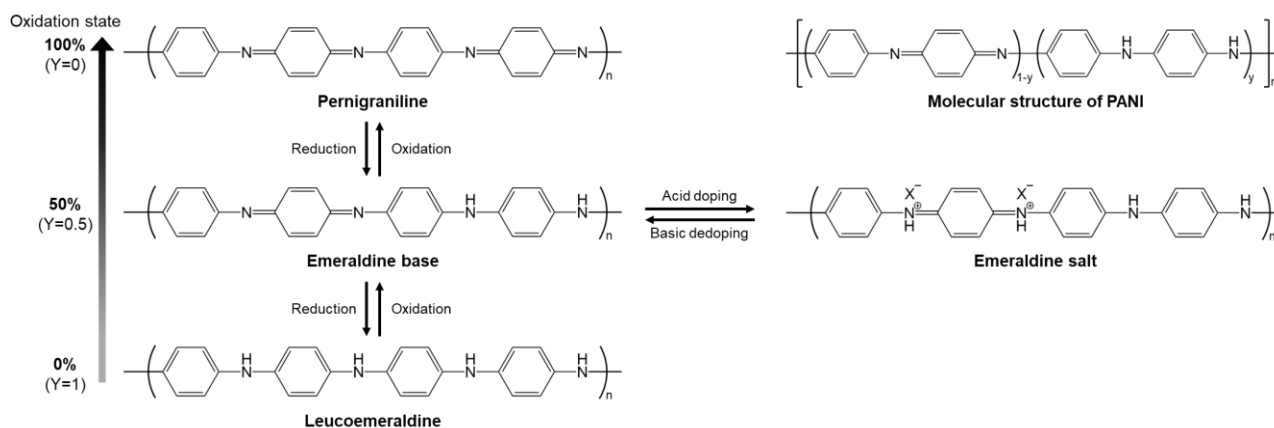

Figure I-10 - Molecular structure and oxidation states of PANI.

The average oxidation state can be defined by (1-Y). The fully reduced form (Y=1) is called leucoemeraldine (base, LEB), consists of only phenylene rings (4:0 benzenoid:quinoid ratio) bonded by amine nitrogen atoms, and presents insulating behavior. Half oxidized form (Y=0.5) is called emeraldine, the ratio of benzenoid to quinoid rings is 3:1, imine and amine nitrogen atoms are in equal numbers, and is the semiconducting form of PANI. Finally, the fully oxidized form, pernigraniline (Y=0) presents imine nitrogens only with benzenoid and quinoid rings present in the same number (1:1 ratio) and has insulating behavior.

Emeraldine is the only PANI form presenting conducting properties, which turns it into the most important oxidation state. Strong acids can dope the emeraldine base (EMB) form, hence, originating the emeraldine salt (EMS) form. In EMS, imine nitrogen atoms are protonated to give a polaronic form where spin and charge are delocalized along the polymer chain. EMS presents conducting properties and can be reversibly dedoped to the insulating EMB. LEB form can also be doped by an oxidative process, however, this mechanism is not explored in the present work. It is possible to assume that, considering the previous statements, a repeating unit of four rings and four nitrogens, a tetra-aniline (TANI) structure, rules PANI.

TANI is the shortest oligoaniline that can fully represent the emeraldine state of PANI and can be divided into three different groups, depending on the end groups it presents. Figure I-11 presents the three possibilities: phenyl/phenyl (Ph/Ph) end-capped TANI; phenyl/amine (Ph/NH$_2$) end-capped TANI and amine/amine end-capped (NH$_2$/NH$_2$) TANI.
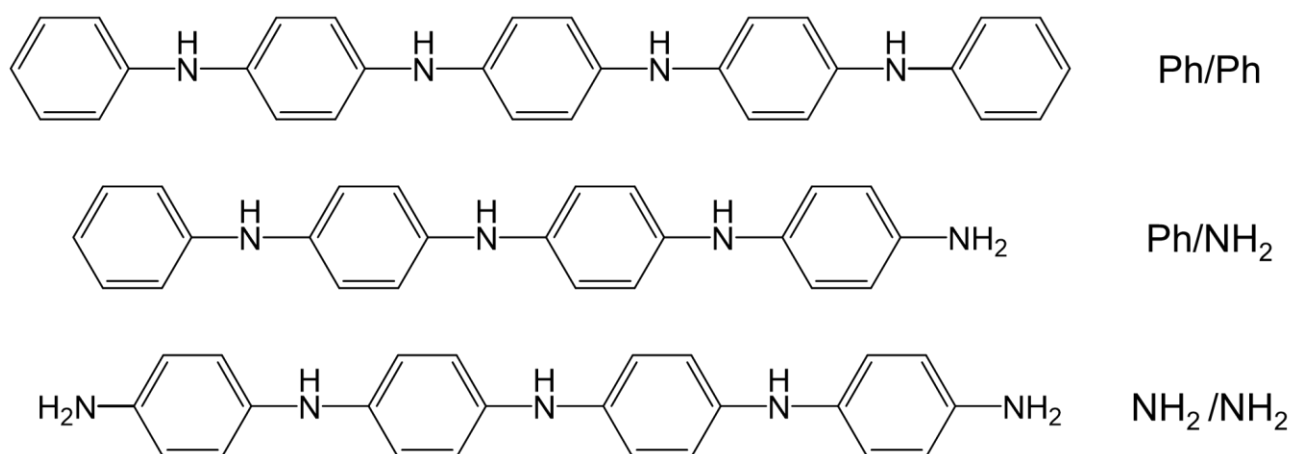
Figure I-11 – TANI with different end groups: phenyl/phenyl (Ph/Ph); phenyl/amine (Ph/NH₂) and amine-amine (NH₂/NH₂) end-capped TANI.

In the first case, a phenyl group is present on both sides of TANI, which does not allow TANI to take further reactions. In the present work, the second case, the Ph/NH$_2$ TANI is of great interest since it preserves the repeating unit of PANI with four rings and four nitrogens and it contains an amine group in one of the ends, thus allowing the coupling of TANI to other blocks.[135–137] Furthermore and contrarily to PANI, TANI possesses excellent solubility in common solvents. Together, the possible post-synthesis functionalization, great solubility, easy synthesis through chemical oxidative coupling, and the optical and electrical properties of TANI make this oligoaniline a designable, tunable, processable, and suitable candidate for different applications.[138,139] The use of TANI has been reported in the literature as a promising material for applications such as catalyst support for a Pt-based methanol oxidation reaction electrocatalyst; electrochromic devices, where TANI provides the coloration; biomedical applications where TANI is used as the electroactive agent; energy storage or molecular electronics.[134,138,140–151]

I.2.3. STRUCTURED MATERIALS

Structured materials are targeted in this work. These materials are of great interest, since the macropores favor the diffusion of molecules, consecutively improving the access to the active sites. Moreover, the size and shape selectivity promoted by the micro- and microporosity may also be of particular interest.[143] The composition of the copolymers has been chosen accordingly. All the structured materials and the method to obtain them are described and commented on within the following chapters and it has been decided to not detail further in this state-of-the-art chapter.

I.2.4. ZINC OXIDE

Zinc oxide (ZnO) is a n-type semiconductor material in group II-VI with a direct wide bandgap of 3.37 eV, *i.e.*, its bandgap sits in the near-UV. Its high exciton binding energy (60 meV) at room temperature. It presents high-thermomechanical stability, and good optoelectronic and piezoelectric properties. Furthermore, it is naturally abundant, presents low cost, has chemical stability in the air,

and is environmentally friendly and biologically safe, *i.e.,* it is compatible with living organisms.[152] Nowadays, 50 to 60 % of the used ZnO is present in rubber, ceramic, concrete manufacturing, cosmetics (as in skin ointment and sunscreens), and food and pigment industries.[153–156] ZnO has also been receiving the attention of the scientific community on ZnO application in devices such as light-emitting diodes (LEDs), gas sensors, solar cells, piezoelectric devices, transparent electronics, photodetectors, field emission devices.[157–162] Additionally, ZnO has been reported as an efficient photocatalyst in the reduction or oxidation of pollutants compounds such as organic dyes.[163]

Over recent years, research efforts were made to tune or improve the properties of ZnO by preparing ZnO nanostructures with different morphologies.[164,165] So far, different methods have been reported to prepare and control the size and morphology of the nanostructures. Most of the methods include multistep and long protocols, high temperature and/or vacuum, and expensive materials and/or equipment. One of the most common methods is vapor transport deposition, nonetheless, other techniques such as hydrothermal growth, sol-gel, electrodeposition, polymer-assisted growth, chemical vapor deposition, and molecular beam epitaxy have been frequently reported in the literature.[166–168] ZnO can be grown in several different nanostructures, due to its crystalline nature and it can be structured as one, two, and three-dimensional (1D, 2D, 3D) structures. 1D occurs as nanoneedles, -rods, -rings, -ribbons, -wires, -helixes, -combs, and -springs, and 2D as nanosheets and nanodisks. Finally, 3D structures of ZnO include nanoflowers and -spindles.[169–173] More recent approaches to ZnO structuration have been focusing on hierarchically mesoporous-macroporous structures of this metal oxide. The major and most promising features of hierarchically porous materials are their large surface area and high surface-to-volume ratio. Hence, the diffusion of reactants and mass transport is facilitated. These two properties demonstrated great potential in applications such as photocatalysis and gas sensors. 3D hierarchical ZnO structures usually derive from the assembly of 0D, 1D, and 2D ZnO nanostructures as building blocks by hydrothermal synthesis, while the pores are given by the removal of sacrificial templates by calcination or dissolution.[174–179]

Within the overall strategy of the present thesis, porous ZnO structures, due to their high surface area and porosity, creating micro reactor-like cavities, are of great interest to be employed as catalyst support in the electrodes. Furthermore, due to its semiconductor nature, ZnO may also be used as a photocatalyst once exposed to UV irradiation, therefore giving perspectives of hybrid photoelectrodes. In such a scenario, the electrons required for the hydrogen evolution reaction would be simultaneously supplied by an external power source by the electron-hole pairs generated through the photoelectric effect on the surface of ZnO.

I.2.5. PRINTED ELECTRONICS AND ELECTRODES: TECHNOLOGY AND FABRICATION TECHNIQUES

Printed electronics is seen as the 21st-century revolution in the printing industry, five hundred years after the establishment of the first prints in 1440 by Johannes Gutenberg. The term "printed electronics" refers to electronic circuits, displays, sensors, actuators, and electronic things produced through printing technology. Its potential low cost and the possibility to produce through large-area and simple fabrication processes are key advantages and explain why printing technology has received more attention and become popular in recent years. The rapid growth of the intelligent packaging and Internet-of-Things (IoT) markets have been strongly contributing to the fast development of printed electronics.[180–182] However, it is not expected that printed electronics will substitute conventional high-end electronics based on silicon. Thus, printed electronics open new opportunities for a new market and world of low-cost electronics fabricated on a variety of flexible, stretchable, and rigid surfaces (substrates) such as paper, textiles, or more conventional substrates such as polymeric films, glass, or wood.[183–190]

I.2.5.1. PRINTING TECHNIQUES

The functional materials printed are inks that can be semiconducting, conducting, or dielectric and can be processed through several fabrication methods divided into contact/analog printing, which requires a mask, and non-contact/digital printing, which does not require a mask. Figure I-12 presents the different manufacturing technologies in printed electronics.[191–193]
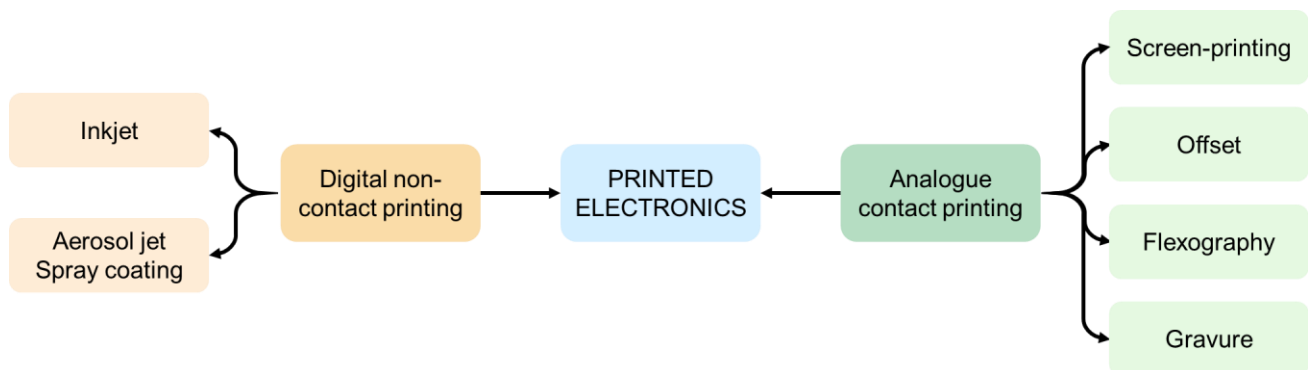
**Figure I-12 –** Printing technologies for printed electronics manufacturing.

Digital printing techniques are usually non-contact methods and include inkjet printing (the dominant) and aerosol printing, more frequently named "spray coating". Electro-photography is also a common technique, however, its industrial application is less significant.[194] In these techniques, the printing head is controlled by a computer which translates the desired design into a digital pattern. The printing head then moves according to the pattern transferring the ink to the substrate. Due to the digital control of the printing head, the ink will only be released, *i.e.*, transferred where it is needed to produce the desired design, which avoids unnecessary and undesired ink waste and promotes controlled deposition of the materials, obtaining thin layers with easy superimposition. However,

when compared to analog printing techniques, digital printing presents a very low throughput (Table I-4).[192,195–197]

Table I-4 – Characteristics of different printing techniques. Adapted from [196].

Technology	Throughput (m²/s)	Resolution (lines/cm)	Printing speed (m/min)
Gravure	3-60	20-400	100-1000
Offset	3-30	100-200	100-900
Screen-printing	2-3	50	10-15
Flexography	3-30	60	100-700
Inkjet	0.01-0.5	60-250	15-500

Analog printing techniques such as flexography, gravure, offset and screen printing is usually more suitable for industrial and large-scale production. Figure I-13 presents a schematic representation of gravure, flexography, and offset printing. These methods provide the fastest printing speeds; however, gravure printing has the highest throughput of them (Table I-4). Screen-printing is usually preferred in a lab and demonstration scale due to its lower throughput and printing speed. In analog printing, a solid object, *i.e.*, a mask, a screen, a roll, or a plate containing the design to be printed is used as the template, which is then transferred to the substrate.[198–201] Contrarily to digital printing techniques, in analog printing changing the design of the masks is a sluggish process since it involves rebuilding the physical template, which increases the costs of the process.
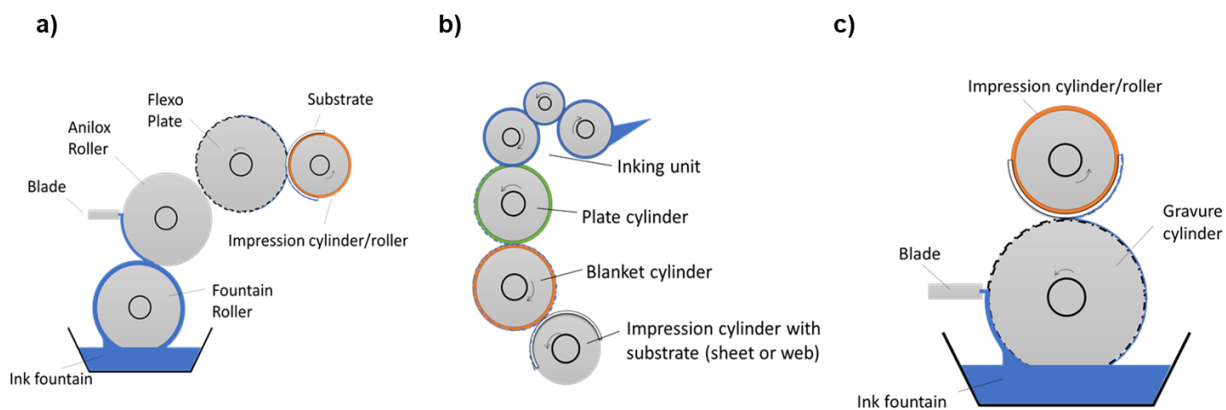

Figure I-13 – Analogue printing methods: **a)** flexography, **b)** offset, and **c)** gravure printing. Adapted from [191].

Printing techniques present a great advantage to the fabrication of PEM electrolyzers, due to their low cost, fast speed, and high throughput. Spray coating, inkjet, and screen printing were already reported in the deposition of the catalyst layer or membrane for fuel cells.[64,202–207] However, fully printed PEM electrolyzers have not been described yet in the literature.

I.2.5.2. SCREEN PRINTING

Screen printing is a well-developed and easy-to-use technique suitable for large-area applications. During its operation a flexible metal or rubber blade (also named a squeegee) moves

squeezed the ink/paste to pass through the mask openings (mesh), producing the desired design on the substrate. The mesh used may be polymeric (polyamide/polyester) or metallic (steel). The inks used in this technique usually present high viscosity (500 – 5000 cP) which is translated into thick layers (5 – 100 μm).[208,209] In its most conventional configuration, screen-printing is used in a flatbed configuration as presented in Figure I-14 a). However, flatbed screen printing is slow and is not suitable for fast large-scale production. Thus, rotary screens were developed to enable a fast and higher throughput continuous rotary screen-printing process. In this case, a printing cylinder containing the ink and a blade inside and the screen around rotates to transfer the ink onto the substrate (Figure I-14 b)).[119,210,211]
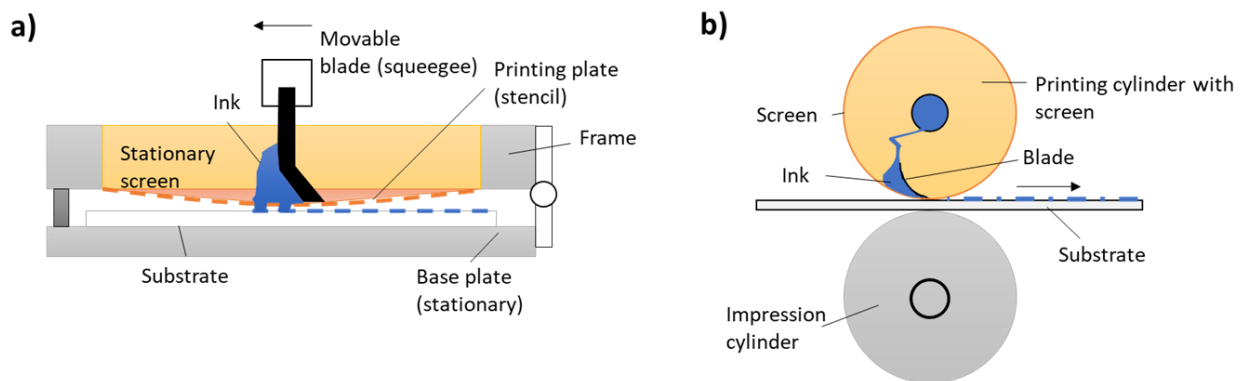
Figure I-14 – Schematic representation of **a)** flat-to-flat and **b)** round-to-round screen-printing techniques. Adapted from [191].

I.2.5.3. SPRAY-COATING

Spray coating is, although it is not always considered a printing technique, a fast, cost-effective, and efficient method, similar to inkjet printing, for large-scale manufacturing. In this technique, the spray head is equipped with a computerized numerical control (CNC) system. The ink infuses rate is set by a syringe pump, while a gas (such as nitrogen) is fed and fluxed through a fluxing system to the nozzle, atomizing the ink (Figure I-15).[212,213]
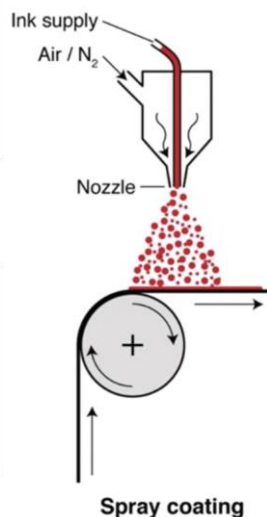
Figure I-15 – Schematic illustration of spray coating. Adapted from [214].

Figure I-16 (left) illustrates an example of the experimental setup including a hot bed that may be used to promote the solvent evaporation and/or adhesion of the deposited materials to the substrate.
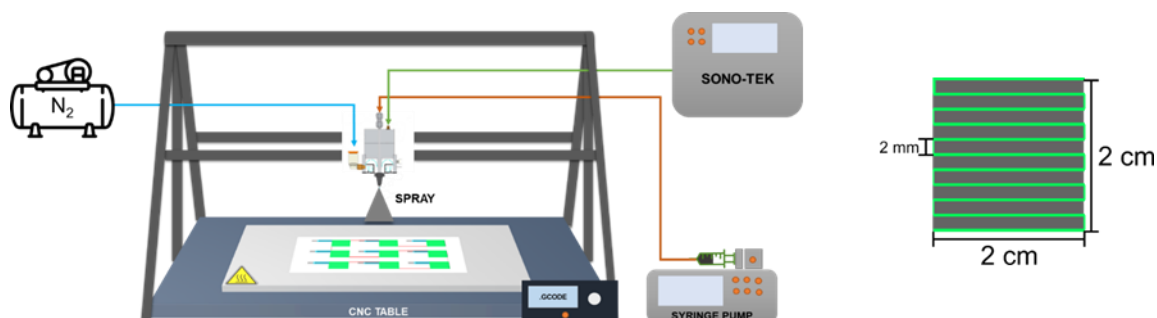

Figure I-16 – Left: Ultrasonic spray setup including a CNC table; heating bed, compressed N_2 feed, ink feed provided by a syringe pump; the Sono-Tek fluxing system, air, and flux controller, and ultrasonic nozzle. **Right:** Spray path for catalyst deposition (green line) over 4 cm^2 printed gas diffusion layer (GDL).

The spraying head then moves at a certain height and speed following a digitally designed path as exemplified in Figure I-16 (right) to produce the desired shape design and homogenous surface coating (shadow masks may be used to help the pattern formation). The inks are usually constituted by high vapor pressure organic solvents so that the droplets dry at their impact against the substrate. However, if the vapor pressure is too high, the adhesion to the substrate is poor. Moreover, if the vapor pressure is low, the ink droplets won't dry fast enough and will be pushed sideward by the spray jet. Spray coating is compatible with roll-to-roll processes, however, the produced ink mist brings risks of contamination, which may be challenging to avoid.[214,215]

I.3. STRATEGY PROPOSED

The general concept of the cathode architecture proposed is presented in Figure I-17 a).
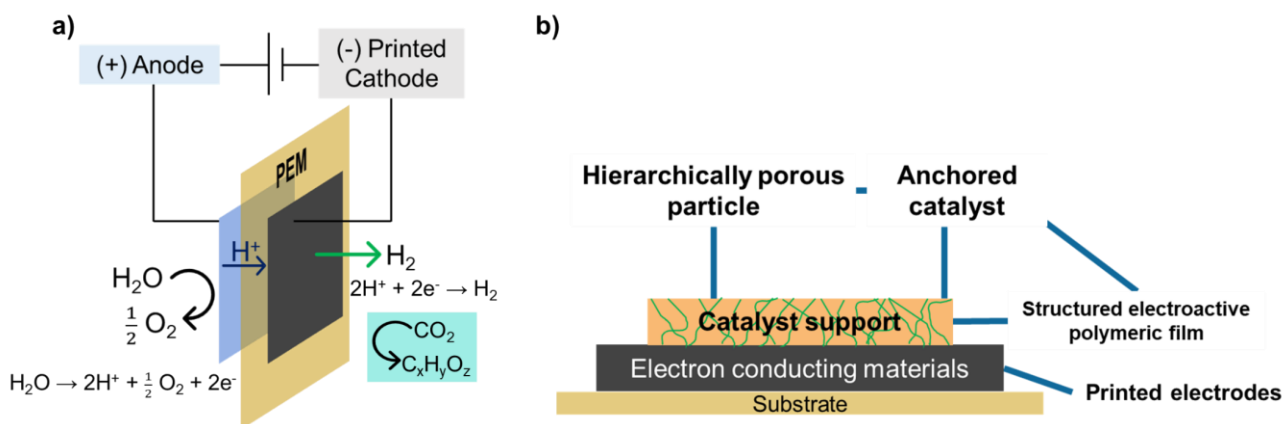
Figure I-17 – Conceptual illustration of a membrane electrode assembly (MEA) containing a printed cathode for H^+/CO_2 reduction **(a)** and a cross-sectional illustration of the architecture of the fully printed cathode.

The strategy presented in this thesis aims for the development of a fully printed cathode for H^+/CO_2 reduction (see Figure I-17 b). Following a bottom-up approach, at first, an electron-conducting carbon-based material is printed, *i.e.*, a printed electrode, on an inert polymer foil or proton exchange membrane as substrate (Figure II-18).
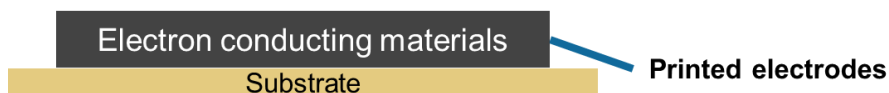

Figure I-18 – The first layer of the proposed fully printed cathode for H^+/CO_2 reduction: a carbon-based electrode printed on a polymer-based flexible substrate.

This first layer is the current collector and, therefore, must present satisfactory electron conductivity and mechanical compatibility with the substrate. Furthermore, the printed electrode must present satisfactory mechanical, chemical, and thermal stability and durability at pH levels between 2 and 7, and temperature ranging from room temperature (RT ≈ 23 °C) to 80 °C.

On top of the printed electrode (see Figure I-19), a catalyst-supporting layer is cast (or printed). This layer must be mechanically compatible with the carbon-based printed electrode and provide an electron-conducting matrix to feed the catalyst with the necessary electrons for the H^+/CO_2 reduction reaction to take place.
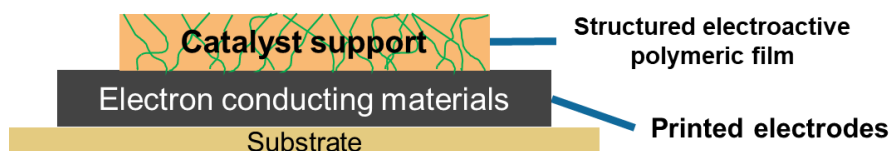
Figure I-19 – Second layer of the fully printed H^+/CO_2 reduction electrode: a catalyst-supporting layer based on a structured electroactive polymeric film.

For this purpose, an electroactive polymeric film will be developed. As starting material, a polystyrene (PS) homopolymer, a standard polymer chemistry point of view, will be prepared by CRP, specifically ATRP. The synthesis of PS through ATRP will be studied by targeting hetero telechelic polymer chains, avoiding the termination of the chains, hence allowing the coupling with conducting block. A Ph/NH_2 TANI was selected as conducting block since it preserves the repeating unit of PANI and its amine group in one of the ends, thus allowing the coupling of TANI to other blocks. The product of the coupling reaction between hetero telechelic PS and Ph/NH_2 TANI, *i.e.*, TANI end-capped PS, will be processed into films. This material should be suitable for film-forming and surface structuration into micropores, promoting the higher active surface area, and increasing the number of active sites for the H^+/CO_2 reduction reaction to take place. To meet the requirements in terms of microporosity, the structuration of the films will be studied through the breath figure technique. If the mechanical and processability properties of the TANI end-capped PS are not satisfactory, a second monomer unit will be required for the optimization of such properties.

Finally, the selected heterogeneous catalysts for H^+/CO_2 reduction to be immobilized on the previous catalyst supporting layer are molecular catalysts from the bipyridine; terpyridine, or cyclam family, following the expertise of the research group in Collège de France and the outputs from other early-stage researchers within the eSCALED Project. Two methods for immobilization of heterogeneous catalysts for H^+/CO_2 reduction are proposed:

1.   The first consists of the functionalization of the heterogeneous catalysts with TANI. In this approach, TANI is expected to act as an electron pathway and adhesion promoter between the molecular catalyst and the TANI end-capped polymer within the supporting matrix by π-π stacking, hence immobilizing the molecular catalyst on the surface of the structured film (see Figure I-20).
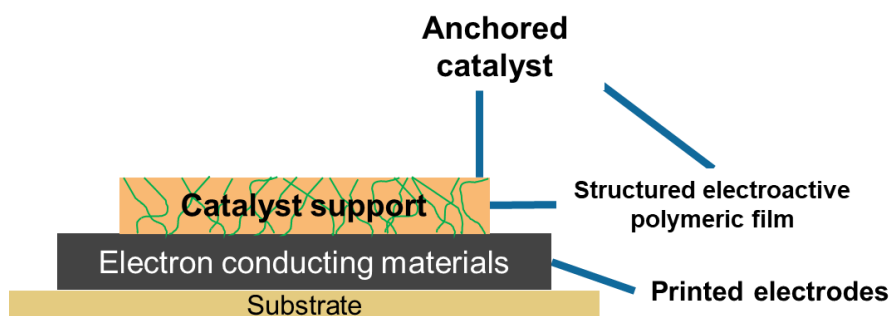
Figure I-20 – First method proposed for the immobilization of the heterogeneous catalysts for H^+/CO_2 reduction on the catalyst supporting layer: anchoring by functionalization of the molecular catalyst.

2.   The second method consists of immobilizing the catalysts into the pores of inorganic hierarchically porous structures (see Figure I-21).
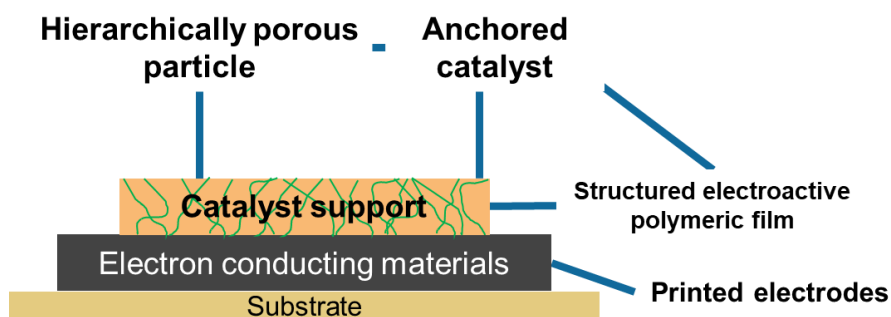
Figure I-21 – The second method proposed for the immobilization of the heterogeneous catalysts for H^+/CO_2 reduction on the catalyst supporting layer: immobilizing the catalysts into the pores of inorganic hierarchically porous structures.

The targeted hierarchically porous materials are derivatives of metal-organic frameworks (MOFs), hence inheriting the porosity of the MOF and creating high surface area structures to host the H^+/CO_2 reduction processes.

In conclusion, the main goal of this thesis is to develop a cathode focused on the synthesis, characterization, and up-scaling of microporous polymer electrodes decorated with a heterogeneous H^+/CO_2 reduction catalyst. To achieve this goal, three main objectives are defined:

- **Objective 1:** to develop structured electroactive polymer films as a catalyst supporting layer.
- **Objective 2:** to investigate strategies to immobilize the catalyst on the catalyst-supporting layer developed and for this purpose two approaches are proposed: anchoring the catalyst by functionalization and developing hierarchical porous particles to carry/host the electrocatalyst.
- **Objective 3:** to study and define a methodology based on printed electronics to achieve novel functional cathodes for artificial photosynthesis.

The works developed in this thesis are presented divided into four chapters presented within the general introduction and the next chapter will be dedicated to structured electron-conducting polymeric film elaboration, describing the works performed to cope with **Objective 1**.

I.4. BIBLIOGRAPHY

[1]   F. Dawood, M. Anda, G. M. Shafiullah, *Int. J. Hydrogen Energy* **2020**, *45*, 3847.

[2]   S. Boehm, K. Lebling, K. Levin, H. Fekete, J. Jaeger, R. Waite, A. Nilsson, J. Thwaites, R. Wilson, A. Geiges, C. Schumer, M. Dennis, K. Ross, S. Castellanos, R. Shrestha, N. Singh, M. Weisse, L. Lazer, L. Jeffery, L. Freehafer, E. Gray, L. Zhou, M. Gidd, M. Gavin, *State of Climate Action 2021: Systems Transformations Required to Limit Global Warming to 1.5°C*, Washington, DC, **2021**.

[3]   IRENA, *REthinking Energy: Renewable Energy and Climate Change*, **2015**.

[4]   T. Bridges, R. Merzian, *Hydrogen and Climate: Trojan Horse or Golden Goose*, **2019**.

[5]   C. Stockwell, A. Geiges, D. Ramalope, M. Gidden, B. Hare, H. Fekete, S. Gonzales-Zuñiga, F. Hans, N. Höhne, *Climate Action Tracker | Climate Summit Momentum: Paris Commitments Improved Warming Estimate to 2.4°C*, **2021**.

[6]   U. Nations, *Paris Agreement*, **2015**.

[7]   H. Fekete, N. Höhne, L. Jeffery, M. Moisio, M. J. de V. Casas, F. Hans, S. Mooldijk, L. Nascimento, N. Illenseer, C. Stockwell, C. Fyson, A. Geiges, D. Ramalope, B. Hare, M. Gidden, J. Horsch, G. Ganti, M. Schaeffer, *Climate Action Tracker | Global Update September 2021*, **2021**.

[8]   European Commission, *The European Green Deal*, Brussels, **2019**.

[9]   European Commission, *A Hydrogen Strategy for a Climate-Neutral Europe*, Brussels, **2020**.

[10]   Hydrogen Europe, *Hydrogen Roadmap Europe: A Sustainable Pathway for the European Energy Transition*, Luxembourg, **2019**.

[11]   European Commission, *Hydrogen Energy and Fuel Cells: A Vision of Our Future*, Brussels, **2003**.

[12]   E. Union, *EU Energy in Figures 2021*, Publications Office Of The European Union, Luxembourg, **2021**.

[13]   T. R. Cook, D. K. Dogutan, S. Y. Reece, Y. Surendranath, T. S. Teets, D. G. Nocera, *Chem. Rev.* **2010**, *110*, 6474.

[14]   N. S. Lewis, *Science (80-.).* **2007**, *315*, 798.

[15]   H. B. Gray, *Nat. Chem.* **2009**, *1*, 7.

[16]   S. Calnan, R. Bagacki, F. Bao, I. Dorbandt, E. Kemppainen, C. Schary, R. Schlatmann, M. Leonardi, S. A. Lombardo, R. G. Milazzo, S. M. S. Privitera, F. Bizzarri, C. Connelli, D. Consoli, C. Gerardi, P. Zani, M. Carmo, S. Haas, M. Lee, M. Mueller, W. Zwaygardt, J. Oscarsson, L. Stolt, M. Edoff, T. Edvinsson, I. B. Pehlivan, *Sol. RRL* **2021**, *2100479*, 2100479.

[17]   H. Stančin, H. Mikulčić, X. Wang, N. Duić, *Renew. Sustain. Energy Rev.* **2020**, *128*, 109927.

[18] A. I. Osman, N. Mehta, A. M. Elgarahy, M. Hefny, A. Al-Hinai, A. H. Al-Muhtaseb, D. W. Rooney, *Environ. Chem. Lett.* **2022**, *20*, 153.

[19] IRENA, *World Energy Transitions Outlook: 1.5°C Pathway*, Abu Dhabi, **2021**.

[20] F. Gérard, L. van Nuffel, T. Smit, J. Yearwood, O. Černý, J. Michalski, M. Altmann, *Opportunities for Hydrogen Energy Technologies Considering the National Energy & Climate Plans*, Rotterdam, **2020**.

[21] G. W. Crabtree, M. S. Dresselhaus, *MRS Bull.* **2008**, *33*, 421.

[22] M. Ozturk, I. Dincer, *Int. J. Hydrogen Energy* **2021**, *46*, 31511.

[23] A. Scipioni, A. Manzardo, J. Ren, Eds. , *Hydrogen Economy. Supply Chain, Life Cycle Analysis and Energy Transition for Sustainability*, Academic Press, **2017**.

[24] J. Chatzimarkakis, C. Levoyannis, A. van Wijk, F. Wouters, *Hydrogen Act: Towards the Creation of the European Hydrogen Economy*, **2021**.

[25] A. Al-Qahtani, B. Parkinson, K. Hellgardt, N. Shah, G. Guillen-Gosalbez, *Appl. Energy* **2021**, *281*, 115958.

[26] G. Pawelec, *Hydrog. Eur. Clean Hydrog. Monit.* **2020**, 6.

[27] M. Newborough, G. Cooley, *Fuel Cells Bull.* **2020**, *2020*, 16.

[28] G. Kakoulaki, I. Kougias, N. Taylor, F. Dolci, J. Moya, A. Jäger-Waldau, *Energy Convers. Manag.* **2021**, *228*, 113649.

[29] M. Carmo, D. Stolten, in *Sci. Eng. Hydrog. Energy Technol.* (Ed.: P.E.V. de Miranda), Elsevier, **2019**, pp. 165–199.

[30] IRENA, *Green Hydrogen: A Guide to Policy Making*, Abu Dhabi, **2020**.

[31] J. Cihlar, A. Villar Lejarreta, A. Wang, F. Melgar, J. Jens, P. Rio, *Hydrogen Generation in Europe: Overview of Costs and Key Benefits*, Luxembourg, **2020**.

[32] IRENA, *Global Renewables Outlook: Energy Transformation 2050*, **2020**.

[33] J. Proost, *Int. J. Hydrogen Energy* **2020**, *45*, 17067.

[34] U. Nations, *The Sustainable Development Goals Report 2021*, **2021**.

[35] S. Kolb, T. Plankenbühler, K. Hofmann, J. Bergerson, J. Karl, *Renew. Sustain. Energy Rev.* **2021**, *146*, 111147.

[36] S. Holger, K. Jan, Z. Petra, S. Andrea, H. Jürgen-friedrich, *Energy Procedia* **2017**, *105*, 3038.

[37] G. Benoît Norris, C., Traverso, M., Neugebauer, S., Ekener, E., Schaubroeck, T., Russo Garrido, S., Berger, M., Valdivia, S., Lehmann, A., Finkbeiner, M., Arcese, Ed. , *Guidelines for Social Life Cycle Assessment of Products and Organizations 2020*, **2020**.

[38] S. Dutta, *Energy & Fuels* **2021**, *35*, 11613−11639.

[39] E. S. Andrews, L.-P. Barthel, B. Tabea, C. Benoît, A. Ciroth, C. Cucuzzella, C.-O. Gensch, J. Hébert, P. Lesage, A. Manhart, P. Mazeau, *Guidelines for Social Lyfe Cycle Assessment of Products*, United Nations Environnement Programme, **2009**.

[40]   IRENA, *Hydrogen: A Renewable Energy Perspective*, **2019**.

[41]   B. Lane, J. Reed, B. Shaffer, S. Samuelsen, *Int. J. Hydrogen Energy* **2021**, *46*, 27293.

[42]   K. Kalyanasundaram, M. Graetzel, *Curr. Opin. Biotechnol.* **2010**, *21*, 298.

[43]   A. Shatskiy, A. A. Bardin, M. Oschmann, R. Matheu, J. Benet-Buchholz, L. Eriksson, M. D. Kärkäs, E. V. Johnston, C. Gimbert-Suriñach, A. Llobet, B. Åkermark, *ChemSusChem* **2019**, *12*, 2251.

[44]   C. Wei, R. R. Rao, J. Peng, B. Huang, I. E. L. Stephens, M. Risch, Z. J. Xu, Y. Shao-horn, *Adv. Mater.* **2019**, *1806296*, 1.

[45]   G. Gahleitner, *Int. J. Hydrogen Energy* **2013**, *38*, 2039.

[46]   A. Smoliński, N. Howaniec, *Int. J. Hydrogen Energy* **2020**, *45*, 5607.

[47]   C. Wulf, P. Zapp, A. Schreiber, *Front. Energy Res.* **2020**, *8*, DOI 10.3389/fenrg.2020.00191.

[48]   C. Lamy, *Int. J. Hydrogen Energy* **2016**, *41*, 15415.

[49]   D. S. Falcão, A. M. F. R. Pinto, *J. Clean. Prod.* **2020**, *261*, 121184.

[50]   D. Bessarabov, P. Millet, *PEM Water Electrolysis, Volume 1*, Academic Press, **2018**.

[51]   D. Ding, J. Huang, X. Deng, K. Fu, *Energy & Fuels* **2021**, *35*, 15472.

[52]   S. Shiva Kumar, V. Himabindu, *Mater. Sci. Energy Technol.* **2019**, *2*, 442.

[53]   L. J. Nuttall, A. P. Fickett, W. A. Titterington, in *Hydrog. Energy* (Ed.: T.N. Veziroglu), Springer US, Boston, MA, **1975**, pp. 441–455.

[54]   J. M. Gohil, K. Dutta, *Polym. Adv. Technol.* **2021**, 1.

[55]   S. Trasatti, *J. Electroanal. Chem.* **1999**, *476*, 90.

[56]   M. Carmo, D. L. Fritz, *Int. J. Hydrogen Energy* **2013**, *38*, 4901.

[57]   A. S. Aricò, S. Siracusano, N. Briguglio, V. Baglio, A. Di Blasi, V. Antonucci, *J. Appl. Electrochem.* **2013**, *43*, 107.

[58]   O. Schmidt, A. Gambhir, I. Staffell, A. Hawkes, J. Nelson, S. Few, *Int. J. Hydrogen Energy* **2017**, *42*, 30470.

[59]   J. Chi, H. Yu, *Chinese J. Catal.* **2018**, *39*, 390.

[60]   F. M. Sapountzi, J. M. Gracia, C. J. (Kees-J. Weststrate, H. O. A. Fredriksson, J. W. (Hans) Niemantsverdriet, *Prog. Energy Combust. Sci.* **2017**, *58*, 1.

[61]   C. Lamy, P. Millet, *J. Power Sources* **2020**, *447*, 227350.

[62]   C. Li, J.-B. Baek, *Nano Energy* **2021**, *87*, 106162.

[63]   A. Léon, A. Micero, B. Ludwig, A. Brisse, *J. Power Sources* **2021**, *510*, 230346.

[64]   A. Mayyas, M. Mann, *Procedia Manuf.* **2019**, *33*, 508.

[65]   A. E. Hughes, N. Haque, S. A. Northey, S. Giddey, *Resources* **2021**, *10*, 93.

[66]   S. Zhang, X. Zhang, Y. Rui, R. Wang, X. Li, *Green Energy Environ.* **2021**, *6*, 458.

[67]   J. N. Hansen, H. Prats, K. K. Toudahl, N. Mørch Secher, K. Chan, J. Kibsgaard, I. Chorkendorff, *ACS Energy Lett.* **2021**, *6*, 1175.

[68]   M. Bernt, A. Hartig-Weiß, M. F. Tovini, H. A. El-Sayed, C. Schramm, J. Schröter, C.

Gebauer, H. A. Gasteiger, *Chemie Ing. Tech.* **2020**, *92*, 31.

[69] K. Ayers, *Curr. Opin. Chem. Eng.* **2021**, *33*, 100719.

[70] J. P. Hughes, J. Clipsham, H. Chavushoglu, S. J. Rowley-Neale, C. E. Banks, *Renew. Sustain. Energy Rev.* **2021**, *139*, 110709.

[71] D. Xu, M. B. Stevens, M. R. Cosby, S. Z. Oener, A. M. Smith, L. J. Enman, K. E. Ayers, C. B. Capuano, J. N. Renner, N. Danilovic, Y. Li, H. Wang, Q. Zhang, S. W. Boettcher, *ACS Catal.* **2019**, *9*, 7.

[72] M. Inaba, A. W. Jensen, G. W. Sievers, M. Escudero-Escribano, A. Zana, M. Arenz, *Energy Environ. Sci.* **2018**, *11*, 988.

[73] M. P. Browne, H. Nolan, G. S. Duesberg, P. E. Colavita, M. E. G. G. Lyons, *ACS Catal.* **2016**, *6*, 1.

[74] H. Nolan, M. P. Browne, *Curr. Opin. Electrochem.* **2020**, *21*, 55.

[75] C. C. L. L. McCrory, S. Jung, J. C. Peters, T. F. Jaramillo, *J. Am. Chem. Soc.* **2013**, *135*, 16977.

[76] A. C. C. L. Mccrory, S. Jung, I. M. Ferrer, S. M. Chatman, C. Jonas, T. F. Jaramillo, *J. Am. Chem. Soc.* **2015**, *137*, 4347.

[77] J. Yang, M. Je, X. Zeng, Y. Sei, J. Lee, S. Mook, Y. Yin, *Electrochem. commun.* **2021**, *131*, 107118.

[78] L. Sun, Q. Luo, Z. Dai, F. Ma, *Coord. Chem. Rev.* **2021**, *444*, 214049.

[79] Y. Zheng, Y. Jiao, Y. Zhu, L. H. Li, Y. Han, Y. Chen, M. Jaroniec, S. Qiao, **2016**, DOI 10.1021/jacs.6b11291.

[80] N. R. Sahraie, U. I. Kramm, J. Steinberg, Y. Zhang, A. Thomas, T. Reier, J. Paraknowitsch, P. Strasser, *Nat. Commun.* **2015**, *6*, 8618.

[81] X. Chia, M. Pumera, *Nat. Catal.* **2018**, *1*, 909.

[82] D. H. Kweon, M. S. Okyay, S. Kim, J.-P. Jeon, H.-J. Noh, N. Park, J. Mahmood, J. Baek, *Nat. Commun.* **2020**, *11*, 1278.

[83] N. Mansor, T. S. Miller, I. Dedigama, A. Belen, J. Jia, V. Brázdová, C. Mattevi, C. Gibbs, D. Hodgson, P. R. Shearing, C. A. Howard, F. Corà, M. Shaffer, D. J. L. Brett, P. F. Mcmillan, *Electrochim. Acta* **2016**, *222*, 44.

[84] H. Yang, M. Driess, P. W. Menezes, *Adv. Energy Mater.* **2021**, *11*, 2102074.

[85] A. Jorge, I. Dedigama, T. Miller, P. Shearing, D. Brett, P. McMillan, *Nanomaterials* **2018**, *8*, 432.

[86] S. Weusten, L. Murrer, M. de Groot, J. van der Schaaf, *AIChE J.* **2021**, *67:e17263*.

[87] A. Zinser, G. Papakonstantinou, K. Sundmacher, *Int. J. Hydrogen Energy* **2019**, *44*, 28077.

[88] H. Ito, T. Maeda, A. Nakano, C. Min, M. Ishida, A. Kato, T. Yoshida, *Int. J. Hydrogen Energy* **2012**, *37*, 7418.

[89] H. Ito, T. Maeda, A. Nakano, A. Kato, T. Yoshida, *Electrochim. Acta* **2013**, *100*, 242.

[90]   S. Toghyani, E. Afshari, E. Baniasadi, *Electrochim. Acta* **2018**, *290*, 506.

[91]   X. Peng, P. Satjaritanun, Z. Taie, L. Wiles, A. Keane, C. Capuano, I. V Zenyuk, N. Danilovic, *Adv. Sci.* **2021**, *2102950*.

[92]   S.-C. Ke, R. Chen, G.-H. Chen, X.-L. Ma, *Energy & Fuels* **2021**, *35*, 12948.

[93]   A. F. Collings, C. Critchley, in *Artif. Photosynth.* (Eds.: A.F. Collings, C. Critchley), Wiley-VCH Verlag GmbH & Co. KGaA, Weinheim, FRG, **2006**, pp. I–XXVI.

[94]   J. T. Muckerman, E. Fujita, in *ACS Symp. Ser.*, Elsevier Ltd, **2010**, pp. 283–312.

[95]   A. Sacco, R. Speranza, U. Savino, J. Zeng, M. A. Farkhondehfal, A. Lamberti, A. Chiodoni, C. F. Pirri, *ACS Sustain. Chem. Eng.* **2020**, *8*, 7563.

[96]   D. Gust, T. A. Moore, A. L. Moore, *ChemInform* **2010**, *41*, DOI 10.1002/chin.201016268.

[97]   C. R. Cox, J. Z. Lee, D. G. Nocera, T. Buonassisi, *Proc. Natl. Acad. Sci.* **2014**, *111*, 14057.

[98]   S. Esiner, R. E. M. Willems, A. Furlan, W. Li, M. M. Wienk, R. A. J. Janssen, *J. Mater. Chem. A* **2015**, *3*, 23936.

[99]   J. J. H. Pijpers, K. Sung, S. Y. Reece, D. G. Nocera, T. D. Jarvi, A. J. Esswein, J. A. Hamel, *Science (80-.).* **2011**, *334*, 645.

[100] D. G. Nocera, *Acc. Chem. Res.* **2017**, *50*, 616.

[101] J. W. Nicholson, *The Chemistry of Polymers*, Royal Society Of Chemistry, **2006**.

[102] J. Brandrup, E. H. Immergut, E. A. Grulke, Eds. , *Polymer Handbook*, John Wiley & Sons, Inc., **1999**.

[103] M. Destarac, *Macromol. React. Eng.* **2010**, *4*, 165.

[104] C. J. Hawker, A. W. Bosman, E. Harth, *Chem. Rev.* **2001**, *101*, 3661.

[105] J. Chiefari, Y. K. B. Chong, F. Ercole, J. Krstina, J. Jeffery, T. P. T. Le, R. T. A. Mayadunne, G. F. Meijs, C. L. Moad, G. Moad, E. Rizzardo, S. H. Thang, *Macromolecules* **1998**, *31*, 5559.

[106] K. Matyjaszewski, J. Xia, *Chem. Rev.* **2001**, *101*, 2921.

[107] M. K. Georges, R. P. N. Veregin, P. M. Kazmaier, G. K. Hamer, *Macromolecules* **1993**, *26*, 2987.

[108] J. Krstina, G. Moad, E. Rizzardo, C. L. Winzor, C. T. Berge, M. Fryd, *Macromolecules* **1995**, *28*, 5381.

[109] J.-S. Wang, K. Matyjaszewski, *J. Am. Chem. Soc.* **1995**, *117*, 5614.

[110] M. Kato, M. Kamigaito, M. Sawamoto, T. Higashimura, *Macromolecules* **1995**, *28*, 1721.

[111] G. Odian, in *Princ. Polym.*, John Wiley & Sons, Inc., Hoboken, NJ, USA, **1992**, pp. 464–543.

[112] W. A. Braunecker, K. Matyjaszewski, *Prog. Polym. Sci.* **2007**, *32*, 93.

[113] T. G. Ribelli, F. Lorandi, M. Fantin, K. Matyjaszewski, *Macromol. Rapid Commun.* **2019**, *40*, 1.

[114] J.-S. Wang, K. Matyjaszewski, *Macromolecules* **1995**, *28*, 7901.

[115] J. Xia, K. Matyjaszewski, *Macromolecules* **1997**, *30*, 7697.

[116] D. Wu, F. Xu, B. Sun, R. Fu, H. He, K. Matyjaszewski, *Chem. Rev.* **2012**, *112*, 3959.

[117] P. Marcasuzaa, S. Reynaud, B. Grassl, H. Preud'homme, J. Desbrières, M. Trchová, O. F. X. Donard, *Polymer (Guildf).* **2011**, *52*, 33.

[118] A. K. Mishra, *J. At. Mol. Condens. Nano Phys.* **2018**, *5*, 159.

[119] S. Lanceros-Méndez, C. M. Costa, Eds. , *Printed Batteries: Materials, Technologies and Applications*, John Wiley & Sons, **2018**.

[120] L. Valassi, D. Tsimpliaras, *Insights Anal. Electrochem.* **2015**, *1*, 1.

[121] C. Parat, S. Betelu, L. Authier, M. Potin-Gautier, *Anal. Chim. Acta* **2006**, *573–574*, 14.

[122] O. Zaouak, L. Authier, C. Cugnet, A. Castetbon, M. Potin-Gautier, *Electroanalysis* **2010**, *22*, 1151.

[123] B. Philip, E. Jewell, P. Greenwood, C. Weirman, *J. Manuf. Process.* **2016**, *22*, 185.

[124] C. K. Chiang, M. A. Druy, S. C. Gau, A. J. Heeger, E. J. Louis, A. G. MacDiarmid, Y. W. Park, H. Shirakawa, *J. Am. Chem. Soc.* **1978**, *100*, 1013.

[125] C. K. Chiang, C. R. Fincher, Y. W. Park, A. J. Heeger, H. Shirakawa, E. J. Louis, S. C. Gau, A. G. MacDiarmid, *Phys. Rev. Lett.* **1977**, *39*, 1098.

[126] M. Tomczykowa, M. Plonska-Brzezinska, *Polymers (Basel).* **2019**, *11*, 350.

[127] T.-H. Le, Y. Kim, H. Yoon, *Polymers (Basel).* **2017**, *9*, 150.

[128] T. Nezakati, A. Seifalian, A. Tan, A. M. Seifalian, *Chem. Rev.* **2018**, *118*, 6766.

[129] E. M. Geniès, A. Boyle, M. Lapkowski, C. Tsintavis, *Synth. Met.* **1990**, *36*, 139.

[130] E. T. Kang, K. G. Neoh, K. L. Tan, *Prog. Polym. Sci.* **1998**, *23*, 277.

[131] A. Eftekhari, P. Jafarkhani, *Polym. J.* **2006**, *38*, 651.

[132] W. J. Zhang, J. Fen, A. G. MacDiarmid, A. J. Epstein, *Synth. Met.* **1997**, *84*, 119.

[133] G. Ciric-Marjanovic, *Synth. Met.* **2013**, *177*, 1.

[134] A. G. MacDiarmid, S. K. Manohar, J. G. Masters, Y. Sun, H. Weiss, A. J. Epstein, *Synth. Met.* **1991**, *41*, 621.

[135] C. U. Udeh, N. Fey, C. F. J. Faul, *J. Mater. Chem.* **2011**, *21*, 18137.

[136] W. Wang, A. G. MacDiarmid, *Synth. Met.* **2002**, *129*, 199.

[137] J. Gao, K. Li, W. Zhang, C. Wang, Z. Wu, Y. Ji, Y. Zhou, M. Shibata, R. Yosomiya, *Macromol. Rapid Commun.* **1999**, *20*, 560.

[138] Z. Wei, C. F. J. Faul, *Macromol. Rapid Commun.* **2008**, *29*, 280.

[139] L. Cao, C. Gong, J. Yang, *Electrochim. Acta* **2016**, *192*, 422.

[140] I. Arioz, O. Erol, G. Bakan, F. B. Dikecoglu, A. E. Topal, M. Urel, A. Dana, A. B. Tekinay, M. O. Guler, *ACS Appl. Mater. Interfaces* **2018**, *10*, 308.

[141] O. A. Bell, G. Wu, J. S. Haataja, F. Brömmel, N. Fey, A. M. Seddon, R. L. Harniman, R. M. Richardson, O. Ikkala, X. Zhang, C. F. J. Faul, *J. Am. Chem. Soc.* **2015**, *137*, 14288.

[142] P. Liu, Q. Wang, D. Wang, X. Kang, J. Niu, *Polymer (Guildf).* **2021**, *215*, 123350.

[143] H. Yan, L. Li, Z. Wang, Y. Wang, M. Guo, X. Shi, J.-M. Yeh, P. Zhang, *ACS Biomater. Sci.*

Eng. **2020**, *6*, 634.

[144] Y. Wang, H. D. Tran, L. Liao, X. Duan, R. B. Kaner, *J. Am. Chem. Soc.* **2010**, *88*, 10365.

[145] A. Pron, P. Rannou, *Prog. Polym. Sci.* **2002**, *27*, 135.

[146] J. Y. Shimano, A. G. MacDiarmid, *Synth. Met.* **2001**, *123*, 251.

[147] C. W. Lin, R. L. Li, S. Robbennolt, M. T. Yeung, G. Akopov, R. B. Kaner, *Macromolecules* **2017**, *50*, 5892.

[148] J.-C. Chiang, A. G. MacDiarmid, *Synth. Met.* **1986**, *13*, 193.

[149] A. G. MacDiarmid, J. C. Chiang, A. F. Richter, A. J. Epstein, *Synth. Met.* **1987**, *18*, 285.

[150] A. Thota, R. Arukula, R. Narayan, P. Sripadi, S. Bojja, C. R. K. Rao, *J. Electrochem. Soc.* **2017**, *164*, F1090.

[151] M. Wang, J. Yang, *Synth. Met.* **2020**, *269*, 116574.

[152] D. C. Look, *Mater. Sci. Eng. B Solid-State Mater. Adv. Technol.* **2001**, *80*, 383.

[153] M. A. Borysiewicz, *Crystals* **2019**, *9*, 505.

[154] C. Klingshirn, *Phys. Status Solidi Basic Res.* **2007**, *244*, 3027.

[155] Y. Li, C. Liao, S. C. Tjong, *Int. J. Mol. Sci.* **2020**, *21*, 1.

[156] A. Janotti, C. G. Van De Walle, *Reports Prog. Phys.* **2009**, *72*.

[157] F. Rahman, *Opt. Eng.* **2019**, *58*, 1.

[158] L. Zhu, W. Zeng, *Sensors Actuators A. Phys.* **2017**, *267*, 242.

[159] A. Wibowo, M. A. Marsudi, M. I. Amal, M. B. Ananda, R. Stephanie, H. Ardy, L. J. Diguna, *RSC Adv.* **2020**, *10*, 42838.

[160] A. T. Le, M. Ahmadipour, S. Y. Pung, *J. Alloys Compd.* **2020**, *844*, 156172.

[161] E. Fortunato, P. Barquinha, R. Martins, *Adv. Mater.* **2012**, *24*, 2945.

[162] X. Li, X. Liu, Y. Li, D. Gao, L. Cao, *IEEE Access* **2021**, *9*, 11954.

[163] H. Zhang, G. Chen, D. W. Bahnemann, *J. Mater. Chem.* **2009**, *19*, 5089.

[164] J. Yu, X. Yu, *Environ. Sci. Technol.* **2008**, *42*, 4902.

[165] X. Han, H. He, Q. Kuang, X. Zhou, X. Zhang, T. Xu, Z. Xie, L. Zheng, *J. Phys. Chem. C* **2009**, *113*, 584.

[166] S. Xu, Z. L. Wang, *Nano Res.* **2011**, *4*, 1013.

[167] K. N. Abbas, N. Bidin, *Appl. Surf. Sci.* **2017**, *394*, 498.

[168] Z. Fan, J. G. Lu, *J. Nanosci. Nanotechnol.* **2005**, *5*, 1561.

[169] Y. Kang, F. Yu, L. Zhang, W. Wang, L. Chen, Y. Li, *Solid State Ionics* **2021**, *360*, 115544.

[170] A. Kolodziejczak-Radzimska, T. Jesionowski, *Materials (Basel).* **2014**, *7*, 2833.

[171] R. Kumar, G. Kumar, A. Umar, *Nano-Micro* **2015**, *7*, 97.

[172] Z. L. Wang, *J. Phys. Condens. Matter* **2004**, *16*, R829.

[173] A. B. Djuriić, A. M. C. Ng, X. Y. Chen, *Prog. Quantum Electron.* **2010**, *34*, 191.

[174] A. Lei, B. Qu, W. Zhou, Y. Wang, Q. Zhang, B. Zou, *Mater. Lett.* **2012**, *66*, 72.

[175] M. Ghorbani, H. Abdizadeh, M. R. Golobostanfard, *SN Appl. Sci.* **2019**, *1*, 267.

[176] J. Li, H. Fan, X. Jia, *J. Phys. Chem. C* **2010**, *114*, 14684.

[177] M. R. Alenezi, S. J. Henley, N. G. Emerson, S. R. P. Silva, *Nanoscale* **2014**, *6*, 235.

[178] J. Zhang, S. Wang, M. Xu, Y. Wang, B. Zhu, S. Zhang, W. Huang, S. Wu, *Cryst. Growth Des.* **2009**, *9*, 3532.

[179] M. A. Desai, A. N. Vyas, G. D. Saratale, S. D. Sartale, *Int. J. Hydrogen Energy* **2019**, *44*, 2091.

[180] V. Kantola, J. Kulovesi, L. Lahti, R. Lin, M. Zavodchikova, E. Coatanéa, in *Bit Bang Rays to Futur.* (Eds.: Y. Neuvo, S. Ylönen), Helsinki University Print, **2009**, pp. 63–103.

[181] R. P. Tortorich, H. Shamkhalichenar, J. Choi, *Appl. Sci.* **2018**, *8*.

[182] D. Gregor-Svetec, in *Nanomater. Food Packag.* (Eds.: M.Â.P.R. Cerqueira, J.M. Lagaron, L.M.P. Castro, A.A.M. de O.S. Vicente), Elsevier, **2018**, pp. 203–247.

[183] J. Wiklund, A. Karakoç, T. Palko, H. Yiğitler, K. Ruttik, R. Jäntti, J. Paltakari, *J. Manuf. Mater. Process.* **2021**, *5*, 89.

[184] P. Rosa, A. Câmara, C. Gouveia, *Open J. Internet Things* **2015**, *1*, 16.

[185] R. Martins, D. Gaspar, M. J. Mendes, L. Pereira, J. Martins, P. Bahubalindruni, P. Barquinha, E. Fortunato, *Appl. Mater. Today* **2018**, *12*, 402.

[186] M. Keskinen, in *Waste Electr. Electron. Equip. Handb.*, Elsevier, **2012**, pp. 352–364.

[187] M. Caironi, Y.-Y. Noh, Eds. , *Large Area and Flexible Electronics*, WILEY-VCH, **2015**.

[188] A. C. Arias, J. D. MacKenzie, I. McCulloch, J. Rivnay, A. Salleo, *Chem. Rev.* **2010**, *110*, 3.

[189] J. A. Rogers, Z. Bao, K. Baldwin, A. Dodabalapur, B. Crone, V. R. Raju, V. Kuck, H. Katz, K. Amundson, J. Ewing, P. Drzaic, *Proc. Natl. Acad. Sci.* **2001**, *98*, 4835.

[190] Z. Cui, *Sci. China Technol. Sci.* **2019**, *62*, 224.

[191] M. Aliqué, C. D. Simão, G. Murillo, A. Moya, *Adv. Mater. Technol.* **2021**, *6*, 2001020.

[192] M. Prudenziati, J. Hromadaly, Eds. , *Printed Films: Materials Science and Applications in Sensors, Electronics and Photonics*, Woodhead Publishing Limited, **2012**.

[193] Q. Huang, Y. Zhu, *Adv. Mater. Technol.* **2019**, *4*, 1800546.

[194] H. Gleskova, S. Wagner, *Mater. Lett.* **2002**, *52*, 150.

[195] K. Chen, W. Gao, S. Emaminejad, D. Kiriya, H. Ota, H. Yin, Y. Nyein, K. Takei, A. Javey, *Mater. Views* **2016**, *28*, 4397.

[196] P. A. V. de J. Rosa, Minimal Computation Structures for Visual Information Applications Based on Printed Electronics, New University of Lisbon, **2015**.

[197] K. Kwon, M. K. Rahman, T. H. Phung, S. Hoath, S. Jeong, J. S. Kim, *Flex. Print. Electron.* **2020**, *5*.

[198] R. Soukup, A. Hamáček, J. Řeboun, *Proc. Int. Spring Semin. Electron. Technol.* **2012**, 19.

[199] M. Pudas, J. Hagberg, S. Leppa, *J. ofthe Eur. Ceram. Soc.* **2004**, *24*, 2943.

[200] H. Kempa, M. Hambsch, K. Reuter, M. Stanel, G. C. Schmidt, B. Meier, A. C. Hübler, *IEEE Trans. Electron Devices* **2011**, *58*, 2765.

[201] E. B. Secor, S. Lim, H. Zhang, C. D. Frisbie, L. F. Francis, M. C. Hersam, *Adv. Mater.* **2014**, *26*, 4533.

[202] M. Breitwieser, C. Klose, M. Klingele, A. Hartmann, J. Erben, H. Cho, J. Kerres, R. Zengerle, S. Thiele, *J. Power Sources* **2017**, *337*, 137.

[203] T. Lagarteira, F. Han, T. Morawietz, R. Hiesgen, D. Garcia Sanchez, A. Mendes, A. Gago, R. Costa, *Int. J. Hydrogen Energy* **2018**, *43*, 16824.

[204] M. Mandal, A. Valls, N. Gangnus, M. Secanell, *J. Electrochem. Soc.* **2018**, *165*, F543.

[205] T. Bayer, H. C. Pham, K. Sasaki, S. M. Lyth, *J. Power Sources* **2016**, *327*, 319.

[206] H. R. Q. Jhong, F. R. Brushett, P. J. A. Kenis, *Adv. Energy Mater.* **2013**, *3*, 589.

[207] Y. Xie, C. Zhang, X. He, T. White, J. D. Demaree, M. Griep, J. Lin, *J. Power Sources* **2018**, *397*, 37.

[208] Z. Cui, C. Zhou, S. Qiu, Z. Chen, J. Lin, J. Zhao, C. Ma, W. Su, *Printed Electronics: Materials, Technologies and Applications*, John Wiley & Sons Singapore Pte. Ltd., **2016**.

[209] H. Kipphan, *Handbook of Print Media*, **2001**.

[210] M. Pavlovic, B. Balint, *Introduction to Printed Electronics*, Springer, **2014**.

[211] P. F. Moonen, I. Yakimets, J. Huskens, *Adv. Mater.* **2012**, *24*, 5526.

[212] Y. Khan, A. Thielens, S. Muin, J. Ting, C. Baumbauer, A. C. Arias, *Adv. Mater.* **2020**, *32*, 1905279.

[213] G. Nisato, D. Lupo, S. Ganz, *Organic and Printed Electronics*, Jenny Stanford Publishing, **2016**.

[214] R. R. Søndergaard, M. Hosel, F. C. Krebs, *J. Polym. Sci. Part B Polym. Phys.* **2013**, *51*, 16.

[215] S. Logothetidis, *Handbook of Flexible Organic Electronics: Materials, Manufacturing and Applications*, **2014**.

CHAPTER II

Synthesis of a processable
conducting material: block
copolymer strategy

CHAPTER II: **SYNTHESIS OF A PROCESSABLE CONDUCTING MATERIAL: BLOCK COPOLYMER STRATEGY**

SHORT CONTEXT

This chapter describes the works performed to cope with **Objective 1** of the present thesis: to develop structure electroactive polymer films to develop structured electroactive polymer films as a catalyst supporting layer.

The strategy focuses on the development of polymer-based cathodes for eSCALED devices. The proposed architecture consists of a current collector prepared from a carbon-based paste of conducting materials such as graphite or multi-walled carbon nanotubes (MWCNTs) with polystyrene (PS) as the binder, printed on a proton-conducting membrane or inert substrate. On top of the current collector, a second electron-conducting layer based on a conducting end-capped polymer, (insulating polymer)-TANI (developed in CHAPTER II:), is cast and the CO_2RR catalyst is grafted on the surface.

The selection of the conducting polymer takes into account the expertise of the UPPA group in the synthesis of intrinsically conducting polymers based on polyaniline. To address the issue of poor solubility, fusibility, and mechanical properties of intrinsically conducting polymers, the strategy involves the synthesis of copolymers in which an insulator polymer moiety is added to the polyaniline-based polymer. The first gives mechanical properties such as flexibility and processability and should offer properties needed for film formation and compatibility with the current collector. In the same manner, an oligomer of polyaniline is preferred, and tetra-aniline (TANI) has been chosen. At last, the polymer material should be suitable for surface structuration into micropores, promoting the higher active surface area, thus increasing the number of active sites for the H^+/CO_2 reduction reaction to take place.

II.1. CONDUCTING BLOCK: TETRA-ANILINE

II.1.1. INTRODUCTION

Here we report the synthesis of tetra-aniline (TANI), which is, as described in CHAPTER I:, the shortest oligoaniline capable of reproducing the conducting properties of polyaniline (PANI), an intrinsically conducting polymer (ICP).

The use of TANI offers great opportunities for an application where properties such as high electron conductivity and low molecular weight are demanded. Moreover, TANI is easy to obtain and the functionality of both ends is easily controllable.[1–8] Figure II-1 presents the three possible structures of TANI: phenyl/phenyl (Ph/Ph) end-capped TANI (structure 1); phenyl/amine (Ph/NH$_2$) end-capped TANI (structure 2) and amine/amine end-capped (NH$_2$/NH$_2$) TANI ((structure 3).[9–11]
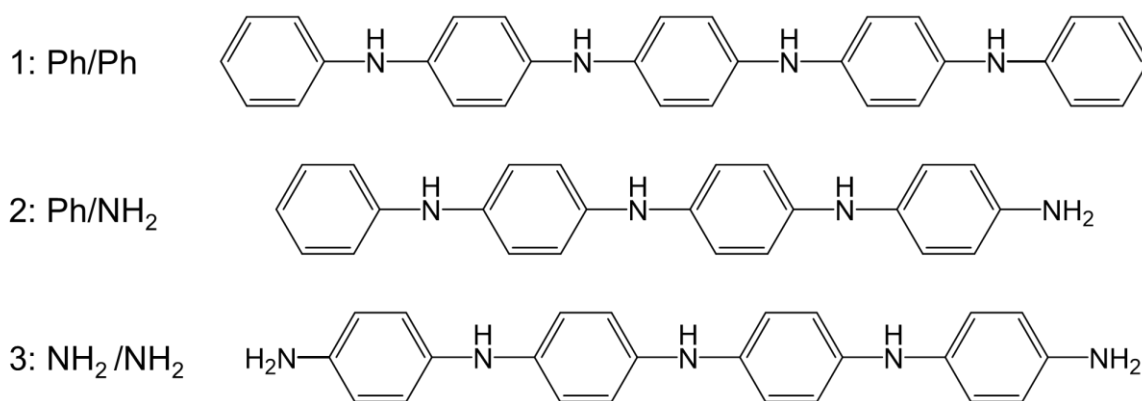
Figure II-1 – TANI with different end groups: phenyl/phenyl (Ph/Ph); phenyl/amine (Ph/NH₂) and amine-amine (NH₂/NH₂) end-capped TANI.

In the present work, structure 2, the monochelic Ph/NH$_2$ TANI was used since it preserves the repeating unit of PANI with four rings and four nitrogens and it contains an amine group in one of the ends, thus allowing the coupling of TANI to the insulating block in a further step.

II.1.2. TANI SYNTHESIS AND CHARACTERIZATION

In this work, the synthesis of structure 2 of Figure II-1 was inspired by the previous works of the group (Marcasuzaa *et al*) and is presented in Figure II-2.[12]
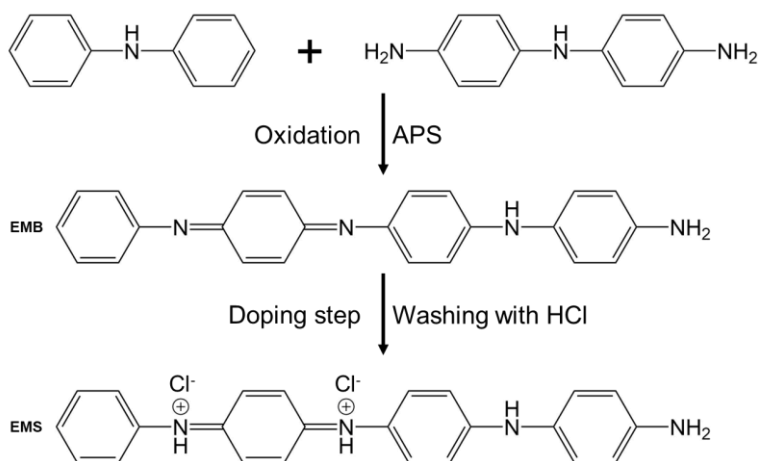
Figure II-2 – Chemical oxidative synthesis mechanism HCl-doped TANI.

The chemical oxidative synthesis of TANI consisted of two steps and is detailed in section II.5.6. At the first step, one Ph-Ph dimer and one NH$_2$-NH$_2$ dimer, diphenylamine (0.016 mol, 1 eq.) and 4-4'diaminodiphenylamine (1 eq.), respectively, react at 5 °C in the presence of an oxidant, ammonium persulfate (APS) (1 eq.), and TANI is obtained in its emeraldine base (TANI EMB) state, the half-oxidized form of TANI. In the TANI EMB state (half oxidized) the ratio of benzenoid to quinoid rings is 3:1, and imine and amine nitrogen atoms are in equal numbers. The second and final step is a doping step and consists of washing TANI with hydrochloric acid (HCl) (doping agent) to achieve its

conducting state, the emeraldine salt (TANI EMS). In TANI EMS, imine nitrogen atoms are protonated to give a polaronic form where spin and charge are delocalized.

Four batches were prepared following the same experimental procedure and called TANI 0, 1, 2, and 3.

II.1.2.1.   UV CHARACTERIZATION

The TANI obtained was characterized by UV-Vis spectroscopy in N-methyl-2-pyrrolidone (NMP) and the spectra obtained for sample TANI 0 is showed in Figure II-3.
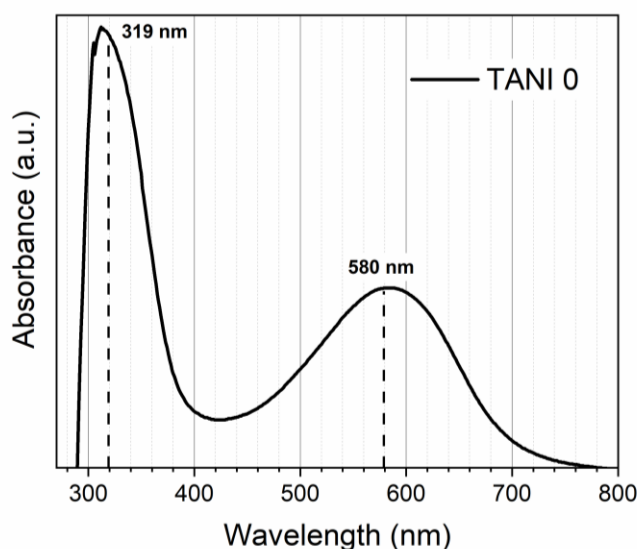
Figure II-3 - UV-Vis spectroscopy characterization of TANI 0 in NMP.

The absorption peaks in the 290 – 320 nm range are assigned to a $\pi-\pi^*$ transition in the benzenoid structure due to nitrogen excitation, while the band in the visible range (580 nm) is due to the polaron/bipolaron transition. These two are characteristics of undoped PANI.[12–14] Other samples of TANI, namely, 1; 2 and 3 presented similar characteristics. The undoped state detected was attributed to the interaction of TANI with the solvent, NMP, which is a polar, basic solvent and has a strong interaction with acids. Thus, in the prepared solution of HCl-doped TANI, NMP interacts through hydrogen bonding with the protons sitting in the TANI molecule and, therefore, leads to the undoping of TANI.[15] In its EMS form, *i.e.*, doped state, the polaron/bipolaron absorption band at 580 nm appears to shift to a higher wavelength (765 – 770 nm), while a second polaron/bipolaron absorption band would be expected to appear at 420-330 nm. Furthermore, the $\pi-\pi^*$ transition absorption band at 290 – 320 nm would not be affected.

The UV-vis characterization confirmed that the TANI structure was successfully obtained for the three batches studied.

II.1.2.2.   MALDI-TOF CHARACTERIZATION

The molecular weight of the synthesized TANI was confirmed by MALDI-TOF (mass spectrometry) as presented in Figure II-4. The species detected at m/z = 366.193 and 436,240 confirmed the presence of different oxidating states of TANI, *i.e.* TANI EMB and TANI EMS forms, respectively.
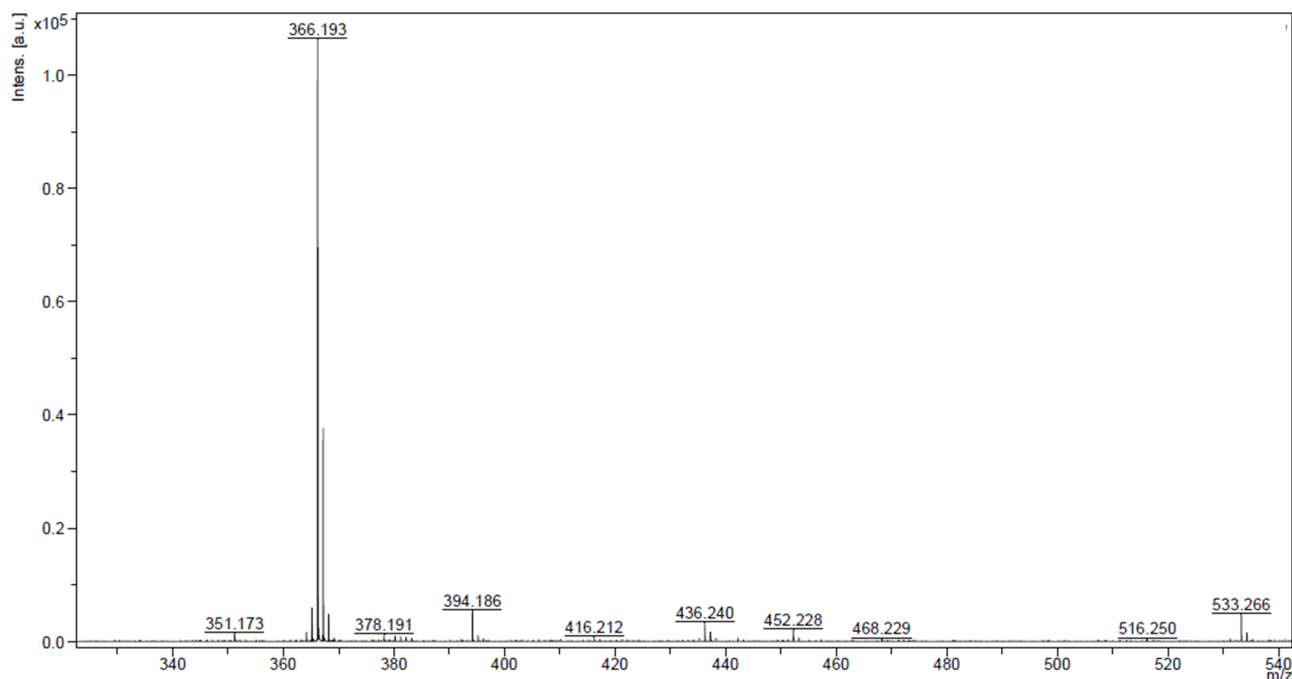

Figure II-4 - MALDI-TOF analysis of TANI 3.

Other oligoanilines may have also been produced such as the Ph/Ph hexaaniline EMB (m/z = 533.266). Moreover, other oxidation states of TANI were attributed to the peaks at m/z = 378.191 (NH$_2$/NH$_2$ TANI pernigraniline base) and m/z = 452.228 (NH$_2$/NH$_2$ TANI EMS). Nevertheless, those are considered negligible amounts.

MALDI-TOF proved that TANI was successfully synthesized, although some other oligo-anilines can be present in small quantities.

II.1.2.3.   NMR CHARACTERIZATION

In TANI's emeraldine state, different positional isomers can be present, as illustrated in Figure II-5 (left)[2,4,16].
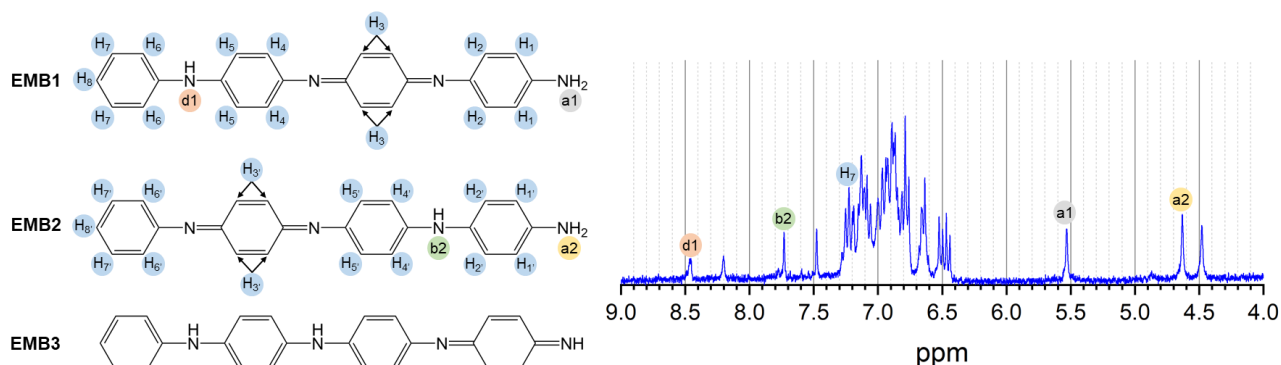
Figure II-5 – Left: Positional isomers of TANI EMB. **Right:** ^{1}H NMR (DMSO-d$_6$) spectre of TANI 3 on EMB state (chemical shift referenced to the residual signal of solvents).

^{1}H NMR (DMSO-d$_6$) studies were performed (see II.5.2.1 Structural analysis for more details on the routine parameters of the spectre acquisition) to evaluate its structure and confirm the presence of positional isomers (Figure II-5, right). To have a clean NMR spectrum, TANI was deprotonated by the addition of a base such as sodium carbonate (Na$_2$CO$_3$) in methanol, followed by a filtration step to isolate the solubilized TANI EMB from sodium carbonate and evaporation of the solvent. This procedure facilitated the solubilization of TANI in DMSO-d$_6$ and comparison with previous works in the literature[16]. The spectrum revealed the presence of a mixture of positional isomers EMB1 and EMB2 by the appearance of two signals at 4.63 and 5.53 ppm, which are assigned to the terminal –NH$_{2(a2)}$ and –NH$_{2(a1)}$ protons, respectively. Moreover, the signals at 7.73 and 8.45 ppm are attributed to –NH– protons b2 and d1 respectively. The peak at 7.27 ppm is assigned to H$_7$ protons, whereas the signal at 7.47 ppm represents the H$_{7'}$ which is known to appear more shifted towards the signal of –NH$_{(b2)}$. Peak signals at 8.20 and 4.48 ppm could not be assigned to any of the proposed structures, however, this possibility is not excluded.

II.1.2.4. DOPING STEP

All the batches synthesized exhibited low conductivity values (measured by colinear four-point probe wire technique) ranging from 10^{-4} to 10^{-5} S cm^{-1}. Inspired by previous works reported in the literature different strategies were proposed for the post-treatment of TANI to increase its conductivity. Resolubilization in ethanol/sulfuric acid blend, followed by a drying step, improved the conductivity from 10^{-4} to 0.1 S cm^{-1}, one order of magnitude lower than the conventional PANI (1 – 10 S cm^{-1}).[1,17]

II.2. INSULATING POLYMER BLOCK - ATRP

The insulator polymer block was synthesized by atom transfer radical polymerization (ATRP), which is a controlled radical polymerization (CRP) technique, previously described in the

bibliographic chapter (see CHAPTER I:). In this work, the end-functionality of the insulating polymer block must be preserved at the end of the polymerization step, so that the polymer chains can later be reactivated and end-functionalized with the TANI block. ATRP allows the uniform growth of the polymeric chains, *i.e.*, narrow molar mass distribution, due to fast initiation and rapidly reversible deactivation of the chains. In ATRP the reaction equilibrium is strongly shifted towards the dormant (deactivated) species, leading to a low concentration of radicals and, therefore, the termination reactions are negligible. These characteristics of ATRP promote the obtention of low molar mass (M_n) hetero telechelic polymers, as targeted in this work. Following the previous works in the group by Marcasuzaa *et al*, we targeted low M_n polymers ($M_n \leq 10000$ g mol^{-1}), promoting the film-forming properties and a high TANI content in the final (insulating polymer)-TANI block copolymer.[12]

In this work, succinimide-terminated insulating polymers are synthesized by ATRP in bulk. The initiator, noted as NHS-Br, is composed of a succinimide function, which enables the coupling reaction with the amino group of TANI in a further step, and an alkyl halide group to initiate the ATRP. Poly(styrene) (PS) and poly(butyl acrylate) (PBuA)-based copolymers are commonly used in the design of adhesives, therefore, styrene (S) and butyl acrylate (BuA) monomers were used in the present work.[18] Styrene is often considered a reference monomer due to its easy-to-control polymerization, while butyl acrylate is a well-known soft phase forming monomer commonly used in thermoplastic elastomers, promoting the mechanical properties required in the eSCALED project, such as flexibility, avoiding film collapse and delamination under deformation of flexible substrates.[19] The radical polymerization is controlled using CuBr and N,N,N',N'',N'''-Pentamethyldiethylenetriamine (PMDETA) playing the role of transition metal and ligand, respectively. The adapted ATRP mechanism is presented in Figure II-6, ATRP is performed under both conventional (oil bath) and microwave heating.
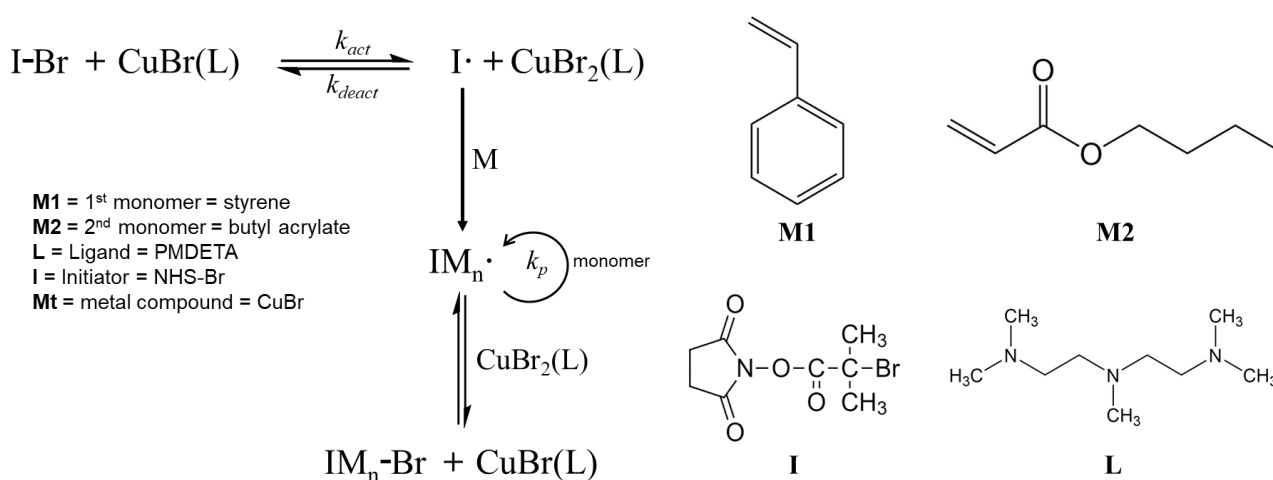

M1 = 1st monomer = styrene
M2 = 2nd monomer = butyl acrylate
L = Ligand = PMDETA
I = Initiator = NHS-Br
Mt = metal compound = CuBr

**Figure II-6 –** Adapted ATRP mechanism and reactants.

The first step of the present study was the synthesis of the ATRP initiator, NHS-Br, and is described in section II.2.1. Then, the second step is discussed in section II.2.2 and consisted of the synthesis and development of hetero telechelic PS through conventional or microwave-assisted heating ATRP. Finally, a statistical copolymer was prepared from styrene and butyl acrylate monomers through ATRP, and the development and optimization of experimental conditions, properties' tuning, and characterization are described in section II.2.3.

II.2.1. SYNTHESIS AND CHARACTERIZATION OF THE ATRP INITIATOR NHS-BR

The initiator, NHS-Br, is obtained by esterification between hydroxysuccinimide and α-bromoisobutyric acid. NHS-Br was synthesized according to the procedure reported within the experimental part later in this chapter.

The product was characterized by ^{1}H NMR (CDCl$_3$) as presented in Figure II-7.
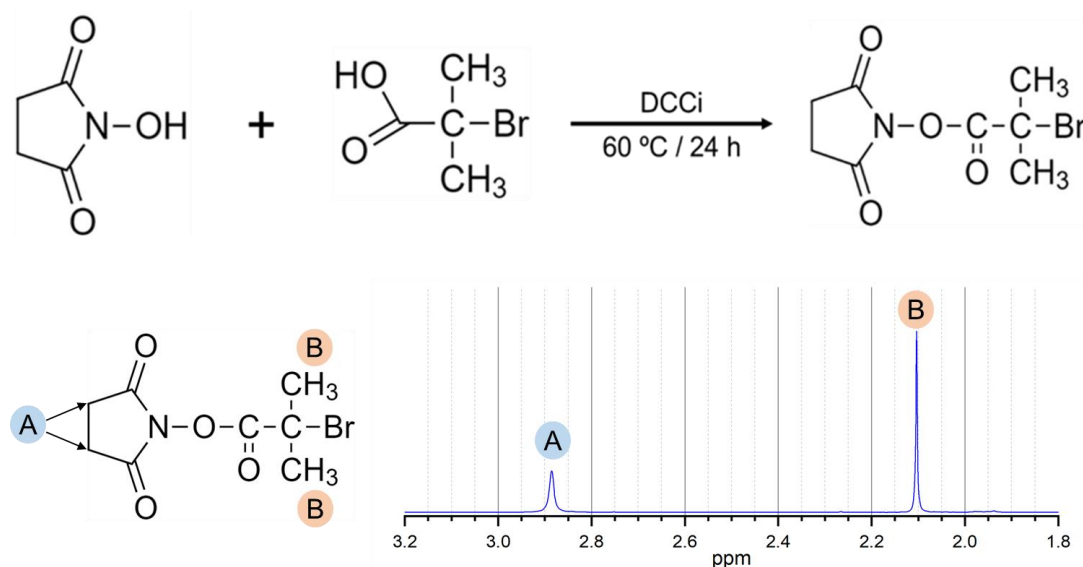
Figure II-7 – Synthesis reaction and ^{1}H NMR (CDCl$_3$) spectre of NHS-Br (ATRP initiator).

Only two different peaks are present, the first at 2.10 ppm which corresponds to 6 protons of the bromine (Br-C-(CH$_3$)$_2$-CO-) end, and the second at 2.88 ppm, which is characteristic of 4 protons of the cyclic succinimide.[12] The integrals of the peaks confirmed the peak attribution. When calibrating the peak succinimide peak at 2.88 ppm to 4.0, the obtained integral for the bromine end was ≈6.0 (see Figure II-24 at II.7 Appendixes), as expected.

The product obtained was considered pure since no trace of the initial reagents was observed at the ^{1}H NMR (CDCl$_3$) spectre (see Figure II-25 in II.7 Appendixes). Therefore, the product was used for the polymerization in the following steps with no further purification.

II.2.2. POLYSTYRENE INSULATING BLOCK

Even though pure PS is not expected to have optimal properties for film formation, PS was synthesized in a first approach to test the proposed strategy. Styrene polymerization by ATRP with a Cu/PMDETA complex and its kinetic has already been described in the literature[13]. Therefore, the experimental conditions (temperature and reacting time) and $[styrene]_0/[NHS-Br]_0/[CuBr]_0/[PMDETA]_0$ ATRP system are based on the previously published work of the UPPA group and target PS homopolymer ranging from 10000 to 20000 g mol^{-1}.[12] ATRP is performed under conventional (oil bath) and microwave-assisted heating.

The crude polymer was characterized by ^{1}H NMR (CDCl$_3$) which allows the estimation of the monomer-to-polymer conversion. The monomer conversion is measured based on residual monomer to polymer peaks (Figure II-26 at II.7 Appendixes), as follows:

$$conv = \frac{I_p/p_p}{I_p/p_p + I_m/p_m}$$ **Equation II-1**

with I_p and p_p the area and number of protons attributed to a PS peak (3 protons between 6.9 and 7.25 ppm), respectively, while I_m and p_m are, respectively the area and number of protons attributed to a peak of residual monomer (1 proton between 5.05 and 5.55 ppm). The degree of polymerization (DP) was calculated from the ^{1}H NMR (CDCl$_3$) spectra after purification. DP, or the number of repeating units, is assessed by Equation II-2:

$$DP = \frac{I_p \times p_{succ} \times n_{succ}}{I_{succ} \times p_p}$$ **Equation II-2**

where I_p and I_{succ} are the area or intensity of ^{1}H NMR peaks; p_p and p_{succ} are the number of protons of the repeating unit and succinimide end-group, respectively. Finally, n_{succ} is the number of succinimide-
end groups.
Considering p_{succ}=4; n_{succ}=1, I_{succ}=4 (integral calibration), and that I_p=$I_{p'}$ after the calibration, Equation II-2 can be rearranged as:

$$DP = \frac{I_{p'}}{p_p}$$ **Equation II-3**

Note that DP was not calculated from the conversion calculated from the NMR analysis of the crude product. For better accuracy, DP was calculated from the NMR of the purified product.

DP is then used to calculate the number-average molar mass $M_{n,DP}$ as follows:

$$M_{n,DP} = DP \times M_{monomer} + M_{initiator}$$ **Equation II-4**

A representative ^{1}H NMR spectrum of purified PS is reported in Figure II-8 with the peak assignation.
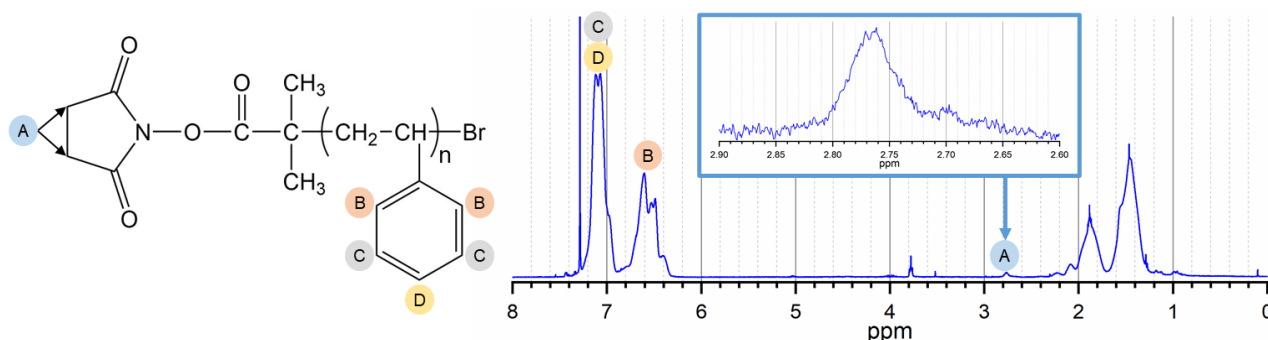
Figure II-8 – ^{1}H NMR (CDCl$_3$) spectre of PS 5 after purification.

The peaks corresponding to the protons of the PS aromatic ring (B, C, and D) appear between 6.20 and 7.50 ppm, while the 4 protons attributed to the succinimide end group (A) were detected at 2.77 ppm. An example of the peak integration analysis performed to calculate DP is demonstrated in Figure II-27 in section II.7 Appendixes.

Size exclusion chromatography in THF (SEC-THF) was used to analyze the number-average molar mass (M$_{n,SEC}$) and dispersity. This characterization was performed using the versatile refractive index (RI) detector and standard PS calibration after the purification of each synthesized PS batch. The estimation of M$_n$ by SEC-THF, M$_{n,SEC}$, is expected to differ from M$_{n,DP}$, calculated by NMR since the latter assumes all the chains are end-functionalized and do not consider the possible presence of terminated polymer chains. M$_{n,DP}$ is expected to be overestimated when compared to M$_{n,SEC}$, with the latter being calculated taking into account the whole experimental M$_n$ distribution.

Table 5 presents the experimental conditions (chemical ratio, temperature, reaction time, heating mode) and properties of the achieved polystyrene (M$_n$, DP, and Đ).

Table 5 – Experimental conditions and results of styrene ATRP under microwave (MW) and conventional heating (CH) conditions.

PS	CH / MW	Time	Power	Temp.	Conv.$_{NMR}$	DP$_{NMR}$	M$_{n,DP}$	M$_{n,SEC}$	Đ
Batch #		(min)	(W)	(ºC)	mol %		(g mol^{-1})	(g mol^{-1})	
[styrene]$_0$/[NHS-Br]$_0$/[CuBr]$_0$/[PMDETA]$_0$ = 200/1/1/1									
2	CH	120	N/A	95	3	14	1800	1900	1.28
3	CH	180	N/A	110	33	95	10200	7100	1.22
4	CH	240	N/A	110	55	145	15300	11600	1.27
5	MW	75	100	100	45	146	15500	10400	1.46
[styrene]$_0$/[NHS-Br]$_0$/[CuBr]$_0$/[PMDETA]$_0$ = 100/1/1/1									
6	CH	240	N/A	110	83	158	16700	11000	1.26

PS	CH / MW	Time	Power	Temp.	Conv.$_{NMR}$	DP$_{NMR}$	M$_{n,DP}$	M$_{n,SEC}$	Đ
Batch #		(min)	(W)	(ºC)	mol %		(g mol^{-1})	(g mol^{-1})	
[styrene]$_0$/[NHS-Br]$_0$/[CuBr]$_0$/[PMDETA]$_0$ = 150/1/1/1									
8	CH	240	N/A	110	69	161	17000	16000	1.10

In the first approach, the PS2 and PS3 revealed that a reaction temperature of 95°C was not high enough to promote the polymerization and 110°C was chosen to be the temperature value for the reaction. The effect of the [styrene]$_0$/[NHS-Br]$_0$/[CuBr]$_0$/[PMDETA]$_0$ ratio was studied on samples PS4, PS6, and PS8, respectively, 200/1/1/1, 100/1/1/1, and 150/1/1/1. The same temperature (110 °C, conventional heating mode) and duration (240 min) were applied for the three scenarios. Whatever the conditions are, the molar mass is similar which is due to the monomer conversion observed. The lower conversion obtained for PS4 was attributed to the fact that, in this case, the initial amount of monomer was higher for an equal amount of initiator and polymerization duration.

Fixing the [styrene]$_0$/[NHS-Br]$_0$/[CuBr]$_0$/[PMDETA]$_0$ ratio to 200/1/1/1 and the same temperature (110 °C, conventional heating mode), the effect of the reaction duration time was studied. Samples PS3 and PS4 were prepared from 180 and 240 min reactions, respectively. As expected, the monomer conversion increased with time reaching 33 mol % in the case of PS 3 to 55 mol % in PS 4. The result comes with a linear increase in the molar mass due to the controlled character of the ATRP process.

To go a step further, the heating mode was tested, and the polymerization was performed under microwave (MW) heating. PS 5 demonstrated that the use of MW increased the kinetics and it is possible to shorten the reaction to 75 min, and at the same time, lower the reaction temperature to 100°C to provide PS with a monomer conversion up to 45% vs. 55% under conventional heating during 240 min and at 110°C. However, the highest Đ (1.46) was registered for this batch, which can mean that ATRP is not perfectly controlled and is surely due to the poor control of the degassing and inert atmosphere in MW vials.

To conclude, it is worth mentioning that the results obtained suggest the success of ATRP with the preserved presence of a succinimide group at one end of the polymer chains, allowing the coupling of the TANI block in a further step.

Even though promising, the optimization of the MW process was not developed further and the experimental conditions: [styrene]$_0$/[NHS-Br]$_0$/[CuBr]$_0$/[PMDETA]$_0$ = 150/1/1/1 ratio performed with conventional heating mode (110 °C) for 240 min were considered for the following.

The mechanical properties of PS remain poor due to its high glass transition temperature (T$_g$≈100 ºC) which leads to brittleness, *i.e.* low flexibility and cracking of films at room temperature. Moreover, it will limit the deformation resistance of the final PS-*b*-TANI films when cast onto flexible
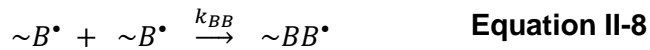
substrates as wanted for the final device. This is the reason why the next part is dedicated to the ATRP involving a monomer of low T_g.

II.2.3. STATISTICAL COPOLYMER: POLY(STYRENE-*STAT*-BUTYL ACRYLATE)

Poly(butyl acrylate) (PBuA) is a well-known polymer with low $T_g \approx -50$ °C. Furthermore, the synthesis of PBuA with good control through ATRP mediated by Cu(I)Br/PMDETA, was successfully described in the literature.[20] In this work, the combination of PBuA with PS is proposed by preparing a statistical copolymer, namely the poly(styrene-*stat*-butyl acrylate) (P(S-*stat*-BuA)). The statistical copolymer is expected to present a single T_g at an intermediate value between the T_g of PS and the T_g of PBuA.[21] Thus, P(S-*stat*-BuA) combines the properties of PS and PBuA, with the expected mechanical resistance improved.[22][19]

During a copolymerization of a monomer A and a monomer B, several cases can be considered depending on the reactivity of each monomer with propagation rate constants k_{ij}:

$$\sim A^\bullet \ + \ A \ \xrightarrow{k_{AA}} \ \sim AA^\bullet \qquad \textbf{Equation II-5}$$

$$\sim A^\bullet \ + \ B \ \xrightarrow{k_{AB}} \ \sim AB^\bullet \qquad \textbf{Equation II-6}$$

$$\sim B^\bullet \ + \ A \ \xrightarrow{k_{BA}} \ \sim BA^\bullet \qquad \textbf{Equation II-7}$$

$$\sim B^\bullet \ + \ \sim B^\bullet \ \xrightarrow{k_{BB}} \ \sim BB^\bullet \qquad \textbf{Equation II-8}$$

with ~A˙ , ~AA˙ and ~BA˙ the active macromolecular chains terminated by the monomer unit A, ~B˙, ~BB˙, and ~AB˙ the active macromolecular chains terminated by the monomer unit B, and k_{AA}, k_{AB}, k_{BA}, and k_{BB} the associated propagation rate constants.

We can then define the separation rates of the two monomers as:

$$-\frac{d[A]}{dt} = k_{AA}[A^\bullet][A] + k_{BA}[B^\bullet][A] \qquad \textbf{Equation II-9}$$

$$-\frac{d[B]}{dt} = k_{AB}[A^\bullet][B] + k_{BB}[B^\bullet][B] \qquad \textbf{Equation II-10}$$

with [A] and [B] the concentrations of monomer A and monomer B (mol/L), respectively, [A˙] and [B˙] the concentrations of the active chains terminated by monomer unit A and monomer unit B (mol/L), respectively.

An equation rearrangement can be done by dividing Equation II-9 by Equation II-10 and integrating the quasi-stationary state of the active centers defined by k_{BA} [B˙][A] = k_{AB} [A˙][B] to obtain a copolymer composition equation (Equation II-11):

$$\frac{d[A]}{d[B]} = \frac{[A](r_A[A] + [B])}{[B]([A] + r_B[B])} \quad with \ r_A = \frac{k_{AA}}{k_{AB}} \ and \ r_B = \frac{k_{BB}}{k_{BA}} \qquad \textbf{Equation II-11}$$

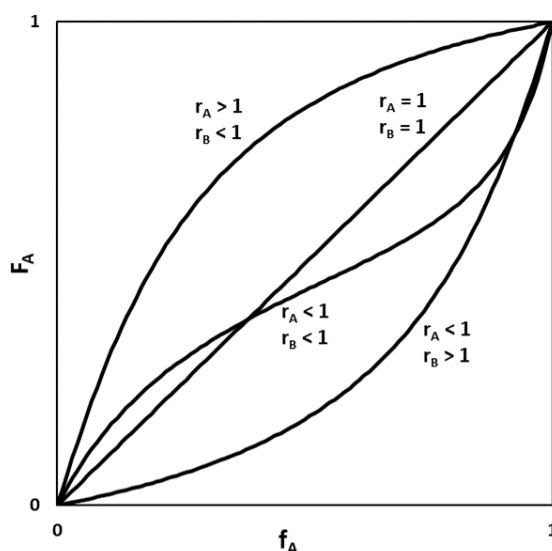with r_A and r_B the reactivity ratios of monomers A and B.

Usually, we define:

- f_A is the molar fraction of monomer A, f_B is the molar fraction of monomer B in the mixture (with $f_A = 1 - f_B$)
- F_A is the molar fraction of monomer units A in the copolymer and F_B is the molar fraction of monomer units B in the copolymer (with $F_A = 1 - F_B$)

These molar fractions F and f are related to the reactivity ratios of monomers A and B (r_A and r_B) according to the following two equations[23]:

$$F_A = \frac{r_A f_A^2 + f_A f_B}{r_A f_A^2 + 2 f_A f_B + r_B f_B^2}$$

Equation II-12

$$\frac{F_A}{F_B} = \frac{f_A (r_A f_A + f_B)}{f_B (r_B f_B + f_A)}$$

Equation II-13

As an example, Figure II-9 shows the variation in f_A and F_A composition of a copolymer composed of A and B monomer units.

Figure II-9 – Instantaneous composition diagram of a copolymer as a function of the proportion of monomers A and B for different values of the reactivity ratios r_A and r_B.

Several scenarios can occur:

- $r_A > 1$ and $r_B < 1$: favoring the consumption of monomer A and thus increasing the number of monomer A units in the copolymer, this is the self-propagation process of monomer A.
- $r_A = 1$ and $r_B = 1$: In the case of azeotropic composition, the rate constants k are equal, and there is a random insertion of the two monomers, it is the phenomenon of cross-propagation.
- $r_A < 1$ and $r_B < 1$: the reactive center ending with a monomer unit A will tend to react on a monomer B, there is thus a disposition to obtain an alternation.

- $r_A < 1$ and $r_B > 1$: the consumption of monomer B is favored and therefore the number of monomer B units in the copolymer increases, this is the self-propagation process of monomer B.

In the case of the system employed in this work, the reactivity ratio values of S (r_S) and BuA (r_{BuA}) for conversions below 15 % are 0.887 and 0.216, respectively, while for conversions above 15 %, $r_S = 1.006$ and $r_{BuA} = 0.232$.[24] Thus we considered it to be in the presence of the $r_A = r_S < 1$ and $r_B = r_{BuA} < 1$ scenario, hence the produced copolymer is expected to present a regular alternating composition equivalent to the initial monomers' molar ratio.[25]

The characterization by ^{1}H NMR (CDCl$_3$) estimates the monomers' conversion; degree of polymerization (DP$_{NMR}$) and number-average molar mass (M$_{n,DP}$), and by adapting the previously presented equations to the presence of a second repeating unit. (M$_{n,DP}$), was compared against M$_n$ obtained from SEC-THF characterization using the RI detector with standard PS calibration (M$_{n,SEC}$). A representative NMR spectrum of the copolymer is reported within Figure II-10 with the respective peak assignation.
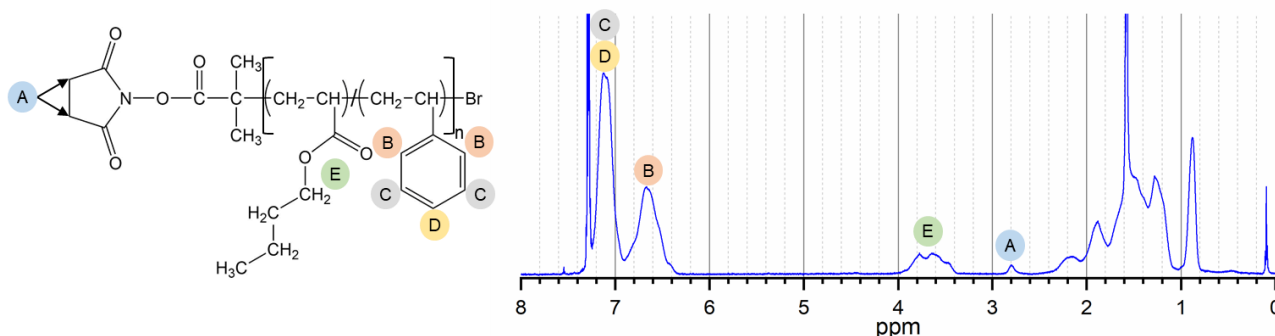
Figure II-10 – ^{1}H NMR (CDCl$_3$) spectre of P(S-*stat*-BuA) 9 after purification. P(S-*stat*-BuA) is presented following the IUPAC nomenclature.[26]

The presence of the succinimide protons (A) is detected at 2.80 ppm, however, this detection does not ensure the functionalization of the polymer chain. The peaks attributed to the proton of the PS aromatic ring (B, C, and D) appear between 6.20 and 7.50 ppm, The -OCH$_2$ proton (E) of the BuA repeating unit appeared as a triplet around 3.3 – 4.1 ppm as an effect of the presence of the BuA-BuA-BuA, BuA-BuA-S and St-BuA-S triads.[27]

The glass transition temperature (T$_g$) obtained from differential scanning calorimetry (DSC) measurements on P(S-*stat*-BuA) was compared to the theoretical prediction from the Fox model (Equation II-14).

$$\frac{1}{T_g} = \frac{w_{PS}}{T_{g,PS}} + \frac{w_{PBuA}}{T_{g,PBuA}}$$ **Equation II-14**

where w is the weight fraction of the repeating unit and $T_{g,PS}$, and $T_{g,BuA}$ are the glass transition temperature of the respective homopolymers, as reported in the literature, 100 and -50 °C, respectively.[18]

Note that, as in section II.2.2, to ensure better accuracy in the characterization of the obtained P(S-stat-BuA) samples, DP was calculated from the NMR of purified product, as previously done, and not calculated from the monomer to polymer conversion estimated through NMR analysis of the crude product.

Table 6 gathers all the P(S-*stat*-BuA) batches prepared and the respective properties for each.

Table 6 – Experimental conditions and results of styrene/butyl acrylate ATRP under microwave and conventional heating conditions. S and BuA represent styrene and butyl acrylate, respectively. F = prediction from the Fox equation. D = as measured by DSC.

P(S-*stat*-BuA) Batch #	Time	Power	Temp.	Conv.$_{NMR}$		DP$_{NMR}$		$M_{n,DP}$	$M_{n,SEC}$	Đ	Ratio		T_g	
				S	BuA	S	BuA				S	BuA	F	D
	(min)	(W)	(°C)	mol %				(g mol^{-1})	(g mol^{-1})		mol %		(°C)	
[styrene]$_0$/[butyl acrylate]$_0$/[NHS-Br]$_0$/[CuBr]$_0$/[PMDETA]$_0$ = 150/50/1/1/1														
1	240	N/A	110	35	36	106	41	16600	12200	1.22	72	28	37	
4	240	N/A	110	62	61	133	42	19600	17400	1.18	76	24	37	56
5	75	120	110	88	85	N/A	N/A	N/A	12800	1.80	75	25	37	46
6	210	N/A	110	38	38	132	44	19700	14500	1.13	75	25	37	53
7	180	N/A	110	14	16	54	16	7900	8000	1.07	77	23	37	55
8	150	N/A	110	12	14				*					
9	180	N/A	110	22	23	84	21	11800	9000	1.07	80	20	37	54
10	150	N/A	110	4	2				*					
[styrene]$_0$/[butyl acrylate]$_0$/[NHS-Br]$_0$/[CuBr]$_0$/[PMDETA]$_0$ = 170/30/1/1/1														
2	240	N/A	110	37	39				*					
[styrene]$_0$/[butyl acrylate]$_0$/[NHS-Br]$_0$/[CuBr]$_0$/[PMDETA]$_0$ = 120/80/1/1/1														
11	240	N/A	110	18	17				*					
[styrene]$_0$/[butyl acrylate]$_0$/[NHS-Br]$_0$/[CuBr]$_0$/[PMDETA]$_0$ = 100/100/1/1/1														
12	240	N/A	110	73	58	150	92	27800	23000	1.11	62	38	-4	25

*Purification not performed

For all the prepared batches the [monomers]$_0$/[NHS-Br]$_0$/[CuBr]$_0$/[PMDETA]$_0$ ratio was 200/1/1/1. To study the effect of the presence of BuA at 15, 25, 40, and 50 mol % on the properties of P(S-*stat*-BuA) copolymers, the initial monomers' ratio [styrene]$_0$/ [butyl acrylate]$_0$ was, respectively, set to 170/30, 150/50, 120/80 and 100/100. The reaction's temperature and duration were kept at 110 °C (conventional heating) and 240 min, respectively, following the best experimental conditions previously found for the synthesis of PS homopolymer.

P(S-*stat*-BuA) 4 was prepared at [styrene]$_0$/ [butyl acrylate]$_0$=150/50, targeting 25 mol % BuA in the produced copolymer. For such conditions, the monomers' conversion values were 62 mol % for S and 61 mol % for BuA, it was thus expected that the initial S/BuA monomer ratio would be preserved in the copolymer. DP calculated from ^{1}H NMR (CDCl$_3$) characterization of the purified sample estimated that the final St/BuA ratio in the copolymer was 76 mol % PS and 24 mol % PBuA. The copolymer obtained presented M$_{n,SEC}$≈17400 g mol^{-1} which was lower than M$_n$ estimated from the DP, M$_{n,DP}$≈19600 g mol^{-1}. It is worth mentioning that the M$_{n,SEC}$ results are given using a PS homopolymer standard calibration curve which may explain the unequal values obtained, among other factors related to data treatment of both techniques. At room temperature (23 °C) the product could be easily manipulated as a powder and DSC characterization estimated a T$_{g,DSC}$≈56 °C.

P(S-*stat*-BuA) 12 was prepared at [styrene]$_0$/ [butyl acrylate]$_0$=100/100, targeting 50 mol % PBuA in the produced copolymer. The copolymer obtained presented M$_{n,SEC}$≈23000 g mol^{-1}, M$_n$ estimated from the DP was M$_{n,DP}$≈27800 g mol^{-1}. The DSC characterization revealed T$_{g,DSC}$≈25 °C and is in agreement with the expected results: increasing the BuA content in the copolymer from 24 mol % (P(S-*stat*-BuA) 4) to 38 mol % (P(S-*stat*-BuA) 12) should have a significant impact on decreasing T$_g$ (here from 56 to 25 °C for, respectively. Furthermore, P(S-*stat*-BuA) 12 was difficult to manipulate at room temperature given its lower T$_g$. Since the P(S-*stat*-BuA) block must provide good film formation properties and film stability at room temperature, P(S-*stat*-BuA) 12 did not present satisfactory properties. Therefore, it was concluded that the initial St/BuA monomers' ratio should target P(S-*stat*-BuA) with PBuA below 38 mol %.

Samples P(S-*stat*-BuA) 2 and P(S-*stat*-BuA) 11, prepared with initial St/BuA monomer ratio 170/30 and 180/20, respectively, were not fully characterized as the samples P(S-*stat*-BuA) 4 and P(S-*stat*-BuA) 12 due to difficulties experienced during the purification process. However, given the previous observations for the fully characterized samples, the proximity of the monomers' conversion values, 37 mol % for PS and 39 mol % for PBuA for P(S-*stat*-BuA) 2 and 18 mol % for St and 17 mol % for BuA for P(S-*stat*-BuA) 11 suggest that the initial St/BuA would have been preserved at the final P(S-*stat*-BuA) copolymers, as observed in P(S-*stat*-BuA) 4. However, if the previous suggestion was true for P(S-*stat*-BuA) 11 ([styrene]$_0$/[butyl acrylate]$_0$=120/80) would have ≈40 mol % PBuA in its composition leading to T$_g$ close to or below room temperature (23 °C), similar to what was previously observed for P(S-*stat*-BuA) 12 (38 mol % PBuA), and does not fit into the requirements of this work.

Given the results obtained, [styrene]$_0$/[butyl acrylate]$_0$=150/50 was defined as the best initial monomers' ratio and was fixed to the following steps of the study, evaluation of the effect of the duration of the polymerization reaction on Mn, Đ and T$_g$. This study was performed at a fixed temperature, 110 °C (conventional heating), and the reaction time (t) studied were 150; 180; 210, and 240 min. The 150 min reactions attempted, namely P(S-*stat*-BuA) 8 and P(S-*stat*-BuA) 10 were

not successful and the polymer recovery was not attempted. All other samples with a polymerization duration of 180, 210, and 240 min for P(S-*stat*-BuA) 7, 6 and respectively gave the same results in terms of polymer composition with a composition of 24±1 mol % PBuA, as targeted. Moreover the longer the polymerization is, the higher the SEC molar mass while keeping low dispersity as it should be with a controlled radical polymerization. The SEC analysis of the sample P(S-*stat*-BuA) 7, is presented in Figure II-11 a).

a)

b)
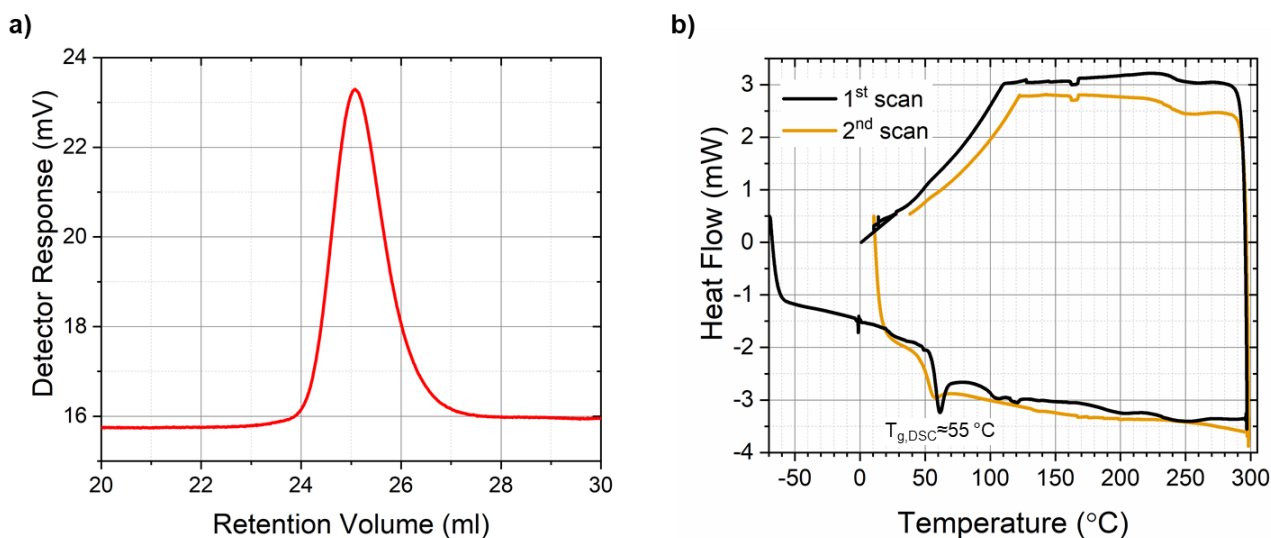
Figure II-11 – a) SEC-THF RI signal and **b)** DSC of P(S-*stat*-BuA) 7.

Furthermore, the DSC characterization is also reported in Figure II-11 b). The first scan of the DSC characterization is displayed in black in Figure II-11 b), showing no endothermic transition below 0 °C which suggests the absence of PBuA homopolymer ($T_g \approx$-50 ºC). In the first scan, the first endothermic peak appears at 55 °C, followed by another endothermic transition between 100 ºC and 120 ºC (attributed to the evaporation of water). The appearance of a single endothermic peak around 55 °C at the second scan, orange line in Figure II-11 b), was attributed to the glass transition temperature of the copolymer ($T_{g,DSC}$), proving the absence of PS or PBuA homopolymer chains in the batch.

As for the synthesis of PS homopolymer, the synthesis of P(S-*stat*-BuA) through microwave heating-assisted ATRP was also studied. P(S-*stat*-BuA) was obtained under microwave heating with [styrene]$_0$/[butyl acrylate]$_0$=150/50 at 110 °C and 120 W irradiation power for 75 min reaction time, P(S-*stat*-BuA) 5. The results give 88 mol % St and 85 mol % BuA conversions, leading to a copolymer composition, estimated by DP, containing 25 mol % PBuA, as targeted, $M_{n,SEC} \approx$12800 g mol^{-1} was obtained with a dispersity of 1.80, which suggests lower control of the polymerization reaction. The estimated $T_{g,DSC}$ was ≈46 °C, which was close to the observed for other samples with the same copolymer composition, namely P(S-*stat*-BuA) 5 with $T_{g,DSC} \approx$53 °C.

The aim of the P(S-*stat*-BuA) is to be coupled to a conducting block (TANI), therefore, to maximize TANI wt% on the final block copolymer, the P(S-*stat*-BuA) with the lowest M_n should be targeted. It was considered that the optimal experimental conditions (180 min reaction duration, 110 ºC conventional heating with 150/50 initial St/BuA monomer ratio) to prepare P(S-*stat*-BuA) by ATRP, concerning the final application, were found on P(S-*stat*-BuA) 7. This experiment produced P(S-*stat*-BuA) with the lowest registered $M_{n,SEC} \approx 8000$ g mol^{-1}, $T_{g,DSC} \approx 55$ ºC, best control of chain growth according to the dispersity index ($Đ \approx 1.07$), and final composition with 23 mol % PBuA. Furthermore, the obtained results suggest the success of ATRP in preserving the presence of a succinimide group at one end of the polymer chains, allowing the coupling of the TANI block in a further step.

A final remark must be added to the fact that for the first time P(S-*stat*-BuA) was synthesized by microwave heating-assisted ATRP, although with lower control of the reactional parameters (P(S-*stat*-BuA) 3 and 5. This approach would deserve to be further studied and optimized in the future.

II.3. TANI END-CAPPED POLYMERS

Having both parts, *i.e.*, monochelic TANI and succinimide end-capped insulating polymer (PS and P(S-*stat*-PBuA), the final step was to proceed to the coupling reaction to obtain the TANI end-capped polymer. The coupling between both blocks is achieved through a substitution reaction between the succinimide end and the amine end group of TANI. To enhance the probability of interaction between the active sites, TANI is added to the reaction medium in wide excess compared to the precursory polymer. The TANI end-capped polymer is synthesized following the reaction reported in Figure II-12.
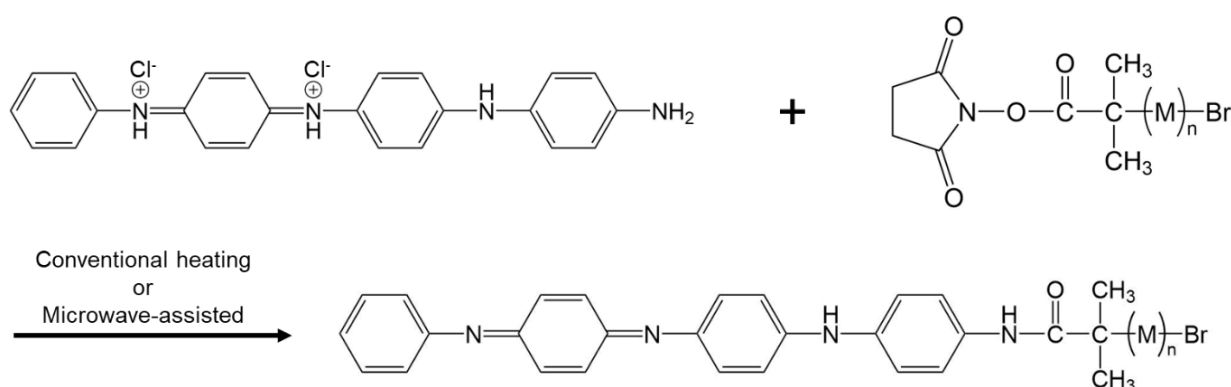
Figure II-12 - Reactive plan of the coupling reaction between a precursory polymer and TANI.

The coupling of the precursory insulating block and TANI was performed through both conventional and microwave heating at a fixed temperature, of 70 °C. Following the previous works within the group, performing the coupling reaction by microwave allows the reduction of the reaction duration

by 10 times, from 5 days by conventional heating to 12 hours under the microwave.[12] Furthermore, microwave-assisted heating is experimentally more convenient to be used due to the safety offered since the reaction takes place inside a locked chamber with pressure and temperature control.

The purification steps of the experimental protocol were optimized to decrease the quantity of product lost. Initially, the purification was performed by precipitation of PS-*b*-TANI in methanol (a nonsolvent of PS, but a solvent of TANI EMB), followed by filtration on filter paper; however, a large portion of PS-*b*-TANI was stuck on the filter paper and was not recoverable. To avoid the loss of material in this step, the filtration was replaced by centrifugation (see the experimental part in section II.5.7).

II.3.1. TANI END-CAPPED POLYSTYRENE: PS-*b*-TANI

PS 3, PS 4, and PS 5 were employed as the insulating precursory block on the synthesis of PS-*b*-TANI. Table 7 summarizes all PS-*b*-TANI batches prepared with the main characteristics of the PS block ($M_{n,SEC}$ and Đ), the TANI batch used, the coupling strategy, and the given name of each PS-*b*-TANI batch.

Table 7 – Precursory PS and TANI coupled under the microwave (MW, 70 °C) and conventional heating (CH, 70 °C), name of each PS-*b*-TANI batch prepared and HCl-doped TANI content in PS-*b*-TANI.

Precursor PS			TANI	Coupling conditions	Final name	Doped TANI content
Batch #	$M_{n,SEC}$ (g mol⁻¹)	Đ	Batch #	Heating mode	PS-*b*-TANI Batch #	wt %
3	7100	1.20	1	CH	1	5.8
4	11600	1.30	1	CH	2	3.6
4	11600	1.30	0	CH	3	3.6
5	10400	1.50	0	MW	4	4.0
5	10400	1.50	0	MW	5	4.0

The effectiveness of the coupling reaction is first evaluated by the disappearance of the succinimide end-group characteristic peak detected on ¹H NMR (CDCl₃) at 2.77 ppm with superimposition of the precursory polymers as shown in Figure II-13.
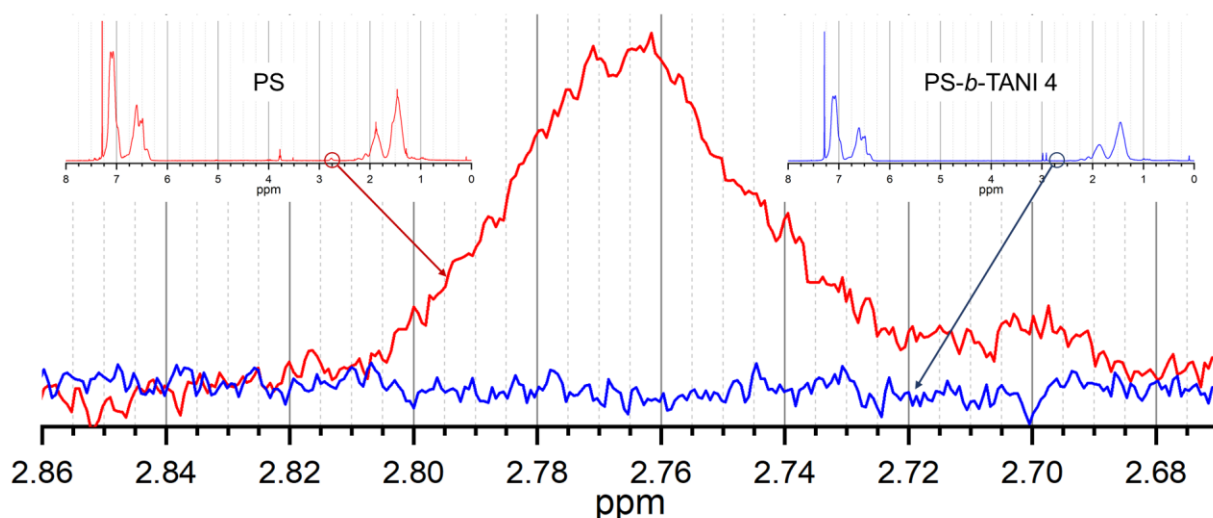
Figure II-13 – ^{1}H NMR (CDCl₃) of PS-*b*-TANI 4 (blue) against its precursor PS (PS 5) (red) standing out the characteristic peak of the succinimide end.

The doped TANI content (wt %) on PS-*b*-TANI is calculated from Equation II-15 considering $M_{HCl\text{-}doped\,TANI}$ = 436 g mol^{-1}:

$$\text{doped TANI wt\%} = \frac{M_{\text{doped TANI}}}{M_{\text{HCl-doped TANI}} + M_{\text{n,SEC,precursor}}} \quad \textbf{Equation II-15}$$

The coupling was considered to be successful by the NMR method described above for all samples, independently from the heating mode employed The TANI content is directly linked to the molar mass of the precursory PS and ranges from 4 to 5.8 wt %, however, the conductivity of the final PS-*b*-TANI remained low after the purification by centrifugation. For instance, for PS-*b*-TANI 4 and 5 with 4wt % HCl-doped TANI in this work 10^{-8} S cm^{-1} and in agreement with the dark blue color of the product, indicating that the TANI block is not doped, *i.e.*, on its EMB state. The conductivity may be restored by a post-treatment with an acidic solution and is reported below (see section II.3.3.2). Performing the coupling reaction by microwave heating proved to be more convenient due to its reduced duration, 12 h, compared to conventional heating, 5 days. Therefore, conventional heating was not used in the next section.

II.3.2. TANI END-CAPPED POLY(STYRENE-*stat*-BUTYL ACRYLATE): P(S-*stat*-BuA)-*b*-TANI

The coupling reaction between P(S-*stat*-BuA) and TANI was performed according to the optimal experimental conditions by microwave heating found in the studies with PS-*b*-TANI and reported above. The established protocol is presented in Figure II-14. P(S-*stat*-BuA)-*b*-TANI was easily prepared following the given protocol, confirmed by ^{1}H NMR (CDCl₃) following the disappearance of the succinimide peak at 2.77ppm.
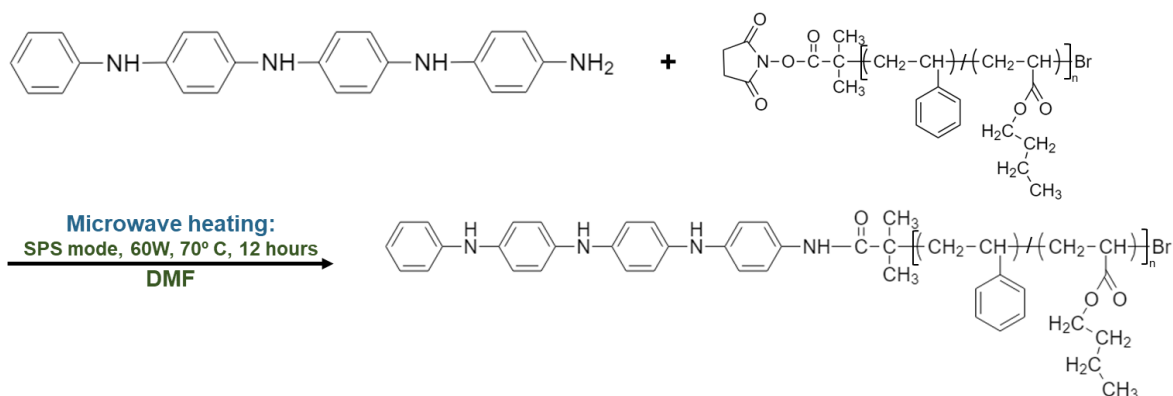
Figure II-14 –P(S-*stat*-BuA) coupling reaction with TANI.

Table 8 summarizes all P(S-*stat*-BuA)-*b*-TANI batches prepared with the main characteristics.

Table 8 - Summary of the experimental condition of the coupling reaction performed under microwave heating mode (70 °C, 12 h) to get the P(S-*stat*-BuA)-*b*-TANI.

| | Precursor P(S-*stat*-BuA) | | | | | TANI | Final name |
| | Ratio (mol %) | | $M_{n,SEC}$ | Đ | $T_{g,DSC}$ | | P(S-*stat*-BuA)-*b*-TANI |
Batch #	St	BuA	(g mol^{-1})		(ºC)	Batch #	Batch #
1	72	28	12200	1.22		0	1
4	76	24	17400	1.18	56	2	2
						2	3
						3	5
7	77	23	8000	1.07	55	3	4
9	80	20	9000	1.07	54	3	6
						3	7
13	77	23	17800	1.10	55	3	8

The coupling reaction was evaluated as described before for PS-*b*-TANI in section II.3.1 and proved to be successful for all batches prepared according to the disappearance of the characteristic peak of the succinimide end-group at 2.80 ppm.

Table 9 summarizes the precipitation method employed for each batch of P(S-*stat*-BuA)-*b*-TANI prepared and the respective HCl-doped TANI composition.

Table 9 – Detailed information about P(S-*stat*-BuA)-*b*-TANI composition in terms of HCl-doped TANI and the precipitation method employed.

| P(S-*stat*-BuA)-*b*-TANI | Doped TANI |
Batch #	wt %
Second precipitation in MeOH	

P(S-*stat*-BuA)-*b*-TANI	Doped TANI
Batch #	wt %
1	3.5
2	2.4
3	2.4
4	5.2
Second precipitation in MeOH/HCl	
5	2.4
6	4.6
8	2.4
Second precipitation in MeOH/H₂SO₄	
7	5.9

Three different methods of precipitation were employed attempting the re-doping of the TANI block, thus increasing the conductivity of the batch. The first consisted of precipitation in pure methanol and, as observed for PS-*b*-TANI, the obtained purified P(S-*stat*-BuA)-*b*-TANI presented dark blue color and conductivity in the 10^{-9} S cm^{-1} range. In the second method, the precipitation was performed in methanol blended with HCl. Although the obtained products presented dark green color, the measured conductivity was in the range of 10^{-8} S cm^{-1}. Finally, the batches precipitated in the methanol/H_2SO_4 blend (third method) registered conductivity in the 10^{-6} S cm^{-1} range, however, this value was still low. When precipitating the crude P(S-*stat*-BuA)-*b*-TANI in methanol blended with a doping agent, it is expected that the free TANI in EMB form will be re-doped to its EMS state and precipitate in methanol together with the TANI end-capped polymer. Hence, a blend of P(S-*stat*-BuA)-*b*-TANI and free TANI EMS is obtained which may improve electron percolation between TANI blocks in the cast P(S-*stat*-BuA)-*b*-TANI films. However, the presence of free TANI EMS in excess may affect the mechanical properties of the film. The film formation and structuration are discussed in II.3.3.2.

As previously observed for the PS-*b*-TANI, the conductivity of the purified P(S-*stat*-BuA)-*b*-TANI remained low, and post-treatment was necessary to reach an acceptable level of conductivity (> 0.01 S cm^{-1}). This has been achieved by mixing P(S-*stat*-BuA)-*b*-TANI with a doping agent, such as HCl or H_2SO_4 as reported in the film elaboration (see below).

II.3.3. FILM STRUCTURATION

II.3.3.1. BREATH FIGURE METHODOLOGY

At the present work, surface structuration into micropores promotes the higher active surface area while preserving a conducting network, increasing the number of active sites for the H^+/CO_2 reduction reaction to take place.

The expression "breath figure" (BF) has its origin in the fog that appears on a window when we breathe on it. BFs can be observed in daily life when foggy arrays of water droplets form on surfaces. This phenomenon was then reported, for the first time in 1994, as the methodology to self-organize polymers into honeycomb-structured, *i.e.*, hexagonally packed pores, films.[28]

A polymer solution is cast under humid air onto a surface. The fast evaporation of the solvent rapidly reduces the temperature of the solution and causes water from the moist air to condense on the cold solution surface forming micron-sized water droplets (Figure II-15) Local capillary forces and surface currents (Bénard-Marangoni convection) force these water droplets, as they see their number increased, to self-assemble into islands of hexagonal close-packing arrays (Figure II-15 b) and c)). The coalescence of the water droplets is avoided by the precipitation of the thin surrounding polymer layer, creating a solid "envelope" around the droplet (Figure II-15 d)). When water and solvent completely evaporate, only a hexagonally organized pore array is left, usually within the micrometer range.[29–34]
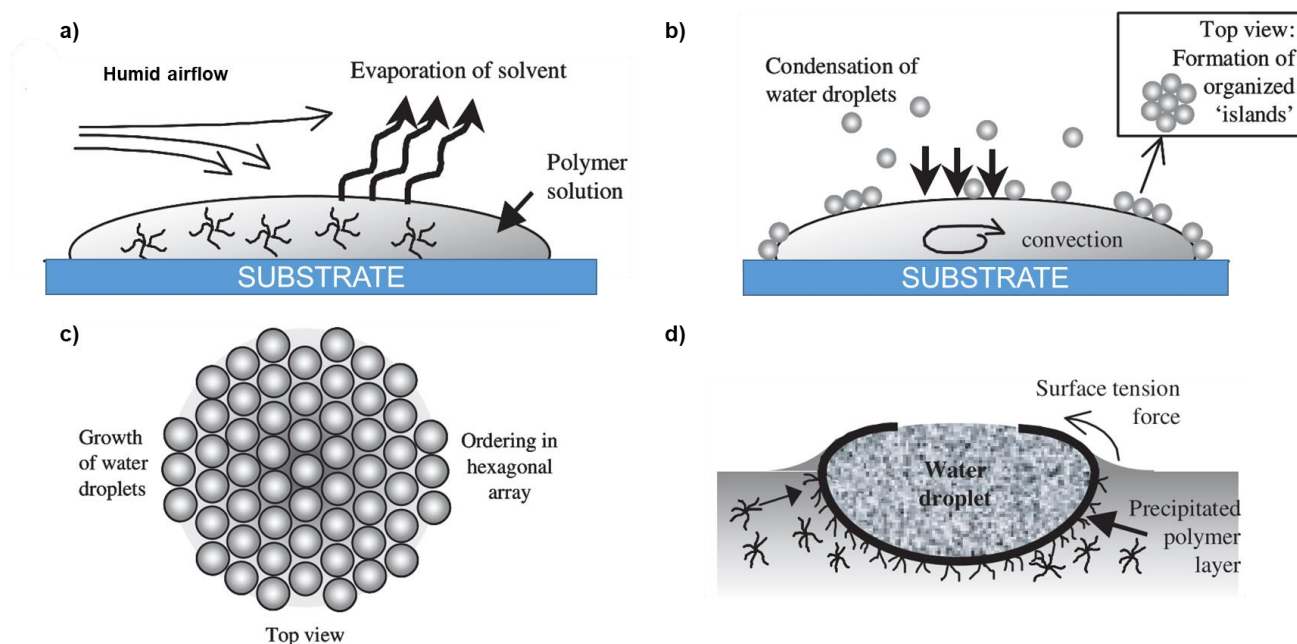
Figure II-15 – Formation of honeycomb-structured porous films. **a)** Evaporation of the solvent in the polymer solution; **b)** condensation of water droplets; **c)** hexagonally packed water droplets on the surface of the solution; **d)** precipitation of the polymer on the interface. Adapted from [33].

The BF technique presents several advantages such as very low cost concerning the equipment and procedure; time-saving since this is a single-step process and easy implementation, *i.e.*, no complex instrumentation, setup, environmental conditions, or facilities are required.[32] However, several factors can influence the formation of pores in polymer films by this method, such as solvent properties; humidity; substrate; airflow; concentration of the casted solution, viscosity; polymer chemical nature, structure, and molar mass; temperature; solution-droplet interactions or

substrate. These variables strongly influence the regularity, pore shape and size, and spacing between pores.[30,32,35–38]

II.3.3.2.   PS-*b*-TANI AND P(S-*stat*-BuA)-*b*-TANI FILMS

PS block copolymers (BCPs) are known to have good solubility in many different solvents, due to PS, which offers a great opportunity for breath figure (BF) methodology[32]. At the time of writing the present thesis and to the extent of the authors' knowledge, PS with TANI end-group (block) processed by BF has not been reported in the literature.

The first test about the structuration of PS-*b*-TANI and P(S-*stat*-BuA)-*b*-TANI was performed on glass slides as substrate. Both materials were solubilized in chloroform (CHCl$_3$) and drop-casted at room temperature with 50-60% relative humidity (RH). As shown in Figure II-16 (left), PS-*b*-TANI films often presented open cracks, as was expected, although porous films were achieved. The films prepared with P(S-*stat*-BuA)-*b*-TANI (Figure II-16, right) also presented porous structuration but no cracks were observed, as expected due to the presence of PBuA and, consequently, lower T$_g$. However, for both materials, it was observed that the porous structuration more often occurred at the films' extremities due to higher film thickness in these regions, similar to the coffee ring effect. Moreover, the films delaminated from glass with time. Having in mind the last statements in combination with the proposed electrode architecture for eSCALED, glass slides were abandoned and replaced by Nafion HP proton-conducting membrane as substrate.
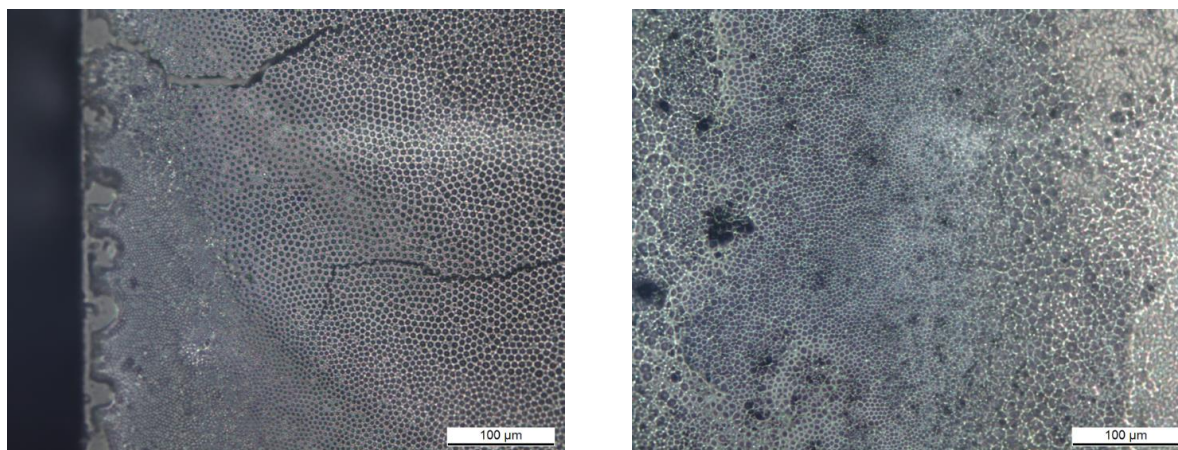
Figure II-16 – Micrographs of PS-*b*-TANI (left) and P(S-*stat*-BuA)-*b*-TANI (right) films cast on a glass slide.

As stated before, the TANI end-capped polymer suffered from poor conductivity properties after its synthesis. Here the films were obtained with crude material. Different strategies were attempted to achieve post-doping. The first strategy is presented in Figure II-17 and consisted of solubilizing P(S-*stat*-BuA)-*b*-TANI as synthesized in dichloromethane (DCM) or chloroform.
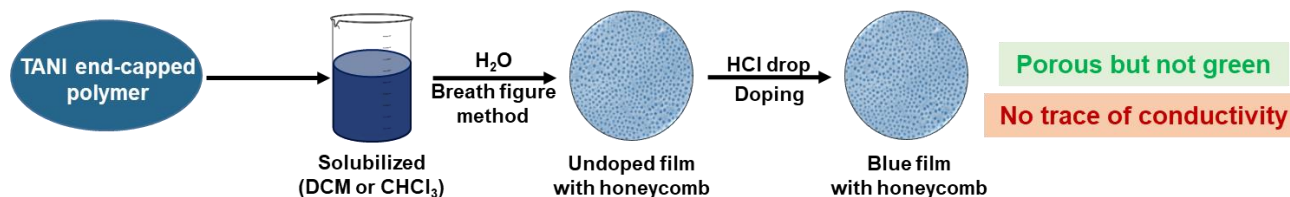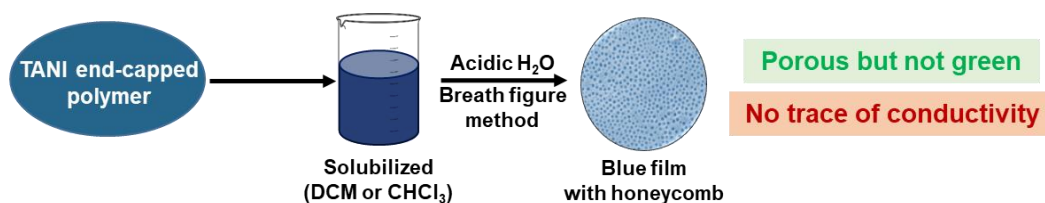
Figure II-17 – The first strategy proposed to obtain porous green films of P(S-*stat*-BuA)-*b*-TANI: post-doping of the film.

The obtained solution was then cast on the substrate producing a porous structured, blue-colored film by BF in a humid environment. The final step of this strategy was meant to dope the P(S-*stat*-BuA)-*b*-TANI film through the addition of HCl on the surface of the film. It was expected that the doping of the film would be confirmed by the transition of the film's color from dark blue to dark green, characteristic of the undoped and doped emeraldine state of TANI, respectively. However, this strategy was not successful since the porous film remained blue and no conductivity was detected or measured by our four-probe technique.

The second strategy to obtain porous dark green films from P(S-*stat*-BuA)-*b*-TANI started, as in the first case, with the solubilization of as-synthesized P(S-*stat*-BuA)-*b*-TANI in DCM or chloroform. However, in this case, the humid environment required for BF was promoted by acidic H_2O, which was expected to promote the doping of film during its formation. However, no improvements were observed, *i.e.*, the obtained films, besides being porous, presented blue color and no trace of electron conductivity was detected. Figure II-18 presents the described strategy.

Figure II-18 – The second strategy proposed to obtain porous green films of P(S-*stat*-BuA)-*b*-TANI: simultaneous doping and film formation.

The third and final strategy attempted in this work is presented in Figure II-19. In this case, the doping of P(S-*stat*-BuA)-*b*-TANI was performed previously to the film formation, by solubilizing P(S-*stat*-BuA)-*b*-TANI in DCM or chloroform blended with a doping agent, namely HCl. After being stirred for several hours, the solution of P(S-*stat*-BuA)-*b*-TANI, which was initially dark blue, presented dark green colored solids in suspension, a synonym of the successful doping. The dark-green colored P(S-*stat*-BuA)-*b*-TANI was then collected and resolubilized in DCM or chloroform.
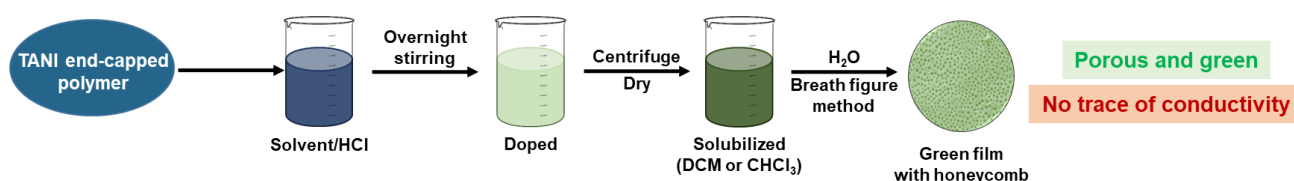
Figure II-19 – The third strategy proposed to obtain porous green films from P(S-*stat*-BuA)-*b*-TANI: pre-doping of P(S-*stat*-BuA)-*b*-TANI.

The porous films obtained presented dark green color. Regardless of being green, no electron conductivity was successfully measured.

The unsuccessful attempts of measuring the films' conductivities, independently of the film color, *i.e.*, doping state or the "real" conductivity level of the material, could be surely attributed to poor contact between the films' surface and the four-probe setup used in this work, due to irregular and porous surface presented by the films and this characteristic has been evaluated in the following.

II.3.3.3. BREATH FIGURE CHARACTERIZATION

P(S-*stat*-BuA)-*b*-TANI porous films on the Nafion HP membrane obtained through the third strategy described above were observed by scanning electron microscopy (SEM). The SEM top view is presented in Figure II-20.

a)

b)
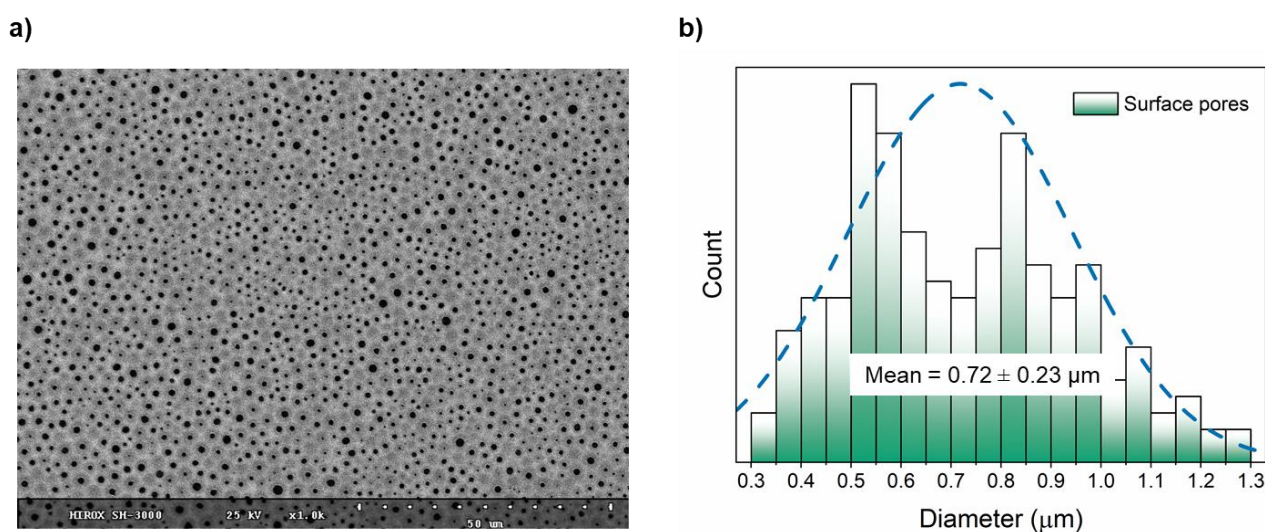
Figure II-20 – a) SEM top view and **b)** pore size distribution of pre-doped P(S-*stat*-BuA)-*b*-TANI film cast on Nafion HP with DCM. The film was green with a white surface.

Figure II-20 a) presents the surface of the P(S-*stat*-BuA)-*b*-TANI film and the image show that the film was porous throughout its extent. The result of the pore size analysis from the SEM images obtained in the top view is given in Figure II-20 b) and demonstrated an average pore diameter of 0.76 ± 0.23 µm. Although without regular size, porosity was observed on the entire surface of the produced films, and an interconnected porous network was revealed below the surface.

The SEM images obtained in a 45 ° view are presented in Figure II-21.

a)

b)

c)

d)
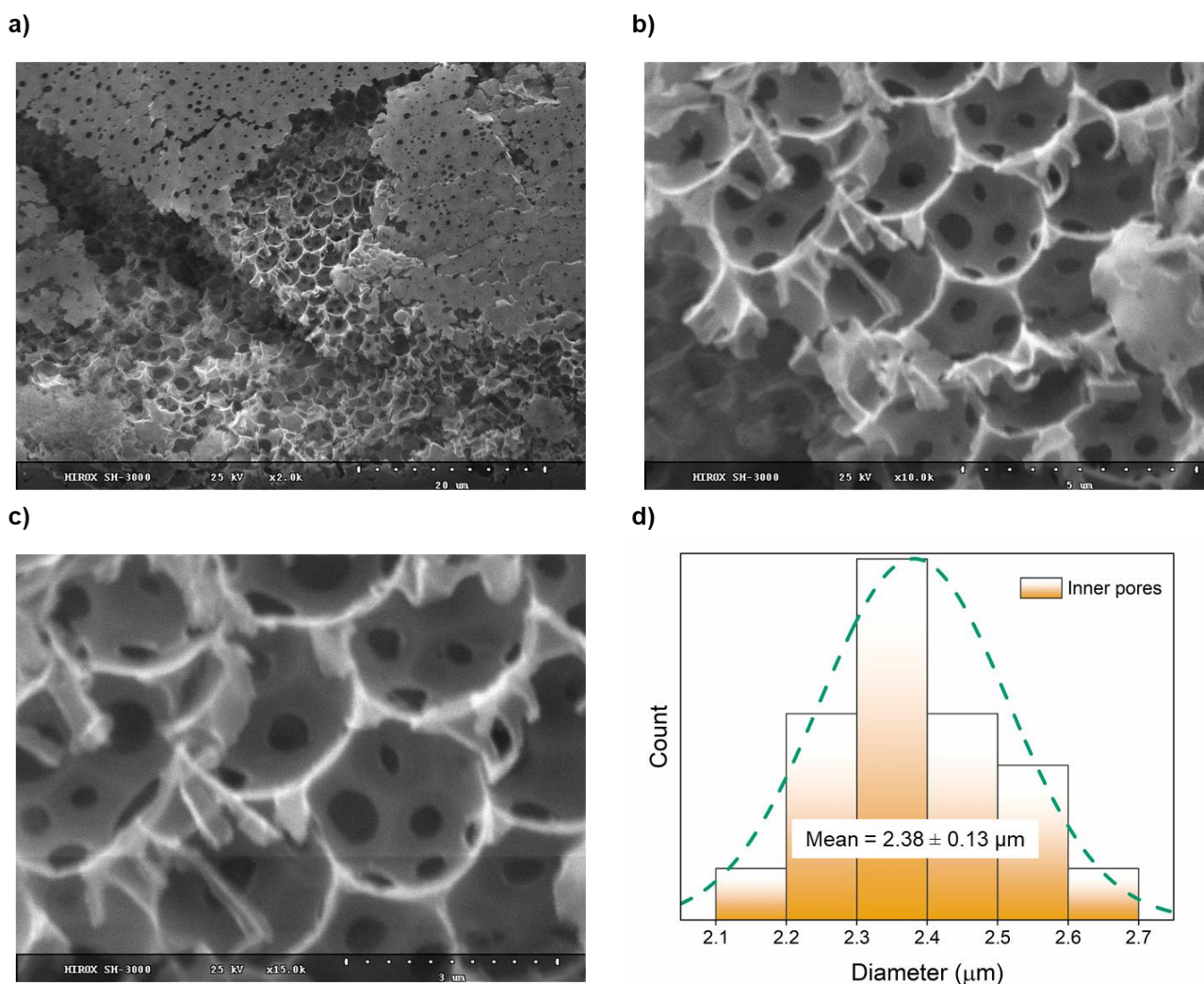
Figure II-21 – a)–c) SEM 45⁰ tilt images and **b)** pore size distribution of pre-doped P(S-*stat*-BuA)-*b*-TANI film cast on Nafion HP with DCM. The film was green with a white surface.

Figure II-21 a)-c) demonstrates that an interconnected porous network was formed below the surface. Moreover, the analysis of these SEM images revealed the internal pores' average diameter of 2.38 ± 0.13 µm. It was observed that the larger internal pores were interconnected through smaller pores, whose size was not analyzed.

PS-*b*-TANI and P(S-*stat*-BuA)-*b*-TANI films were described for the first time, showing the best results when cast onto Nafion HP membrane as substrate. Furthermore, porous dark green colored films of doped P(S-*stat*-BuA)-*b*-TANI were obtained. The analysis of the films by SEM demonstrated the bulk porous structuration of the films. However, the conductivity of the produced doped films was not proved by the four-probe technique surely due to poor contact with the electrodes. Hence, electrochemical studies were performed to assess the conductivity of the P(S-*stat*-BuA)-*b*-TANI films.

II.3.4. ELECTROCHEMICAL CHARACTERIZATION

To prove the electroactivity of films obtained with P(S-*stat*-BuA)-*b*-TANI, cyclic voltammetry studies were performed. The electrolyte selected was H_2SO_4 (pH 2) to promote the stability of TANI EMS, *i.e.*, the acid doping of the emeraldine state of TANI and consequent electron conductivity of the films throughout the experiment. This study aimed to detect the presence of a redox probe If the oxidation and reduction mechanisms of the redox probe were detected, it would prove the electroactivity of the P(S-*stat*-BuA)-*b*-TANI film cast.

Films of H_2SO_4-doped P(S-*stat*-BuA)-*b*-TANI 3 were cast on top of the bare-Pt electrode. PGMEA was used as a solvent to produce flat non-porous films, which presented dark green color, characteristic of the EMS (doped state) of TANI. The modified Pt electrode was tested in H_2SO_4 (pH 2) without a redox probe. A picture of the Pt electrode with the non-porous film of H_2SO_4-doped P(S-*stat*-BuA)-*b*-TANI 3 and the result of the CV experiment performed are presented in Figure II-22 a) and c).
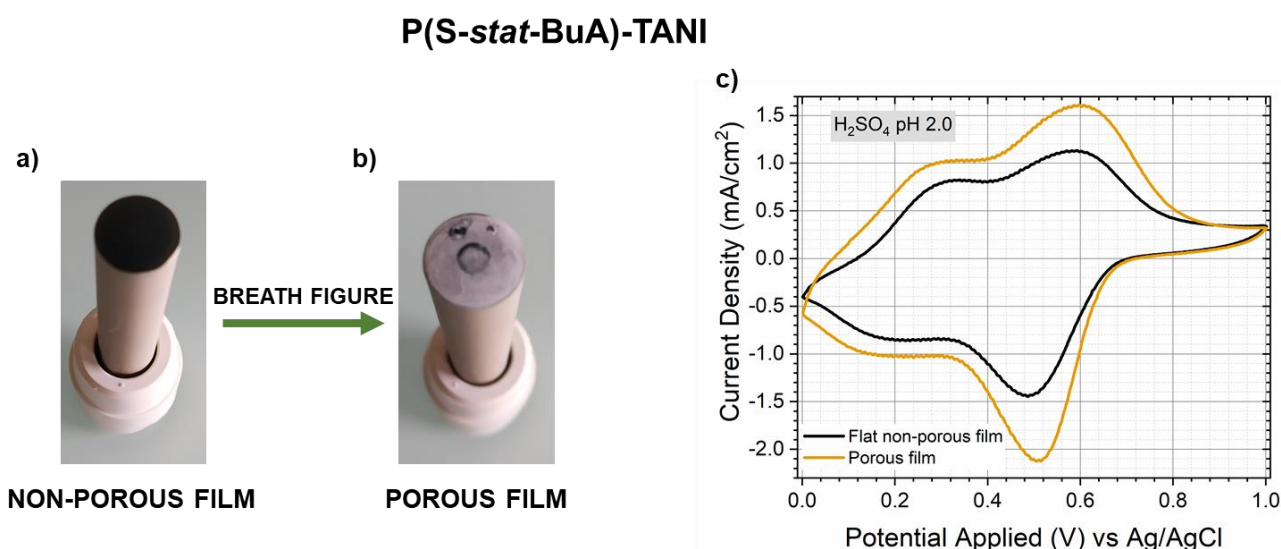
Figure II-22 – Pictures of H_2SO_4-doped the, **a)**, non-porous and, **b)**, porous films of P(S-*stat*-BuA)-*b*-TANI characterized electrochemically, and, **c)**, cyclic voltammetry results obtained in H_2SO_4 (pH 2) as the electrolyte at room temperature.

Two oxidation peaks were observed on the forward part of the CV and two other peaks were observed in the reverse scan of the CV. Due to the absence of a redox probe in the electrolyte, the origin of the redox mechanism detected could only be the P(S-*stat*-BuA)-*b*-TANI film. Further, the first peak of the forward scan, centered at +0.31 V (vs Ag/AgCl) was attributed to the oxidation of the fully reduced state of TANI *i.e.,* leucoemeraldine (LE) to the emeraldine salt. The second oxidation peak, centered at +0.57 V (vs Ag/AgCl) was then attributed to the transition of the emeraldine state to the fully oxidized state of TANI, *i.e.*, pernigraniline (PNG). Consequently, the first peak of the reverse scan, centered at +0.49 V (vs Ag/AgCl), and the second negative peak, centered

at +0.21 V (vs Ag/AgCl) were attributed to the reversible reactions, *i.e.*, the reduction of PNG to EMS and the reduction of EMS to LE, respectively.[39][40]

The detection of the redox mechanism of TANI proved that the films of P(S-*stat*-BuA)-*b*-TANI are electroactive, *i.e.*, the films (P(S-*stat*-BuA)-*b*-TANI) are electron-conducting. Thus, the addition of a redox probe such as potassium ferrocyanide ($K_4[Fe^{II}(CN)_6]$) was not required to prove the electroactivity of the P(S-*stat*-BuA)-*b*-TANI films.

The non-porous film of H_2SO_4-doped P(S-*stat*-BuA)-*b*-TANI previously prepared was then converted to a porous film by adding a few drops of dichloromethane (DCM) to its surface and the porosity was achieved by "Breath Figure". As a result, a fully white film was obtained as presented in Figure II-22 b). The porous film was then submitted to the same electrochemical protocol as the non-porous film. The obtained CV is presented in Figure II-22 and the same CV pattern was observed as a footprint of the redox mechanism of TANI, despite minimal shifts of the peaks' center (Table 10).

Table 10 – Redox peaks detected by CV experiments of a Pt electrode modified with non-porous and porous films of H_2SO_4-doped P(S-*stat*-BuA)-*b*-TANI.

Film	LE → EMS Center (V)	LE → EMS Height (mA/cm²)	EMS → PNG Center (V)	EMS → PNG Height (mA/cm²)	PNG → EMS Center (V)	PNG → EMS Height (mA/cm²)	EMS → LE Center (V)	EMS → LE Height (mA/cm²)
Non-porous	+0.31	+0.51	+0.57	+0.61	+0.49	-1.20	+0.21	-0.40
	Charge forward scan: 3.61×10^{-4} C				**Charge reverse scan: -3.56×10^{-4} C**			
Porous	+0.28	+0.65	+0.59	+1.22	+0.50	-1.82	+0.14	-0.53
	Charge forward scan: 4.76×10^{-4} C				**Charge reverse scan: -4.32×10^{-4} C**			

Furthermore, as demonstrated in Table 10, it was observed that the height of the peaks in the case of the porous film was higher than the non-porous film. The height of the peak attributed to the LEB-EMS transition had its height increased by ≈28 %, while the peak height of EMS to PNG was increased by ≈100 %. The integrals of the forward and reverse scans were calculated to estimate the charge transferred by the two films (see Figure II-28 in section II.7 Appendixes). The porous film demonstrated a higher charge transferred in both forward and reverse scans, 4.76×10^{-4} C and -4.32×10^{-4} C, respectively, compared to the non-porous films (see Table 10). This may be attributed to the increase of the active surface area due to the induced porosity and structuration, promoting the exposure of a higher number of TANI sites to the electrolyte. Moreover, and contrarily to what was observed for pure doped TANI, the films produced were stable in solution, *i.e.*, the films of P(S-*stat*-BuA)-*b*-TANI did not delaminate from the Pt electrode and were not dispersed in the electrolyte during the experiment.

The porosity of the white film produced was confirmed by optical microscopy as shown in Figure II-23.
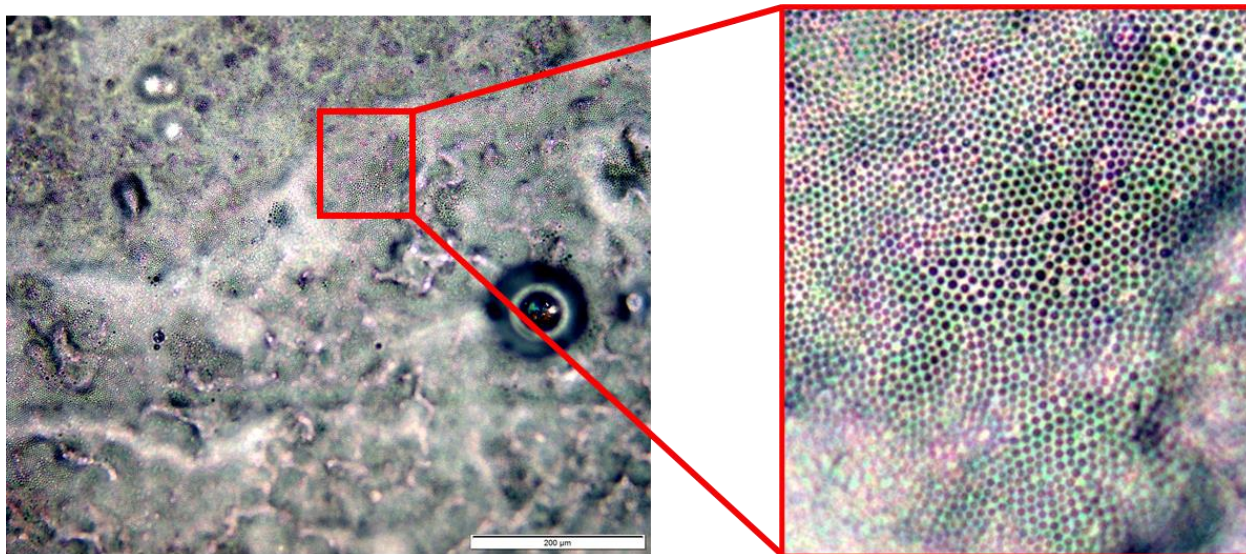
Figure II-23 – Optical micrographs of the porous film H_2SO_4-doped P(S-*stat*-BuA)-*b*-TANI cast on top of a Pt electrode for electrochemical characterization.

The optical microscopy analysis of the P(S-*stat*-BuA)-*b*-TANI films which showed electroactivity revealed that the films' surface was porous and the porosity was homogenously distributed.

The experiments performed demonstrated promising and outstanding results. We demonstrated that a conducting film containing TANI may be turned from dark color, often seen as an obstacle for many applications, to a white color film by the structuration of the film. Furthermore, the right formulation of the insulating block of the TANI end-capped polymers leads to an active film while casting onto electrodes or substrates with no delamination observed, nor TANI leaching within the electrolyte. TANI end-capped polymers such as P(S-*stat*-BuA)-*b*-TANI exhibit excellent film-forming properties, are suitable for breath figures, and lead to a homogeneous porous and conducting material. The electroactive properties of the P(S-*stat*-BuA)-*b*-TANI porous films were observed with 3 to 5 wt % of TANI and it is expected that even less TANI content may demonstrate similar results.

II.4. CONCLUSION AND PERSPECTIVES

PS and P(S-*stat*-BuA) were successfully synthesized by ATRP. Microwave heating decreased the PS synthesis reaction by ARTP from 4 h to 75 min for the same initial monomer concentration. P(S-*stat*-BuA) was synthesized with low registered M_n (8000 g mol^{-1}), $T_g \approx 55$ ºC, with good control of chain growth according to the dispersity index ($Đ \approx 1.07$) and a final ratio of 77 mol % PS to 23 mol % PBuA, keeping the succinimide end functionality key to the coupling of TANI. It is relevant to remark that for the first time it was reported the successful synthesis of P(S-*stat*-BuA) by microwave-assisted ATRP was, although the protocol still needs optimization.

HCl-doped TANI was successfully prepared, and 10^{-4} S cm^{-1} conductivity was registered at the end of the synthesis protocol. This value was increased to 0.1 S cm^{-1} by a post-synthesis treatment with ethanol/H_2SO_4 solution. TANI structure and length were confirmed by UV-Vis and MALDI-TOF, respectively. ^{1}H NMR (DMSO-d_6) revealed the presence of its characteristic EMB state positional isomers.

PS-*b*-TANI and P(S-*stat*-BuA)-*b*-TANI were prepared, and the success of the coupling reaction was confirmed by ^{1}H NMR. Precipitation of P(S-*stat*-BuA)-*b*-TANI in methanol/doping agent proved to successfully dope TANI block. Yet, both PS-*b*-TANI and P(S-*stat*-BuA)-*b*-TANI registered lower conductivity than what was previously reported in the literature. Porous films of PS-*b*-TANI and P(S-*stat*-BuA) were prepared by BF methodology on different substrates: glass, Nafion HP membrane, and Kapton. Honeycomb-like porosity was observed in the inner part of the porous films, producing a network of interconnected micropores. PS-*b*-TANI and P(S-*stat*-BuA)-*b*-TANI films were described for the first time, showing the best results when cast onto Nafion HP membrane as substrate. Furthermore, porous dark green colored films of doped P(S-*stat*-BuA)-*b*-TANI were obtained. The analysis of the films by SEM demonstrated the bulk porous structuration of the films and turned the film color from dark to white without altering the electroactive properties. The choice of an insulating block copolymer containing a low T_g material as poly(butyl acrylate) leads to an active film with no delamination nor TANI leaching within the electrolyte solution medium.

The results achieved present great potential for organic electronics. The white-colored look of the structured P(S-*stat*-BuA)-*b*-TANI films open the opportunity for embedded electronic circuits "invisible" to the user on common white surfaces, such as walls, tables, paper, or polymer substrates. Moreover, the activity of H_2SO_4-doped P(S-*stat*-BuA)-*b*-TANI films was improved by the porous structuration of the films which presents a great interest in gas sensing and electrocatalysis fields. Besides the promising application of P(S-*stat*-BuA)-*b*-TANI as catalyst support, it is important to consider the suitable operating potential window of such material. In the eSCALED context, TANI end-capped polymers may not be suitable for CO_2 reduction since an acidic environment would be

required to preserve the electron conductivity of TANI, thus favoring the hydrogen evolution reaction (HER).

II.5. EXPERIMENTAL PROCEDURES

II.5.1. MATERIALS

Table 11 presents the chemicals used in the experimental procedures. CuBr is purified by dispersion in glacial acetic acid and overnight under stirring at room temperature before being filtered. After filtration, without removing it from the filter, the light blue product is washed with absolute ethanol and manually agitated with a spatula. This step is repeated until all product presents light yellow color. The final washing step is performed with diethyl ether as before with manual agitation until all product is light green.[41] The product is then dried under vacuum for 5 h. Yield: 97% as a light green powder.

Other participating chemicals did not require any specific purification.

Table 11 - List of chemicals used for synthesis protocols.

Material	Provider/grade
α-bromoisobutyric acid	Honeywell Fluka
4,4'-Diaminodiphenylamine Sulfate Hydrate >97.0 %	TCI Chemicals
Ammonium persulfate for molecular biology, suitable for electrophoresis, ≥98 %	Sigma-Aldrich
Butyl acrylate ≥99%, contains 10-60 ppm monomethyl ether hydroquinone as an inhibitor	Sigma-Aldrich
Chloroform EMPROVE® ESSENTIAL	Merck
Chloroform D 100 %	Eurisotop
Cu(I)Br (98 %)	Alfa Aesar
Dichloromethane ≥99.5 % stabilized, AnalaR NORMAPUR® ACS, Reag. Ph. Eur. analytical reagent	VWR Technical
Dimethylformamide	VWR
Dimethylsulfoxide D6 99.8 %	Eurisotop
Diphenylamine ACS reagent > 99%	Sigma-Aldrich
HCl 1M	Fixanal
Methanol > 99%	VWR
N,N,N',N'',N''-Pentamethyldiethylenetriamine 99 %	Sigma-Aldrich
N,N'-Dicyclohexylcarbodiimide 99 % (DCCi)	Sigma-Aldrich
$Na_2HPO_4 \cdot H_2O$ BioUltra >99.0 %	Sigma-Aldrich
NaH_2PO_4, BioXtra >99.0 %	Sigma-Aldrich
Nafion HP membrane	IonPower
n-heptane GPR RECTAPUR®	VWR
N-hydroxysuccinimide 98 %	Sigma-Aldrich

Material	Provider/grade
n-methyl-2-pyrrolidone (NMP)	Carlo Erba
PGMEA	TCI
Potassium ferricyanide(III)	Sigma-Aldrich
Sodium sulfate, anhydrous, 99 %	Alfa Aesar
Styrene ReagentPlus® containing 4-tert-butylcatechol as a stabilizer, ≥99 %	Sigma-Aldrich
Tetrahydrofuran for liquid chromatography LiChrosolv®	Merck

II.5.2. PHYSICO-CHEMICAL CHARACTERIZATION

II.5.2.1. STRUCTURAL ANALYSIS

Nuclear magnetic resonance (NMR) spectra were recorded on a Bruker DPX-400 spectrometer. This characterization was performed following a standard routine procedure from the NMR technical services at the Institut des Sciences Analytiques et de Physico-Chimie pour l'Environnement et les Matériaux (IPREM) for the obtention of ^{1}H NMR spectra. Figure II-29 at II.7 Appendixes displays some of the routine parameters.

Size exclusion chromatography (SEC) was performed with tetrahydrofuran (THF) as eluent at 30 °C at a 1.0 mL min^{-1} flow rate using a setup of 4 columns (Shodex KF801, 802.5, 804, and 806) of 300 mm × 8 mm each, a pump (Viskotek, VE1122) and an autosampler (Sil-20AHT) connected to a Malvern VE3580 refractive index (RI) detector. Calibration was performed against polystyrene standards.

Matrix-assisted laser desorption/ionization – time-of-flight mass spectrometry (MALDI-TOF) experiments were performed with an Autoflex® maX MALDI system (Bruker) by the mass spectrometry service at Centre d'Etude Structurale et d'Analyse des Molécules Organiques (CESAMO) platform at the Institut des Sciences Moléculaires (ISM) from Université de Bordeaux.

UV–visible absorption spectra were obtained with a Shimadzu UV-2450PC spectro-photometer.

Fourier-transform infrared spectroscopy-attenuated total reflectance (FTIR-ATR) was performed to validate the nature of the PVC substrates provided.

II.5.2.2. THERMAL CHARACTERIZATION

DSC experiments were performed using a Q100 DSC from TA instruments under a nitrogen atmosphere (50.0 mL min^{-1}). For each sample, the temperature was initially lowered to -70 °C, then increased to 300 °C with a ramp of 20 °C min^{-1} followed by a new cooling step to -65 °C at the same ramp.

II.5.2.3. MORPHOLOGICAL CHARACTERIZATION

Microscopy pictures were obtained from a microscope DMLM (LEICA©) equipped with DFC280 camera.

Scanning Electron Microscopy (SEM) images were taken with a Hirox© SH-3000 microscope.

II.5.2.4. ELECTRICAL MEASUREMENTS

Conductivity measurements were performed through a colinear four-point probe wire technique using a current source SMU Keithley 237 and a Multimeter Keithley 2010 voltmeter with a 2000 SCAN 10-channel scanner card. The measurements were performed on films or a pellet compressed at 5 tons cm^{-2} with a manual hydraulic press.

II.5.2.5. ELECTROCHEMICAL STUDIES

The electrochemical experiments to evaluate the electroactivity of P(St-*stat*-BuA)-TANI were carried out in H_2SO_4 (pH 2) using a 3 mm Pt electrode tip as WE, a Ag/AgCl/KCl 3 M RE, and a Pt sheet electrode as CE, all provided from Metrohm. A solution (5 g L^{-1}) of P(St-*stat*-BuA)-TANI in PGMEA was cast on the surface of the Pt WE to form a continuous film. The honeycomb-structured films were obtained by resolubilizing the previous films with a few drops of DCM in the conditions described in II.5.8.

II.5.3. SYNTHESIS OF THE INITIATOR FOR ATRP

The following protocol describes the synthesis of NHS-Br, the initiator for all the ATRP in this work. 500 mL three-neck round-bottom flask is equipped with a magnetic stirrer and a reflux condenser before being charged with α-bromoisobutyric acid (1.670 g, 0.010 mol) and N-hydroxysuccinimide (1.380 g, 0.012 mol) in 200 mL dichloromethane (CH_2Cl_2, DCM). The reaction mixture is then heated up to 60 °C (the inert atmosphere is not needed) under stirring to achieve complete solubilization of reactants. Dicyclohexylcarbodiimide (DCCi) (2.060 g, 0.010 mol, in 10 mL of DCM) is added dropwise and the reaction mixture is kept at 60 °C for 24 h, under stirring.

After cooling, the reaction mixture is filtered to separate a white by-product (urea). The filtrate is then transferred to a 500 mL separating funnel and 150 mL distilled water is added for rinsing followed by liquid-liquid extraction on which the desired product is the densest. This procedure is repeated three times to remove the excess N-hydroxysuccinimide and dried over sodium sulfate (Na_2SO_4). The liquid product is concentrated under vacuum with a rotavapor and purified by recrystallization in n-heptane. Yield: 72% as white crystals. ^{1}H NMR (400 MHz, CDCl$_3$): 2.10 ppm (s, 6H, Br-C(CH$_3$)$_2$-CO-), 2.88 ppm (s, 4H, -OCCH$_2$-CH$_2$-CO).

II.5.4. HETERO TELECHELIC POLYSTYRENE SYNTHESIS BY ATRP

Styrene bulk polymerization is performed by ATRP with a Cu/PMDETA complex in a [styrene]/[NHS-Br]/[CuBr]/[PMDETA] = 200/1/1/1 system.

II.5.4.1. CONVENTIONAL HEATING

A 25 mL round-bottom flask equipped with a magnetic stirrer is charged with 31 mg of CuBr (0.22 mmol), 57 mg of previously synthesized NHS-Br (0.22 mmol), 5 mL of styrene (43.5 mmol), and 45.4 µL of PMDETA (0.22 mmol). Solid chemicals are weighed individually and then mixed in the flask, followed by the monomer addition and, finally, the ligand. The flask is sealed with a rubber septum and two needles are inserted through the septum. One needle has its end immersed in the reaction mixture (N_2 inlet), while the other works as the gas outlet. The mixture is deoxygenated by N_2 bubbling for 10 min, the needles are removed (outlet before needle with flowing N_2) and the septum is sealed with parafilm. The flask is then placed into an oil bath at 110 ºC under magnetic stirring for 4 h.

II.5.4.2. MICROWAVE-ASSISTED HEATING

A 10 mL standard micro-wave-transparent Pyrex microwave process vial (obtained from CEM), proper for microwave synthesizer equipment (CEM-Discover SP) is charged with a magnetic stirrer. Reactants are added to the flask in the same order as described for conventional heating and bubbled with N_2 before being closed and introduced inside the microwave reactor. SPS has been used, it is a pulsed power mode in which the reaction temperature of 100 ± 2 °C is set and attained by irradiation power while using a cooling feature consisting of compressed air. The microwave power irradiation is set at a fixed value (100 W).[12,42]

In both protocols, the purification steps are as follows. The reaction is stopped by cooling the flask in an ice bath. A sample is collected for ^{1}H NMR ($CDCl_3$) and the monomer conversion is calculated considering the residual monomer and polymer peaks. Tetrahydrofuran (THF) is added to the crude product to reduce its viscosity and the polymer is purified by passing it through a silica column before being precipitated in methanol. After filtration, PS white powder is dried under vacuum at 40 ºC for 3 h. Second precipitation is then performed by re-solubilization in chloroform (CH_3Cl) and precipitation in methanol. The product is collected and dried as before. The number-average molar mass (M_n) and dispersity (Đ) are determined by size exclusion chromatography with THF as eluent (SEC-THF). Yield: 25 % (conventional heating) and 33 % (microwave-assisted) as a white powder.

II.5.5. STATISTICAL COPOLYMER POLY(STYRENE-*STAT*-BUTYL ACRYLATE) SYNTHESIS BY ATRP

Statistical P(S-*stat*-BuA) copolymer is obtained by using an adapted protocol. [styrene]/[butyl acrylate]/[NHS-Br]/[CuBr]/[PMDETA] = 150/50/1/1/1 system is used for the present study. In a typical procedure, a 50 mL round-bottom flask equipped with a magnetic stirrer is charged with 125 mg of CuBr (0.87 mmol), 226 mg of NHS-Br (0.87 mmol), 15 mL of styrene (130.5 mmol), 6.26 mL of butyl acrylate (43.5 mmol) and 181.6 µL of PMDETA (0.87 mmol). As before, solid chemicals are weighed individually and then mixed in the flask, followed by the monomers' addition and, finally, the ligand. The mixture is deoxygenated by N_2 bubbling for 10 min (procedure described before for PS) and then placed into an oil bath at 110 ºC under magnetic stirring for 3 h. Purification is performed as previously described for PS. In this case, the white gum-like product is collected by filtration with conventional filter paper if dispersed in methanol or with a spatula if agglomerated in a sphere-like shape. ^{1}H NMR ($CDCl_3$) provides information about monomer-to-polymer conversion and PS/PBuA ratio. The number-average molar mass (M_n) and dispersity (Đ) are determined by SEC-THF using polystyrene standard calibration. Yield: 14% as a white gum-like solid.

II.5.6. TETRA-ANILINE SYNTHESIS

The synthesis of Ph/NH_2 end-capped tetramer of aniline by chemical oxidation of two dimers of aniline. This procedure allows for good quality control of the molecule size. The following synthesis occurs without an inert atmosphere or catalyst.

The following synthesis occurs without any inert atmosphere or catalyst. In a round bottom flask of 250 mL, the diphenylamine (2.704 g, 0.016 mol) and 4-4'diaminodiphenylamine (5.6 g, 0.016 mol) are added in a mixture of 100 mL of DMF, 20 mL of distilled water, and 15 mL of HCl (1 M). The mixture is then placed at 5 °C in a bath of ice. After total dissolution, an aqueous solution of ammonium persulfate (APS) (3.648 g, 0.016 mol) in 10 mL of distilled water is added dropwise to the initial mixture. The reactional mixture is kept under stirring for 1 hour at 5°C. The reaction is kept at 5 ºC by refilling the bath with ice. The product is then precipitated in distilled water, filtered, washed three times with 100 mL HCl 1 M, and dried under vacuum for 72 hours. The structure of the obtained product was characterized through ^{1}H NMR (DMSO-d_6), UV-Vis spectroscopy in N-Methyl-2-pyrrolidone (NMP), and matrix-assisted laser desorption/ionization – time-of-flight mass spectrometry (MALDI-TOF). The electron conductivity of TANI was characterized by a colinear four-point probe wire method with a pellet prepared under 5 tons cm^{-2} press.

II.5.7. COUPLING OF INSULATING POLYMER BLOCK AND TETRA-ANILINE

II.5.7.1. CONVENTIONAL HEATING

Considering M_n = 10000 g/mol. In a 50 mL round bottom flask, the precursory polymer (1.00 g, 10^{-4} mol) and TANI (0.40 g, 10^{-3} mol) are stirred in 10 mL of DMF. The reaction is left under stirring at 70 °C for 5 days. The product is then precipitated in methanol until a colorless filtrate is observed.

II.5.7.2. MICROWAVE HEATING

The precursory polymer (500 mg, 10^{-4} mol) and TANI (200 mg, 10^{-3} mol) are weighed individually and mixed in a 10 mL microwave glass vial previously equipped with a magnetic stirrer. The two powders are manually milled with the spatula to allow better solubilization of TANI. The reaction mixture is stirred in 5 mL of DMF and then irradiated in the mode SPS (microwave CEM) with a set power of 60 W, at 70 ± 1 °C, under magnetic stirring for 12 hours. The equivalency between precursory polymer and TANI is the same as above within conventional heating. The product is purified through first precipitation in methanol, followed by a centrifuge step and solvent evaporation under vacuum at 40 ºC.

Doping step: The TANI end-capped polymer is solubilized in Chloroform and precipitated in Methanol blended with a doping agent either 1M HCl (60 mL methanol + 5 mL 1M HCl) or H_2SO_4, centrifuged (10000 rpm, 4 ºC, with FEP tubes. After the centrifuge step, the liquid phase is removed with a pipette and the solid is collected to a vial and dried under vacuum at 40 ºC for 3h. ^{1}H NMR (CDCl$_3$) provides information about the success of the coupling.

The copolymer is characterized in terms of conductivity by the conventional four parallel wire method with a pellet prepared under 5 tons/cm^2 press.

II.5.8. SURFACE STRUCTURATION

Static breath-figure was carried out as described by Li *et al* DCM, THF, DMF, or CHCl$_3$ as solvent.[43] 100 µL of PS-*b*-TANI and P(St-*stat*-BuA)-TANI solutions were drop-casted on a glass slide, Nafion HP membrane, or Kapton film. The best structures were obtained with the Nafion membrane and P(St-*stat*-BuA)-TANI solutions in DCM with a concentration of 5 g L^{-1} in a controlled relative humidity above 60 %. Static breath-figure was carried out as described by Li *et al* DCM, THF, DMF, or CHCl$_3$ as solvent.[43] 100 µL of PS-*b*-TANI and P(St-*stat*-BuA)-TANI solutions were drop-casted on a glass slide, Nafion HP membrane, or Kapton film. The best structures were obtained with the Nafion membrane and P(St-*stat*-BuA)-TANI solutions in DCM with a concentration of 5 g L^{-1} in a controlled relative humidity above 60 %.

II.6. BIBLIOGRAPHY

[1]   Y. Wang, H. D. Tran, L. Liao, X. Duan, R. B. Kaner, *J. Am. Chem. Soc.* **2010**, *88*, 10365.

[2]   Z. Wei, C. F. J. Faul, *Macromol. Rapid Commun.* **2008**, *29*, 280.

[3]   A. Pron, P. Rannou, *Prog. Polym. Sci.* **2002**, *27*, 135.

[4]   J. Y. Shimano, A. G. MacDiarmid, *Synth. Met.* **2001**, *123*, 251.

[5]   A. G. MacDiarmid, S. K. Manohar, J. G. Masters, Y. Sun, H. Weiss, A. J. Epstein, *Synth. Met.* **1991**, *41*, 621.

[6]   C. W. Lin, R. L. Li, S. Robbennolt, M. T. Yeung, G. Akopov, R. B. Kaner, *Macromolecules* **2017**, *50*, 5892.

[7]   J.-C. Chiang, A. G. MacDiarmid, *Synth. Met.* **1986**, *13*, 193.

[8]   A. G. MacDiarmid, J. C. Chiang, A. F. Richter, A. J. Epstein, *Synth. Met.* **1987**, *18*, 285.

[9]   C. U. Udeh, N. Fey, C. F. J. Faul, *J. Mater. Chem.* **2011**, *21*, 18137.

[10]   W. Wang, A. G. MacDiarmid, *Synth. Met.* **2002**, *129*, 199.

[11]   J. Gao, K. Li, W. Zhang, C. Wang, Z. Wu, Y. Ji, Y. Zhou, M. Shibata, R. Yosomiya, *Macromol. Rapid Commun.* **1999**, *20*, 560.

[12]   P. Marcasuzaa, S. Reynaud, B. Grassl, H. Preud'homme, J. Desbrières, M. Trchovà, O. F. X. Donard, *Polymer (Guildf).* **2011**, *52*, 33.

[13]   J. E. Albuquerque, L. H. C. Mattoso, D. T. Balogh, R. M. Faria, J. G. Masters, A. G. MacDiarmid, *Synth. Met.* **2000**, *113*, 19.

[14]   B. M. Mills, Z. Shao, S. R. Flynn, P. Rannou, D. M. Lindsay, N. Fey, C. F. J. Faul, *Mol. Syst. Des. Eng.* **2019**, *4*, 103.

[15]   Y. Geng, J. Li, X. Jing, F. Wang, *Synth. Met.* **1997**, *84*, 97.

[16]   I. Kulszewicz-Bajer, I. Rozalska, M. Kuryłek, *New J. Chem.* **2004**, *28*, 669.

[17]   Y. Wang, J. Liu, H. D. Tran, M. Mecklenburg, X. N. Guan, Z. Stieg, B. C. Regan, D. C. Martin, R. B. Kaner, A. Z. Stieg, B. C. Regan, D. C. Martin, R. B. Kaner, *J. Am. Chem. Soc.* **2012**, *134*, 9251.

[18]   A. E. Chalykh, U. V. Nikulova, A. A. Shcherbina, *Polym. Sci. Ser. A* **2015**, *57*, 445.

[19]   Y. Luo, X. Wang, Y. Zhu, B. Li, S. Zhu, *Macromolecules* **2010**, *43*, 7472.

[20]   M. Reyes, X. Yu, D. A. Shipp, *Macromol. Chem. Phys.* **2001**, *202*, 3268.

[21]   F. Soriano-Corral, L. F. Ramos-de Valle, F. J. Enríquez-Medrano, P. A. De León-Martínez, M. L. López-Quintanilla, E. N. Cabrera-Álvarez, *J. Nanomater.* **2012**, *2012*, 1.

[22]   J. Fage, K. Knoll, N. Niessner, O. Carstensen, T. Schulz, F. Malz, M. Döring, F. Schönberger, *Polymers (Basel).* **2019**, *11*, 1317.

[23]   G. Odian, in *Princ. Polym.*, John Wiley & Sons, Inc., Hoboken, NJ, USA, **1992**, pp. 464–543.

[24]   F. Ziaee, M. Nekoomanesh, *Polymer (Guildf).* **1998**, *39*, 203.

[25]   M. A. Dubé, E. Saldívar-Guerra, I. Zapata-González, in *Handb. Polym. Synth. Charact. Process.*, John Wiley & Sons, Inc., Hoboken, NJ, USA, **2013**, pp. 105–125.

[26]   R. G. Jones, T. Kitayama, K. H. Hellwich, M. Hess, A. D. Jenkins, J. Kahovec, P. Kratochvíl, I. Mita, W. Mormann, C. K. Ober, S. Penczek, R. F. T. Stepto, K. Thurlow, J. Vohlídal, E. S. Wilks, *Pure Appl. Chem.* **2016**, *88*, 1073.

[27]   A. S. Brar, Sunita, C. V. V Satyanarayana, *Polym. J.* **1992**, *24*, 879.

[28]   G. Widawski, M. Rawiso, B. François, *Nature* **1994**, *369*, 387.

[29]   X.-Y. Yang, L.-H. Chen, Y. Li, J. C. Rooke, C. Sanchez, B.-L. Su, *Chem. Soc. Rev.* **2017**, *46*, 481.

[30]   P. Escalé, L. Rubatat, L. Billon, M. Save, *Eur. Polym. J.* **2012**, *48*, 1001.

[31]   M. H. Stenzel, C. Barner-Kowollik, T. P. Davis, *J. Polym. Sci. Part A Polym. Chem.* **2006**, *44*, 2363.

[32]   A. Zhang, H. Bai, L. Li, *Chem. Rev.* **2015**, *115*, 9801.

[33]   M. H. Stenzel, *Aust. J. Chem.* **2002**, *55*, 239.

[34]   L. Pessoni, S. Lacombe, L. Billon, R. Brown, M. Save, *Langmuir* **2013**, *29*, 10264.

[35]   B. Su, C. Sanchez, X. Yang, Eds. , *Hierarchically Structured Porous Materials*, Wiley, **2011**.

[36]   J. Peng, Y. Han, Y. Yang, B. Li, *Polymer (Guildf).* **2004**, *45*, 447.

[37]   U. H. F. Bunz, *Adv. Mater.* **2006**, *18*, 973.

[38]   M. S. Silverstein, N. R. Cameron, M. A. Hillmyer, Eds. , *Porous Polymers*, Wiley And Sons Ltd, **2011**.

[39]   R. Li, C.-W. Lin, Y. Shao, C. Chang, F.-K. Yao, M. Kowal, H. Wang, M. Yeung, S.-C. Huang, R. Kaner, *Polymers (Basel).* **2016**, *8*, 401.

[40]   M. Canales, J. Torras, G. Fabregat, A. Meneguzzi, C. Alemán, *J. Phys. Chem. B* **2014**, *118*, 11552.

[41]   R. N. Keller, H. D. Wrcoff, L. E. Marchi, in *Inorg. Synth.* (Ed.: W.C. Fernelius), McGraw-Hill Book Company, Inc., **2007**, pp. 1–4.

[42]   N. E. Leadbeater, *Microwave-Assisted Synthesis: General Concepts*, **2016**.

[43]   X.-Y. Li, Q.-L. Zhao, T.-T. Xu, J. Huang, L.-H. Wei, Z. Ma, *Eur. Polym. J.* **2014**, *50*, 135.

II.7. APPENDIXES
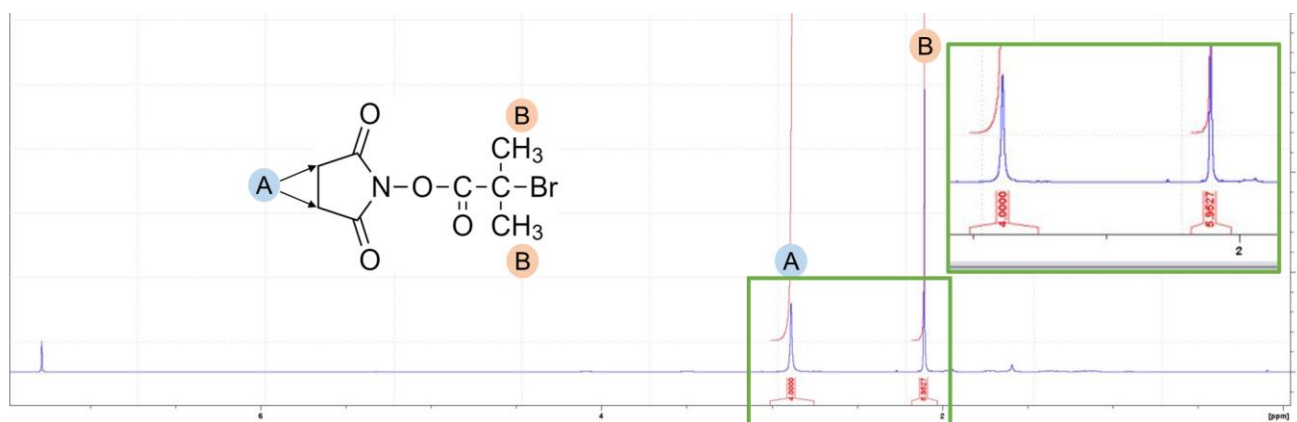
Figure II-24 – ^{1}H NMR (CDCl$_3$) spectre of the purified NHS-Br product with peak integration
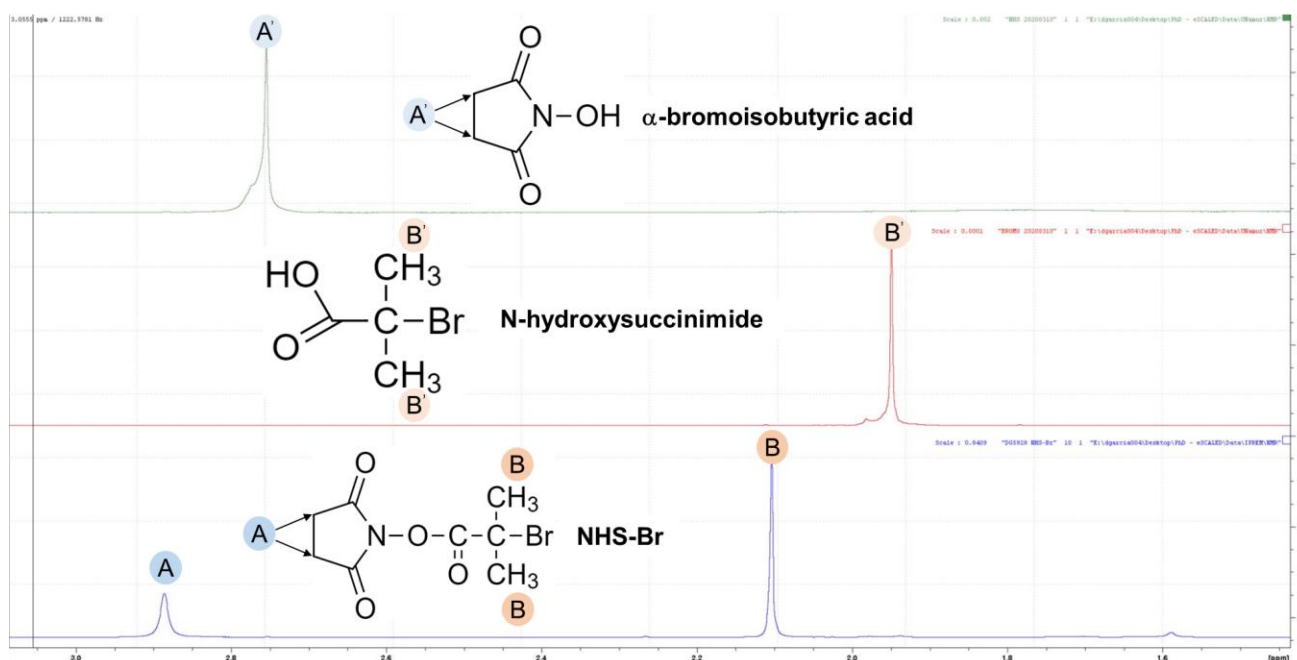
Figure II-25 – ^{1}H NMR (CDCl$_3$) spectre of the purified NHS-Br product (bottom) to the reagents used, namely α-bromoisobutyric acid (top) and N-hydroxysuccinimide (middle).
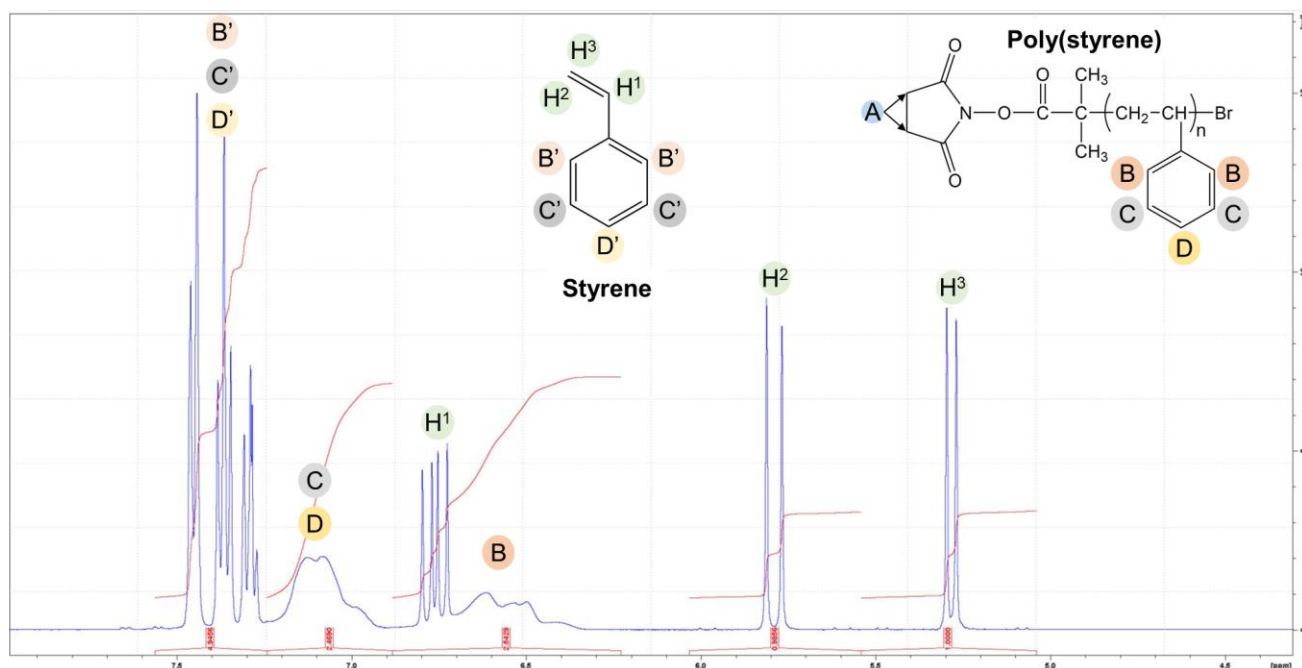
Figure II-26 – ^{1}H NMR (CDCl$_3$) spectre of the crude PS 5 before purification with peak integration. The peak attributed to cyclic succinimide group protons (A) at 2.8 ppm is not shown in this specter.
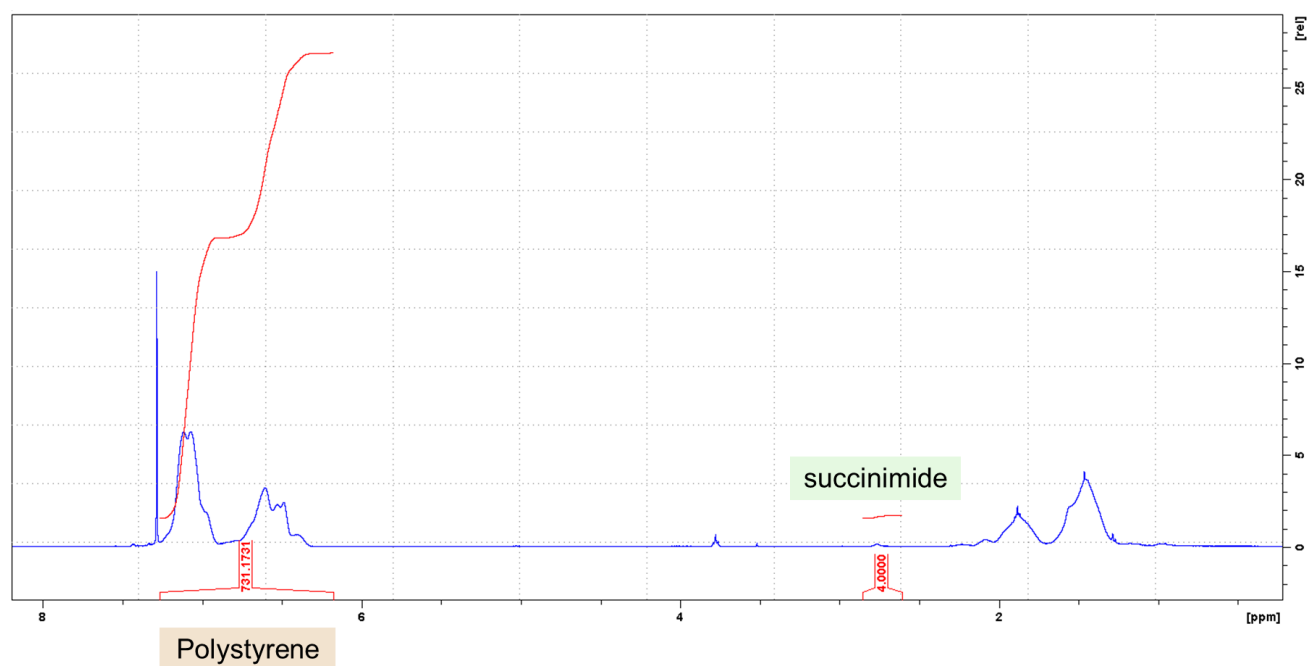
Figure II-27 – ^{1}H NMR (CDCl$_3$) spectre of the PS 5 after purification with peak integration.
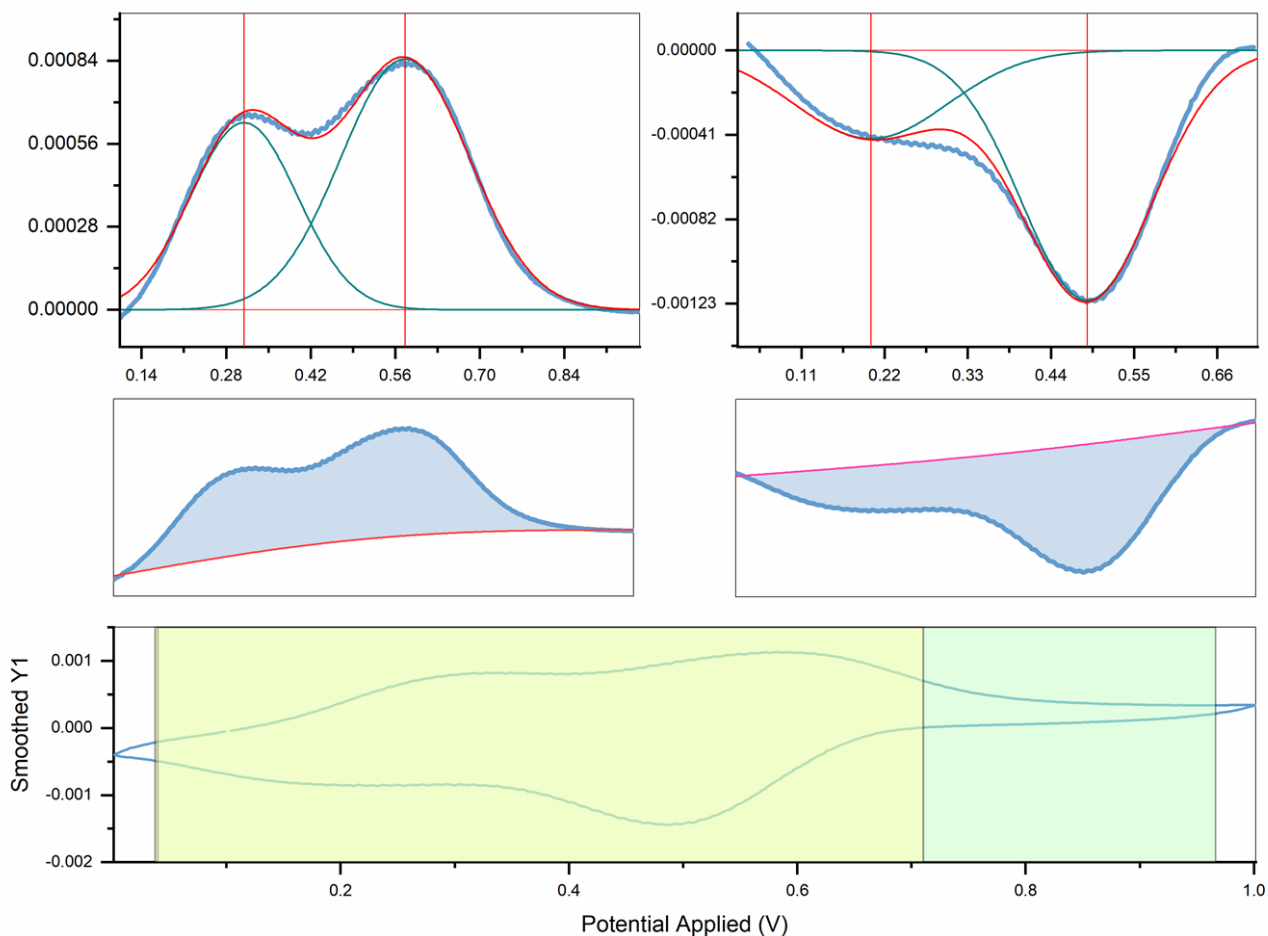
Figure II-28 – Integration of the forward and reverse scans of a cyclic voltammogram of a Pt electrode modified with non-porous and porous films of H_2SO_4-doped P(S-*stat*-BuA)-*b*-TANI. Integration performed with Cyclic Voltammetry app from OriginLab software.

Figure II-29 – NMR spectra acquisition routine parameters used at Institut des Sciences Analytiques et de Physico-Chimie pour l'Environnement et les Matériaux (IPREM).

CHAPTER III

Preparation of bipyridine-TANI-based catalyst for H^+/CO_2 reduction

CHAPTER III: **PREPARATION OF BIPYRIDINE-TANI-BASED CATALYST FOR H^+/CO_2 REDUCTION**

SHORT CONTEXT

This chapter describes the works performed to cope with the first method proposed to meet **Objective 2** of the present thesis: to investigate strategies to immobilize the catalyst on the catalyst-supporting layer developed, anchoring the catalyst by functionalization.

In this work, we aimed for the synthesis of the well-known [Re(bpy)(CO)$_3$Cl] (bpy = 2,2'-bipyridine), a molecular catalyst with high selectivity for CO_2 to CO conversion, functionalized with two TANI groups.[1–3] Figure III-1 demonstrates the proposed molecular catalyst.
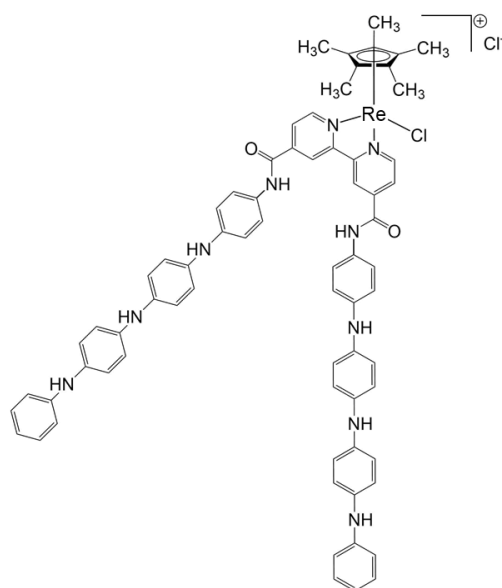
Figure III-1 – Proposed TANI-functionalized [Re(bpy)(CO)₃Cl], a molecular catalyst for heterogeneous electrochemical H⁺/CO₂ reduction.

TANI acts as an electron pathway and adhesion promoter between the molecular catalyst and the TANI end-capped polymer (developed in CHAPTER II:) within the supporting matrix by π-π stacking, thus immobilizing the molecular catalyst on the surface of the structured film. This approach combines the expertise of the group at UPPA in electron-conducting polymers and structured polymer films with the know-how in the field of H⁺/CO₂ reduction from the group at Collège de France. Figure III-2 illustrates the cross-sectional view of a carbon-based electrode with the TANI-modified [Re(bpy)(CO)₃Cl] catalyst immobilized on the TANI-capped polymer porous film.
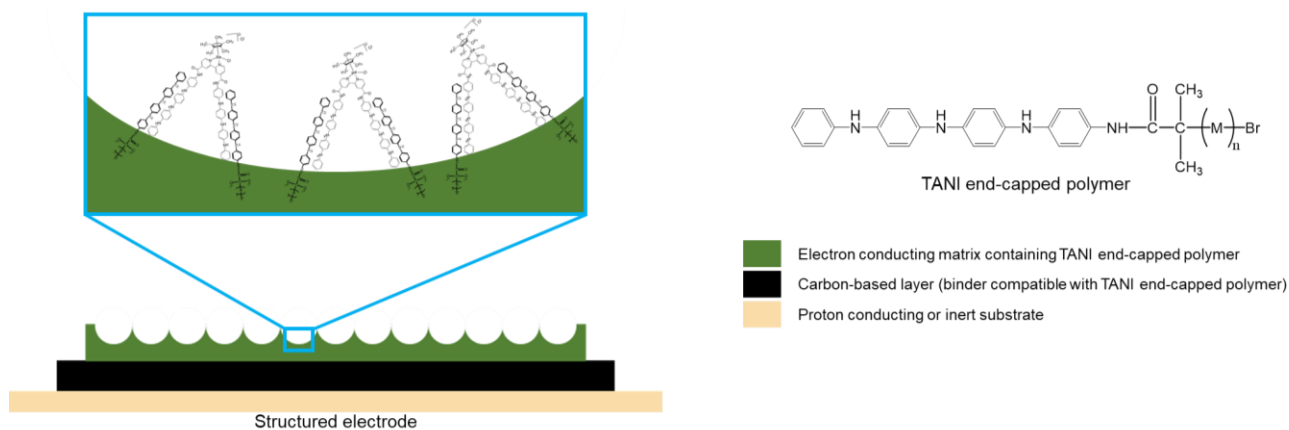
Figure III-2 – Immobilization of TANI-functionalized [Re(bpy)(CO)₃Cl] molecular catalyst on TANI end-capped electron-conducting structured films cast on carbon-based electrodes.

Conscious that TANI (as PANI) may present different oxidation states it is important to consider that these may affect the performance of the catalyst.

Hence, it is of previous importance to study the redox state, structure, purity, and isomer's presence of the synthesized TANI to avoid perturbations such as a variety of redox processes in the catalyst electrochemical performance. With this purpose, TANI must be reduced to its LEB form, on

which positional isomers can be avoided, and then coupled to bpy and this step will be the first of this coupling strategy.

III.1. TANI PRE-TREATMENT

The coupling of TANI to bpy includes first the reduction of TANI to its leucoemeraldine base (LEB) form, on which positional isomers can be avoided.

Indeed, it is expected that positional isomers can lead to a TANI-bpy-based catalyst for CO_2/H^+ with complex and different electrochemical mechanisms, difficult to interpret. For this reason, it is needed to reduce TANI to its most reduced state, LEB form. The latter (Figure III-3, left) was achieved by dispersion of TANI synthesized previously (see CHAPTER II:) in distilled water with $NaBH_4$. Along with the reaction, a color change was observed from dark blue, characteristic of EMB, to violet. Different authors in the literature reported the observation of different colors for the LEB state of TANI, for this reason, it was assumed that it is not possible to predict the structure and oxidation state of TANI taking into consideration only the color.

The oxidation state was thus analyzed by ^1H NMR (DMSO-d_6) (see III.4.3 Characterization methods for more details on the spectra acquisition routine parameters), presented in Figure III-3 (right) confirming that the protocol followed was successful and TANI was reduced from EMB to LEB.
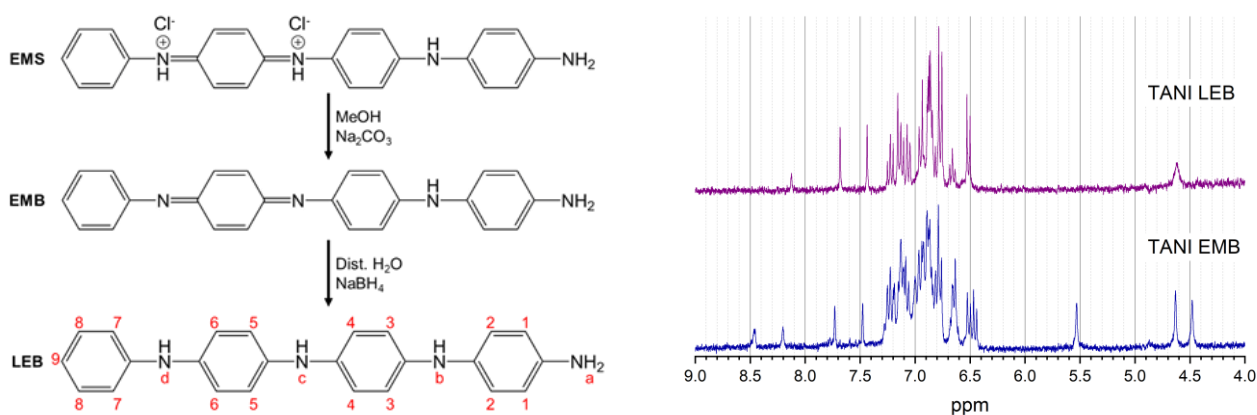
Figure III-3 – Left: Schematic representation of the protocol followed to reduce TANI from its EMS form to LEB. **Right:** ^1H NMR (DMSO-d_6) spectrum of Ph/NH_2 TANI EMB and LEB states.

The signal of terminal $NH_{2(a)}$ appears at 4.61 ppm, while the $-NH_c-$ and $-NH_d-$ signals were identified at 7.43 and 7.68 ppm, respectively. The appearance of the triplet at 6.66 ppm (H_9) and the peaks at 7.02-7.14 ppm (H_8) confirm the phenyl ring in the molecule. Signals at 6.50-6.52, 6.66-6.68, 6.75-6.78, and 6.96-6.96 ppm confirmed the presence of H_1, H_9, H_2+H_3, and H_7 protons, respectively. H_4+H_5+H_6 was attributed to the peaks in the 6.80-6.90 ppm region. In opposite to what was previously reported, no singlet was observed for $-NH_b-$ at 7.17 ppm, in the present results a triplet centered at 7.22 ppm was attributed to this proton. H_8 protons were not observed as a single triplet at 7.11 ppm as described in the literature but as five different peaks. In both cases, it could be related

to the presence of trimers and pentamers of aniline, whose presence was observed by MALDI-TOF analysis previously performed on the present batch of TANI. TANI LEB presented purple color.[4,5]

As demonstrated by ^{1}H NMR characterization, TANI was successfully reduced from EMB to LEB, although shorter or longer aniline oligomers might be present, the results are satisfactory enough. TANI now verifies the requirements for the coupling reaction with bipyridine.
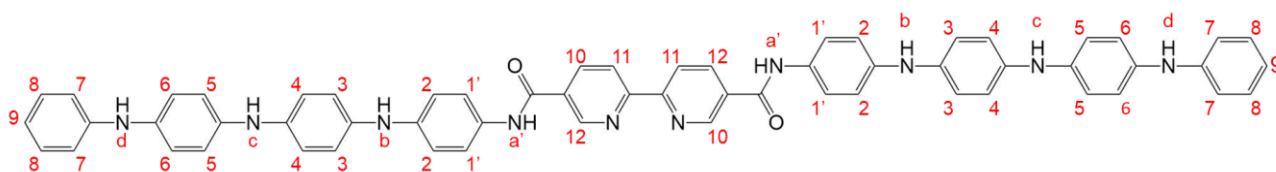
III.2. TANI-BPY COUPLING

Figure III-4 illustrates the three different strategies for the coupling between TANI and [2,2'-bipyridine]-5,5'-dicarboxylic acid. These three strategies have been chosen due to their simple and well-described protocols ease to adapt to this case and include a few steps only, without the expected appearance of many undesired by-products, hence leading to a facilitated purification process. The first approach uses 1-[Bis(dimethylamino)methylene]-1H-1,2,3-triazolo[4,5-b]pyridinium 3-Oxide (HATU), which is a well-known and commercially available amide coupling agent. The second approach consists of the pre-treatment of bpy with thionyl chloride (SOCl$_2$). Finally, the last strategy attempts to replicate the coupling mechanism used for the coupling between TANI and PS by functionalization of bpy with two succinimide groups.[6–12]
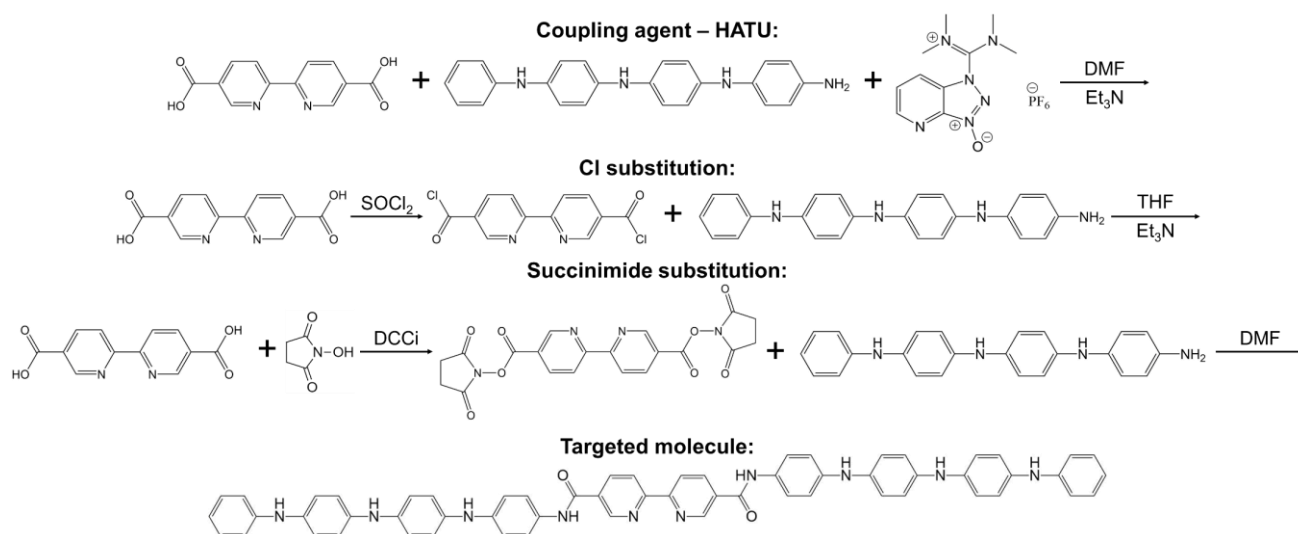
**Figure III-4 -** Strategies for the synthesis of bisTANI-[2,2'-bipyridine]-5,5'-dicarboximide.

In this section, each strategy will be analyzed and discussed individually. Figure III-5 illustrates the targeted molecule ($C_{60}H_{48}N_{10}O_2$) with the assignments. All materials (bpy-diCOOH and HATU) crude products' NMR spectra not described in the following can be found in III.6.

Figure III-5 - Targeted TANI-bpy molecule.

III.2.1. VIA COUPLING AGENT - HATU

The proposed protocol was performed in two different solvents, acetonitrile (ACN) and dimethylformamide (DMF). The first did not allow good solubilization of TANI and this experiment was abandoned. DMF provided better solubilization of all solid reagents[6,7]. The crude product from the reaction performed in DMF was thus studied by thin-layer chromatography (TLC) which showed three isolated spots. One of these was attributed to residual TANI LEB, a second one at the origin possibly attributed to side products from reacted HATU, and a third one positioned between the first two which could be the desired product. The crude product was analyzed by ^1H NMR (DMSO-d_6) (Figure III-6) and then purified by Al_2O_3 column chromatography.
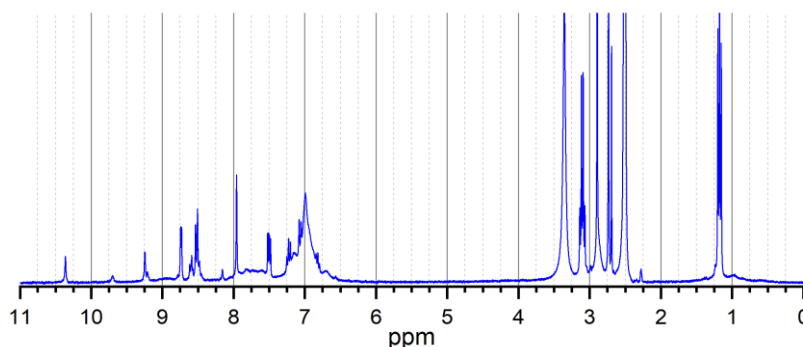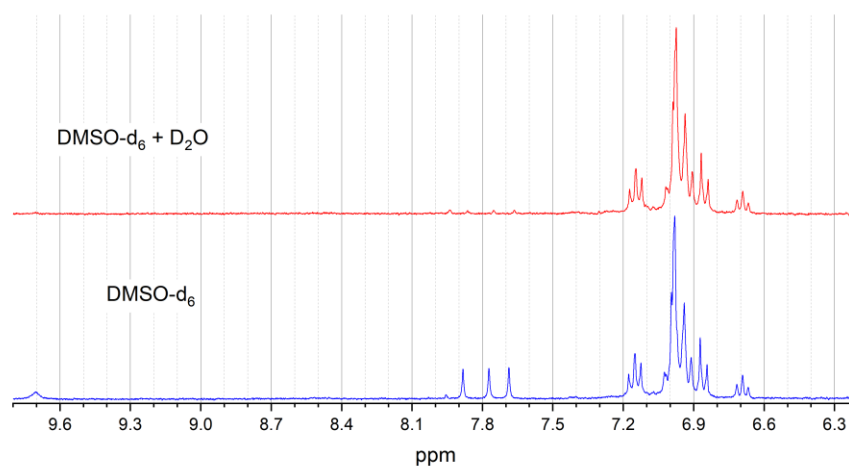

Figure III-6 - ^1H NMR (DMSO-d_6) spectrum of the crude product from TANI-bpy coupling by HATU coupling agent in DMF.

Different colors were observed on the extracted products for different methanol percentages in 100 mL of DCM. Between 1 and 2 %, the color was dark blue, changing to dark purple above 3 % and becoming colorless after 5 %. When 100 % methanol was added the product was again dark blue. Since TANI in its LEB form was originally purple, it was expected that TANI-bpy would possibly keep this color, being aware that TANI could be easily oxidized during the reaction and resulting in a color change. For this reason, it was considered of greatest interest to perform more detailed studies on the products isolated from DCM/MeOH above 3 % since these presented a more intense purple color. TLC was performed on the mentioned fraction and it was decided to perform ^1H NMR (DMSO-d_6) on the sample extracted with 3 % MeOH.

The results from ^1H NMR (DMSO-d_6) are presented in Figure III-7. Four peaks were observed at 9.70, 7.88, 7.77, and 7.69 ppm which could be attributed to -NH- a', b, c, and d protons (see Figure III-5), respectively. The peak integration of these peaks revealed that they are present in equal amounts. This attribution was confirmed by the addition of D_2O which lead to the disappearance of the peaks as expected.[13]

Figure III-7 - ¹H NMR (DMSO-d₆) spectrum of isolated product from TANI-bpy coupling by HATU coupling agent, extracted with basic DCM/MeOH (3 %) solution.

The peaks attributed to the bipyridine group were expected to appear as two doublets (four protons) close to each other between 8.40 and 8.65 ppm and one singlet (two protons) at 9.20 ppm (see Figure III-15 in section III.6) and were not present within the NMR spectrum.

The integration of the region between 6.60 and 7.20 ppm, which is usually known to be attributed to aromatic protons, was approximately fifty-eight, *i.e.*, 18 protons more than expected as reported in Figure III-8. This result can be explained by the presence of aniline oligomers. This statement is eventually in agreement with the appearance of a peak at 7.96 ppm, which could be related to a secondary amine since it is known that the chemical shift of amine protons depends on the length of the oligoaniline.

The product was diluted with a strong acid during its preparation for MALDI-TOF characterization and this step lead to a color change from violet to dry green due to the TANI behavior upon its oxidation state, the EMS obtained in an acidic medium being known to be green. The TANI-bpy molecule, if TANI is kept at its LEB state, is described by the $C_{60}H_{48}N_{10}O_2$ formula, and is expected to present 941.09 g/mol as molecular weight and 940.40 u as the exact mass. Figure III-9 presents the MALDI-TOF results.
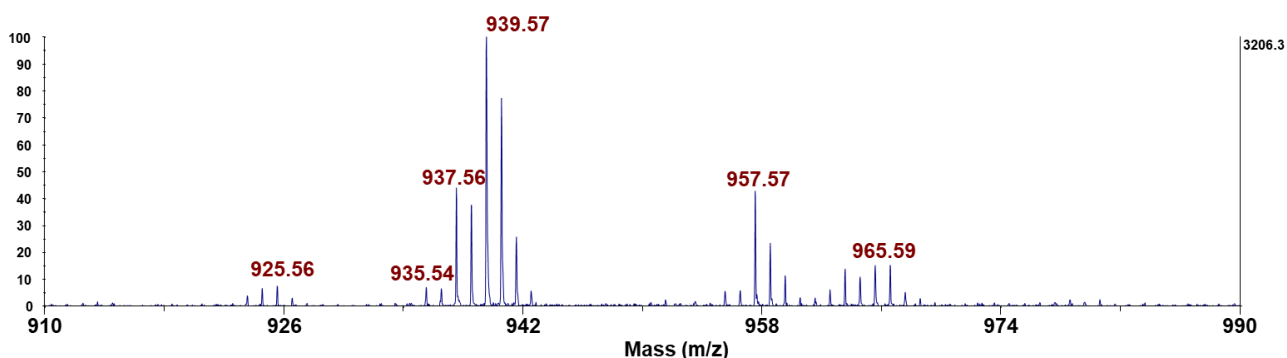
Figure III-9 – MALDI-TOF results from the analysis of the TANI-bpy coupling reaction (via HATU) product.

The species at 939.57 could be attributed to the remaining TANI(LEB)-bpy structure, while the species at 937.56 and 935.54 m/z could be attributed to two oxidized emeraldine-like TANI-bpy structures, as suggested in Figure III-10 or their positional isomers. Nevertheless, it was not possible to predict and explain the species present with 925.56, 957.57, and 965.59 m/z.
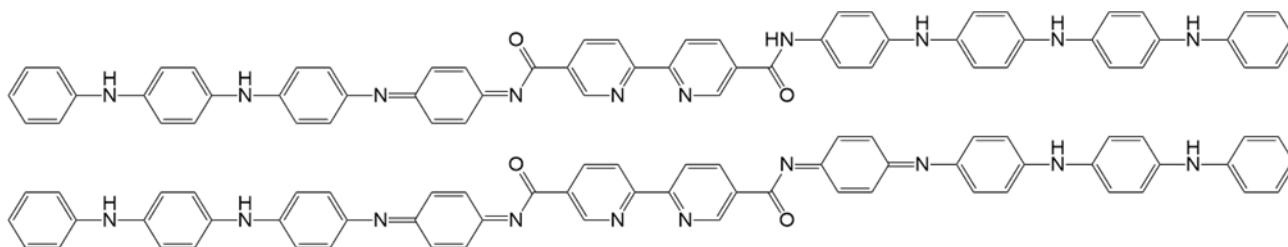

Figure III-10 - Proposed structures for oxidized TANI-bpy molecule: $C_{60}H_{46}N_{10}O_2$ (top) and $C_{60}H_{44}N_{10}O_2$ (bottom).

The protocol was repeated two more times with TANI in its EMS state but without success. Further studies would need to be performed to confirm the previous hypothesis and especially to confirm the presence of bipyridine in the structure, such as ^{15}N NMR, X-ray photoelectron spectroscopy (XPS), Fourier-transform infrared spectroscopy (FTIR), and UV-Vis. Another hypothesis considered was that two TANI LEB molecules could be coupled together by HATU. However, the analysis of the product obtained by the reaction performed in DMF with the absence of bpy did not lead to a clear conclusion. (^1H NMR within Figure III-17 in section III.6).

The results obtained by this strategy were not conclusive. The MALDI-TOF analysis of the sample purified with a basic DCM/MeOH (3 %) solution may suggest that the bpy-TANI coupling via the HATU coupling agent is successful and, therefore, promising. However, the fact that other unknown species may be present suggests that the purification protocol required to isolate the desired product may be complex. Therefore, the experimental conditions need to be optimized and a more extensive and detailed characterization of the products obtained should be performed.

III.2.2. Cl SUBSTITUTION

The protocol for TANI-bpy synthesis consisted of reacting TANI LEB with bpy-diCl in THF.[8,9] This reaction was also performed in DMF but its crude product was then abandoned, giving priority to the reaction in THF as reported within the literature. The purification of the crude product was performed by Al_2O_3 and extracted with 2 % of methanol. The NMR spectra are reported in Figure III-11.
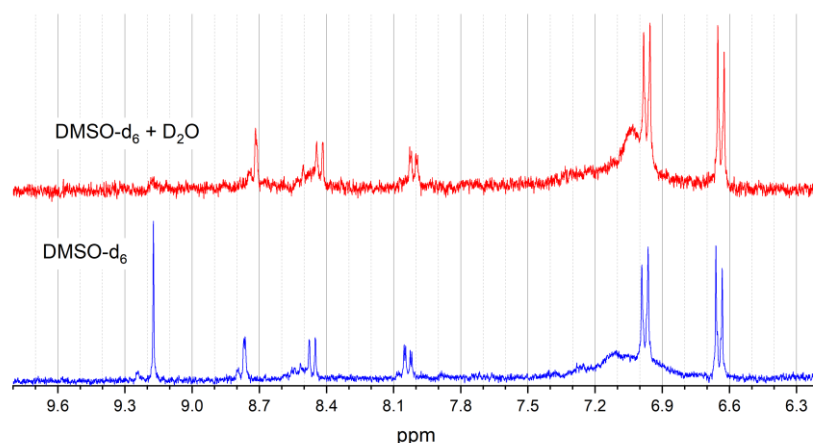
Figure III-11 – ^{1}H NMR (DMSO-d[6]) spectrum of isolated product from TANI-bpy coupling by Cl substitution, extracted with basic DCM/MeOH(2 %) solution.

The addition of D_2O did not lead to the disappearance of any peaks, except the disappearance of the peak at 9.17 ppm which could be due to mobile protons. This suggests the absence of any amine protons. MALDI-TOF characterization of TANI-bpy ($C_{60}H_{48}N_{10}O_2$) is expected to present 941.09 g/mol as molecular weight and 940.40 u as exact mass. None of the detected species was present m/z close to the expectations. It was then concluded that the targeted product was not successfully achieved. It is important to mention that the bpy-diCl product was not used immediately after preparation, which can explain the loss of Cl functionality if the product was exposed to humidity.

III.2.3. SUCCINIMIDE SUBSTITUTION

This last strategy is reported in Figure III-12.
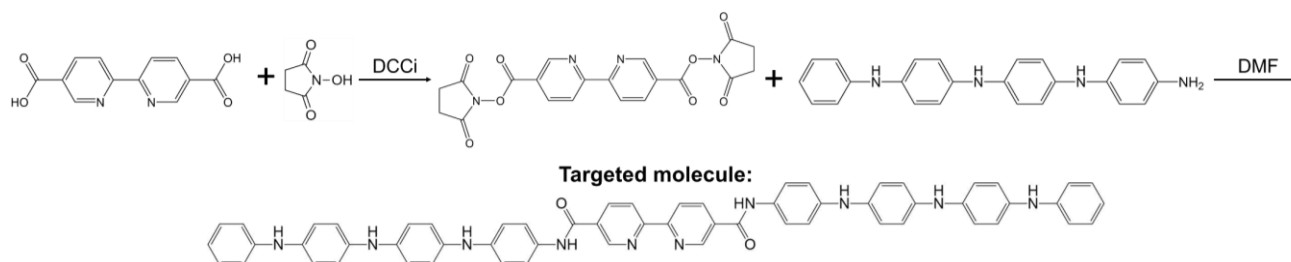
Figure III-12 – Coupling mechanism used for the coupling between TANI and PS by functionalization of bpy with two succinimide groups

The first step is bipyridine functionalization which was performed following the protocol previously described by Yamamoto *et al.*[10,11]. The crude product obtained was purified by precipitation in an ethanol/cyclohexane blend followed by filtration and drying under vacuum (see section III.4.2.3). ^{1}H NMR (DMSO-d[6]) of the purified product is reported in Figure III-13.
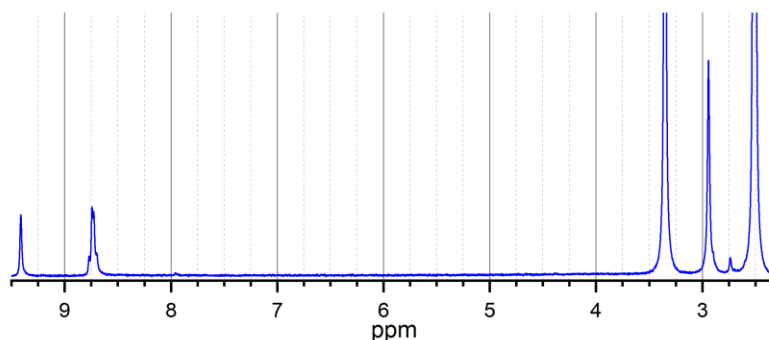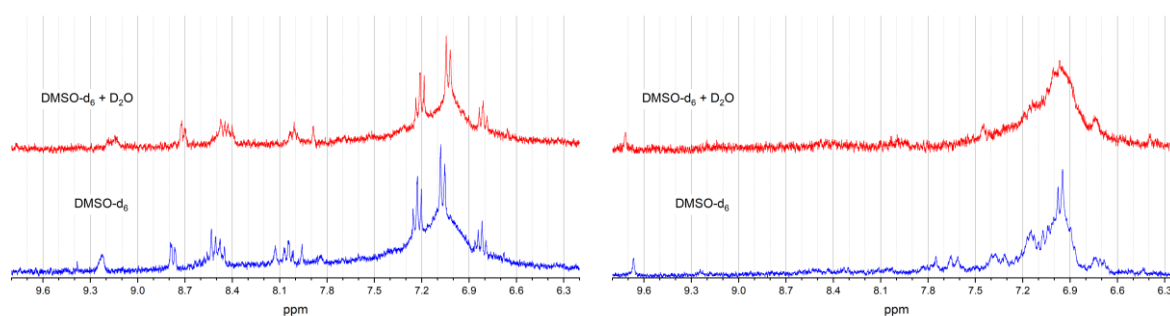
Figure III-13 - ¹H NMR (DMSO-d₆) spectrum of the purified bpy-disuccinimide molecule.

The NMR spectrum confirmed that the targeted structure was achieved as shown by the integration of the peaks (see Figure III-18 in section III.6) at 9.41 (two protons from bpy), 8.74 (four protons from bpy), and 2.94 ppm (eight protons from the two cyclic succinimide groups). The product (bpy-succ) was obtained as a thin white powder.

In the second step of this strategy, the TANI LEB reacts with bpy-succ in DMF at 40 °C, and the crude product is analyzed by TLC that revealed three different spots, the first (the leas polar) attributed to residual unreacted TANI LEB, the second (the most polar) closer to the origin that was not perfectly defined and assumed as the presence of many identical species with similar polarity. Finally, the third and well-defined spot indicated the presence of a species with intermediate polarity, *i.e.*, situated between the first and second spots described.

The crude product was purified by Al_2O_3 column chromatography targeting the spot with intermediate polarity. Two isolated products were considered of greater interest for further structural studies. These were extracted with 2 and 5% methanol and characterized by ¹H NMR (DMSO-d₆) and the spectra are reported in Figure III-14.

Figure III-14 - ¹H NMR (DMSO-d₆) spectrum of purified products from TANI-bpy coupling by succinimide substitution extracted with 2 (left) and 5 % (right).

In both cases, it is possible to observe a broad peak region from 6.6 to 7.5 ppm, which is expected to be related to aromatic protons from TANI. The addition of D_2O, expected to indicate the presence of peaks from –NH– protons by the disappearance of the related peaks, did not show any effect for the product extracted with 2 % MeOH. Contrarily, D_2O addition leads to the disappearance

of the peaks originally at 7.5-7.8 ppm of the analysis of the product extracted with 5 % MeOH. Both samples were compared in TLC, the product extracted with 2 % MeOH showed a single spot while the product extracted with 5 % MeOH revealed two different spots with different polarity, which indicates the presence of more than one species.

Yet, these studies were not clear and not enough to conclude if the protocol followed was successful or not. Nevertheless, MALDI-TOF measurements could be performed on isolated products. Moreover, it would be of great interest to repeat the protocol with microwave-assisted heating, since the same coupling mechanism was used and successful in the preparation of TANI end-capped polymers in the catalyst elaboration strategies did not go further because the product mixture obtained, the multi-step purification needed and at the same time the lack of time spent at Collège de France. Nevertheless, this work opened perspectives for the following students. Although the coupling strategy via HATU seemed promising, the purification was complex, and a mixture of unidentified species was obtained. Therefore, and since it was previously demonstrated to be successful, together with the simplicity of the experimental setup and protocol, the succinimide substitution coupling strategy may have a bigger potential to successfully synthesize the targeted TANI-bpy and should be studied in more detail.

III.3. CONCLUSION AND PERSPECTIVES

LEB state was successfully achieved by reacting TANI with NaBH$_4$ in distilled water. Three different strategies were defined to couple TANI LEB to bpy. The first consists of the Cl substitution of a previously functionalized bpy. This protocol was considered unsuccessful according to NMR and MALDI TOF results. The second strategy functionalizes bpy with two succinimide groups which are then substituted to couple TANI by an amide bond. MALDI TOF studies are still to be performed to conclude if the protocol was successful or not. The last protocol reacts TANI, bpy, and HATU on a suitable solvent. DMF was found to promote better solubilization of all reactants. ^{1}H NMR (DMSO-d$_6$) spectra were found to be difficult to interpret due to the absence of the bpy protons close to their original chemical shift and to the excess of detected protons. Yet, the MALDI TOF results suggested the presence of species possibly derived from the oxidation of the TANI(LEB)-bpy molecule. Further studies should be performed to evaluate the hypothesis considered in the present work, considering a deep and complete study on the NMR characterization of TANI and the TANI-bpy products obtained so that the full peak assignment is possible.

The manipulation of TANI was found to be difficult due to its sensitivity to pH and solvents. Different oxidation states of TANI are known to present characteristic colors. Yet, in this work, a broad variety of colors was observed, some were not described before in the literature or attributed to different oxidation states.

III.4. EXPERIMENTAL PROCEDURES

Table III-1 - List of chemicals used for synthesis protocols.

Material	Provider/grade
[2,2'-bipyridine]-5,5'-dicarboxylic acid	TCI
Chloroform D 100 %	Eurisotop
CH_3CN anhydrous	Sigma-Aldrich
D_2O	Eurisotop
N,N'-Dicyclohexylcarbodiimide 99 % (DCCi)	Alfa Aesar
DCM	Sigma-Aldrich
N,N-Diisopropylethylamine 99 % (DIPEA)	Sigma-Aldrich
DMF anhydrous	Sigma-Aldrich
DMSO-d_6	Eurisotop
Et_3N	Roth
HATU	Alfa Aesar
K_2CO_3	Sigma-Aldrich
Methanol	Carlo Erba
$NaBH_4$	Fisher Chemical
$NaCO_3$	Sigma-Aldrich
NH_4OH	Alfa Aesar
N-hydroxysuccinimide	Alfa Aesar
$SOCl_2$	Sigma-Aldrich
THF	Sigma-Aldrich

III.4.1. TANI REDUCTION TO LEUCOEMERALDINE STATE

In a round bottom flask, equipped with a stirring bar, TANI EMS (500 mg, 1 eq.) is added with MeOH. Under stirring, Na_2CO_3 (1.46 g, 10 eq.) was added. The solution is filtered after 10 min under stirring to isolate solubilized TANI EMB from sodium carbonate. MeOH is evaporated with rotovapor. Distilled water is added to TANI EMB and an ultrasonic bath is used to disperse the solid. $NaBH_4$ (26.9 g, 52.3 eq). is added carefully in five portions. The addition of $NaBH_4$ is performed while cooling the system on an ice bath. The reaction occurs for 48 hours under Argon with continuous stirring. The reactional mixture is then filtered and washed with distilled water. Initially, the filtrate is strongly basic, the purple filtered product is then washed until the filtrate pH is neutral. The product is collected and dried under vacuum at room temperature for 24 hours. ^{1}H NMR (DMSO-d_6) confirms the LEB structure of TANI.[14]

Alternatively, the steps involving deprotonation of TANI EMS in MeOH with Na_2CO_3 can be skipped, *i.e.*, TANI EMS, and be directly dispersed in distilled water, following the previously described steps.

III.4.2. TANI-BPY COUPLING

All synthesis protocols are assisted by thin-layer chromatography (TLC) on Al_2O_3 plates in DCM (2, 5, and 10% MeOH) with NH_4OH to create basic conditions.

III.4.2.1. VIA COUPLING AGENT - HATU

To a round bottom flask, filled with Argon, [2,2'-bipyridine]-5,5'-dicarboxylic acid (12 mg, 1 eq.), HATU (52 mg, 3 eq.), and TANI LEB (52 mg, 3 eq.) are added. 2 mL of anhydrous DMF is added followed by Et_3N (20 µL, 3 eq.) to solubilize all the solid reactants under stirring. The reaction occurs at room temperature for 48 h, under Argon. The solvent is then evaporated under a vacuum and the crude product is characterized by ^1H NMR (DMSO-d_6)[6,7].To a round bottom flask, filled with Argon, [2,2'-bipyridine]-5,5'-dicarboxylic acid (12 mg, 1 eq.), HATU (52 mg, 3 eq.), and TANI LEB (52 mg, 3 eq.) are added. 2 mL of anhydrous DMF is added followed by Et_3N (20 µL, 3 eq.) to solubilize all the solid reactants under stirring. The reaction occurs at room temperature for 48 h, under Argon. After this time, the solvent is evaporated under a vacuum and the crude product is characterized by ^1H NMR (DMSO-d_6)[6,7].

The crude product is purified by Al_2O_3 column chromatography as follows. Ten solutions of 100 mL of DCM with increasing methanol content from 1 to 10% are prepared and two drops of NH_4OH are added to each of them. The crude is solubilized in DCM and added to the column. DCM/methanol solutions are added in ascending order of methanol content. The extracted products are collected in 20 mL glass test tubes. This protocol applies to all purifications performed along with this work.

III.4.2.2. Cl SUBSTITUTION

The first part of the protocol consists of the synthesis of [2,2'-bipyridine]-5,5'-dicarbonyl dichloride. [2,2'-bipyridine]-5,5'-dicarboxylic acid (0.500 g, 2.047 mmol) and thionyl chloride (8 mL, 110 mmol) are added to a 50 mL Schlenk flask and heated under reflux and Argon for 24 hours. The reactional mixture is then cooled down to room temperature and the volatiles are evaporated under a vacuum. The desired product (yellow solid) is stored under Ar without further purification.

For the coupling reaction with TANI LEB, [2,2'-bipyridine]-5,5'-dicarbonyl dichloride (74.5 mg, 1 eq.) is added to a 50 mL round bottom flask, previously filled with Ar, and solubilized in 10 mL of dry tetrahydrofuran (THF). This solution is then cooled to 0 ºC and kept under an Ar blanket. TANI LEB (208 mg, 2.2 eq.) is solubilized in 10 mL dry THF with trimethylamine (Et_3N) (108 µL, 3eq.) and added dropwise to the solubilized bpy. The reaction is kept under stirring, under an Ar blanket. After 40 min, the ice bath is removed and let to warm up to room temperature. If a slurry is formed, 5 mL of THF is added. The reaction occurs for 20 h and DMF is then evaporated under a vacuum. ^1H NMR (DMSO-d_6) characterizes the crude product.[8,9]

III.4.2.3. SUCCINIMIDE SUBSTITUTION

[2,2'-bipyridine]-5,5'-dicarboxysuccinimidyl is prepared by solubilization of [2,2'-bipyridine]-5,5'-dicarboxylic acid (501 mg, 1 eq.) in 20 mL of dry DMF in the presence of DCCi (850 mg, 2.01 eq.) and NHS (475 mg, 2.01 eq.). The reaction occurs for 15 h at 40 ºC, under continuous stirring. The reaction mixture is filtered to remove insoluble products. A mixture of ethanol (20 mL) and cyclohexane (60 mL) is added to the filtrate to precipitate the desired product. The product is a thin white powder and is collected by filtration, followed by drying under a vacuum for the complete removal of solvents. The product structure is confirmed by ^{1}H NMR (DMSO-d_6). Yield: 61 % as a thin white powder.

The coupling reaction between TANI LEB (50 mg, 2.2 eq.) and [2,2'-bipyridine]-5,5'-dicarboxysuccinimidyl (27 mg, 1 eq.) is performed in DMF (2 mL). The reaction occurs for 48 h at 40 ºC, under continuous stirring. ^{1}H NMR (DMSO-d_6) characterizes the crude product after solvent evaporation under a vacuum.[10,11]

III.4.3. CHARACTERIZATION METHODS

^{1}H NMR spectra are performed with Bruker Avance III 300 NMR spectrometer at room temperature. This characterization was performed following a standard routine procedure from the NMR technical services at Collège de France for the obtention of ^{1}H NMR spectra. Figure III-20 at III.6 Appendixes displays some of the routine parameters.

MALDI-TOF was performed in Plateforme de Protéomique 3P5, Université de Paris, Institut Cochin, INSERM, U1016, CNRS, UMR8104. Positively charged MALDI-TOF studies were carried out on α-cyano-4-hydroxy-cinnamic acid (CHCA) 5 mg/mL matrix. The sample is solubilized in MeOH, followed by the addition of 0.1 % TFA.

III.5. BIBLIOGRAPHY

[1]   L. Yoon Suk Lee, K.-Y. Wong, *Chem* **2017**, *3*, 717.

[2]   J. Hawecker, J. -M Lehn, R. Ziessel, *Helv. Chim. Acta* **1986**, *69*, 1990.

[3]   J. Hawecker, J.-M. Lehn, R. Ziessel, *J. Chem. Soc., Chem. Commun.* **1984**, *984*, 328.

[4]   I. Kulszewicz-Bajer, I. Rozalska, M. Kuryłek, *New J. Chem.* **2004**, *28*, 669.

[5]   I. Rozalska, P. Kułyk, I. Kulszewicz-Bajer, *New J. Chem.* **2004**, *28*, 1235.

[6]   Y. Li, H. Wang, B. Tarus, M. R. Perez, L. Morellato, E. Henry, V. Berka, A. L. Tsai, B. Ramassamy, H. Dhimane, C. Dessy, P. Tauc, J. L. Boucher, E. Deprez, A. Slama-Schwok, *Proc. Natl. Acad. Sci. U. S. A.* **2012**, *109*, 12526.

[7]   D. A. Roberts, A. M. Castilla, T. K. Ronson, J. R. Nitschke, *J. Am. Chem. Soc.* **2014**, *136*, 8201.

[8]   F. Camerel, G. Albert, F. Barrière, C. Lagrost, M. Fourmigué, O. Jeannin, *Chem. - A Eur. J.* **2019**, *25*, 5719.

[9]   M. Aizenberg, K. Okeyoshi, J. Aizenberg, *Adv. Funct. Mater.* **2018**, *28*, 1.

[10] K. Yamamoto, K. Kitamoto, K. Yamauchi, K. Sakai, *Chem. Commun.* **2015**, *51*, 14516.

[11] F. Grimm, K. Hartnagel, F. Wessendorf, A. Hirsch, *Chem. Commun.* **2009**, 1331.

[12] P. Marcasuzaa, S. Reynaud, B. Grassl, H. Preud'homme, J. Desbrières, M. Trchovà, O. F. X. Donard, *Polymer (Guildf).* **2011**, *52*, 33.

[13] T. Hirao, K. Iida, *Chem. Commun.* **2001**, 431.

[14] D. Moon, M. Ezuka, K. Osakada, T. Yarnarnoto, *Macromol. Chem. Phys.* **1993**, *194*, 3149.

III.6. APPENDIXES

Table III-2 - List of crude products, starting materials, and strategy used.

	Strategy	TANI	Solvent
C2	HATU	LEB	DMF(Et$_3$N)
C3	HATU	LEB	CH$_3$CN(Et$_3$N)
C4	Succ	LEB	DMF
C5	Cl	LEB	DMF(Et$_3$N)
C6	Cl	LEB	THF(Et$_3$N)
C7	HATU	EMS	DMF(Et$_3$N)
C8	HATU	EMS	CH$_3$CN(Et$_3$N)
C9	Cl	EMS	THF(Et$_3$N)
C10	Cl	EMS	THF(DIPEA)
C11	Cl	LEB	THF(DIPEA)
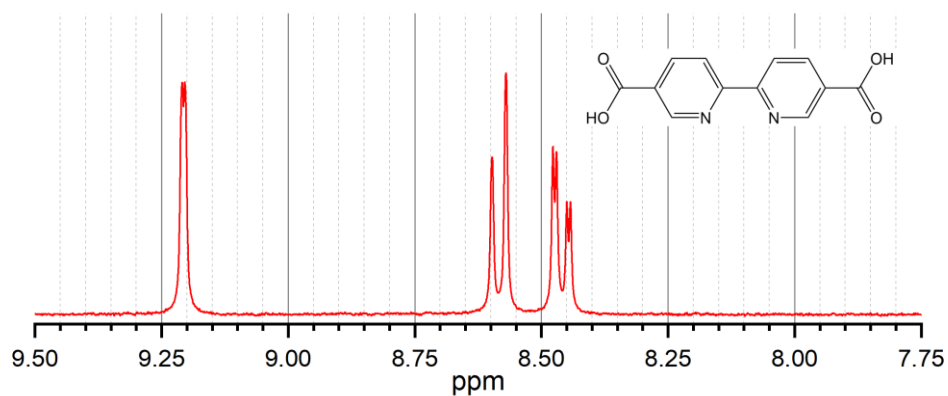
Figure III-15 - ^{1}H NMR (DMSO-d$_6$) spectrum of [2,2'-bipyridine]-5,5'-dicarboxylic acid.
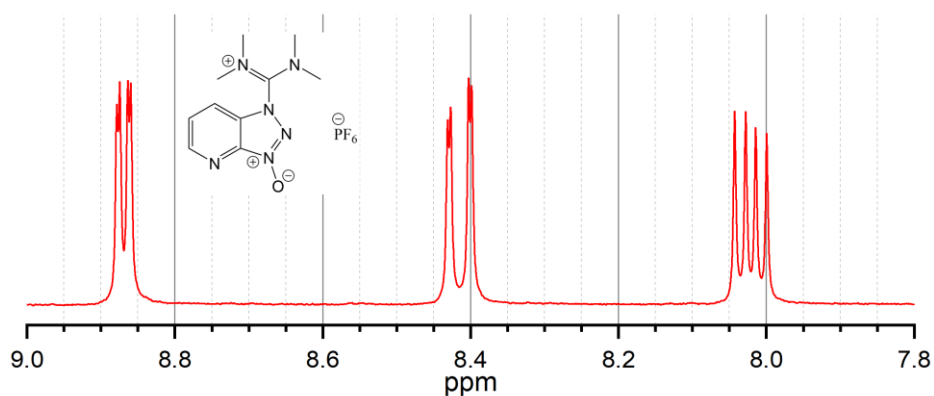
Figure III-16 - ^{1}H NMR (DMSO-d$_6$) spectrum of HATU.
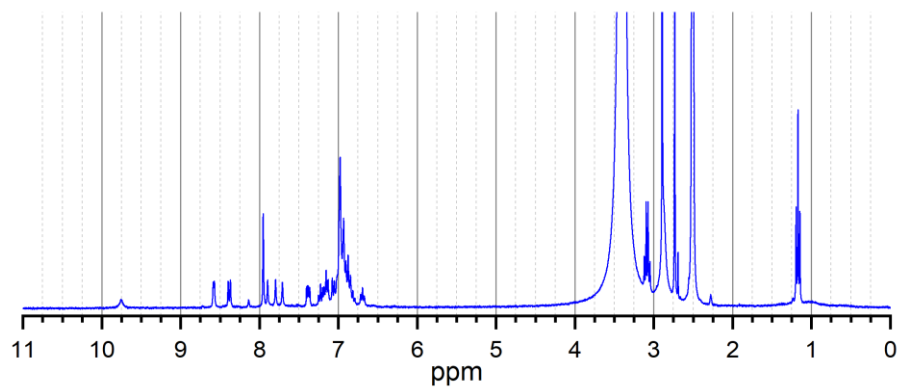
Figure III-17 – ^{1}H NMR (DMSO-d_6) spectrum of the crude product from TANI-HATU reaction in DMF.
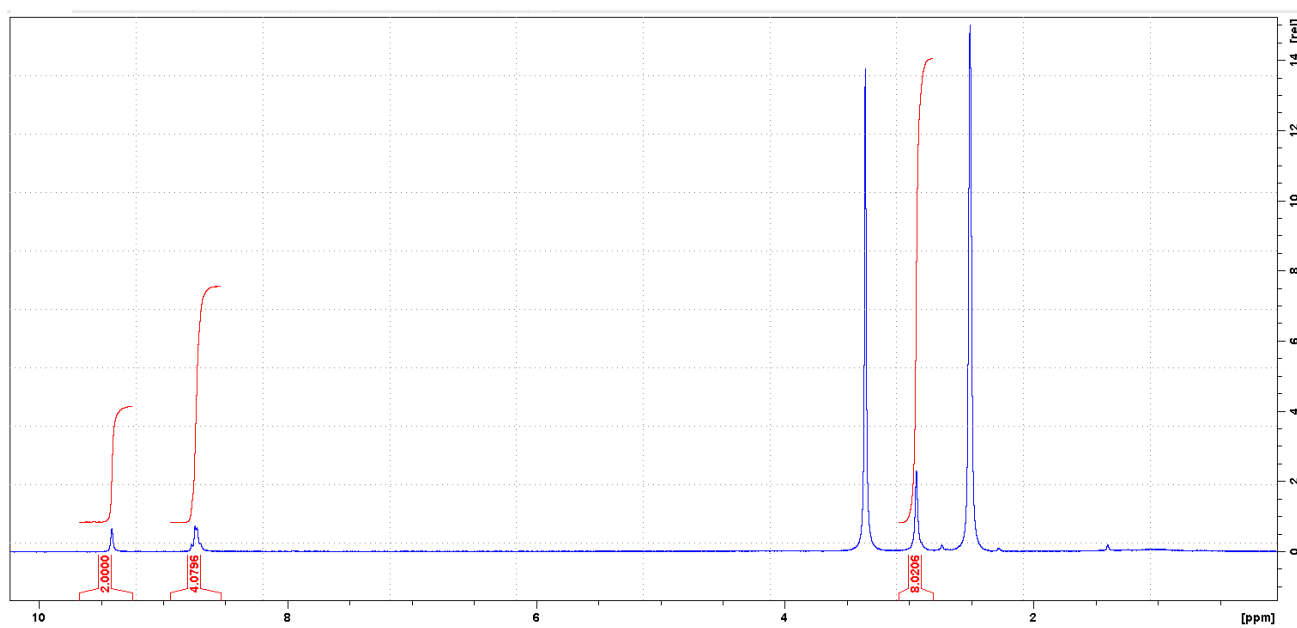
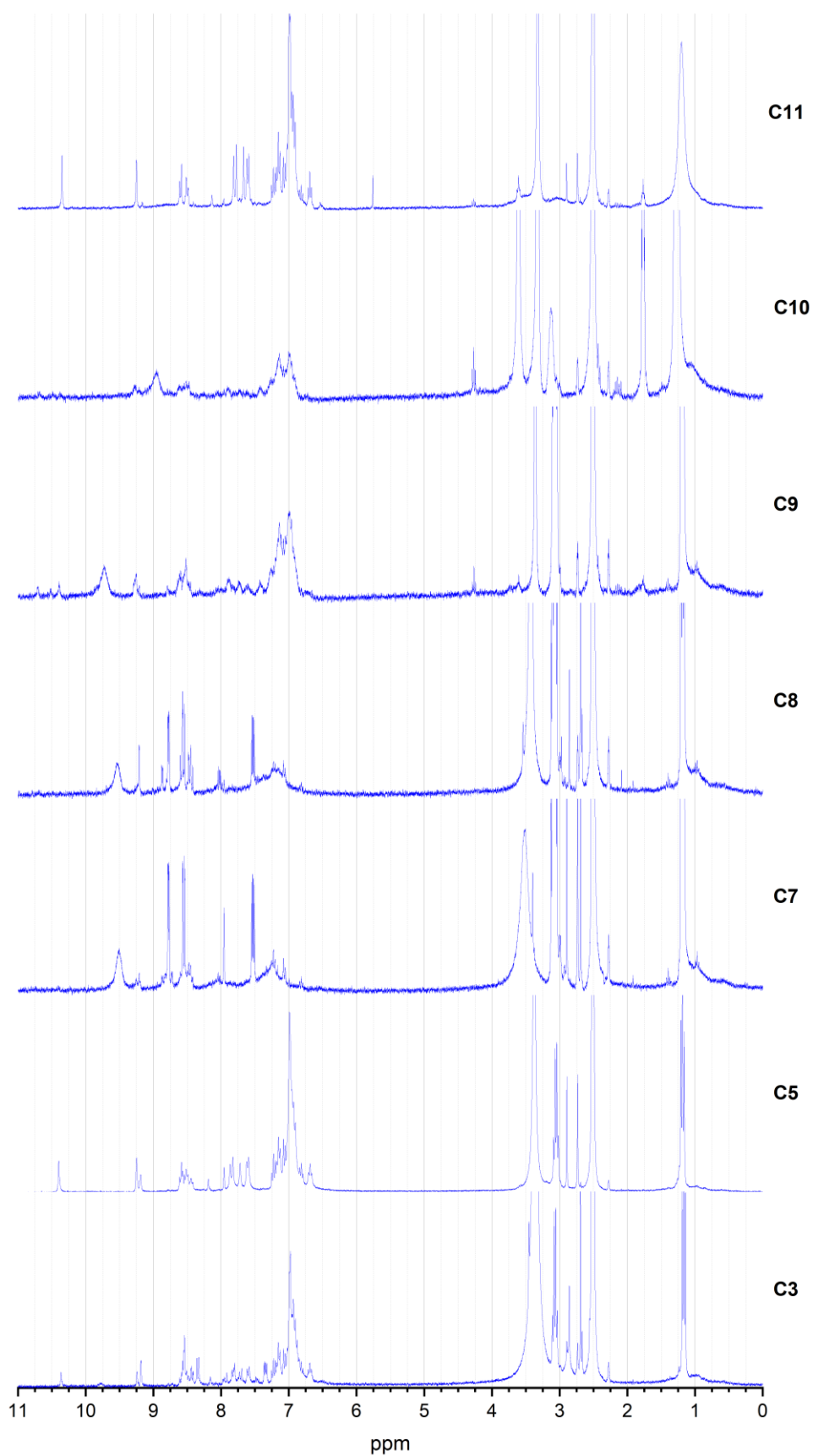**Figure III-18 –** ^{1}H NMR (DMSO-d_6) spectrum of the purified bpy-disuccinimide molecule with peak integration.

Figure III-19 - ^{1}H NMR (DMSO-d$_6$) of other crude products that were not purified.

Figure III-20 – NMR spectra acquisition routine parameters used at Collège de France.

CHAPTER IV

Synthesis of ZIF-8 templated macro-microporous zinc oxide and its photocatalytic activity

CHAPTER IV: **SYNTHESIS OF ZIF-8 TEMPLATED MACRO-MICROPOROUS ZINC OXIDE AND ITS PHOTOCATALYTIC ACTIVITY**

SHORT CONTEXT

This chapter describes the works performed to cope with the second method proposed to meet **Objective 2** of the present thesis: to investigate strategies to immobilize the catalyst on the catalyst-supporting layer developed, developing hierarchical porous particles to carry/host the electrocatalyst. This approach explores an alternative to the catalyst immobilization method investigated in CHAPTER III:. The hierarchically porous particles developed are expected to facilitate the heterogenization of electrocatalysts on the surface of the structured electroactive P(S-*stat*-BuA)-*b*-TANI films developed as catalyst supporting layer in CHAPTER II:.

Hereby, we report the synthesis of macro-micro porous 3D-ordered ZnO obtained from zeolitic imidazolate framework-8 (ZIF-8) and its application in the photodegradation of Rhodamine-B. ZIF, which consists of metal ions (Zn^{2+}, Co^{2+}) and imidazolate linkers that form a 3D tetrahedral framework, is a subclass of metal-organic frameworks (MOFs). Previous works report that ZnO can be obtained from the calcination of ZIF-8 in the air. Due to the microporous character of ZIF-8, the obtained ZnO will partially inherit this property.[1–14] Here, a polystyrene (PS) template was used to

induce the formation of tetrakaidecahedron macro-microporous ZIF-8, through colloidal templating, as reported before.[15–17] Upon calcination, ZnO was for the first time obtained with a porous tetrakaidecahedron morphology.

IV.1. PREPARATION OF 3D MATERIALS FROM MONODISPERSE COLLOIDAL SPHERES

Colloidal templating is a method popularly employed in the fabrication of macroporous materials.[18] This technique is a hard-templating technique in which the periodic pore structures are molded by a colloidal crystal. The molds, *i.e.*, colloidal crystals, most commonly employed are opaline structures of face-centered cubic (fcc) arrays of monodisperse spheres, most typically silica[19,20] or polymer[21] spheres. Figure IV-1 illustrates the steps of the colloidal crystal templating method.
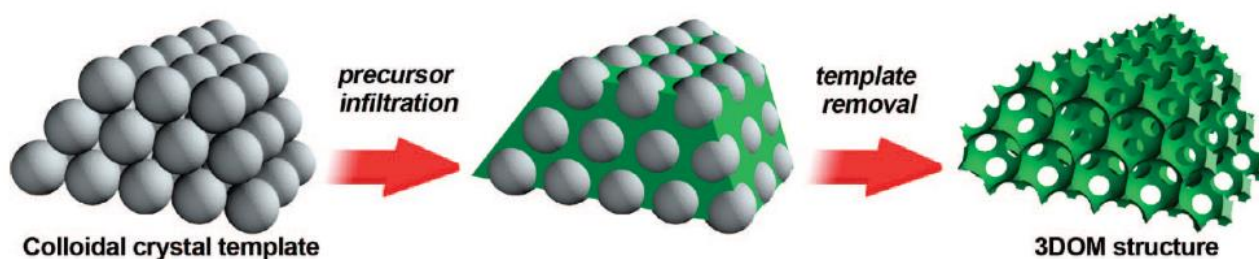
Figure IV-1 – Steps of colloidal crystal templating for the fabrication of a three-dimensionally ordered macroporous (3DOM) structure. Adapted from [22].

At first, the interstitial voids between the monodisperse spheres of the colloidal crystal are filled with the precursor of the targeted material (precursor infiltration). Then, a thermal process is applied to the impregnated template for the growth of the desired material around the spheres. Finally, when the template is removed, the negative replica of the crystal is obtained. Hence, the obtained material presents a network of spherical pores interconnected by twelve pore windows.[23]

Despite the scarcity of hard templates available for this method, the colloidal crystal templating method provides materials of high surface areas and effective mass transport through large and small interconnected pores.[24] Materials with such properties are promising for catalysis support [25], hence being aligned with the objectives of this thesis.

IV.2. RESULTS AND DISCUSSION

Figure IV-2 presents the strategy followed to obtain hierarchically porous ZIF-8-derived ZnO with tetrakaidecahedron morphology.[15]
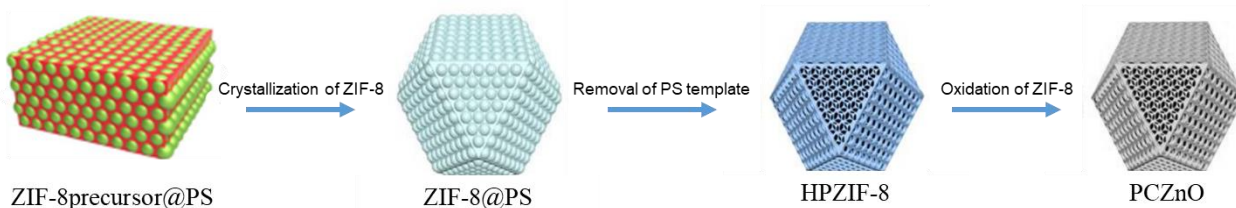
Figure IV-2 - Strategy defined to obtain ZIF-8 porous crystals. Adapted from[15,16].

First, the ZIF-8 precursor is impregnated into the voids of the 3D-ordered polystyrene (PS) template. The ZIF-8 is crystallized around the PS template following a double solvent-induced nucleation process which allows the homogeneous growth of the crystals, producing ZIF-8 tetrakaidecahedron structures filled with the PS template, ZIF-8@PS. The PS template is removed to produce the macroporosity of the hierarchically porous ZIF-8 (HPZIF-8). Finally, HPZIF-8 is thermally treated to produce the ZIF-8 derived ZnO tetrakaidecahedron porous structures, oxidizing the Zn center at the ZIF-8 structure (Figure IV-3).
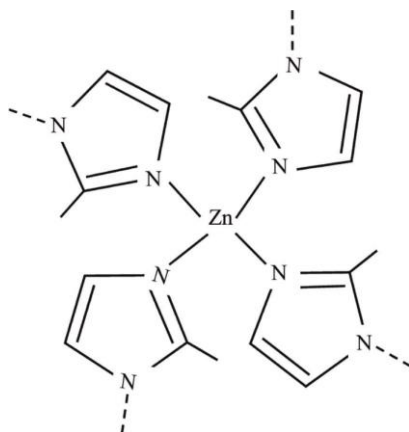
Figure IV-3 – Structure of ZIF-8 framework.

The study performed and described in the result and discussion part is illustrated in Figure IV-4.
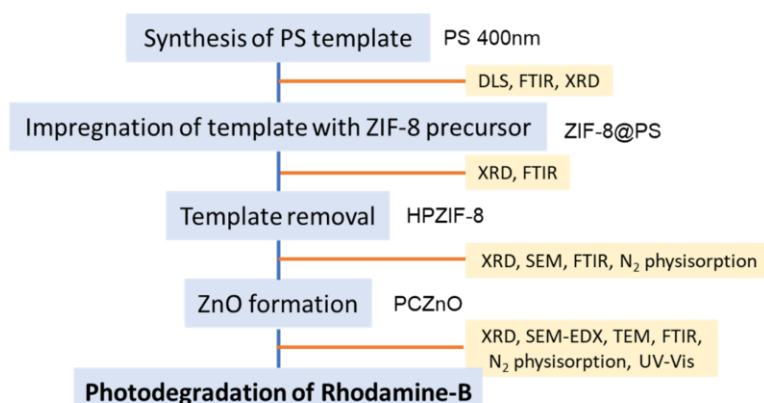
Figure IV-4 – Schematic representation of the study described in this work.

Section IV.2.1 describes the synthesis and characterization Zinc of the PS template.

Section IV.2.2 is focused on the impregnation and growth of ZIF-8 at the PS template.

Section IV.2.3 describes the removal of the PS template, two strategies are discussed and compared.

Section IV.2.4 details the preparation of HPZIF-8-derived ZnO.

Finally, the application of porous tetrakaidecahedron structures of ZnO as efficient photocatalysts for the degradation of water contaminants is described in section IV.2.5.

IV.2.1. SYNTHESIS OF POLYSTYRENE TEMPLATE

The synthesis of 3D-ordered PS spheres (PSs) templates is performed by emulsion polymerization. Following the previous work from Grammatico *et al*, done within this eSCALED Project, PS spheres with a diameter of 340 and 400 nm were prepared.[16] The experimental conditions for the synthesis of these PSs templates followed protocols described by Shen *et al*.[15] PSs were prepared by emulsion polymerization, using poly(vinylpyrrolidone) (PVP) as emulsifier and potassium persulfate ($K_2S_2O_8$) as initiator. Table IV-1 presents the experimental conditions applied and the average diameter of the PS spheres obtained for each sample.

Table IV-1 – Summary of PSs template synthesis conditions and average diameter (d) measured by DLS, standard deviation (σ), and polydispersity.

PSs Sample	Styrene (mL)	PVP (g)	$K_2S_2O_8$ (g)	H_2O (mL)	Temperature (°C)	d (nm)	σ (nm)	Polydispersity
Targeted diameter: 340 nm								
1						330	80	0.24
2						390	10	0.03
3						380	10	0.03
4	65	2.5	1.0	500	60	400	10	0.03
5						430	40	0.09
6						400	10	0.03
7						360	10	0.03
Targeted diameter: 400 nm								
8						370	10	0.03
9						380	10	0.03
10						380	10	0.03
11						400	10	0.03
12						350	10	0.03
13	59	0.6	0.2	500	75	400	20	0.05
14						370	30	0.08
15						390	20	0.06
16						360	10	0.04
17						350	20	0.06
18						340	30	0.09
19						330	30	0.08

The size of the PS spheres was studied by Dynamic Light Scattering (DLS) and the results were treated with the OriginLab software to obtain the size distribution; average diameter (d) and standard deviation (σ). The polydispersity (p) of each batch is calculated following Equation IV-1:

$$p = \frac{\sigma}{d} \qquad \textbf{Equation IV-1}$$

Where p is the polydispersity, σ is the standard deviation, and d is the particle average diameter from DLS studies.

Samples 1 to 7 targeted PS spheres with 340 nm diameter. PSs 1 presents the average sphere diameter of 330 nm, the closest to the targeted 340 nm, however, it demonstrated high polydispersity (0.24) due to the high standard deviation demonstrated (± 80 nm). Such high deviation suggested poor control of the experimental techniques. Samples 2, 3, 4, 6, and 7 show low polydispersity (0.03) and, therefore, the narrow size distribution of the PSs, however, all of these batches achieved an average diameter above the targeted diameter of 340 nm. Given the lower polydispersity of the samples, it was considered that the experimental technique was improved, and the obtention of PSs with a size above the targeted was attributed to poor control of the reactional temperature, which may have influenced the polymerization and growth of PSs.

PSs samples 8 to 19 targeted sphere diameter of 400 nm. The experimental conditions followed the successful protocols described by previous works in the literature.[15] The targeted average diameter was successfully achieved in batches 11 and 13 with low polydispersity, 0.03 and 0.05, respectively. The remaining batches present average diameters below 400 nm, from 330 to 390 nm, however, the cause of such variation between the samples was not found.

This study revealed imperfect size control as demonstrated in Figure IV-5 (left). Sample 11 was the closest to the objective with an average diameter size of 400 ± 10 nm with a low polydispersity (0.03) (Figure IV-5, right).
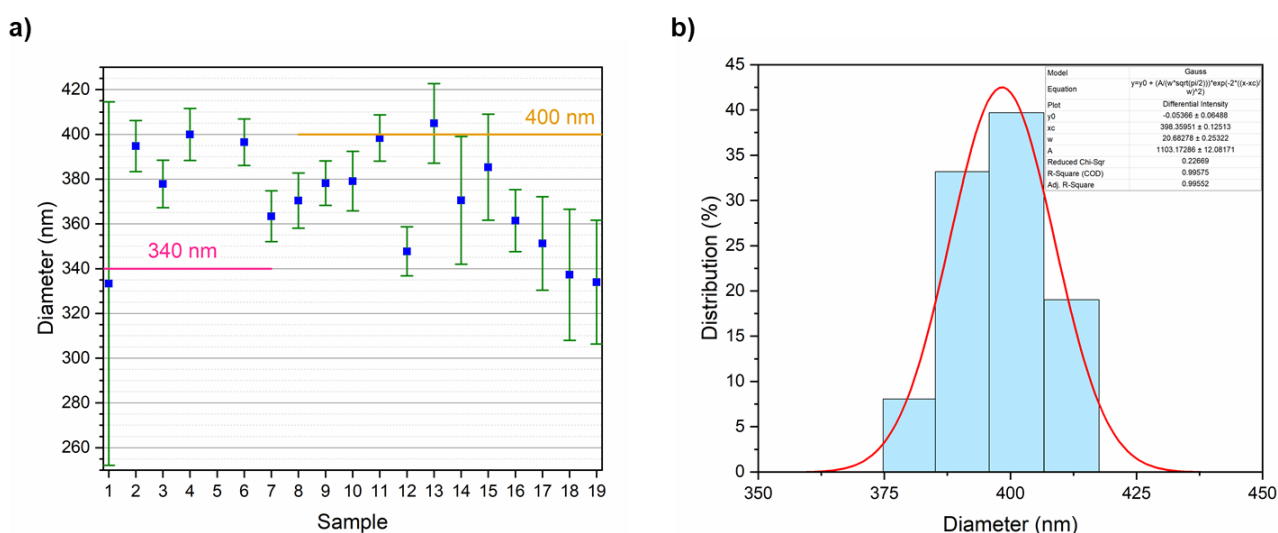
Figure IV-5 – DLS study performed on PS nanoparticle batches. **a)** average diameter size with target diameters of 340 and 40 nm. **b)** size distribution of sample 11.

The increasing polydispersity is expected to reduce the long-range order of PS templates since the presence of smaller or larger spheres may induce defects in the order of the template. The long-

range order of the PS templates is crucial in the present work to ensure the porosity of the final ZnO product.[26]

Despite the lack of size control during synthesis, the colloidal PS suspensions were dried in the oven at 40 °C for three days until complete evaporation of water and residual monomers. The formation of the desired 3D-arranged PS template was achieved by gravitational self-assembly (sedimentation) of the PS spheres. Despite the poor diameter size control, all the PSs batches demonstrated satisfactory long-range orders. Figure IV-6 a) presents the SEM top-view image of the obtained template from PSs 9, exemplifying the long-range ordered hexagonally close-packed PS spheres.

a)

b)
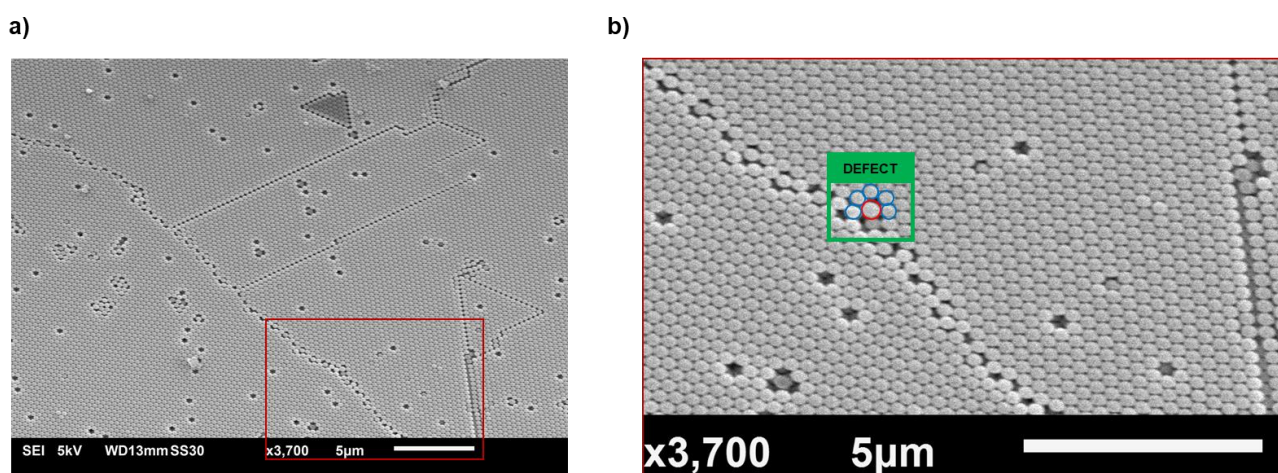
Figure IV-6 – a) Top view SEM images of the obtained PS templates (sample 9). **b)** Defect detected in the PSs template (sample 9) attributed to the presence of a PS sphere larger (red circle) than the neighbor PS spheres (blue circles).

Some crack-like defects attributed to the manipulation of the PSs template during the sample preparation may be observed in the SEM image given in Figure IV-6 a). Figure IV-6 b) highlights the presence of a defect caused by the presence of a single PS sphere larger (red circle) than the surrounding PS spheres (blue circles).

In a conclusion and due to the characterization of the PS templates, all the batches were considered "good to go". The PSs templates were selected according to their polydispersity and priority was given to those demonstrating the lowest: 0.03. Hence, PSs 2; 3; 4; 6; 9; 10; 11, and 12 were selected to be used in the next steps.

IV.2.2. SYNTHESIS OF ZIF-8 SINGLE-ORDERED MACRO-MICROPOROUS CRYSTALS

IV.2.2.1. SYNTHESIS OF ZIF-8@PS

ZIF-8 precursor was prepared from zinc nitrate hexahydrate ($Zn(NO_3)_2 \cdot 6H_2O$) and 2-methylimidazole solutions before being added into the PS templates (PSs 2; 3; 4; 6; 9; 10; 11 and 12).

At this step, two protocols have been followed to verify the effect of the grinding procedure:

(i)   The use of the "crude" PS template as obtained above.

(ii)   The use of a ground PS template.

The infiltration of the ZIF-8 precursor within the template is helped by a vacuum degassing step.[15]

After this step, two procedures were followed to isolate ZIF-8@PS.

(i)   The supernatant solution was removed. In that case, the potential "free" ZIF-8, *i.e.* with no embedded PS particles, within the supernatant may be removed. The residue was then dried.

(ii)   The total experimental medium is dried under ventilation. In that case, the potential "free" ZIF-8, *i.e.* with no embedded PS particles is expected to be adsorbed onto ZIF-8@PS.

Table IV-2 presents the conditions and the results of the ZIF-8@PS synthesis.

Table IV-2 – Summary of the synthesis of ZIF-8@PS.

ZIF-8@PS Sample name	#	Precursor PS template Mass (g)	Precursor PS template Pre-treatment Ground?	Supernatant removal	ZIF-8@PS Mass (g)	ZIF-8@PS Weight gain (wt%)
1	2	14.88	Yes	No	18.14	22
2	3	14.88	Yes	No	16.60	12
3	3	14.88	Yes	No	19.67	32
4	4	14.85	Yes	No	17.55	18
5*	4	4.95	No	No	8.32	68
6	4	14.98	Yes	No	22.20	48
7	6	14.44	No	No	20.60	43
8	6	14.96	Yes	No	17.06	14
9	6	14.46	No	No	16.04	11
10	9	14.07	Yes	No	16.66	18
11	9	14.88	Yes	No	20.13	35
12	10	10.64	No	No	16.31	53
13-	10	10.33	No	Yes	9.95	-4
14	10	8.96	No	Yes	9.24	3
15	10	7.81	No	Partially	9.95	27
16	11	10.53	No	Partially	12.82	22
17+	11	15.16	No	No	20.99	38
18+	11	20.1	No	No	26.64	33
19+	12	19.7	No	Yes	20.04	2
20+	12	18.9	No	Yes	19.92	5

* Increased amount of 2-Mim and $Zn(NO_3)_2 \cdot 6H_2O$
- Product partially lost during purification

ZIF-8@PS		Precursor PS template		Supernatant removal	ZIF-8@PS	
Sample name	#	Mass (g)	Pre-treatment Ground?		Mass (g)	Weight gain (wt%)

+ PS amount increased

From Table IV-2, several conclusions may be reached.

Without supernatant removal and grinding PS: ZIF-8@PS samples 2 and 3 were prepared from ground PS template # 3 and ZIF-8 supernatant solution was not removed; registered weight gains are 12 and 32% respectively. Some comments may be done on ZIF-8@PS samples 4 and 6.

Without supernatant removal and crude PS: The grinding step did not have any effect since ZIF-8@PS samples 7 and 9 were prepared from crude PS template # 6 and ended with the removal of ZIF-8 supernatant exhibiting weight gains are 43 and 11% respectively. ZIF-8@PS samples 17 and 18, done from a higher amount of PS template (#11) show closer weight gain, 38 and 33% respectively but the reaction was not reproduced a third time to confirm or deny.

With supernatant removal and crude PS: ZIF-8@PS samples 19 and 20 were prepared from crude PS template # 12 and ZIF-8 supernatant solution was removed; registered similar weight gains, *i.e.* 2 and 5% respectively. However, this low gain as compared to those obtained above suggests material lost during this step, not all the ZIF-8 present in ZIF-8precursor@PS crystallized or may have crystallized into small crystals, small enough to be washed out and lost during the purification step.

From these results, the grinding step seems to be not necessary while the supernatant removal step was preferred within the purification procedure as ZIF-8@PS 19 and 20.

The samples with ZIF-8 crystals around the PS template (ZIF-8@PS) were characterized by X-ray Powder Diffraction (XRD). Figure IV-7 presents the XRD pattern of ZIF-8@PS.
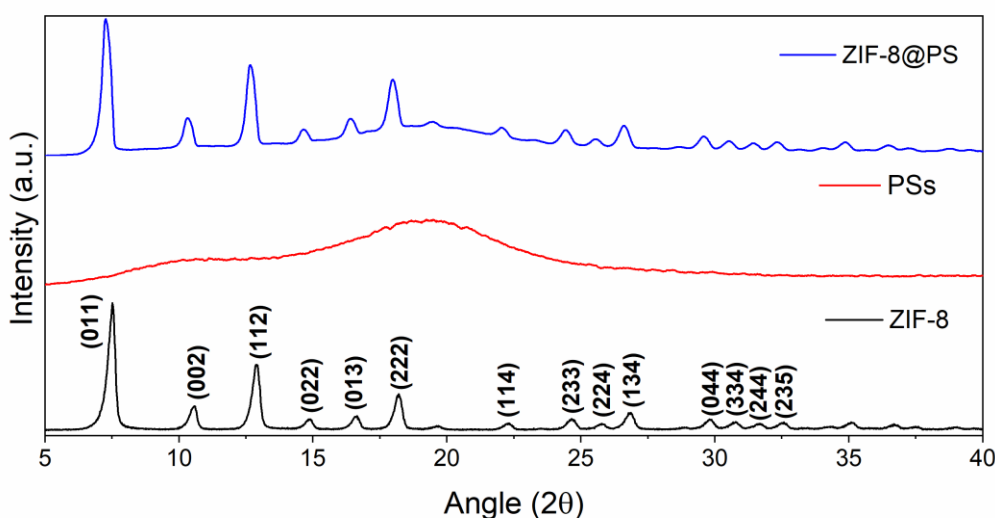

**Figure IV-7 -** XRD diffractogram of ZIF-8, PS template, and ZIF-8@PS.

The amorphous footprint of PSs (red line) was observed between 5° to 30°. The XRD reflections of pure ZIF-8 are presented by the black line in Figure IV-7. The same characteristic ZIF-8 reflections were presented on the ZIF-8@PS powders (blue line) confirming the formation of phase-pure ZIF-8 with good crystallinity.[27] The ZIF-8@PS diffractogram also showed the amorphous PS template. This characterization confirmed that ZIF-8 was successfully synthesized within the PS template.

IV.2.3. TEMPLATE REMOVAL

PS templates can be removed by two distinct methods: solvation or calcination. Both approaches to remove the PS template and thus obtain HPZIF-8 were carried out.[21,26]

IV.2.3.1. CALCINATION APPROACH

The calcination approach consists of thermal treatment at 450 °C under an argon atmosphere to remove the PS template.[16] To study the weight variation of ZIF-8@PS during such a thermal process, the samples were characterized by differential scanning calorimetry (DSC) and thermogravimetric analysis (TGA). Figure IV-8 presents the results obtained from the DSC/TGA characterization of ZIF-8@PS #19.
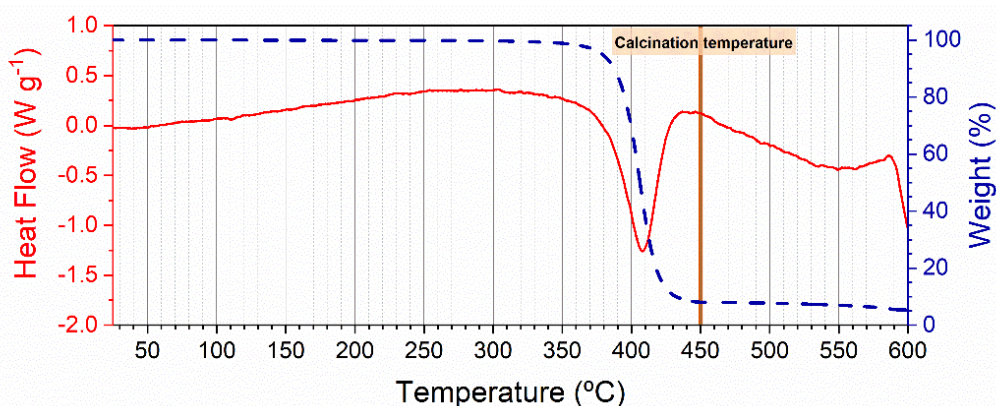
Figure IV-8 – DSC (red line) and TGA (blue dashed line) characterization of ZIF-8@PS 19 under nitrogen flow.

The DSC characterization (Figure IV-8) revealed the endothermic peak at 407 °C attributed to the degradation of PS. Thermogravimetric analysis (TGA) demonstrated that at 450 °C approximately 92 % of the sample weight would be lost. This value was later confirmed when the same sample was calcined to prepare samples HPZIF-8 25 and 27 (see Table IV-3). Table IV-3 reports the calcination of the ZIF-8@PS reported within Table 2 whatever the procedure was.

Table IV-3 - Summary of HPZIF-8 synthesis obtained by calcination of ZIF-8@PS in Argon.

HPZIF-8	ZIF-8@PS	Temperature	Duration	Weight loss
Sample	Sample	°C	h	%
1	1	450	4	79
2	1	450	4	74

HPZIF-8	ZIF-8@PS	Temperature	Duration	Weight loss
Sample	Sample	°C	h	%
3	3	450	4	74
4	4	450	4	73
5	4	450	6	74
6	4	450	8	73
10	5	450	4	74
11	11	450	4	74
14	11	450+550	4+3	75
15	12	450+550	4+3	69
16	13	450+550	4+3	91
23	17	450	4	75
24	18	450	4	79
25[+]	19	450	4	92
26[+]	20	450	4	92
27[+]	19	450	4	96
28[+]	20	450	4	92

+Tubular oven accidentally opened during calcination

Samples HPZIF-8 4; 5 and 6 were prepared from ZIF-8@PS 4 and were calcined at 450 °C for 4; 6 and 8 hours, respectively. The weight loss (measured gravimetrically) of HPZIF-8 4; 5 and 6 was found to be 73; 74 and 73 %, hence meaning that increasing the duration to longer periods is not translated into a higher quantity of PS template elimination. Furthermore, it was also observed that the addition of a second calcination step at a higher temperature (550 °C for 3 h) does not significantly improve the quantity of PS template eliminated (≤1 %) as demonstrated by the experiments to obtain HPZIF-8 11 and 14, which are both products of the same ZIF-8@PS 11. It was then concluded that a single calcination step at 450 °C for 4 h was sufficient to effectively and completely remove the PS template.

Samples HPZIF-8 25-28 from ZIF-8@PS 19 and 20 were considered to be the best in terms of homogeneity of crystal size and porosity as confirmed by SEM analysis (Figure IV-9 a) and b)).
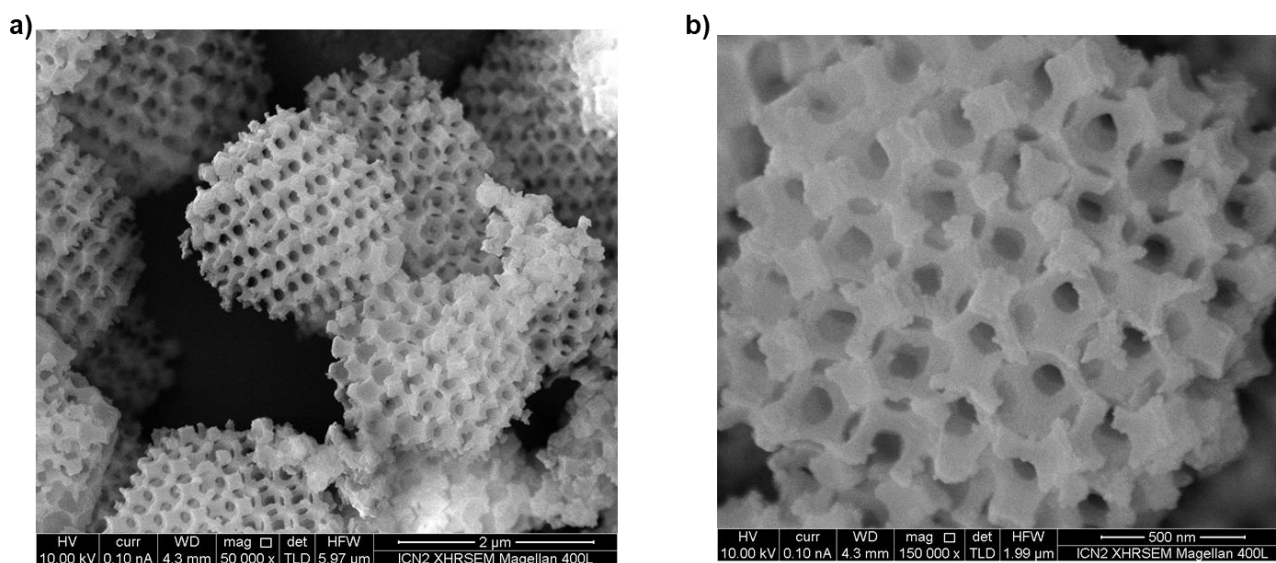
Figure IV-9 – SEM images of HPZIF-8 sample obtained by the calcination method (sample 25).

The samples consisted of porous crystals with 301.2 ± 14.5 nm pore size and average crystal size of 2.14 ± 0.12 µm.[16]

IV.2.3.2.   SOLVATION APPROACH

The solvation method consists of the solubilization of the PS template in a solvent such as tetrahydrofuran (THF) and/or dimethylformamide (DMF). After several washes of ZIF-8@PS in one of the solvents, the sample is finally washed with dichloromethane (DCM) and dried. Table IV-4 summarizes the results of the experiments carried out by this solvation method.

Table IV-4 - Summary of HPZIF-8 synthesis obtained by solvation of PS template.

HPZIF-8	ZIF-8@PS	Solvent	Duration	Weight loss
Sample	Sample		day	%
8	9	DMF	4	75
12	10	DMF+THF	4	72
13	11	DMF+THF	4	73
17	13	DMF+THF	4	94
18	14	DMF+THF	4	94
19	15	DMF+THF	4	76
20	16	DMF+THF	4	82
21	17	THF	2	70
22	18	THF	2	77

Similar weight loss to those obtained by the calcination approach has been obtained by the solvation method for the same ZIF-8@PS precursors.

The SEM characterization of sample 18 is presented in Figure IV-10.
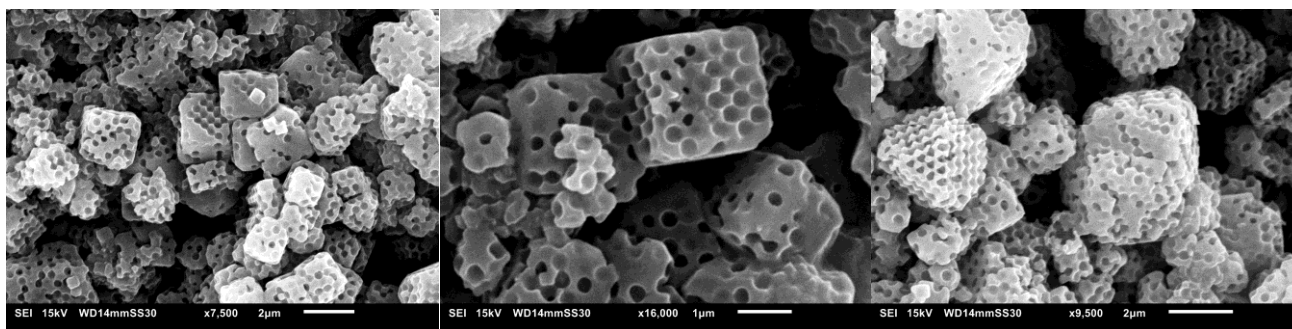
Figure IV-10 – SEM images of HPZIF-8 sample obtained by the solvation method (sample 18).

The SEM images suggested that after four days of washings with THF and DMF, PS spheres were no longer present in the sample which was then confirmed by XRD. SEM images from the sample HPZIF-8 18. Despite the lack of homogeneity in terms of crystal size and porosity, the template removal was considered successful with a 94 % weight loss of the original sample (ZIF-8@PS 14). The high value of this parameter can be explained by the removal of liquid precursor in excess before ZIF-8 crystallization which led to low weight gain (3 %), *i.e.*, ZIF-8 crystals formation.
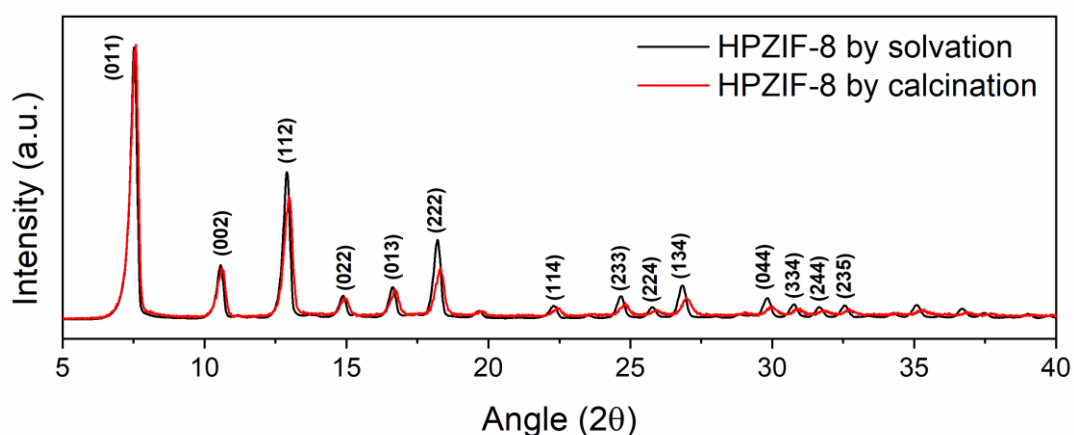
Both methods, solvation, and calcination successfully obtained pure ZIF-8 phase crystals (except samples HPZIF-8 25-28 which will be discussed in section IV.2.4) as confirmed by the XRD diffractograms in Figure IV-11.[27]

Figure IV-11 - XRD diffractogram of HPZIF-8 11 and 13 obtained by calcination and solvation, respectively.

Samples HPZIF-8 11 and 13 were both derived from ZIF-8@PS 11 and were prepared by calcination and solvation, respectively, obtaining the same weight loss (74 %, see Table IV-3 and Table IV-4) which validates the viability of both methods for template removal.

The solvation process is much more time-consuming but offers the advantages of not requiring specific equipment such as a calcination oven, avoiding high energy consumption usually linked to thermal treatment protocols, and the possibility to reprecipitate PS in a non-solvent such as H_2O for further recycling and reuse in other applications.

IV.2.4. PREPARATION OF ZIF-8 DERIVED ZnO

Figure IV-12 compares the XRD diffractograms of two HPZIF-8 samples obtained through the calcination method.
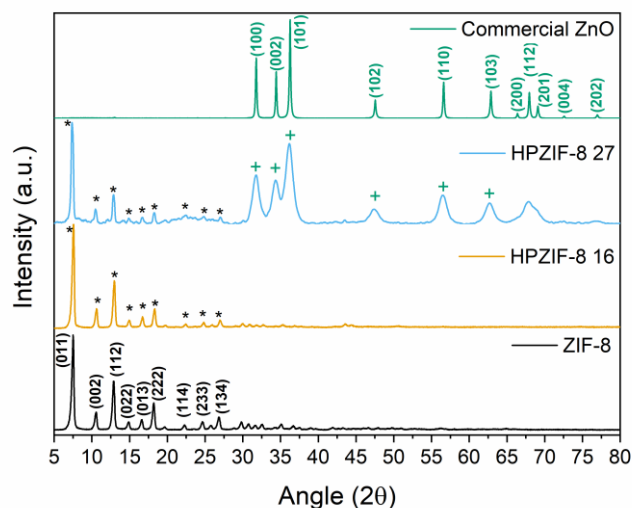
Figure IV-12 - XRD diffractograms of ZIF-8; HPZIF-8 16; HPZIF-8 25 and commercial ZnO sample. *ZIF-8 phase, +ZnO wurtzite phase.

The inert atmosphere was preserved during the full duration of the calcination procedure to obtain sample HPZIF-8 16 and the XRD characterization confirmed that pure ZIF-8 was obtained, demonstrating the typical plane reflections of ZIF-8 from 5° to 30°. However, sample HPZIF-8 27 demonstrated not only the presence of the ZIF-8 phase from 5° to 30° but also the presence of the typical wurtzite phase reflections of ZnO from 30° to 80°. The presence of oxygen inside the calcination chamber, breaking the inert argon atmosphere, during the calcination process may have led to the formation of the ZnO.[2] The presence of oxygen in HPZIF-8 25 was confirmed by energy dispersive spectroscopy (EDS) analysis as demonstrated in Figure IV-13.
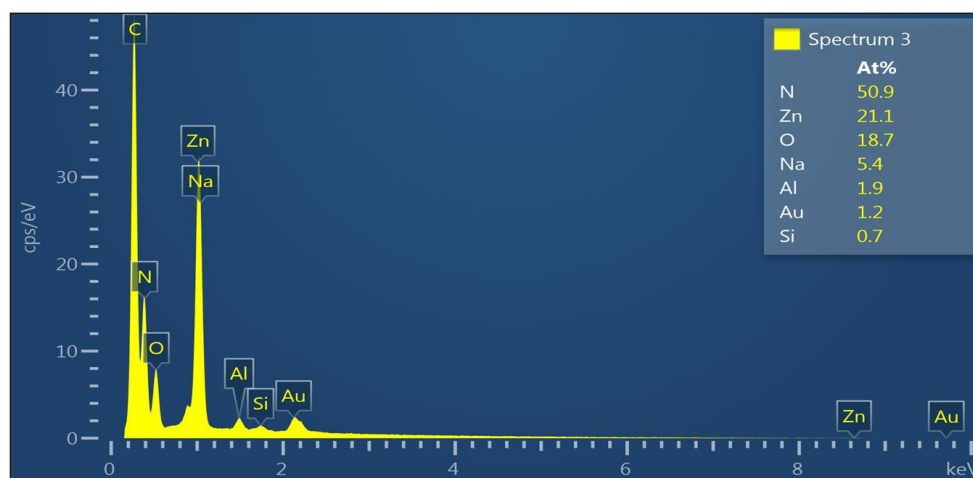
Figure IV-13 - EDS analysis of HPZIF-8 25 sample obtained by the calcination method.

These results suggested that the synthesis of hierarchically porous ZIF-8-derived ZnO could be performed in a single calcination step where the removal of the PS template and oxidation of ZIF-8 to ZnO occur simultaneously. However, due to a lack of time to optimize the conditions of the single-step ZIF-8@PS to ZnO conversion protocol, the oxidation of HPZIF-8 to ZnO was performed in a second step after the PS template removal step.

Polycrystalline ZnO (PCZnO) was successfully obtained by calcining HPZIF-8 in an air atmosphere. Table IV-5 presents a list of the prepared ZnO samples and respective HPZIF-8 used and weight loss.

Table IV-5 - Summary of synthesized PCZnO samples, HPZIF-8 sample used for each batch, and respective weight loss.

	PCZnO																							
	1*	2*	3*	4*	5*	6*	7	8	9	10	11	12	13	14	15	16	17	18	19	20	21	22	23	24
HPZIF-8	1	2	2	2	3	4	4	9	10	11	12	13	14	15	16	17	18	19	20	21	22	23	25	26
Weight loss (%)	47	62	63	63	61	64	63	68	65	63	68	70	65	64	66	67	70	71	67	73	65	65	69	68

*Heat ramp: 2 °C min^{-1}

Results shown in Table IV-5 are in agreement with previous works reported in the literature with ≈61 % weight loss for the thermal decomposition (200-700 °C, 10 °C/min) of ZIF-8 to ZnO through TGA experiments performed in air.[28]

In section IV.2.3.1, samples HPZIF-8 25-28 were considered to be the best in terms of homogeneity of crystal size and porosity. Therefore, the ZnO samples from HPZIF-8 25-28 were studied in more detail, namely PCZnO 23, the product of HPZIF-8 25. PCZnO 23 was characterized by field emission scanning electron microscopy (FESEM) which revealed the preservation of tetrakaidecahedron morphology given by HPZIF-8 (Figure IV-14).[15]
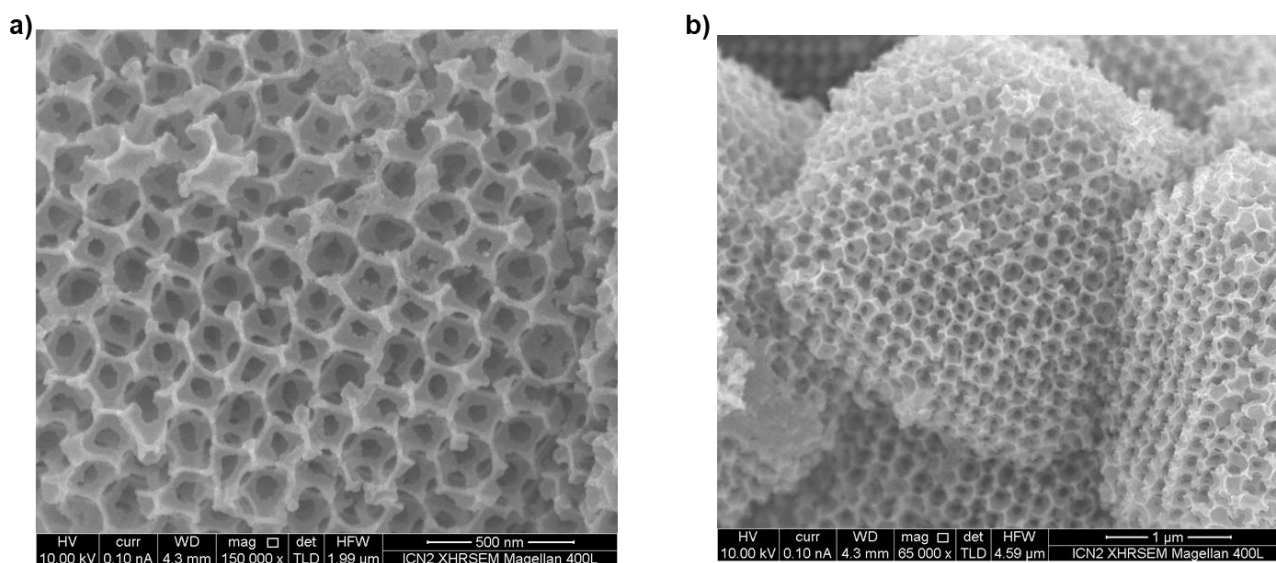
Figure IV-14 – SEM images of PCZnO 23.

The PCZnO crystals presented an average size of 2.62 ± 0.84 µm (calculated from the analysis of the SEM images in Figure IV-14) which is consistent with the size of its precursor HPZIF-8 25 sample (2.14 ± 0.12 µm). However, significant changes in the pore size were observed between the HPZIF-8 25 and PCZnO 23. PCZnO 23 presented an average pore diameter of 191.4 ± 8.2 nm (calculated from the analysis of the SEM images in Figure IV-14), which reveals a shrinkage from the 301.2 ± 14.5 nm pore diameter of HPZIF-8 25.

Figure IV-15 presents the EDS spectrum of PCZnO 23.

Figure IV-15 – EDS characterization of PCZnO 23.
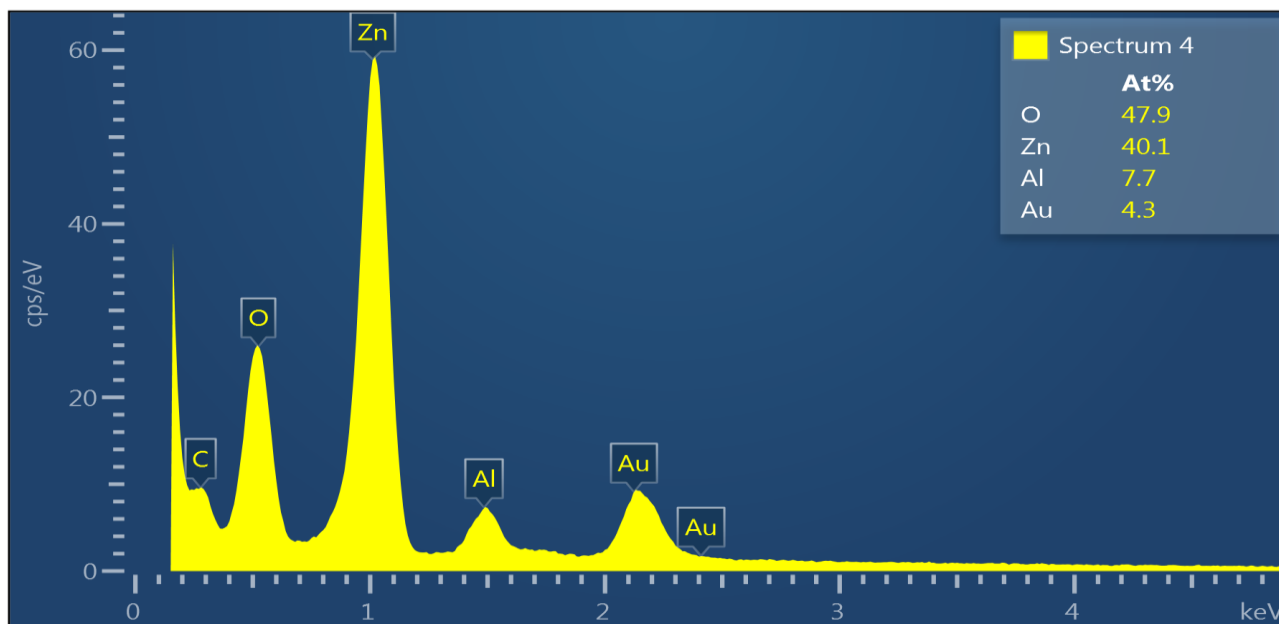
The analysis revealed the presence of carbon, aluminum, and gold attributed to the supporting conductive tape, sample holder, and sputtered conductive coating, respectively. The same technique confirmed that PCZnO structures were composed of zinc and oxygen only.

XRD analysis revealed well-defined diffraction reflections of the pure wurtzite phase of ZnO (Figure IV-16).
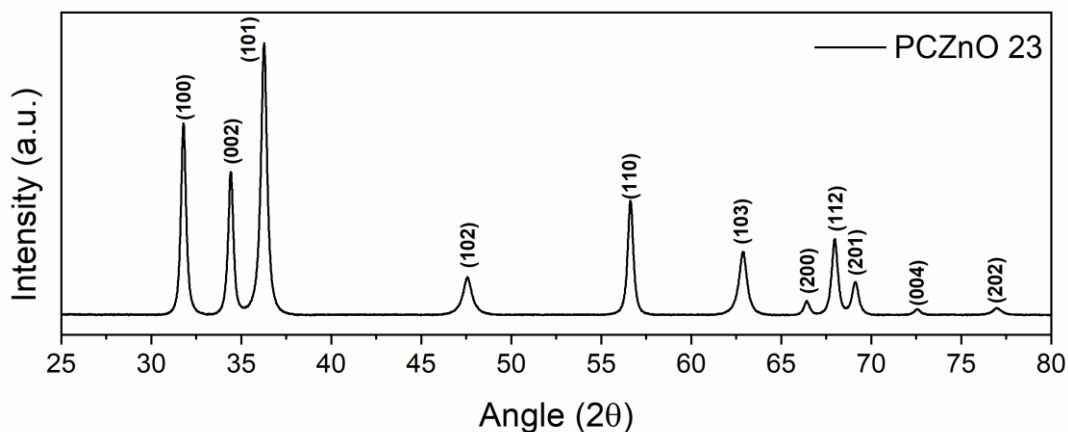
Figure IV-16 – X-ray diffraction pattern of PCZnO 23.

The peaks appeared at 31.8°, 34.4°, 36.3°, 47.6°, 56.6°, 62.9°, 66.4°, 68.0°, 69.1°, 72.6°, and 77.0° correspond to the lattice planes (100), (002), (101), (102), (110), (103), (200), (112), (201), (004) and (202), respectively. The absence of other reflections revealed the high purity and crystallinity of the synthesized PCZnO. The detected diffraction pattern matched the standard Joint Committee on Powder Diffraction Standards (JCPDS) data card no.36-1451.[29,30] The high-resolution transmission electron microscopy (HRTEM) and selected area electron diffraction (SAED) images of PCZnO 23 in Figure IV-17 confirmed the polycrystalline nature of the ZIF-8 derived ZnO synthesized.
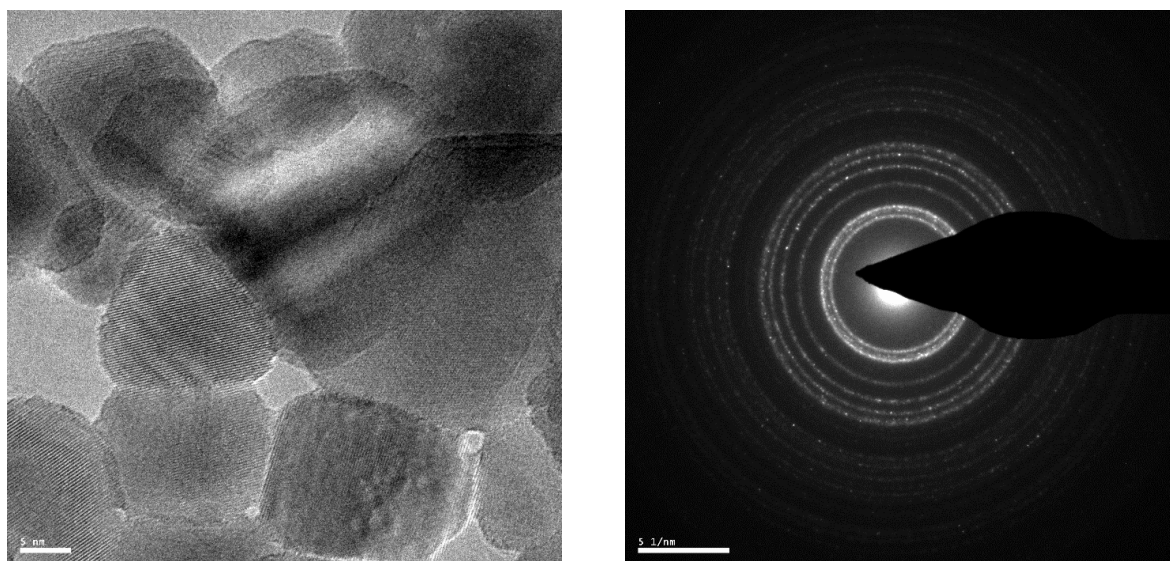
Figure IV-17 – HRTEM and SAED images of PCZnO 23.

IV.2.5. PHOTOCATALYTIC DEGRADATION OF A DYE BY HIERARCHICALLY POROUS ZIF-8 DERIVED ZnO

The semiconducting nature of ZnO allows for exploring the obtained PCZnO structures as photocatalysts. The electron-hole pairs generated through the photoelectric effect on the surface of ZnO may be explored as an electron source for the hydrogen evolution reaction in the scope of this

thesis. Within the overall strategy of the present thesis, the obtained PCZnO structures, if presenting suitable surface area, porosity, and photocatalytic properties may be employed as catalyst support in the electrodes of eSCALED Project devices.

Organic dyes such as rhodamine are commonly found in water contaminated by the textile industry. These species present high toxicity and threaten human health.[31] The degradation of dyes and other organic pollutants through photocatalysis on metal oxide semiconductor catalysts is seen as promising for wastewater treatment.[32] In this process, the degradation reactions of the dye are driven by the electron-hole pairs generated on the semiconductor photocatalyst surface by absorption of radiation with higher energy than the bandgap of the semiconductor.

The ZnO powders obtained were tested as photocatalysts for the degradation of Rhodamine B (RhB) under UV-light irradiation. To study the influence of PCZnO porosity and size in a photocatalytic mechanism, three samples were selected: PCZnO samples 3; 19, and 23. The morphological differences of samples PCZnO 3 and 19 may be observed in Figure IV-18, while sample PCZnO 23 has been previously presented in Figure IV-14.
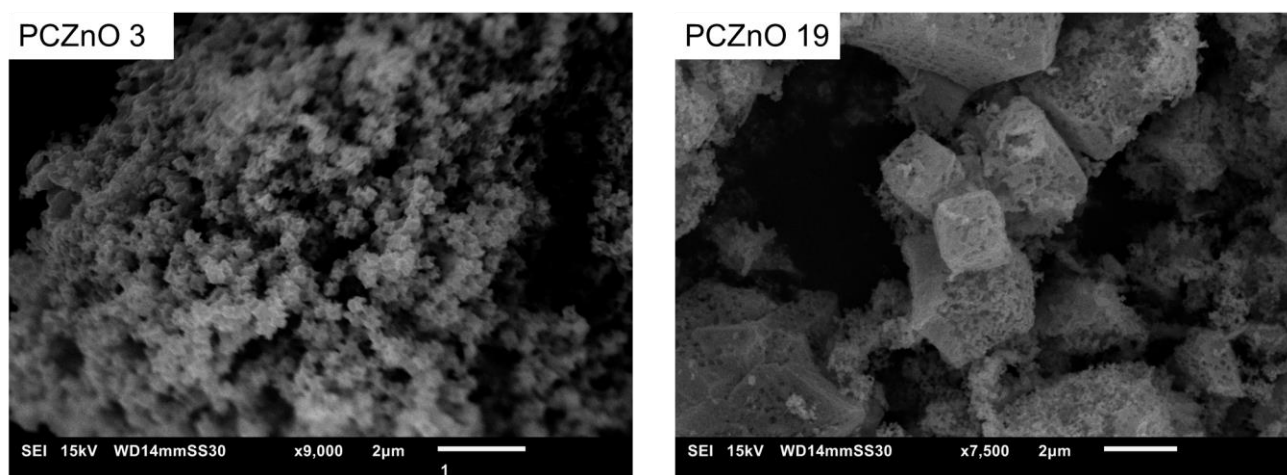
Figure IV-18 – SEM images of PCZnO samples used for photocatalytic testing.

The crystal size of PCZnO samples is presented in Table IV-6.

Table IV-6 – Crystal size of PCZnO samples used for photocatalytic degradation of Rhodamine B.

PCZnO Sample	Crystal size µm
3	0.254 ± 0.026
19	2.52 ± 1.02
23	2.62 ± 0.84

PCZnO 3 presented the smallest crystal size without porosity, PCZnO 19 had a very heterogeneous crystal size with nonorganized pores and PCZnO 23 with organized porosity (191.4 ± 8.2 nm).

The photodegradation of RhB was calculated according to Equation IV-2:

$$\text{Photodegradation (\%)} = \frac{C_0 - C}{C_0} \times 100 \quad \textbf{Equation IV-2}$$

Where C_0 is the concentration at $t_0=0$ min and C denotes the concentration at the t time. This equation can then be re-written considering the maximum absorption peak characteristic of RhB at 553 nm as the following (Equation IV-3):

$$\text{Photodegradation (\%)} = \frac{A_0 - A}{A_0} \times 100$$ **Equation IV-3**

Where A_0 is the initial absorbance at t_0 and A the absorbance at t.[29]

The experiments consisted of dispersing the ZnO powders in a rhodamine water-based solution under continuous stirring inside a transparent glass vial. The setup was exposed to UV irradiation and an aliquot of the RhB solution was analyzed by UV-Vis spectroscopy at each 10 min interval.

Figure IV-19 a) presents the UV-Vis spectral changes of 10 µM RhB in the presence of PCZnO 19 at the time of exposure.
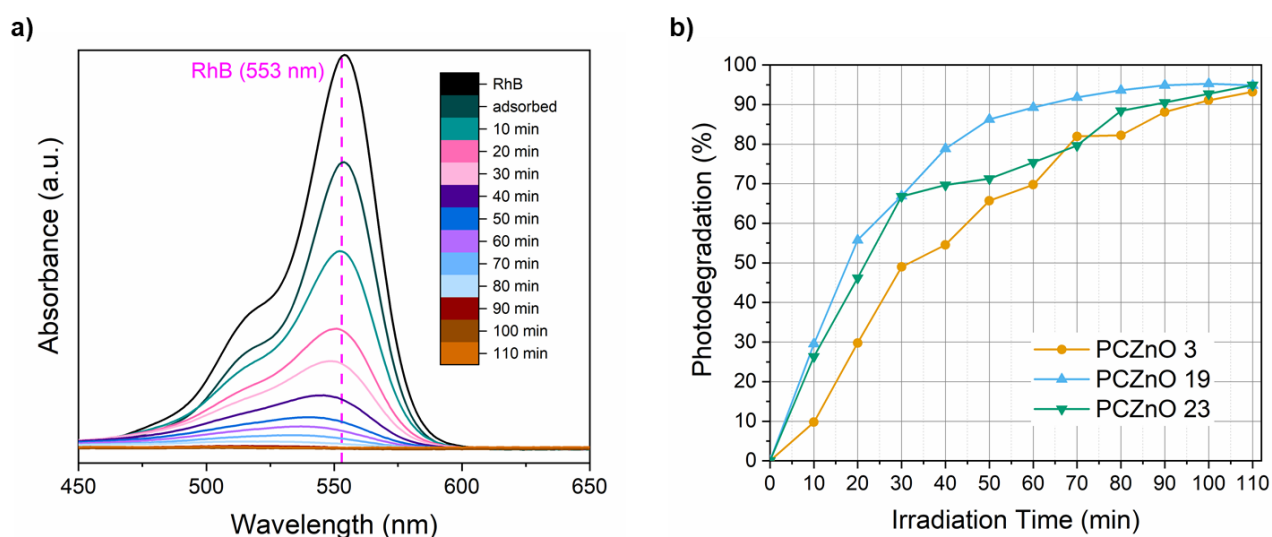
Figure IV-19 – a) UV-Vis spectral changes of 10 µM RhB after UV irradiation (10 min interval) in the presence of PCZnO 19. **b)** Photodegradation of RhB measured at the characteristic absorption peak of RhB (553 nm) versus irradiation time.

It was observed that the absorbance intensities decreased with increasing exposure times. In Figure IV-19 b) the photodegradation of RhB assisted by the PCZnO samples is presented. The tested PCZnO samples revealed different catalytic activity. For instance, sample PCZnO 19 required only 20 min of UV irradiation to degrade 50 % of the initial concentration of RhB. PCZnO 23 required 30 min UV irradiation to achieve 50 % degradation, while PCZnO 3 required 40 min to achieve the same degradation (see Table IV-9 in section IV.6 Appendixes for more details).

The kinetics of the RhB photodegradation reaction by PCZnO photocatalysts are presented in Figure IV-20.
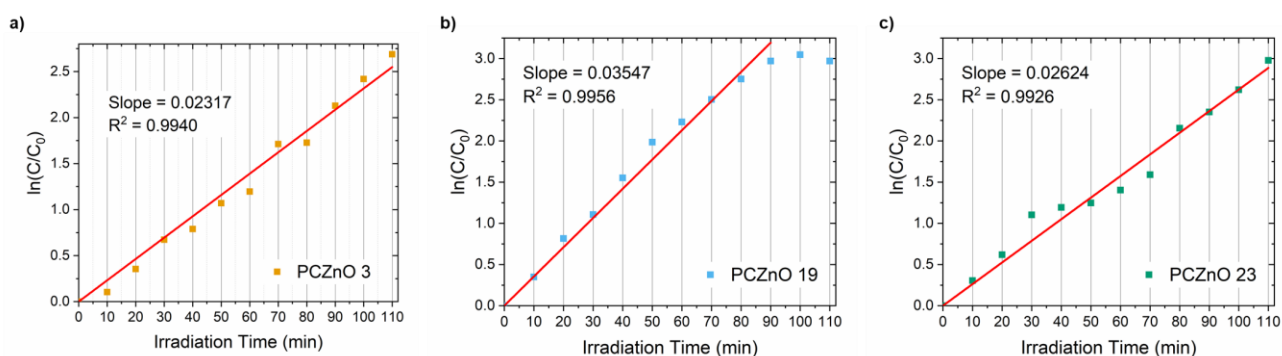
Figure IV-20 – Photocatalytic activity of PCZnO: first-order linear plot $\ln(C_0/C)$ vs irradiation time reflecting the kinetics of RhB photodegradation mediated by PCZnO 3 (**a**); PCZnO 19 (**b**) and PCZnO 23 (**c**).

Samples PCZnO 3 (Figure IV-20 a)) and 19 (Figure IV-20 b)) followed first-order kinetics in agreement with a general Langmuir-Hinshelwood mechanism, *i.e.*, the plot of $\ln(C_0/C)$ versus time fits a straight line. The apparent first-order reaction rate constant, K_{app} (min^{-1}), estimates the photodegradation efficiency and is given by $\ln(C_0/C)=k_{app}t$.[33][34] PCZnO 19 exhibits an apparent reaction rate of 0.03547 min^{-1}, which is higher than what PCZnO 3 registered (0.02317 min^{-1}). The $\ln(C_0/C)$ plot of PCZnO 23 (Figure IV-19 c)) demonstrated an apparent reaction rate of 0.02624 min^{-1}. Interestingly, this sample, PCZnO 23, which was previously considered to present the best morphology, *i.e.*, closer to the targeted porous tetrakaidecahedron, did not show the highest reaction rate, contrary to what was expected due to its morphology. The 0.02624 min^{-1} reaction rate demonstrated by PCZnO 23 was considerably lower than the 0.03547 min^{-1} presented by PCZnO 19 and close to the 0.02317 min^{-1} registered for PCZnO 3. Further experiments should be performed to study and understand the parameters, such as geometry, crystal size or porosity affecting the performance of the ZIF-8 derived ZnO as photocatalyst.

At the time that this thesis was written and to the extent of the authors' knowledge, we described here for the first time the synthesis of ZIF-8-derived ZnO with porous tetrakaidecahedron morphology. These ZnO porous materials proved to be efficient photocatalysts for the degradation of water contaminants such as rhodamine dye. Furthermore, the porous ZnO structures may be promising photocatalysts for the decontamination of polluted water or gas-sensing applications. Within the frame of the eSCALED project, these porous ZnO structures may be employed as physical support for electrocatalysts for the water-splitting reaction in photoelectrodes. However, further studies are required to optimize the experimental protocols and evaluate the mechanical and chemical stability of the produced ZnO structures *in operando*.

IV.3. CONCLUSION AND PERSPECTIVES

Pure ZIF-8 single crystals with macro-micro porosity were successfully obtained by both calcination and solvation procedures employed to remove the colloidal PS templates used. Macro-micro porous 3D-arranged ZnO was obtained by calcination of macro-micro porous ZIF-8 single crystals. The tetrakaidecahedron morphology was kept after the calcination of ZIF-8. The powders obtained were white and presented a pure wurtzite phase in XRD. The obtained ZnO powders of 2.62 ± 0.84 µm (average size) and 191.4 ± 8.2 nm (average pore diameter) were polycrystalline as shown by HRTEM. The removal of excessive ZIF-8 precursor before crystallization of ZIF-8 impregnated in the PS template voids represented a crucial step to control the porosity and size homogeneity of the obtained crystals. Three samples of ZnO with different pores and crystal sizes were tested for photocatalytic degradation of RhB and exhibited efficient photocatalytic activity. However, contrary to what was expected, the ZnO sample with the highest porosity did not present the highest reaction rate. Further studies are required to better describe the performance of ZIF-8-derived macro-micro porous 3D-arranged ZnO as an efficient photocatalyst. This innovative ZnO morphology raises the expectations of its application in devices such as gas sensors or photoelectrodes, where deformation is not implied, and its properties could be further explored.

IV.4. EXPERIMENTAL PROCEDURES

The experimental protocol for the synthesis of ZIF-8-derived ZnO with porous tetrakaidecahedron morphology is schematized in Figure IV-21.
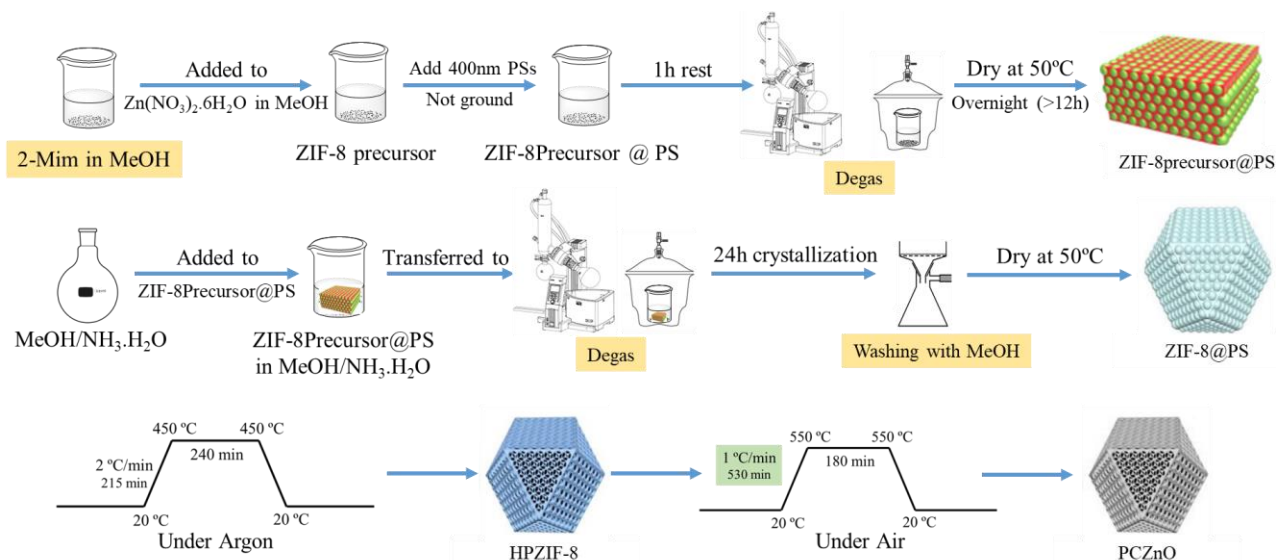
Figure IV-21 – Scheme of the experimental procedure for the synthesis of ZIF-8 derived ZnO with porous tetrakaidecahedron morphology.

Table IV-7 presents the list of chemicals used in the experimental procedures.

Table IV-7 - List of chemicals used for synthesis protocols.

Material	Provider/grade
2-Methylimidazole 99 %	Sigma-Aldrich
Ammonia solution S.G. 0.88 (35 %)	Fisher Scientific
Dichloromethane ≥ 99.5 % stabilized, AnalaR NORMAPUR® ACS, Reag. Ph. Eur. analytical reagent	VWR
Dimethylformamide 99 %	Carl Roth
Methanol ≥ 99 %, for synthesis	Carl Roth
Poly(vinylpyrrolidone) K30 MW av. 40000	TCI
$K_2S_2O_8$	Sigma-Aldrich
Rhodamine B	Alfa Aesar
Styrene, 99%, extra pure, stabilized	Acros Organics
Tetrahydrofuran 99 %	Carl Roth
Zinc nitrate hexahydrate, metal basis 99 %	Alfa Aesar
Zinc oxide 184-B	Torrecid

Styrene monomer was purified by washing with 10 wt% NaOH solution to remove stabilizers. None of the other reactants required purification before use.

IV.4.1. SYNTHESIS OF POLYSTYRENE TEMPLATE

The following synthesis is given as an example and targets the synthesis of PS spheres of 400 nm diameter. The synthesis of PS sphere templates is performed by emulsion polymerization.

Distilled H_2O (500 mL) and polyvinylpyrrolidone (PVP, 0.6 g) are added in a 1 L two-neck round bottom flask equipped with a magnetic stirrer. The mixture is stirred until complete solubilization of PVP and purified styrene monomer (59 mL), is added. The mixture is bubbled with N_2 for 15 min and is then heated up at 75 ºC, refluxed under argon, and stirred for 30 min. The initiator, $K_2S_2O_8$ (0.2 g) is solubilized in distilled H_2O (50 mL) and quickly added to the previous mixture to initiate the polymerization reaction. The reaction is performed for 24 h, under argon, at 75 ºC and stirring (500 rpm)[15] before being cooled down to room temperature, and the reaction product (milk-like colloidal suspension) is transferred to a crystallization dish where the PS template will be formed by drying at 40 ºC for three days.

IV.4.2. SYNTHESIS OF ZIF-8 SINGLE-ORDERED POROUS CRYSTALS

ZIF-8 precursor solution: $Zn(NO_3)_2 \cdot 6H_2O$ (8.15 g) and 2-methylimidazole (6.75 g) are solubilized separately in CH_3OH (25 and 20 mL, respectively) inside 50 mL round bottom flasks and magnetically stirred until complete solubilization. The 2-methylimidazole solution is added to a 100 mL beaker, and put under magnetic stirring, before slowly adding the $Zn(NO_3)_2 \cdot 6H_2O$ solution. The beaker is covered and the mixture is left under stirring for 10 min at room temperature.

The PS template (19 g) is added to the beaker containing the ZIF-8 precursor. The mixture is left for one hour under static conditions, covered to avoid the evaporation of the solvent, at room temperature. To infiltrate the ZIF-8 precursor into the interstitial voids of the template, the beaker with the previous mixture is transferred to a vacuum to be degassed for 30 min at 150-300 mbar. Before drying the impregnated template (ZIF-8precursor@PS), the liquid part of the ZIF-8 precursor/PS template mixture is removed to avoid the accumulation of ZIF-8 precursor outside the template, therefore leading to the formation of bulk ZIF-8 crystals. The solid ZIF-8precursor@PS is dried for 8 h at 50 ºC in a ventilated oven. The crystallization of ZIF-8 is performed by soaking ZIF-8precursor@PS in CH_3OH/NH_4OH solution (50 mL, 1:1 v/v) and consecutive degassing in a vacuum chamber 10 min at 300-450 mbar. The beaker containing the ZIF-8precursor@PS in CH_3OH/NH_4OH solution is then covered and let for 24 h at room temperature (≈23 °C) and under normal pressure conditions. Finally, the product is quickly filtered under a vacuum over Whatman® Grade 42 filter paper and washed with methanol. The collected product (ZIF8@PS) is dried in the air at room temperature.

IV.4.2.1. TEMPLATE REMOVAL

Hierarchical porous ZIF-8 (HPZIF-8) is prepared from ZIF-8@PS as follows. Preferably, the PS template is removed from ZIF-8@PS by calcination under an argon atmosphere (2 ºC min^{-1} heating ramp from room temperature) and kept at 450 ºC for 4 h, followed by slow cooling of the sample until room temperature. HPZIF-8 is obtained as a brown powder.[16]

IV.4.3. ZnO FORMATION

To achieve the desired ZnO with porous tetrakaidecahedron morphology (PCZnO), HPZIF-8 is thermally oxidized (in the air) inside a muffle furnace. The sample is heated up with a 1 ºC min^{-1} heating ramp from room temperature until 550 ºC and therefore kept at this temperature for 3 h following previous works in literature.[7] Finally, the sample is naturally cooled down until room temperature. PCZnO is obtained as a white powder.

IV.4.4. PHOTOCATALYTIC TESTING

ZnO (10 mg) was dispersed in a 10 μM rhodamine B-(RhB) aqueous solution (20 mL) under constant magnetic stirring (400 rpm) in a 50 mL beaker. The suspension is stirred for 1 h and the aqueous suspension is exposed to UV light illumination (Camag 366 nm 8 W 1400 μW cm^{-2}) under constant stirring. A 3 mL aliquot is periodically withdrawn from the decomposed sample and subjected to filtration (0.45 μm PTFE Sartorius filter) to separate the ZnO. Finally, the concentration of RhB is determined by UV-Vis (Perkin Elmer LAMBDA 950), regarding its characteristic absorption peak at 553 nm.[33,35,36]

IV.4.5. CHARACTERIZATION INSTRUMENTS

Dynamic light scattering (DLS) measurements were performed with NanoPlus HD Zeta Potential and Particle Size Analyzer from Particulate Systems. Analyzer from Particulate Systems and the average particle size and standard deviation were calculated with NLFit (Gauss) function from OriginLab software.

ZIF-8@PS, HPZIF-8, and PCZnO are characterized by X-ray diffraction (XRD) on Panalytical X'Pert PRO diffractometer (Cu Kα radiation, Bragg-Brentano geometry, sealed tube operated at 45 mA 30 kV X'Celerator linear detector).

UV-VIS analysis was carried out on Perkin Elmer LAMBDA 950 UV/Vis/NIR spectrophotometer.

Thermal analysis has been performed on TGA/DSC 3+ from Mettler Toledo. Solid samples were analyzed in Al_2O_3 pans from 25 to 800 ºC (5 ºC min^{-1} scanning rate) under N_2 flow (80 mL min^{-1}).

Low-resolution scanning electron microscopy (SEM) was performed with JSM-6010/LV microscope from JEAL, and high magnification SEM and energy dispersive spectroscopy (EDX) were performed with Magellan 400L XHR SEM from ThermoFisher Scientific. The samples were coated with a 10 nm Au coating by sputtering before SEM characterization.

Transmission electron microscopy (TEM) was performed with a FEI Tecnai G^2 F20 S-Twin HR(S)TEM apparatus.

IV.5. BIBLIOGRAPHY

[1]   Y. Pan, Y. Liu, G. Zeng, L. Zhao, Z. Lai, *Chem. Commun.* **2011**, *47*, 2071.

[2]   Y. Du, R. Z. Chen, J. F. Yao, H. T. Wang, *J. Alloys Compd.* **2013**, *551*, 125.

[3]   X. Yang, L. Qiu, X. Luo, *RSC Adv.* **2018**, *8*, 4890.

[4]   X. Zhang, W. Lan, J. Xu, Y. Luo, J. Pan, C. Liao, L. Yang, W. Tan, X. Huang, *Sensors Actuators, B Chem.* **2019**, *289*, 144.

[5]   L. Zhang, Q. Liang, P. Yang, Y. Huang, Y. Liu, H. Yang, J. Yan, *New J. Chem.* **2019**, *43*, 2990.

[6]   G. Du, P. Feng, X. Cheng, J. Li, X. Luo, *J. Solid State Chem.* **2017**, *255*, 215.

[7]   Y. Feng, H. Lu, X. Gu, J. Qiu, M. Jia, C. Huang, J. Yao, *J. Phys. Chem. Solids* **2017**, *102*, 110.

[8]   H. Zhang, Y. Wang, W. Zhao, M. Zou, Y. Chen, L. Yang, L. Xu, H. Wu, A. Cao, *ACS Appl. Mater. Interfaces* **2017**, *9*, 37813.

[9]   X. Chang, K. Li, X. Qiao, Y. Xiong, F. Xia, Q. Xue, *Sensors Actuators B. Chem.* **2021**, *330*, 129366.

[10]   P. D. Du, N. T. Hieu, T. V. Thien, *J. Nanomater.* **2021**, *2021*, 1.

[11]   S. Liu, J. Wang, J. Yu, *RSC Adv.* **2016**, *6*, 59998.

[12]   P. Liang, C. Zhang, H. Sun, S. Liu, M. Tadé, S. Wang, *RSC Adv.* **2016**, *6*, 95903.

[13]   H. Chen, K. Shen, J. Chen, X. Chen, Y. Li, *J. Mater. Chem. A* **2017**, *5*, 9937.

[14]   J. Troyano, A. Carné-Sánchez, C. Avci, I. Imaz, D. Maspoch, *Chem. Soc. Rev.* **2019**, *48*, 5534.

[15]   K. Shen, L. Zhang, X. Chen, L. Liu, D. Zhang, Y. Han, J. Chen, J. Long, R. Luque, Y. Li, B. Chen, *Science (80-.).* **2018**, *359*, 206.

[16]   D. Grammatico, H. N. Tran, Y. Li, S. Pugliese, L. Billon, B. Su, M. Fontecave, *ChemSusChem* **2020**, *13*, 6418.

[17]   H. Hong, J. Liu, H. Huang, C. Atangana Etogo, X. Yang, B. Guan, L. Zhang, *J. Am. Chem. Soc.* **2019**, *141*, 14764.

[18]   H. M. Lal, A. Uthaman, S. Thomas, in (Eds.: A. Uthaman, S. Thomas, T. Li, H. Maria), Springer International Publishing, Cham, **2022**, pp. 1–15.

[19]   P. Jiang, J. F. Bertone, K. S. Hwang, V. L. Colvin, *Chem. Mater.* **1999**, *11*, 2132.

[20]   P. Jiang, K. S. Hwang, D. M. Mittleman, J. F. Bertone, V. L. Colvin, *J. Am. Chem. Soc.* **1999**, *121*, 11630.

[21]   K. Abitaev, Y. Qawasmi, P. Atanasova, C. Dargel, J. Bill, T. Hellweg, T. Sottmann, *Colloid Polym. Sci.* **2021**, *299*, 243.

[22]   A. Stein, F. Li, N. R. Denny, *Chem. Mater.* **2008**, *20*, 649.

[23] N. D. Petkovich, A. Stein, in *Hierarchically Struct. Porous Mater.* (Eds.: B. Su, C. Sanchez, X. Yang), Wiley, **2011**, pp. 55–129.

[24] W. Li, J. Liu, D. Zhao, *Nat. Rev. Mater.* **2016**, *1*, 16023.

[25] X.-Y. Yang, L.-H. Chen, Y. Li, J. C. Rooke, C. Sanchez, B.-L. Su, *Chem. Soc. Rev.* **2017**, *46*, 481.

[26] S. Kousik, D. Sipp, K. Abitaev, Y. Li, T. Sottmann, K. Koynov, P. Atanasova, *Nanomaterials* **2021**, *11*, 196.

[27] K. S. Park, Z. Ni, A. P. Côté, J. Y. Choi, R. Huang, F. J. Uribe-Romo, H. K. Chae, M. O'Keeffe, O. M. Yaghi, *Proc. Natl. Acad. Sci.* **2006**, *103*, 10186.

[28] U. P. N. Tran, K. K. A. Le, N. T. S. Phan, *ACS Catal.* **2011**, *1*, 120.

[29] S. A. Khayyat, M. S. Akhtar, A. Umar, *Mater. Lett.* **2012**, *81*, 239.

[30] A. Mclaren, T. Valdes-Solis, G. Li, S. C. Tsang, *J. Am. Chem. Soc.* **2009**, *131*, 1.

[31] A. Rovisco, R. Branquinho, J. Deuermeier, T. Freire, E. Fortunato, R. Martins, P. Barquinha, *ACS Appl. Nano Mater.* **2021**, *4*, 1149.

[32] M. Saeed, S. Adeel, M. Muneer, A. ul Haq, *Bioremediation and Biotechnology, Vol 2*, Springer International Publishing, Cham, **2020**.

[33] Q. I. Rahman, M. Ahmad, S. K. Misra, M. Lohani, *Mater. Lett.* **2013**, *91*, 170.

[34] Y. F. Li, D. Xu, J. Il Oh, W. Shen, X. Li, Y. Yu, *ACS Catal.* **2012**, *2*, 391.

[35] J. Yu, X. Yu, *Environ. Sci. Technol.* **2008**, *42*, 4902.

[36] Q. I. Rahman, M. Ahmad, S. K. Misra, M. B. Lohani, *Superlattices Microstruct.* **2013**, *64*, 495.

IV.6. APPENDIXES

Table IV-8 – List of the different ZIF-8@PS samples and the respective PSs template used.

ZIF-8@PS	PSs template used	
Sample	Sample	Diameter (nm)
1	2	390
2	3	380
3	3	380
4	4	400
5	4	400
6	4	400
7	6	400
8	6	400
9	6	400
10	9	380
11	9	380
12	10	380
13	10	380
14	10	380
15	10	380
16	11	400
17	11	400
18	11	400
19	12	350
20	12	350

Table IV-9 – Photodegradation of RhB after UV exposure of PCZnO samples.

t min	Photodegradation (%)		
	PCZnO 3	PCZnO 19	PCZnO 23
10	9.77	29.5	26.4
20	29.8	55.7	46.2
30	49.0	66.9	66.8
40	54.6	78.8	69.7
50	65.7	86.3	71.3
60	69.6	89.3	75.4
70	82.0	91.8	79.6
80	82.2	93.6	88.4
90	88.1	94.9	90.5
100	91.1	95.3	92.7
110	93.2	94.9	94.9

IV.6.1. XRD OF PCZnO

(hkl)	Angle (2θ)	d (Å)
Table IV-10 – PCZnO 23 XRD		
100	31.805	2.811
002	34.433	2.693
101	36.308	2.472
102	47.556	1.911
110	56.599	1.625
103	62.887	1.477
200	66.415	1.407
112	67.987	1.378
201	69.124	1.358
004	72.565	1.302
202	76.967	1.238

IV.6.2. TEM ANALYSIS PCZnO

HRTEM image used for d-space analysis.
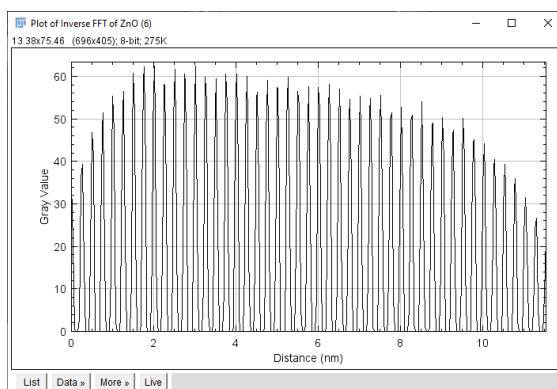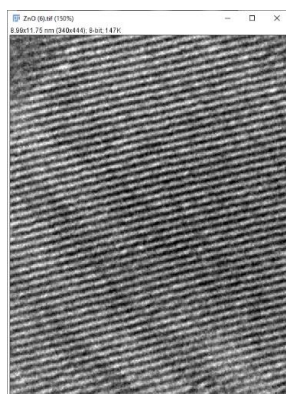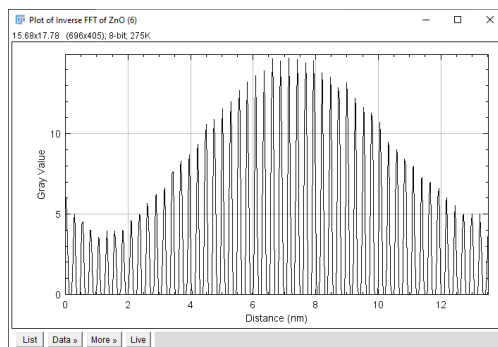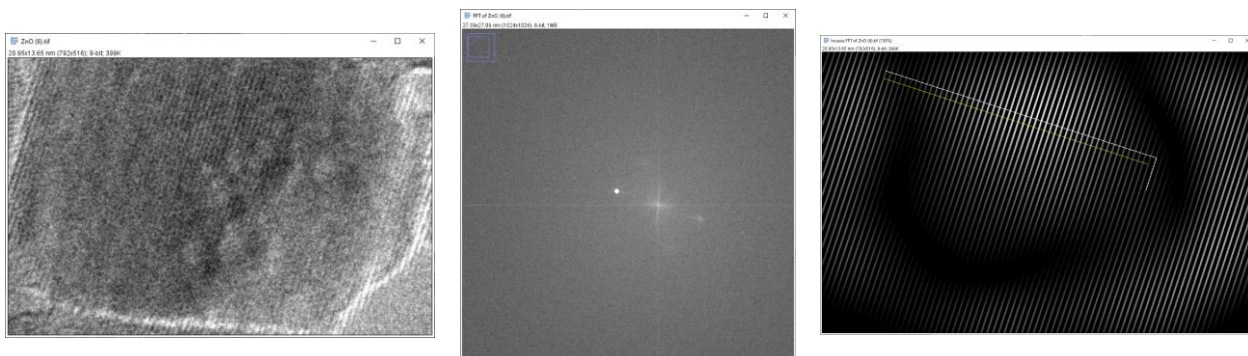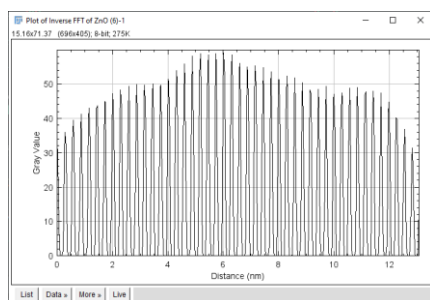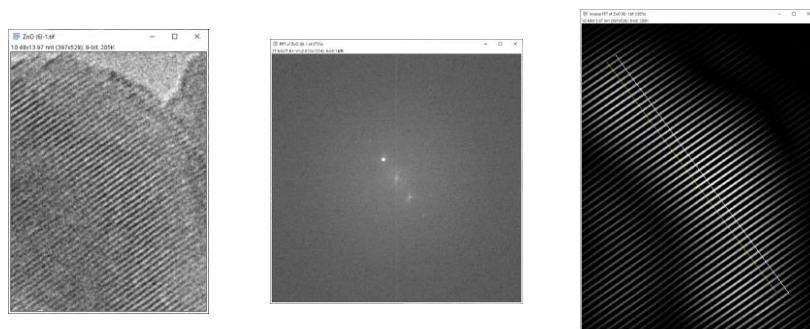
HRTEM	range	peaks	d (Å)	hkl
6.1	11.53	46	2.507	
6.2	13.07	50	2.614	
6.3	13.52	51	2.651	

Table IV-11 – PCZNO 23 XRD

(hkl)	Angle (2θ)	d (Å)
100	31.805	2.811

(hkl)	Angle (2θ)	d (Å)
002	34.433	2.693
101	36.308	2.472
102	47.556	1.911
110	56.599	1.625
103	62.887	1.477
200	66.415	1.407
112	67.987	1.378
201	69.124	1.358
004	72.565	1.302
202	76.967	1.238

Table IV-12 – SAED analysis.

S. No	1/2r (nm-1)	1/r (nm-1)	r (nm)	d (Å)	(hkl)
	7.437	3.719	0.269	2.689	
	8.525	4.263	0.235	2.346	
	10.894	5.447	0.184	1.836	
	12.951	6.476	0.154	1.544	
	14.203	7.102	0.141	1.408	
	15.216	7.608	0.131	1.314	
	19.314	9.657	0.104	1.036	
	21.520	10.760	0.093	0.929	
	23.279	11.640	0.086	0.859	
	16.781	8.391	0.119	1.192	
	20.313	10.157	0.098	0.985	
	25.306	12.653	0.079	0.790	
	27.407	13.704	0.073	0.730	

CHAPTER V

Novel printed devices for hydrogen evolution

CHAPTER V: **NOVEL PRINTED DEVICES FOR HYDROGEN EVOLUTION**

SHORT CONTEXT

This chapter describes the works performed to meet **Objective 3** of the present thesis: to study and define a methodology based on printed electronics to achieve novel functional cathodes for artificial photosynthesis.

The accumulation of carbon dioxide with anthropogenic origin in the atmosphere has resulted in a climate change that threatens humanity and the planet itself. Artificial photosynthesis (APS), mimicked through a photo-electrolyzer cell, presents great opportunities to convert solar energy, H_2O, and CO_2 to "solar fuels" or other stable products with important value for the industry. However, the large-scale implementation of such technology presents high costs. Thus, alternative earth-abundant and low-cost materials and up-scalable manufacturing processes need to be explored.[1] The use of cheap and easy printing techniques and the large production volume achievable can strongly contribute to the cost reduction of APS devices.

After investigating novel conductive polymers in CHAPTER II: and novel porous materials for catalyst loading in CHAPTER IV:, this chapter it is investigated the preparation of printed cathodes and MEA devices for hydrogen generation. In this study we propose, for the first time, the use of screen-printed electrodes (SPEs) as the cathode in such devices. SPEs with different designs and working areas prepared from carbon-based commercially available printing pastes provide sufficient electron conductivity to promote the hydrogen evolution reaction (HER) in neutral pH buffered solution at -1.6 V and -2.0 V (vs Ag/AgCl). Pt/C is deposited on the SPEs by automatic ultrasonic spray coating as the catalyst for HER and its loading effect is evaluated. The stability of SPEs is assessed through the electrochemical performance and mechanical stability in different pH and temperatures. The electrochemical performance of bare and Pt-coated carbon-based SPEs with different designs is described by chronoamperometric tests in different electrolyzer cell configurations: H-cell, flow cell, and proton exchange membrane electrode assembly (MEA).

This study validates the application SPEs on the cathode of a proton exchange membrane electrolyzer cell. This new manufacturing process shows an advantage over conventional processes by using mild conditions, being large area and high throughput, and using a drastically reduced number of materials, making it a cost-effective approach. Using SPEs is also differential by allowing disruptive integration strategies of membrane electrode assemblies and compatibility with a new catalyst and membrane materials. In conclusion, enabling automatization and fast production of

SPEs for MEAs opens the opportunity for new developments and advances in the energy conversion storage and printed electronics fields.

The works presented in this chapter are part of a filed patent: D. Garcia, V. Nguyen, M. Berenguel, P. Lacharmoise, C. Simão, *Fabrication method of a membrane electrode assembly (MEA), MEA, cell and uses thereof*. Fundació Eurecat. App. Nr. EP21383086.2, **2021**, Spain.
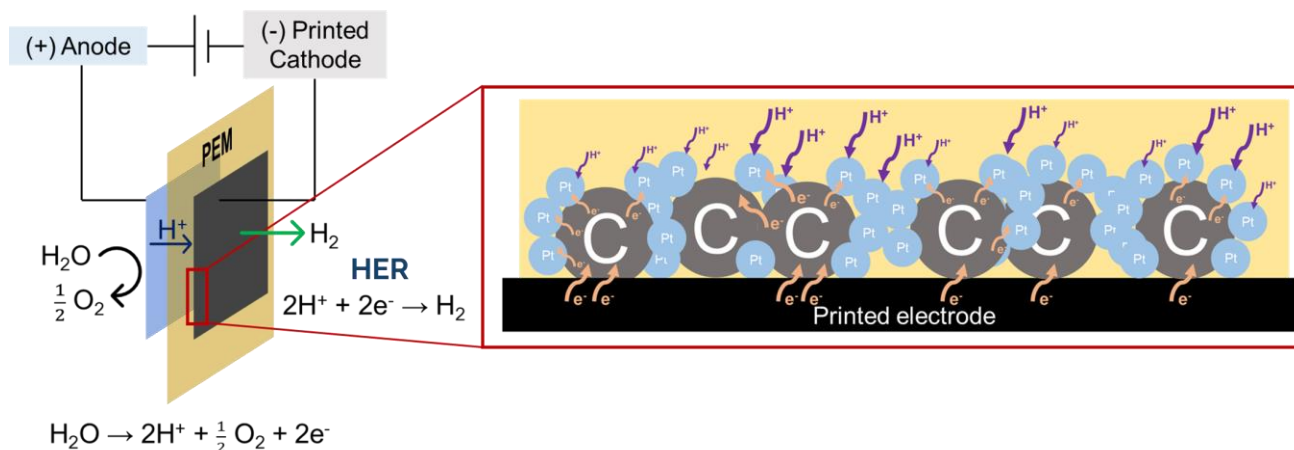
Figure V-1 – Visual abstract.

V.1. A MONOLITHIC FULLY PRINTED MEMBRANE ELECTRODE ASSEMBLY

Inspired by printed electronics and in previous printed batteries research[1], novel designs of membrane electrode assemblies (MEA) are proposed to be investigated in this chapter as monolithic printed MEAs. The concept of a monolithic printed MEA consists of the three elements of a MEA (membrane, catalysts, and gas diffusion layers) prepared through a layer-by-layer printing process. Two design hypotheses are defined: unsupported and supported monolithic fully printed MEAs (Figure V-2). Taking into account the printing techniques available, the catalysts will always be spray-coated, and the gas diffusion layers (GDL) will be substituted by screen-printed carbon electrodes to substitute carbon GDL.

Conceptually, a fully printed MEA device would require a supporting substrate to print each element (gas diffusion layers, catalyst layers, and membrane) in a layer-by-layer process. The supporting substrate acts as a mere carrier without any other function in the device itself. This monolithic fully printed MEA will be referred to as "Supported printed MEA" (Figure V-2 b)). In this type of MEAs, it is possible to use both nonporous substrates (such as polymer foils, metals, *etc.*) or porous substrates such as nonwoven textiles, cellulose-based or polymer-based.
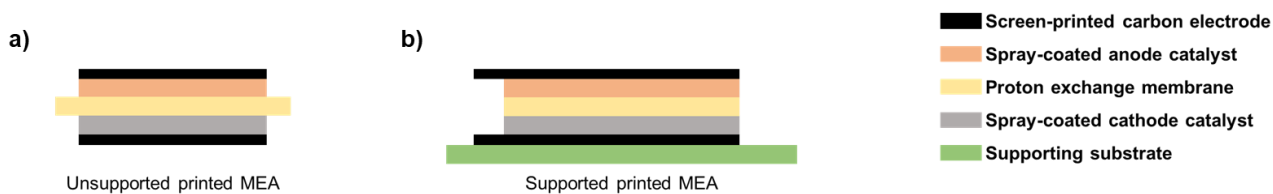
Figure V-2 – Schematic cross-sectional representation of monolithic fully printed MEAs types: unsupported **(a)** and supported printed MEAs **(b)**.

Additionally, the Nafion membrane is a polymer foil that can be considered a printing substrate on its own, and in this case, the Nafion is both the membrane and supporting substrate of the device. Thus, an unsupported fully printed MEA would consist of printing catalysts and gas diffusion layers on a membrane, such as Nafion. In this case, thus this type of fully printed device will be referred to as an "Unsupported printed MEA" (Figure V-2 a)).

These two fully printed MEAs preparation approaches allow the creation of MEAs in different materials, more or less conventional, in a modular approach. Combinations of printed elements and non-printed elements, with conventional materials, can be arranged, creating a versatile modular toolbox to prepare MEAs for different application scenarios.

V.1.1. MONOLITHIC FULLY PRINTED MEA DESIGN RULES

To understand the role of each printed element in the performance of the MEA, a set of variables needs to be defined and investigated to find out how these modules can be assembled and create fully or partially printed MEAs. For that purpose, printing design rules must be investigated for each printed element.

- Printed gas diffusion/electrode layers: printing technique, materials, thin film thickness, resistivity, micro and macro-porosity, and, macropores' geometrical shape and size.
- Printed membrane: printing technique, materials, and, composition.
- Printed catalyst layers: printing technique, number of layers, composition, and, materials.

In the present thesis, the investigation of the design rules to prepare printed gas diffusion layers is the center of the study. Since it is a novel approach to preparing MEAs it is compulsory to investigate which are the parameters that affect the fully printed MEA preparation and what is their impact on the cell performance.

Printed membrane elements have been developed within the eSCALED project as a disruptive and novel approach to preparing proton exchange membranes (PEMs) by scalable printing techniques, such as doctor blade. Membranes for the supported printed MEA type were co-developed with Bruno Branco and paper-based membranes were co-developed with Van Nguyen for the unsupported printed MEA type.

In the case of the catalyst layers, these are, nowadays, MEA elements that are already commonly printed by spray-coating[2], and extensive studies of polymer binders, composition, and printing strategies (catalyst-coated membrane or substrate) are important research and industrial development topics.[3] Therefore, in this work, the studies concerning the printed catalyst layer focus on the investigation of the deposition of different catalyst loads by varying the number of catalyst layers deposited through an automatized ultrasonic spray-coating setup.

V.1.2. SUPPORTING SUBSTRATE

The materials to be used as a substrate should be robust, flexible, lightweight, and compatible with printing techniques. Therefore, poly(ethylene terephthalate) (PET) was selected as a standard substrate for the overall studies, matching the overall requirements of this work. As a side study, complimentary to the collaboration with paper-based membrane MEAs developed with Van Nguyen, it also preliminarily investigated the use of plain paper as an example of a porous support substrate to prepare printed GDL electrodes.

V.1.3. GAS DIFFUSION LAYERS/ELECTRODE DESIGN RULES

A schematic representation of the proposed printed gas diffusion layer and gas diffusion electrode is given in Figure V-3.
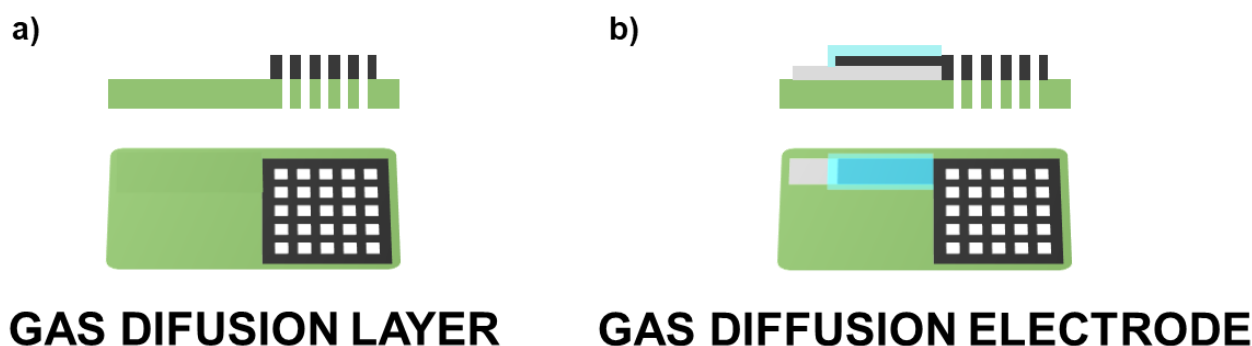
Figure V-3 – Schematic representation of the screen-printed gas diffusion layer **(a)** and gas diffusion electrode **(b)**.

The screen-printed GDL comprises a single carbon layer designed to allow gas diffusion. The printed gas diffusion electrode comprises a screen-printed carbon GDL connected to a metallic screen-printed current collector.

V.1.3.1. PRINTED GDL MATERIAL

Two commercially available conductive carbon-based screen-printing inks were defined as candidates to play the role of the carbon-based layer at the printed GDL layer: Carbon Creative 122-49 and Graphite Sunchemical C2030519P4. These two inks were selected to act as standard materials to make the basic characterization of the printed devices before using eSCALED-made

materials like inks, since both are commonly used for electrochemical applications, in particular the Sunchemical ink. The Creative ink is a low-temperature curing ink (it can be cured with temperatures as low as 80 ºC, in contrast with the typical 110-120 ºC for screen-printing inks), which is an advantage when using temperature-sensitive materials catalysts, for example.

Alternative inks were prepared in the lab, following an eSCALED internal formulation[4] based on commercially available polymeric binders, namely, poly(methyl methacrylate-butyl acrylate-methyl methacrylate) (MBM) and poly(styrene-butadiene-styrene) (SBS). The conductivity of such inks was promoted by graphite particles.

V.1.3.2. PRINTING TECHNIQUE AND MATERIALS

The approach herein proposed is to screen-print conductive inks, carbon-based, to substitute expensive and mechanically placed carbon-based cloths as gas diffusion layers. Screen-printing enables the printing of a broad variety of materials and composite inks, with controllable microporosity by geometrical design.

V.1.3.3. GEOMETRICAL DESIGN OF PRINTED GDLs

The GDLs/electrodes were designed to match the 3D-printed electrolyzer cell used to evaluate MEAs in this work (Figure V-4 a)). The GDLs will have a 2.0 x 2.0 cm^2 working area, fitting in the flow distribution area of the testing electrolyzer cell, and a 2.25 x 0.5 cm^2 connector.
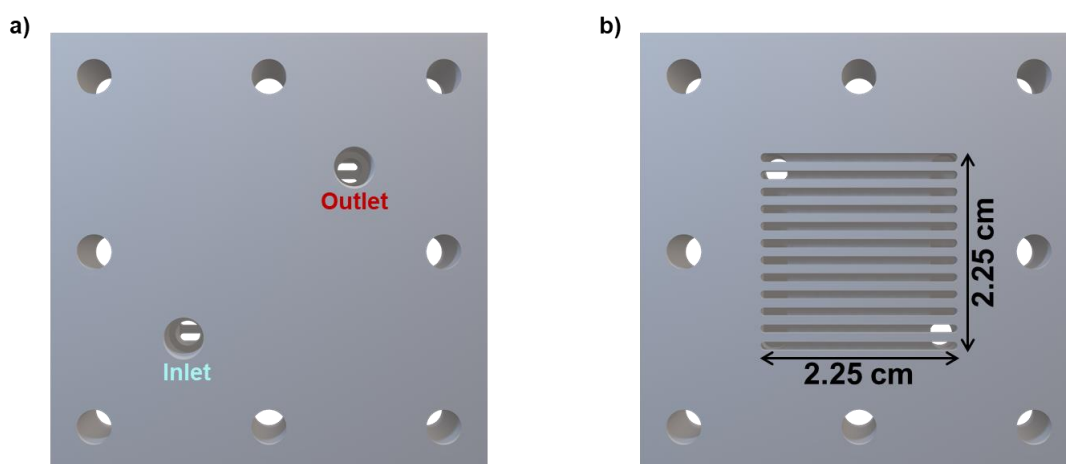
Figure V-4 – End-plate design of the conventional electrolyzer cell available for the testing of the MEAs: **a)** external side with flow inlet and outlet, **b)** inner side of the end plate with 2.25 x 2.25 cm^2 flow distribution area.

Moreover, the printed GDLs need to have a certain "porosity" to allow the formed gases to escape. To achieve this, the design of the screen-printed GDL will have a combination of openings (no ink) and ink areas. The openings were designed to match the flow distribution area of the 3D electrolyzer cell (Figure V-4 b)) following two distinct geometries: squares and rectangles. In the first case, the square-shaped openings are called "windows".

Figure V-5 a) gives an example of an electrode designed with two window-like openings.

a)

Electrode with windows · Window-like openings

b)

Electrode with slits · Slit-like openings

c)

Electrode with open mesh · 100 window-like openings
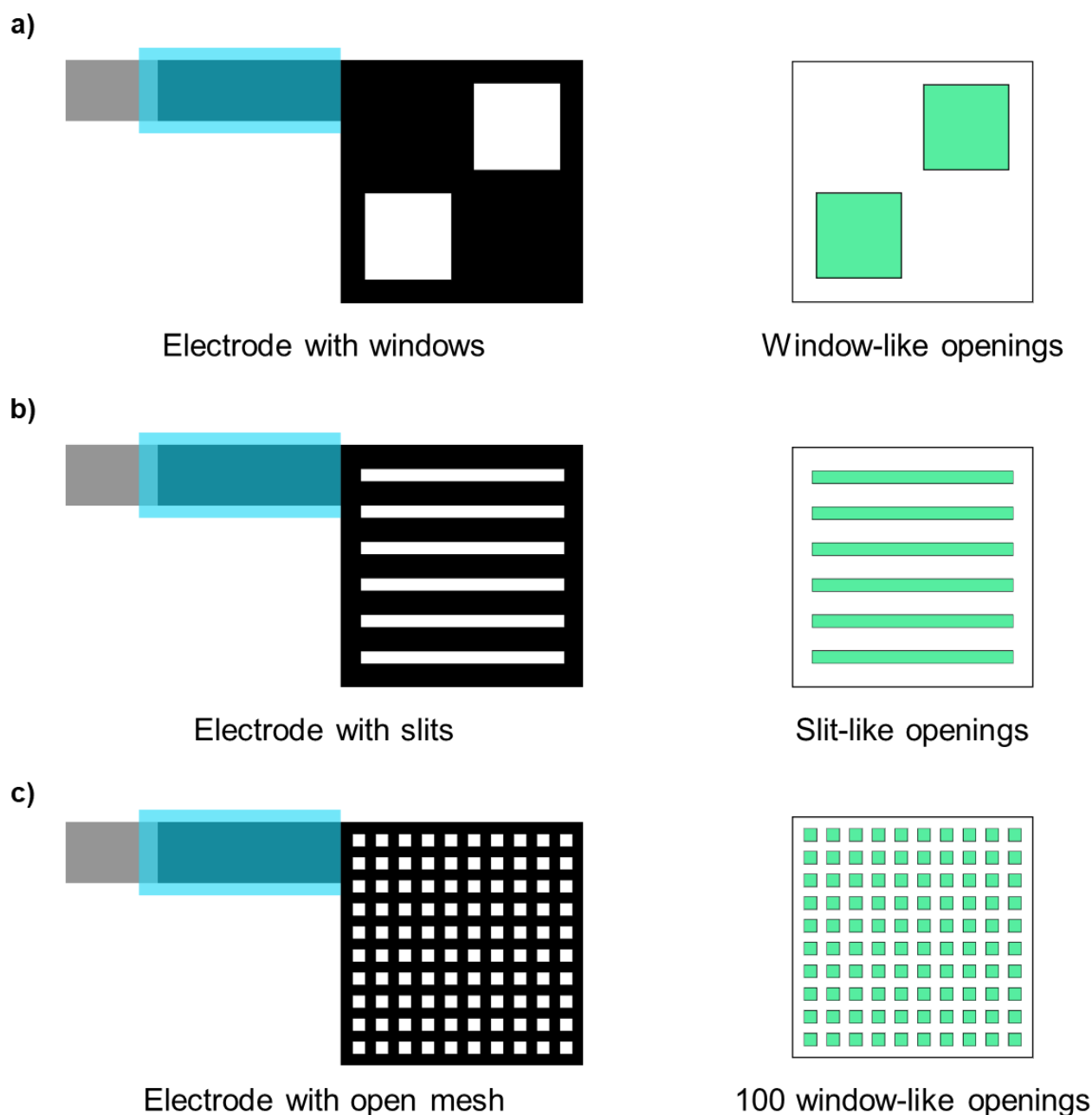
Figure V-5 – a) Electrode containing two square-shaped openings, *i.e.*, windows, on its working area. **b)** Electrode containing six rectangular openings, *i.e.*, slits, on its working area. **c)** Electrode with an open-mesh design containing one hundred window-like openings.

The rectangular-shaped openings are here called "slits". Slits were designed for conventional bipolar plates and electrolyzer cells with flow-distributing channels with a slit-like design, such as the cell available (see Figure V-4 b)).[5] An example of an electrode containing slit-like openings is given in Figure V-5 b).

The "open mesh" design targeted a more homogeneous gas diffusion from the electrode's surface, independently from the electrolyzer cell end-plates' flow distribution design. In this design, the electrode contains square-shaped openings equally spaced between them and homogenously distributed throughout the electrode's working area. Figure V-5 c) illustrates one open mesh design.

The proposed printed GDL designs are a strategy to introduce means for gas escaping when using conventionally non-permeable materials, such as a common conductive screen-printed electrode (SPE) based on commercial ink, polymer foils, *etc.* Moreover, this approach enables the preparation of controlled "macro"-porosity through geometrical design. More interestingly, screen-printed electrodes may have controlled microporosity, through strategies such as the breath figure method tested in CHAPTER II: of this thesis, or by incorporating microporous nanoparticles prepared by metal-organic frameworks (MOFs) templates, such as the ones developed in CHAPTER IV:.

V.1.3.4. GDL BUILDING BLOCKS

The three types of design families (windows, slits, and open mesh) will be designed with different combinations of line widths and, opening spatial distribution dimensions to investigate the parameters that greatly affect the MEA performance in the following sections. To normalize the comparison between electrodes and regardless of the openings' design, the ratio between openings and ink areas was kept to 1:3, *i.e.*, the sum of all opening areas was fixed to 1 cm^2, while the ink area was kept equal to 3 cm^2. The number of openings (N^{open}) ranges from 0 to 100. Figure V-6 represents the electrode designs classified by their openings' geometry composing the complete building block toolbox to prepare MEAs.
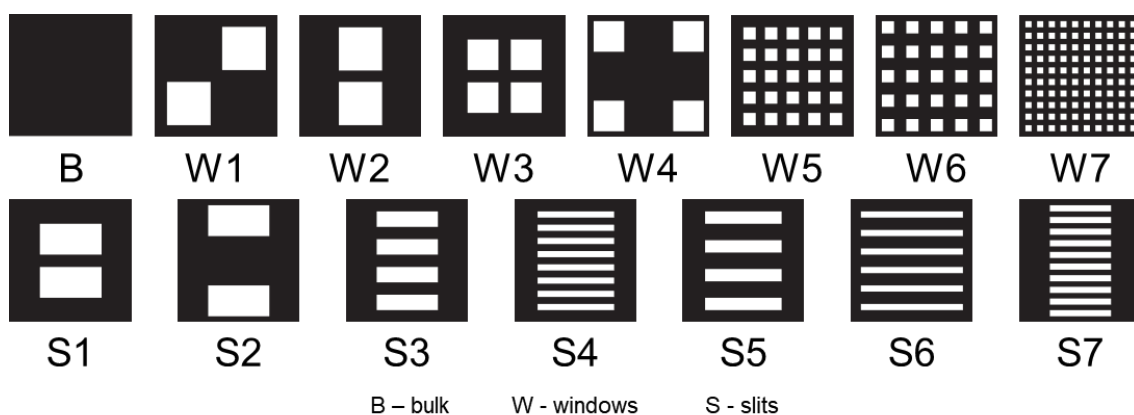
Figure V-6 – Printed GDL building blocks toolbox: electrodes designed according to the openings' geometry, dimensions, and spatial distribution.

More design combinations or completely different geometries can be realized with this SPE approach, which is an advantageous feature of using printing techniques. In this work, the building blocks are limited to these combinations to have controlled geometrical dimensions to be able to parametrize variables affecting the MEA performance in the following sections.

V.1.4. PRINTED GDL ELECTRODES DESIGN

After the GDLs' design is proposed, the complete printed device requires a combination of materials extra to act as an efficient electrode. A screen-printed silver nanoparticle ink bottom layer is added to act as the current collector to lower the contact resistance and a topmost dielectric ink

screen-printed layer protects the connector and defines the working area. These are represented in Figure V-7 in grey and light blue color, respectively, while the black color represents the carbon-based layer to be printed between silver and dielectric.

■ Carbon electrode
■ Dielectric layer
■ Silver current collector
■ Supporting substrate

Figure V-7 – Illustrative representation of the complete screen-printed gas diffusion electrode containing a silver current collector, a dielectric layer in blue, and the carbon electrode. GDL design type **B** is represented.

A 125 µm thick poly(ethylene terephthalate) (PET) substrate is used to prepare the final printed GDL electrode device. The full fabrication protocol of the screen-printed electrodes is described in section V.9.2 of this chapter. The controlled geometrical parameters that are preliminarily identified in this building blocks approach are demonstrated in Figure V-8, where the following parameters apply:

- a is the width of the opening
- b is the height of the opening
- c is the distance between the electrodes' connector and the nearest opening
- d is the distance between the opening considered to define c) and the top border of the electrode
- e is the longitudinal distance between openings
- f is the latitudinal distance between openings.
- g is the distance between the electrodes' connector and the nearest opening at the same latitude (only applicable to **W1**).

Table V-13 (see section V.11 Appendixes) summarizes these dimensional parameters defined in Figure V-8 for all the designs proposed.
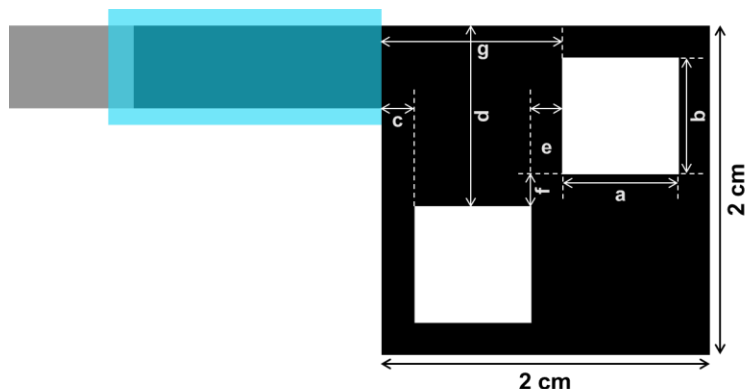
Figure V-8 – Parametrization of dimensions design of screen-printed gas diffusion layers. GDL design type **W1** is represented.

These proposed combinations and variations were defined to find the most balanced design rules in terms of the number of openings, opening dimension, and distribution in the working area, promoting

the best performance of the electrode. Increasing the number of openings is expected to contribute to more homogenous gas diffusion from the electrode. However, the number of openings may be reduced if the size of the openings is increased, thus increasing the width of solid areas and/or lines between openings and avoiding high resistance spots in the electrode.

In the open mesh designs (W3, W4, W5, W6, and W7), as the number of openings increases, the thickness of the solid lines between openings is decreased. In this case, thinner lines are expected to increase the resistance of the electrode and, therefore, limit the charge distribution across the electrodes' working area, thus limiting the number of reactional sites. However, this design is also expected to promote a more homogeneous gas diffusion from the electrodes' working area, *i.e.*, the formed gas, when released from the electrode's surface, has a higher probability of finding an opening to escape through. The prevalence of one of these events is expected to affect cell stability.

In the following sections, the design rules are tested with bare electrodes to validate printed electrodes as current collectors and support the hydrogen evolution reaction (HER) to take place.

V.2. PRINTED GDL ELECTRODE RESULTS

Figure V-9 illustrates the workflow methodology followed in the present chapter.
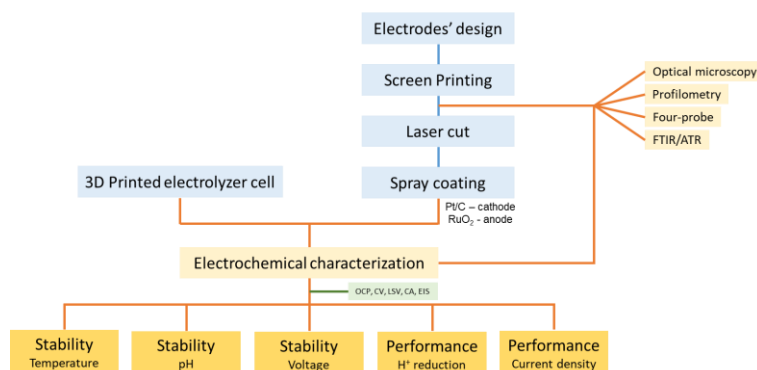
Figure V-9 – Workflow methodology.

After the different GDL electrode designs were defined, the electrodes were screen-printed and then had their morphology and electrical properties characterized. A laser cutting step was applied to remove the supporting printing substrate used from the open areas of the GDL designs. Part of the electrodes was coated with catalysts by spray coating. Finally, the printed GDL electrodes were electrochemically characterized to evaluate their stability against temperature, pH and voltage applied and their performance as cathodes for H^+ reduction reaction was compared in terms of current density.

V.2.1. PREPARATION METHODOLOGY OF THE PRINTED GDL ELECTRODES

The preparation of a printed GDL electrode for the investigation of design rules is depicted in Figure V-10.
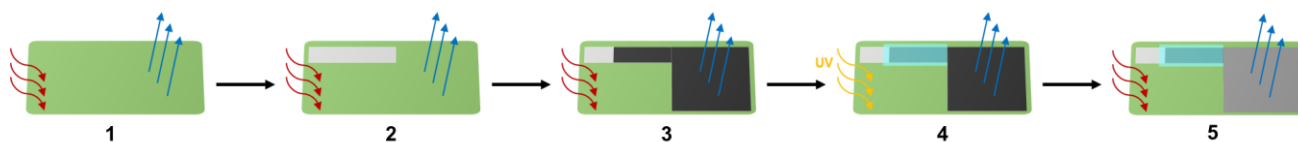
Figure V-10 – Printed GDL electrode generic fabrication methodology representation. The screen-printing and spray-coating processes are illustrated in steps 1-4 and 5, respectively. **(1)** Pre-treatment of the substrate at 140 °C (30 min). **(2)** Printing of silver connector and subsequent thermal curing at 130 °C (15 min) **(3)** Carbon-graphite electrode is printed above the previous silver layer and thermally cure at 130 °C (10 min). **(4)** A dielectric film is printed to set the electrode active area and UV cured (65 W/cm). **(5)** Catalyst ink deposited by ultrasonic spray-coating on a hotbed at 50 °C (dried at the same temperature, 5 min). The printed GDL design B is used for generic representation. The red and blue arrows illustrate the drying step and evaporation of solvents, respectively.

The generic procedure starts with the thermal pretreatment of the supporting substrate. The first printing step consists of the silver nanoparticle layer, followed by thermal curing. Secondly, the carbon layer is printed and thermal cured, and afterward the dielectric layer is screen-printed and cured in a combination of thermal and UV-light curing. The final and topmost layer of a printed GDL electrode for the design studies is the spray-coated catalyst layer. This procedure was repeated for the two commercial carbon inks (Creative and Sunchemical). The resulting printed GDL electrodes are depicted in Figure V-11.
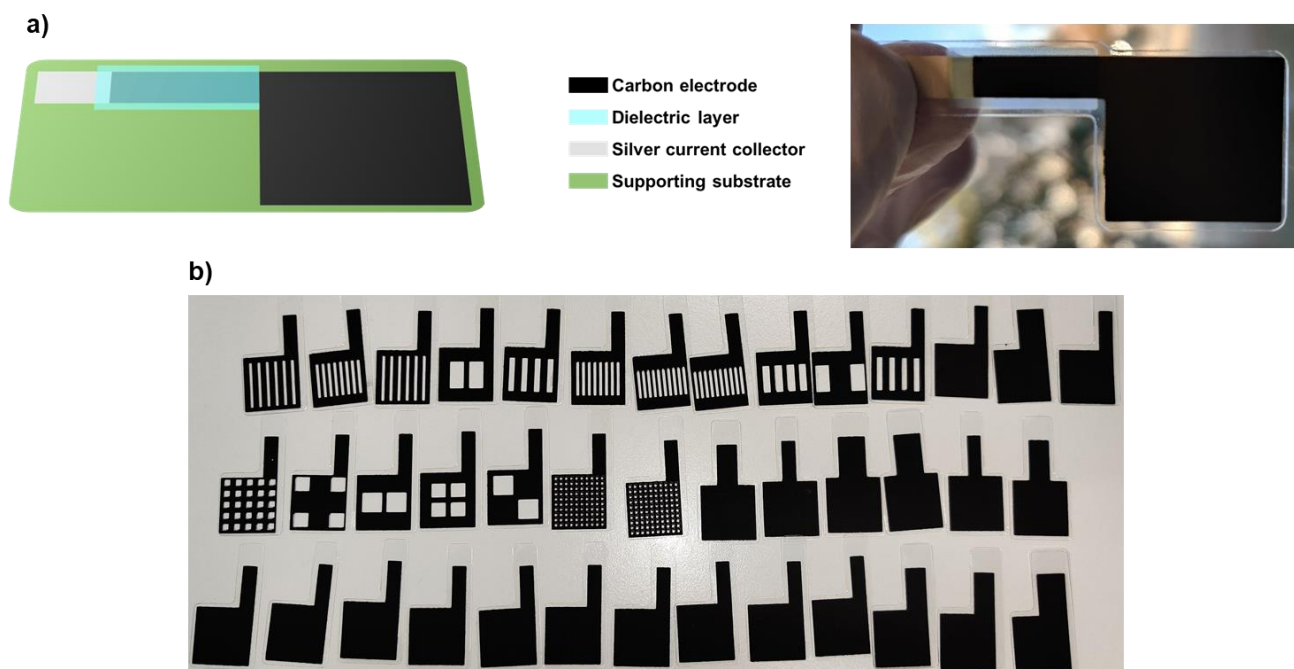
Figure V-11 – Screen-printed GDL electrode (design type **B**) schematic representation **(a)** and picture of a prepared sample on polymer foil **(b)**. Printed GDL samples prepared in all building blocks designed and proposed.

The printed devices showed very good ink compatibility between the layers and mechanical stability without delamination or shrinkage.

The electrical and morphology characterization and evaluation of these two inks were done to select the best in terms of conductivity and film homogeneity for the printed MEA application and then compared as a standard to in-lab prepared inks.

V.2.2. ELECTRICAL AND MORPHOLOGY CHARACTERIZATION

Samples of printed GDL electrodes (type **B**) were prepared with Sunchemical and Creative inks. The surface roughness and homogeneity and thickness of the electrodes were evaluated by optical microscopy and profilometry. Figure V-12 presents the optical microscopy images from Sunchemical and Creative. It was observed by optical microscopy that the Creative ink promotes a smoother surface than the Sunchemical.
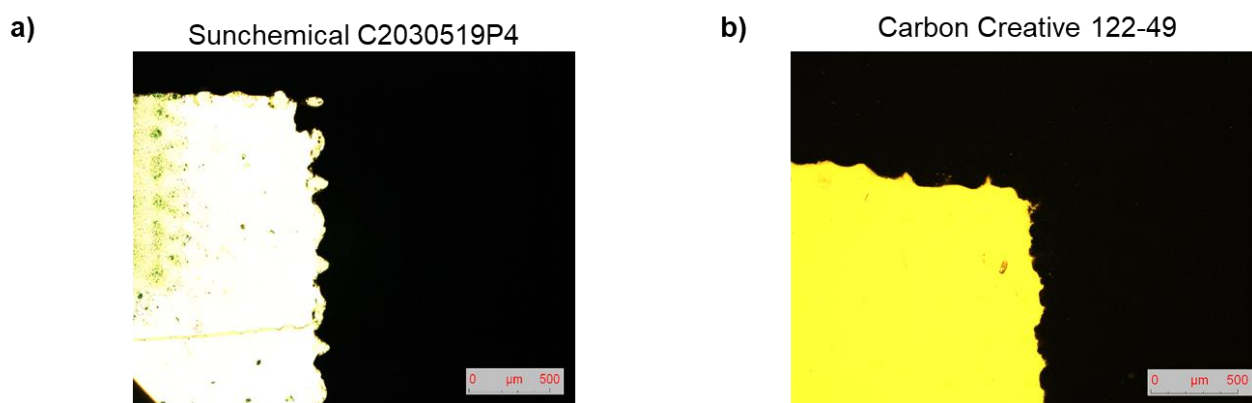
Figure V-12 – Micrographs and pictures from screen-printed electrodes from **a)** Graphite Sunchemical C2030519P4 and **b)** Carbon Creative 122-49.

The measured thicknesses of the electrodes characterized by profilometry are presented in Table V-14 (see section V.11 Appendixes). The electrodes printed from commercial inks, Carbon Creative, and Graphite Sunchemical generated thicknesses of 12.1 ± 1.2 µm and 10.6 ± 3.8 µm, respectively. It is worth noticing that these values are in the range of the expected screen-printing technique (10 – 200 µm).[6] Figure V-13 presents the height profiles of the electrodes produced from the previous four inks.
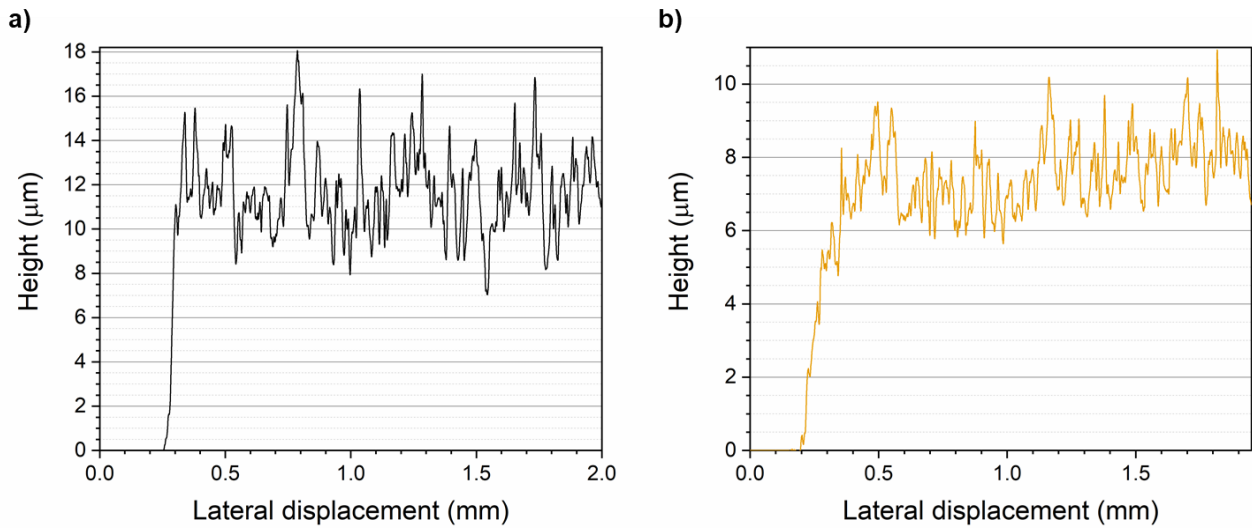
Figure V-13 – Height profiles of the electrodes from **a)** Creative (two wets on wet layers) and **b)** Sunchemical (two wet on wet layers).

The conductivity of the printed layers was measured with a Four-Point Probe (4-pp) system as illustrated in Figure V-14 a).
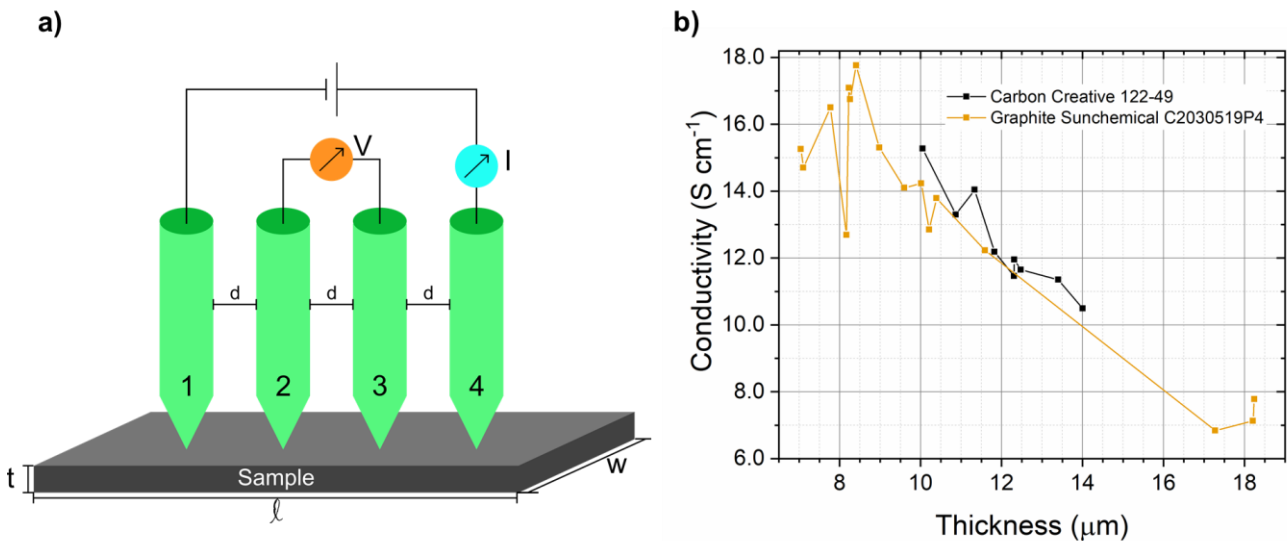
Figure V-14 – a) Four-Point Probe system where t, w, and ℓ represent the thickness, width, and length of the sample, respectively, and d is the distance between probes. **b)** Measured conductivity of screen-printed electrodes from different inks.

This technique is the most used to measure the sheet resistance of thin films. In this technique, four equally spaced and co-linear probes are used to make electrical contact with the material to be characterized. In 4-pp, a current (I) is injected between two probes (1 and 4), while the resulting voltage (V) is measured by the other two probes (2 and 3).[7,8] The sheet resistance is then calculated following Equation V-1:

$$R_s = \frac{\pi}{\ln 2} \frac{\Delta V}{I} = 4.5324 \frac{\Delta V}{I} \qquad \textbf{Equation V-1}$$

Where R_s is the sheet resistance (measured in ohms per square, Ω sq^{-1}), ΔV is the potential difference between the probes, and I is the applied current.[9,10] The resistivity of the film is calculated according to Equation V-2:

$$\rho = R_s \times t \qquad \textbf{Equation V-2}$$

Here, ρ is the film resistivity ($\Omega \cdot m$), and t is the thickness measured by profilometry. Finally, the conductivity, σ, is given in S m^{-1} by Equation V-3:

$$\sigma = \frac{1}{\rho} \qquad \textbf{Equation V-3}$$

Figure V-14 b) it is presented the measured electrode's conductivity *vs.* thickness relationship. For both commercial inks, it was observed that the increase in thickness led to a decrease in conductivity, as expected from Equation V-2 (higher thickness leads to higher resistivity) and Equation V-3 (higher resistivity means lower conductivity). The highest conductivity, 17.8 S cm^{-1} (two wet on wet printed layers, 8.41 µm film) was registered for Graphite Sunchemical ink, while Carbon Creative ink had its highest conductivity at 15.3 S cm^{-1} for a 10.1 µm film (three wet on wet printed layers).

Finally, due to its high conductivity, Graphite Sunchemical was selected as the ink to prepare screen-printed electrodes (SPEs) to be integrated into H$^+$ reduction electrochemical devices.

V.2.3. DETERMINATION OF PRINTED GDL ELECTRODES ELECTROCHEMICALLY ACTIVE SURFACE AREA

Determining the electrochemically active surface area (ECSA) is necessary for the normalization of the electrochemical reaction rates and contributes to the direct comparison and reproducibility of the results between and among different labs.[11,12] The ECSA of a commercially available glassy carbon electrode with 0.071 cm^2 geometrical area (A_{geo}) and a Sunchemical SPE (A_{geo}= 4 cm^2) was characterized through a voltage scan rate study (SRS). This study consisted of recording cyclic voltammograms in a ferro-ferricyanide system in a buffer solution having the potential scanned at different rates.

Figure V-15 is represented the SRS performed for glassy carbon electrodes and printed GDLs prepared with Sunchemical inks.
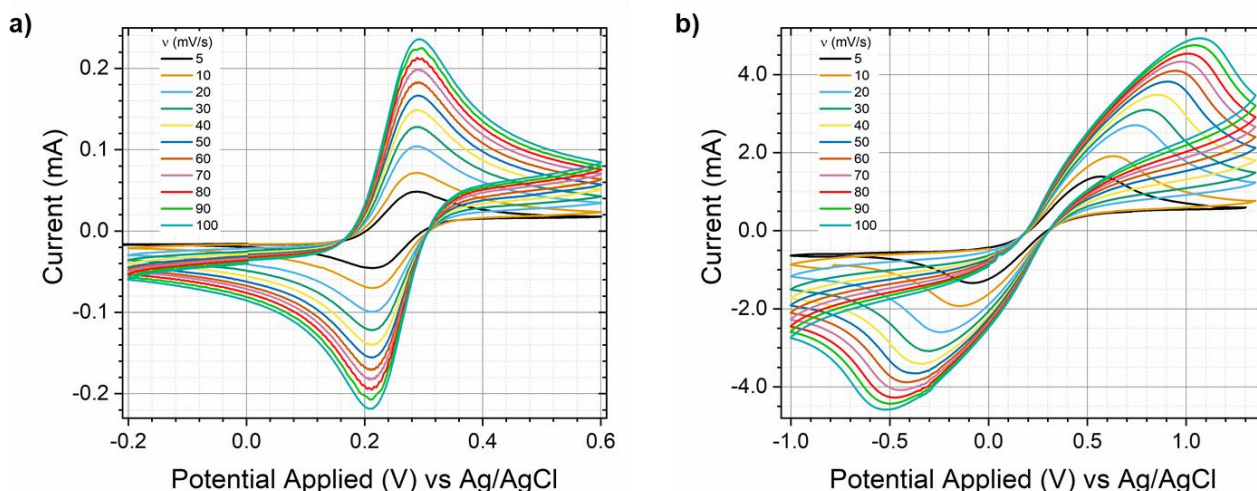
Figure V-15 – SRS (the second cycle from the CV obtained from each scan rate studied) on **a)** glassy carbon electrode (A_{geo} = 0.071 cm^2) and **b)** printed GDL electrode (A_{geo} = 4 cm^2).

The SRS obtained for the glassy carbon electrode is presented in Figure V-15 a). The obtained CVs present one anodic and cathodic peak, *i.e.*, the oxidation of ferrocyanide ($Fe^{II}(CN)_6^{4-}$) to ferricyanide ($Fe^{III}(CN)_6^{3-}$) at the forward scan and the following reduction of $Fe^{III}(CN)_6^{3-}$ to $Fe^{II}(CN)_6^{4-}$, respectively, as demonstrated in Equation V-4 and Equation V-5.

$$Fe^{II}(CN)_6^{4-} \rightarrow Fe^{III}(CN)_6^{3-} + e^- \quad \textbf{Equation V-4}$$

$$Fe^{III}(CN)_6^{3-} + e^- \rightarrow Fe^{II}(CN)_6^{4-} \quad \textbf{Equation V-5}$$
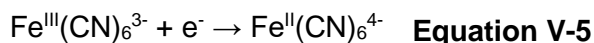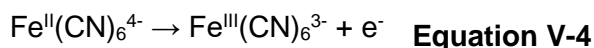
In Figure V-15 b) the SRS performed with a Sunchemical SPE is presented and two peaks, one anodic and one cathodic were also observed. These two peaks were attributed, again, to the oxidation and reduction mechanisms described in Equation V-4 and Equation V-5.

From the visual comparison of the SRS from both electrodes, one may observe that the potential distance between anodic and cathodic peaks (ΔE_{pp}) was increased in the case of the printed GDL electrode. ΔE_{pp} was calculated by Equation V-6:

$$\Delta E_{pp} = |E_p(anodic) - E_p(cathodic)| \quad \textbf{Equation V-6}$$

For each voltage scan rate, ΔE_{pp} is presented together with E_p vs v plots in Figure V-16 a) and b) from a glassy carbon electrode and printed GDL electrode, respectively.
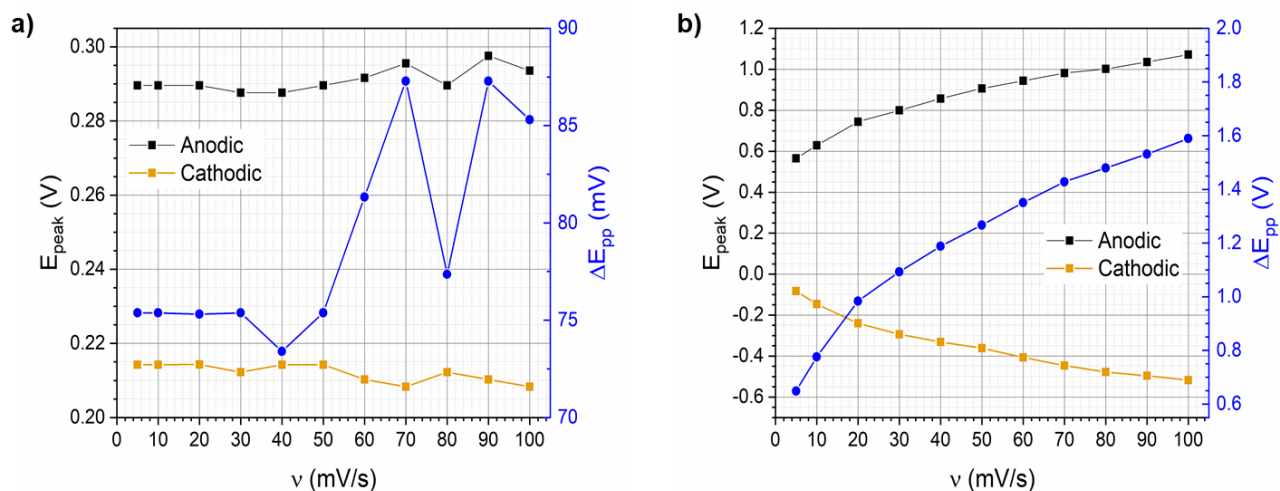
Figure V-16 – E_p vs v plots obtained from the SRS study performed on **a)** glassy carbon electrode and **b)** printed GDL electrode.

In a perfect reversible electron transfer reaction, E_p is not affected by the scan rate, *i.e.*, there is no shift in potential, which is a characteristic of rapid electron transfer kinetics. Furthermore, the lower the ΔE_{pp} the better the electron transfer ability of the electrode.[13] Following the previous statements and by comparison of their respective ΔE_{pp}, it is possible to observe that the glassy carbon electrode has a better electron transfer ability than the printed GDL electrode since the first presented ΔE_{pp} in the 75.4 - 85.3 mV range, while the second had its ΔE_{pp} between 0.585 and 1.77 V. This result agrees with the expectation since the printed GDL electrode has higher electrical resistance than the glassy carbon electrode. In the case of the glassy carbon electrode, the peak potential is independent of the applied voltammetric scan, which indicates a reversible reaction, and the electron transfer rate is higher than the mass transport rate. However, the same does not apply to the printed GDL electrode whose peak potentials increase with the applied scan rate, a synonym of a quasi-reversible system, *i.e.*, the electron transfer rate is equal/similar to the mass transport rate.[13,14]

The peak current (i_p) of a reversible system cyclic voltammogram (CV) is governed by the Randles-Ševčik relation.[14–16] This function describes the effect of scan rate and diffusion coefficient as presented by Equation V-7:

$$i_{p,reversible} = 0.446nFAC\left(\frac{nv\mathrm{FD}_0}{\mathrm{RT}}\right)^{1/2} \quad \textbf{Equation V-7}$$

where n is the number of electrons transferred in the electrochemical reaction (n=1 in the ferricyanide-ferrocyanide reaction), v is the scan rate (V/s), F is the Faraday constant (C mol^{-1}), R is the universal gas constant, T is the temperature in Kelvin (room temperature, 298.15 K), A is the ECSA of the electrode (cm^2), C is the concentration of redox couple ions in solution (mol/L) and D is its diffusion coefficient (7.09×10^{-6} cm^2 s^{-1} considered).[17] The development of this equation leads to Equation V-8 from which is possible to assume that i_p is proportional to the squared root of v (Equation V-9). Therefore, the slope of a linear plot of I_p vs $v^{1/2}$ can be used to estimate the ECSA

(Equation V-10 and Equation V-11). The surface roughness factor (RF) of the electrodes is calculated by the ratio of the ECSA to the geometrical surface area.[18,19]

$$i_p = (2.69 \times 10^5)\, n^{3/2}\, A\, C\, D^{1/2}\, v^{1/2} \qquad \textbf{Equation V-8}$$

$$i_p \propto v^{1/2} \qquad \textbf{Equation V-9}$$

$$slope = (2.69 \times 10^5)\, n^{3/2}\, A\, C\, D^{1/2} \qquad \textbf{Equation V-10}$$

$$ECSA = \frac{slope}{(2.69 \times 10^5)\, n^{3/2}\, C\, D^{1/2}} \qquad \textbf{Equation V-11}$$

Figure V-17 a) and b) present the Randles-Ševčik plots (i_p vs $v^{1/2}$) for the glassy carbon electrode and Sunchemical SPE tested, respectively.
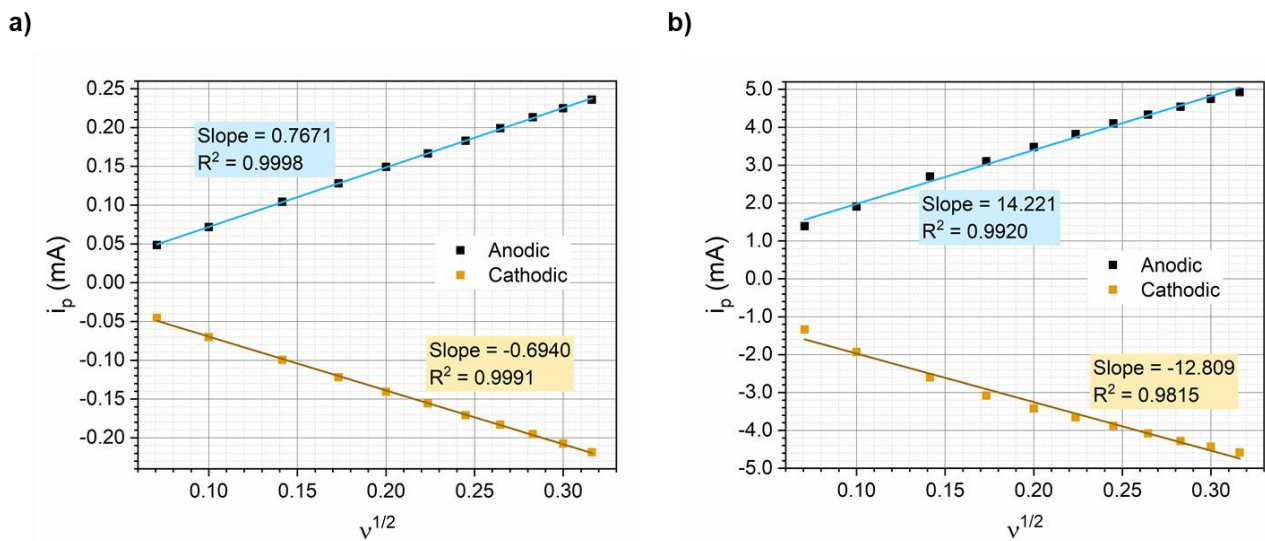
Figure V-17 – Randles-Ševčik plots i_p vs $v^{1/2}$ obtained for **a)** glassy carbon electrode and **b)** printed GDL electrode.

In both cases, the Randles-Ševčik plots verified the linearity between the peak current and the square root of the scan rate. The linear fit of the Randles-Ševčik plot of the glassy carbon electrode with $R^2 \approx 1$ (both anodic and cathodic) illustrates a reversible process. However, in the case of the printed GDL electrode, one may observe that the linear fit quality (R^2) is lower, *i.e.*, the current peaks may not be a function of the scan rate, and in this case, the process is quasi-reversible. This analysis agrees with the analysis of E_p and ΔE_{pp}.

Table V-1 presents and compares the calculated ECSA and RF for the glassy carbon electrode and the printed GDL electrode following the procedure described above.

Table V-1 – Summary of the geometric area (A_{geo}), calculated ECSA, and surface roughness factor (RF) for the studied electrodes.

Electrode	A_{geo} (cm^2)	$ECSA_{ano}$ (cm^2)	RF (%)
Glassy carbon	0.071	0.107	151.8
Printed GDL electrode	4	1.792	49.7

For the analysis performed, only the anodic peak was considered. The calculated ECSA for the glassy carbon of 0.107 cm^2 represents a RF of 152 %, however, the Sunchemical SPE's ECSA represented only 50 % of its geometrical area.

The ECSA determination studies performed were not conclusive and, therefore, the calculated ECSA will not be used for further analysis.

V.2.4. ELECTROCHEMICAL CHARACTERIZATION OF BARE AND MODIFIED SPEs FOR HYDROGEN EVOLUTION REACTION

After assessing the electrical and electrochemical key characteristics of the screen-printed layers of the printed GDL electrode and selecting the Sunchemical ink as the best ink for the electrochemical studies, the investigation of design rules for preparing printed gas diffusion electrodes was performed. Since this thesis is focused on the development of electrodes for hydrogen evolution reaction (HER), an ink of Pt/C, a benchmark catalyst for HER[20], was spray-coated on the surface of the screen-printed GDL as the final step of the preparation methodology described in the previous section.

To investigate the printed GDL electrodes, the following scientific questions were addressed:

- How do parameters such as pH and temperature of the reactant limit or enhance the performance of printed GDL electrodes?
- What is the role of the pattern and catalyst load in printed GDL electrode's current density in electrochemical experiments?
- What other parameters may affect the performance of printed GDL electrodes?

In each experiment, the printed GDL electrode used was "as prepared", *i.e.*, the electrode was not submitted to any electrochemical study before. The studies in this section were performed in a three-electrode cell configuration (Figure V-18) with Ag/AgCl (3 M KCl) reference electrode (RE) and Pt sheet electrode as the counter electrode (CE).
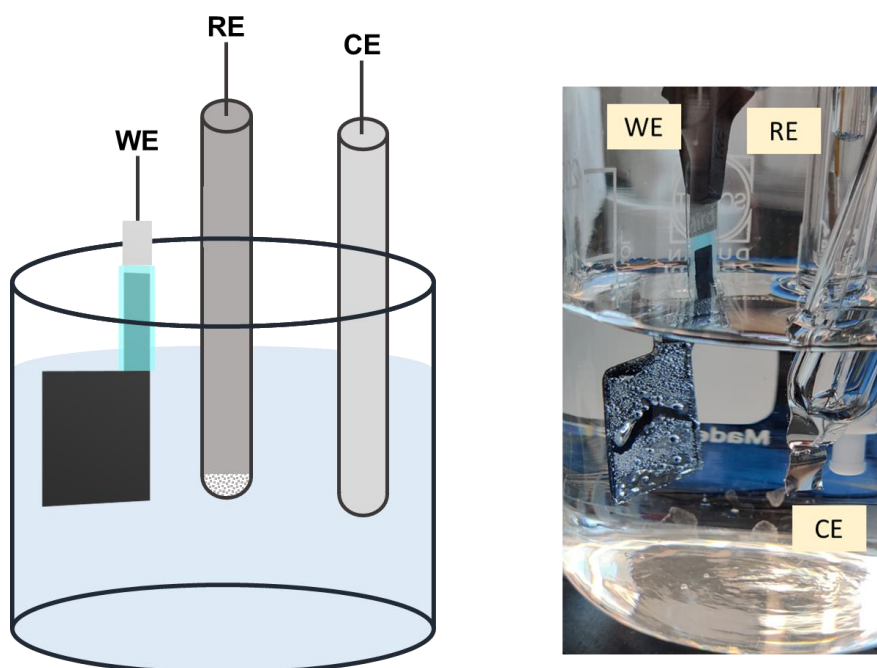
Figure V-18 – Three electrode cell configuration containing a screen-printed GDL electrode as working electrode (WE), Ag/AgCl (3 M KCl) reference electrode (RE), and Pt sheet electrode as the counter electrode (CE): schematic representation **(left)** and setup picture **(right)**.

The measured potentials vs Ag/AgCl were converted to a reversible hydrogen electrode (RHE) following Equation V-12:

$$E_{RHE} = E_{Ag/AgCl} + 0.059 pH + E^0_{Ag/AgCl} \qquad \textbf{Equation V-12}$$

Where E_{RHE} is the converted potential vs RHE, $E^0_{Ag/AgCl}$ = 0.1976 (at 25 °C), and $E_{Ag/AgCl}$ is the potential measured in the experiment against Ag/AgCl reference.[21–23]

In this work, the current density is calculated by dividing the experimental current measured by the geometric area of the electrode's working area. The current density was evaluated to compare the performance of the electrodes. Since the measurements were performed at negative applied potentials to simulate HER conditions, the measured current densities were, therefore, negative. From now on, we consider more negative current density as "higher current density". Moreover, we considered "higher current density" as "better performance".

V.2.4.1. ROLE OF CATALYST LOADING IN PRINTED GDL CATHODE PERFORMANCE

One of the parameters that may influence the performance (current density) of the device is the catalyst load.[24] In this work, printed GDL electrodes (GDL design B) were modified by ultrasonic spray coating a Pt-based ink on their surface, since Pt is the benchmark HER catalyst, as described in CHAPTER I:.[25] To study the influence of catalyst load on the performance (produced current density) of the electrode, the amount of Pt cast onto the printed GDL electrodes was varied. Changing the number of passes the spraying nozzle on top of the printed GDL electrodes, *i.e.,*

depositing a different number of layers, the catalyst load was changed as confirmed by the gravimetric method.[26] To ensure the reproducibility of this casting method, the printed GDL electrodes were prepared in a single run of the CNC system with a modified path to produce modified printed GDL electrodes with 2-18 layers of deposited Pt. Table V-2 summarizes the produced modified printed GDL electrodes by the number of layers and respective Pt load.

Table V-2 – Catalyst load influence in produced current density on printed GDL electrodes (type B) at -2.0 V (vs Ag/AgCl) in PBS (pH 7) at RT.

Number of layers	Pt load (mg/cm^2)	$J_{t=0\ min}$ (mA/cm^2)	$J_{t=30\ min}$ (mA/cm^2)
-	0	-1.54	-1.65
2	0.062	-3.33	-3.32
4	0.110	-3.31	-3.26
5	0.243	-3.57	-3.54
8	0.285	-3.71	-3.69
10	0.374	-3.64	-3.62
12	0.450	-3.43	-3.49
14	0.533	-3.83	-3.81
16	0.631	-3.63	-3.59
18	0.682	-3.72	-3.69

The modified printed GDL electrodes were characterized by SEM and energy dispersive spectroscopy EDS and compared against bare (non-modified) printed GDL electrodes. The cross-sectional images of both electrodes are presented in Figure V-19 a) and b).
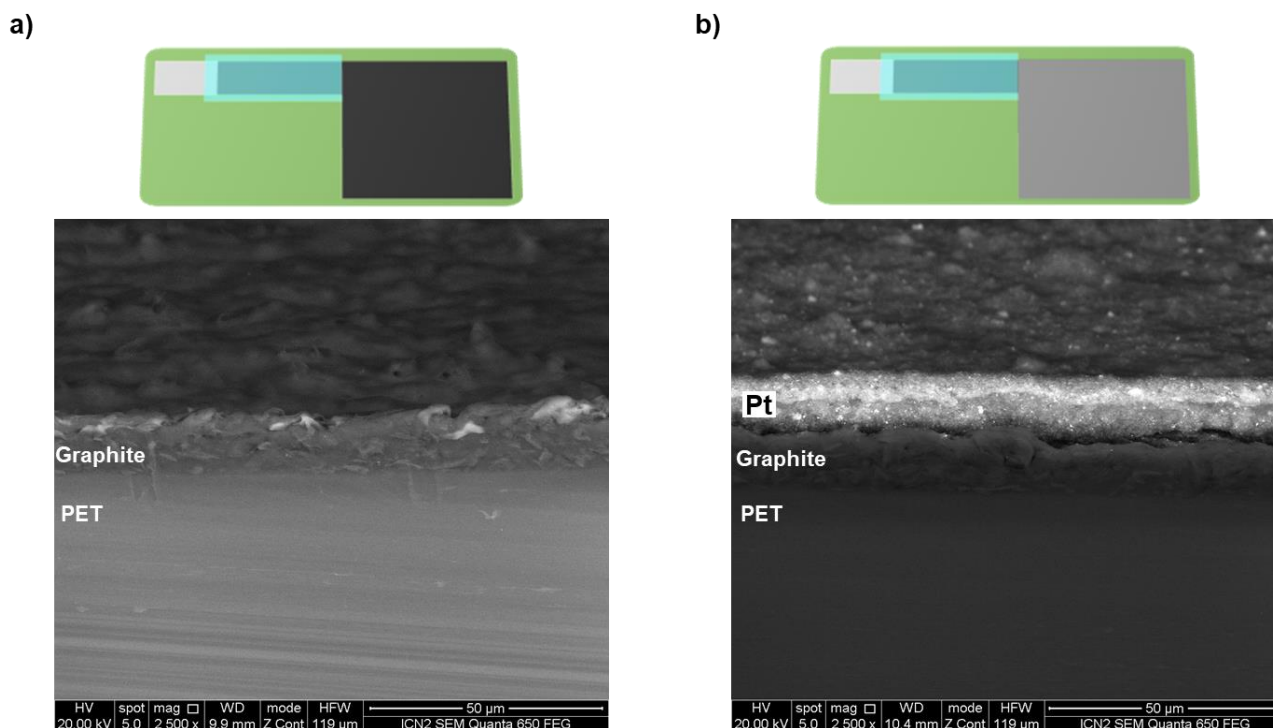
Figure V-19 - Cross-sectional SEM images of **a)** bare printed GDL electrodes with type B design and **b)** Pt-coated (0.17 mg/cm^2) SPE.

In both cases, the graphite layer appears as an 11-14 μm thick layer deposited on top of the PET film. In Figure V-19 b) the spray-coated Pt catalyst layer is observed with a thickness range from 11 to 13 μm.

The SEM-EDS analysis performed on bare and Pt-coated printed GDL electrodes is summarized in Table V-3.

Table V-3 – Atomic percentage of the detected elements through SEM-EDS on a bare printed GDL electrode and Pt-coated printed GDL electrode.

Element	Atomic %	
	Bare electrode	**Pt-coated - electrode**
C	91.9	50.1
O	8.1	4.5
F	-	42.9
Pt	-	1.1
Na	-	0.8
S	-	0.6

The presence of F, O, and S in Pt-coated printed GDL electrodes is directly attributed to the presence of these elements in Nafion, part of the Pt ink formulation, and composition. As expected, the presence of Pt was only detected at the Pt-coated printed GDL electrodes. Regarding the bare printed GDL electrodes, only C and O were detected and attributed to graphite content and other compounds that may be present in this commercial ink such as the binder and other additives. In the case of Pt-coated printed GDL electrodes, the C detected may come not only from Nafion composition but also from the graphitized carbon, the support of Pt. Na was also detected in the case of Pt-coated printed GDL electrodes, this is attributed to the fact that the electrode submitted to analysis was previously exposed to a Na-rich environment (PBS). Although it was thoroughly washed after the exposure, residual Na may have been retained in the printed GDL electrodes. The elemental mapping of the Pt-coated printed GDL electrode (Figure V-20) validated the established deposition method for the homogeneous distribution of Pt electrocatalyst along the surface.
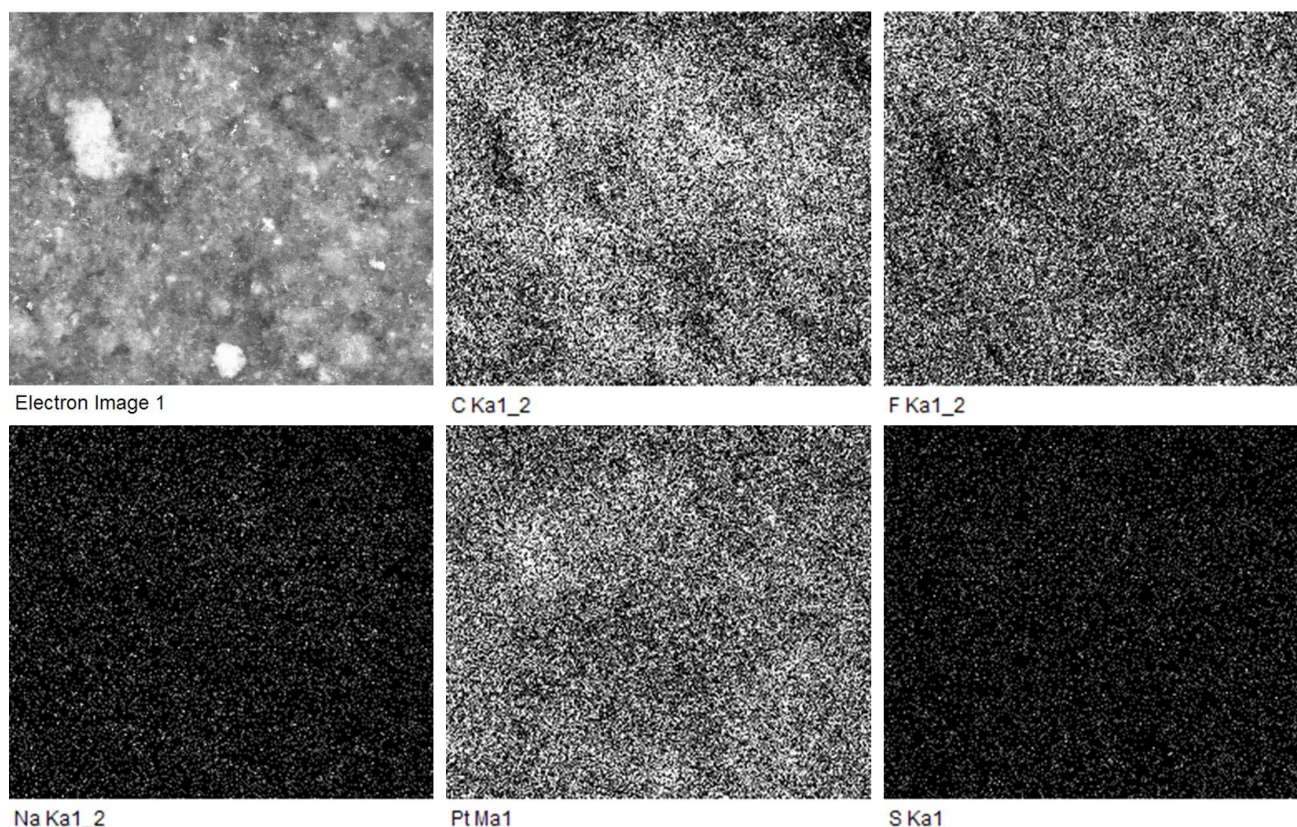
Figure V-20 – SEM-EDS elemental mapping of Pt-coated (0.17 mg/cm^2) printed GDL electrode.

To study the electrochemical response, the printed GDL electrodes were submitted to a polarization curve with applied potentials between -1 and -2.1 v (vs Ag/AgCl) followed by 30 min CA at -2.0 V (vs Ag/AgCl) applied to observe the current density related to each catalyst load. The current density vs time curves obtained are represented in Figure V-21 a).
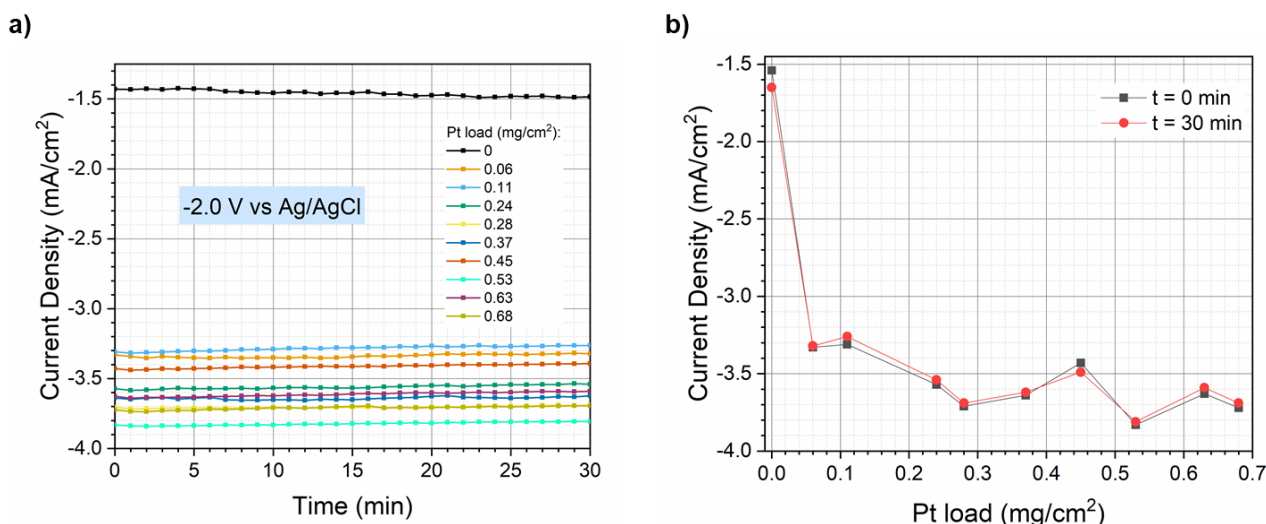
Figure V-21 – a) 30 min CA at -2.0 V (vs Ag/AgCl) performed at room temperature (RT, 23 °C) in PBS (pH 7) for printed GDL electrodes (GDL type B) modified with Pt. **b)** current density registered during the chronoamperometry experiments at t = 0 and 30 min versus the Pt load of printed GDL electrodes.

It was expected that a higher catalyst load would be translated into higher current density due to the increased number of active Pt sites for the HER, however, this was not observed in these experiments. It was observed that the highest current density, -3.83 mA/cm^2, was given by the electrode loaded with 0.53 mg/cm^2 Pt, while the current density produced by the electrode with the highest Pt load, 0.77 mg/cm^2, was -3.72 mA/cm^2. Moreover, the electrode with the lowest Pt load, 0.06 mg/cm^2, did not produce the lowest current density. When the current density is plotted against the Pt load of the modified printed GDL electrodes, as in Figure V-21 b), a trend may be observed. It suggests that the increase of catalyst load may lead to the production of higher current densities (more negative).

To understand thoroughly the role of catalyst load in the printed electrode, it is important to consider the formulation of the Pt ink used. The ink formulation leads to a dry solid content of 55 wt% of Nafion, 27 wt% of graphitized carbon (Pt support), and only 18 wt% Pt. Although the presence of Nafion brings the binding properties required for the adhesion of Pt to the printed GDL electrodes, the performance of the electrode may also benefit from the proton-conducting properties of Nafion. It may provide a continuous path for the protons to easily arrive at the Pt where they meet the electrons and get reduced to H$_2$. Considering that Nafion has poor electron conductivity, high Nafion content in the catalyst layers acts as a dielectric barrier hindering the electron percolation through the platinum particles as illustrated in Figure V-22.
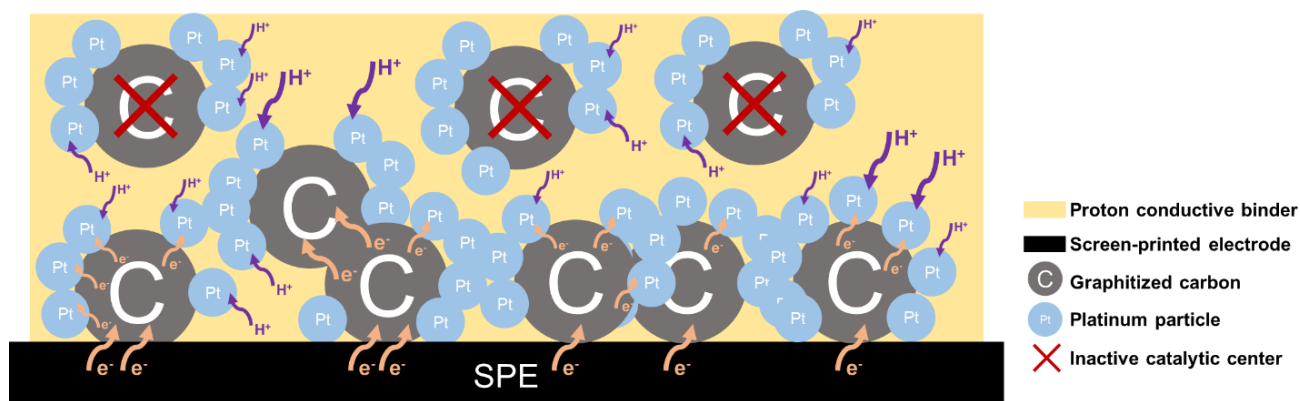
Figure V-22 – Cross-sectional illustration of proton and electron transport paths on a Pt-coated printed GDL electrodes. In the case of the present thesis, the proton conductive binder used was Nafion.

Thus, thicker layers of catalyst ink showed reduced current density, meaning that the performance of the electrode is compromised since the goal is to have electrodes with the highest current density possible.[27] This limitation may be improved by investigating different ratios of Pt and Nafion materials in the ink formulation and identifying the best compromise between Nafion and Pt content.[28,29] Nevertheless the system here developed was satisfactory to proceed to the next steps and no ink optimization study was performed.

Since no significant increase in terms of current density was observed as the catalyst load increased, the Pt catalyst loading to be used in the next sections was set at 0.2 mg/cm^2. Therefore, the number of layers of sprayed catalyst ink was fixed at 5 (see Table V-2) when preparing the Pt-

loaded electrodes for the next tests. Although the typical cathode catalyst loading for PEM water electrolysis is kept at $0.5 - 1$ mg/cm^2, we found that 0.2 mg/cm^2 is better aligned with the future perspectives and strategies in PEM water electrolysis, hence aiming for a more cost-effective approach.[30]

V.2.4.2. ROLE OF PH IN PRINTED GDL ELECTRODES' PERFORMANCE AND STABILITY

To investigate what are the parameters limiting and enhancing the performance of printed GDL electrodes, the electrodes were tested under different pH values from 2 to 9. This study was performed with printed GDL electrodes with a type B design (see Figure V-23), with and without catalyst load.

Figure V-23 – Printed GDL electrode with type B design used in the present section.

The samples without catalyst were noted as "bare", while the samples with catalyst were noted as "Pt" referring to the catalyst used. The Pt-loaded electrodes were prepared by spraying five layers of the catalyst ink, as defined in the previous section.

The stability of the printed GDL electrodes against pH was tested in 0.1 M phosphate-buffered (PBS) at pH 7 and 9 (see section V.9.4 for the experimental protocol) and pure distilled H_2O. To prepare pH 2 and pH 4 reactants, 0.1M H_2SO_4 was added to PBS. The characterization protocol consisted of a polarization curve with applied potentials between -1 and -2.1 v (vs Ag/AgCl) followed by 30 min chronoamperometry (CA) at -1.6 and -2.0 V (vs Ag/AgCl) applied. Figure V-24 a) presents the polarization curves of bare printed GDL electrodes, demonstrating that for any potential applied, a higher current density was obtained as pH was decreased.
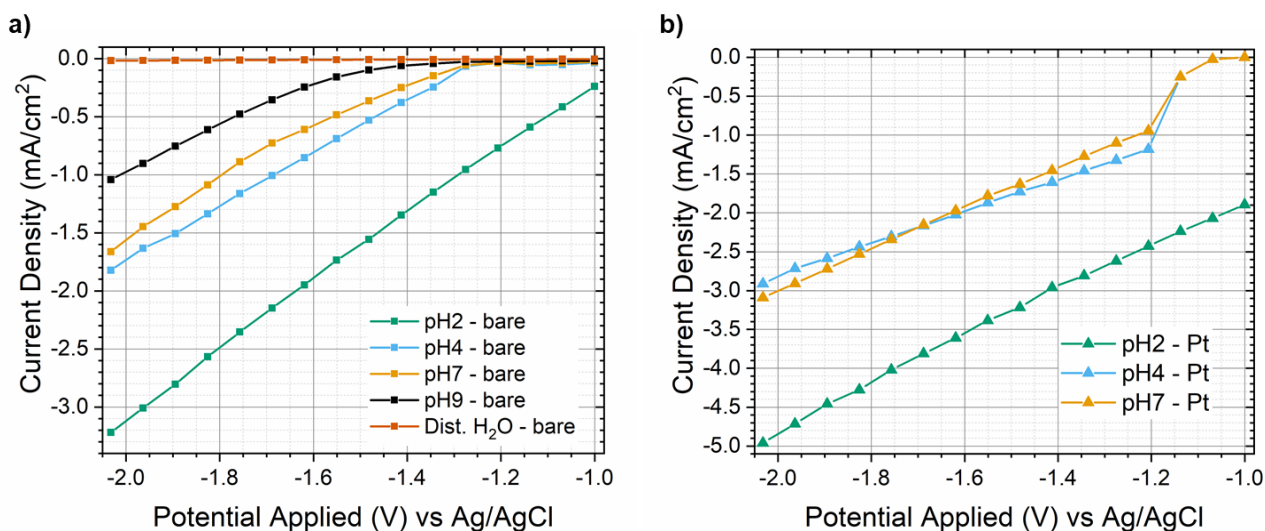
Figure V-24 – Polarization curves obtained in different pH for bare **(a)** and Pt-loaded **(b)** SPEs. Experiments were performed at room temperature (RT ≈ 23 °C).

The performance of the bare printed GDL electrodes in distilled H_2O was negligible due to the poor ionic conductivity of this reactant. In the case of the Pt-loaded printed GDL electrodes (Figure V-24 b)), the polarization curves in pH 7 and 4 overlap, hence, suggesting that the printed GDL electrodes present similar performance in these conditions. However, at pH 2, the Pt-loaded printed GDL electrode demonstrated a higher current density than pH 4 and 7.

Figure V-25 is supported by Table V-4 and summarizes the measured current density after 30 min CA ($J_{t=30\ min}$) for bare and Pt-loaded printed GDL electrodes.
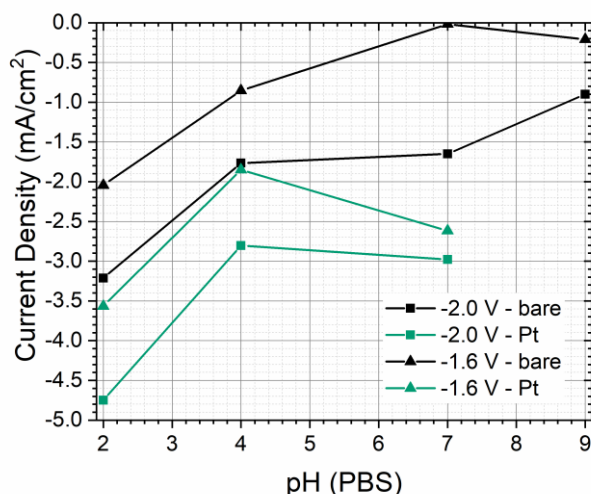
Figure V-25 – Current density measured after 30 min ($J_{t=30}$) CA vs pH. Experiments were performed at room temperature (RT ≈ 23 °C).

It was observed that bare printed GDL electrodes may tend to have improved performance, in terms of J, with decreasing pH. However, the same behavior was not observed for Pt-loaded printed GDL electrodes, since the performance worsened from pH 7 to 4, before a significant improvement at pH 2. The achieved current density was improved by the presence of Pt catalyst, at any pH and potential

applied. In particular, the improvement registered ($\Delta J_{t=30\ min}$) at pH 4 (-1.6 v (vs Ag/AgCl) applied) was higher than 100 %, *i.e.*, double than J measured for the respective bare SPE.

Table V-4 – Comparison of $J_{t=30\ min}$ between bare and Pt-loaded electrodes for each pH and potential applied at room temperature (RT ≈ 23 °C).

Reactant	pH	Potential applied (V vs Ag/AgCl)	$J_{t=30\ min}$ bare (mA/cm^2)	Pt load (mg/cm^2)	$J_{t=30\ min}$ Pt (mA/cm^2)	$\Delta J_{t=30\ min}$ (mA/cm^2)	$\Delta J_{t=30\ min}$ (%)
PBS+H$_2$SO$_4$	2	-1.6	-2.04	0.15	-3.56	-1.52	+74.5
PBS+H$_2$SO$_4$	2	-2.0	-3.21	0.17	-4.75	-1.54	+48.0
PBS+H$_2$SO$_4$	4	-1.6	-0.85	0.16	-1.85	-1.00	+117.6
PBS+H$_2$SO$_4$	4	-2.0	-1.77	0.12	-2.81	-1.04	+58.8
PBS	7	-1.6	-0.02	0.45	-2.62	-2.60	+13000
PBS	7	-2.0	-1.65	0.14	-2.98	-1.33	+80.6

The CA measurements at -1.6 and -2.0 V (vs Ag/AgCl) are presented in Figure V-26 a) and b), respectively.
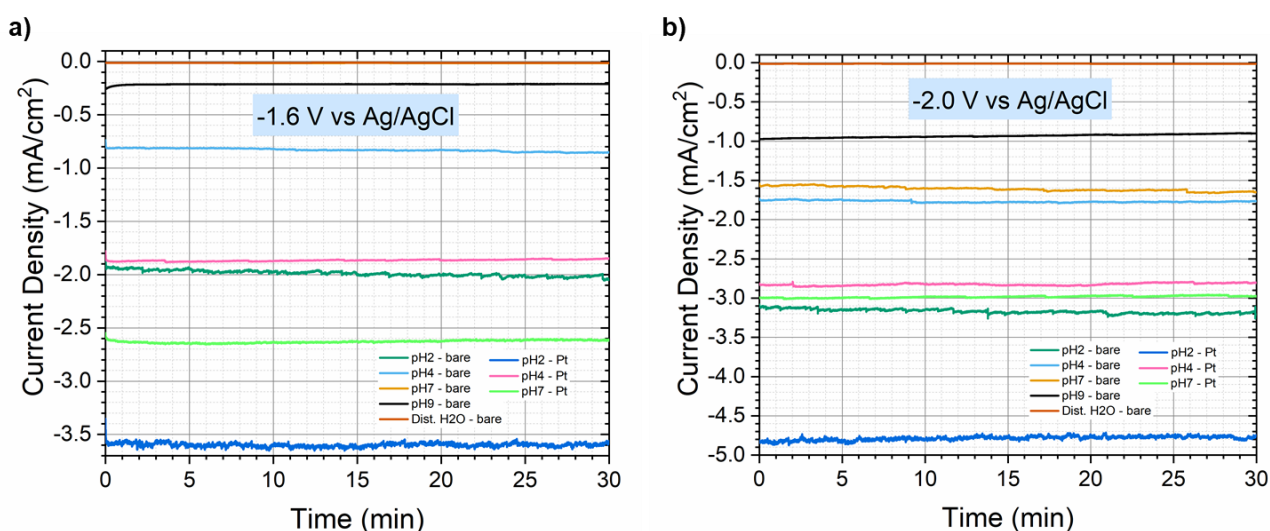
Figure V-26 – pH influence study on printed GDL electrodes: **a)** 30 min CA at -1.6 V (vs Ag/AgCl); **b)** 30 min CA at -1.6 V (vs Ag/AgCl). Experiments were performed at room temperature (RT ≈ 23 °C).

At -1.6 V (vs Ag/AgCl) the highest current density (J) was registered for Pt-loaded printed GDL electrode (0.15 mg/cm^2) in pH 2 reactant after 30 min CA ($J_{t=30\ min}$): -3.56 mA/cm^2. The highest $J_{t=30min}$ for bare electrodes at -1.6 V (vs Ag/AgCl), -2.04 mA/cm^2, was achieved at the same pH conditions. This value was, in fact, higher than the one registered for the Pt-loaded (0.16 mg/cm^2) printed GDL electrode at pH 4, which may suggest that the performance of the printed GDL electrode might be improved by decreasing the pH level of the working system, without requiring the addition of a catalyst. At -2.0 V (vs Ag/AgCl) a similar behavior was observed since the highest $J_{t=30}$ was again measured with Pt-loaded (0.14 mg/cm^2) printed GDL electrode, -4.75 mA/cm^2. This time, the second-highest performance was registered for a bare printed GDL electrode also at pH 2, $J_{t=30\ min}$=-3.21

mA/cm^2. As expected, due to the low ionic conductivity of the reactant, the worst-performing printed GDL electrodes were observed in distilled H$_2$O.

The stability of printed GDL electrodes was addressed by the variation (ΔJ) between J$_{t=0\ min}$ and J$_{t=30\ min}$ and the results are reported in Table V-15 (see section V.11 Appendixes). In this work, we consider as "not stable" the electrodes with ΔJ$\leq$-10 %. This scenario was only observed for the test with a bare printed GDL electrode in pH 9 at -1.6 V (Ag/AgCl), which registered ΔJ= -12.5 %. In the case of ΔJ$\geq$ 0 %, the electrodes were considered to have improved their performance during the 30 min CA. The best J improvement was registered for a bare printed GDL electrode in pH 4 at -1.6 V (Ag/AgCl) with ΔJ= +14.9 %.

The bare-printed GDL electrodes were considered to be stable at pH levels below 7. To meet the specifications defined within the eSCALED Project for the water electrolyzer demonstrator, the electrodes were further tested at pH 7.

V.2.4.3. ROLE OF TEMPERATURE IN PRINTED GDL ELECTRODES' PERFORMANCE AND STABILITY

To address the performance and stability of the printed GDL electrodes (design B, see Figure V-23) against temperature the electrodes were tested at pH 7 (PBS) over a temperature range from room temperature (RT$\approx$ 23°C) to 80°C. The Pt-loaded electrodes were prepared as defined in section V.2.4.1 of this chapter, *i.e.*, 5 layers of the catalyst ink were sprayed. The CA measurement was performed for a single potential applied, -2.0 V (vs Ag/AgCl). Figure V-27 a) presents the CA measurements for the different temperatures.
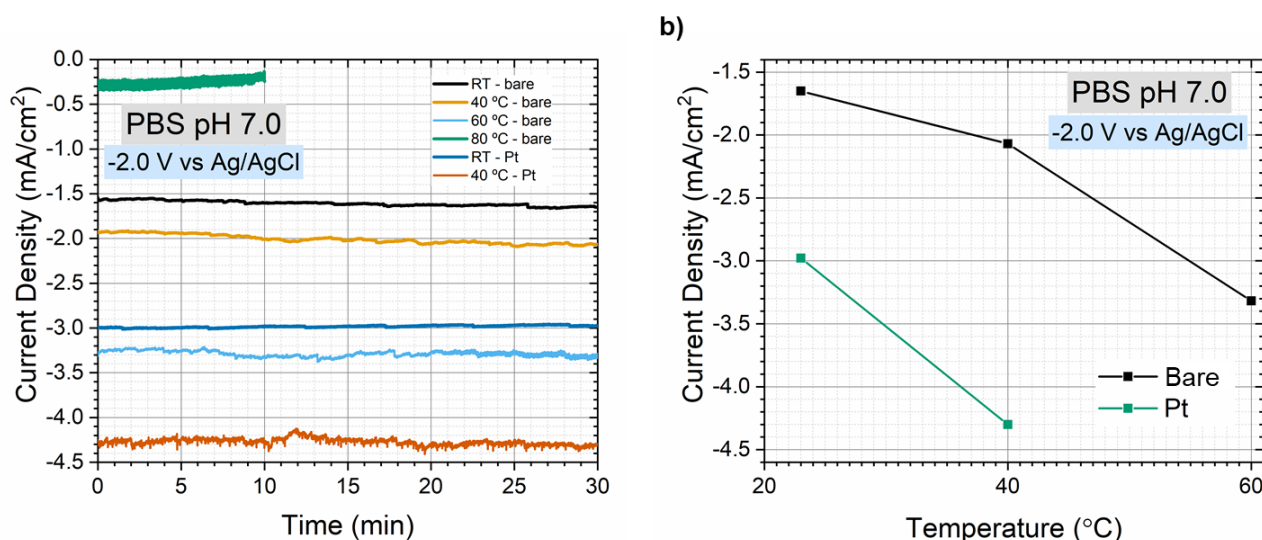
Figure V-27 – Temperature study performed in 0.1 M PBS pH 7. **a)** 30 min CA at -2.0 V (vs Ag/AgCl) performed at room temperature (RT, 23 °C); 40; 60 and 80 °C. **b)** Summary of J$_{t=30\ min}$ at -2.0 V (vs Ag/AgCl) for bare and Pt-loaded printed GDL electrode at different temperatures.

In this figure, it is observed that the measurement for a bare printed GDL electrode at 80 °C was shorter due to the destruction of the printed GDL electrode's connection to the potentiostat.

Therefore, the studies at 80 °C were not repeated for Pt-loaded printed GDL electrodes. It was observed that temperature may influence printed GDL electrode's activity with a tendency of J improvement, *i.e.*, higher temperature leads to more negative J, as illustrated in Figure V-27 b). According to Table V-5, the electrodes are stable from RT to 60 °C with ΔJ>-10 % in the whole temperature range. Although ΔJ may indicate that printed GDL electrodes are "stable", the analysis of this parameter only evaluates stability in terms of their electrochemical response and does not consider the mechanical, physical, and chemical stability.

Table V-5 - Current density variation in CA measurements at room temperature (RT); 40; 60 and 80 °C. Pt-loaded printed GDL electrodes tested at RT and 40 °C had a catalyst load of 0.14 and 0.17 mg cm^{-2}, respectively. Experiments were performed in PBS (pH 7).

Electrode	Temperature (° C)	$J_{t=0 \text{ min}}$ (mA/cm^2)	$J_{t=30 \text{ min}}$ (mA/cm^2)	ΔJ (mA/cm^2)	ΔJ (%)
Bare	RT	-1.54	-1.65	-0.11	+7.14
Pt	RT	-2.99	-2.98	+0.01	-0.33
Bare	40	-1.92	-2.07	-0.15	+7.81
Pt	40	-4.25	-4.30	-0.05	+1.18
Bare	60	-3.30	-3.32	-0.02	+0.61
Bare	80	-0.28	*	-	-

*Electrode destroyed before the end of CA

Figure V-28(III and IV) presents photographs of the bare printed GDL electrode tested at 80 °C and it is possible to verify that the connection between the printed GDL electrode's working and the silver connector was destroyed during the electrochemical testing.
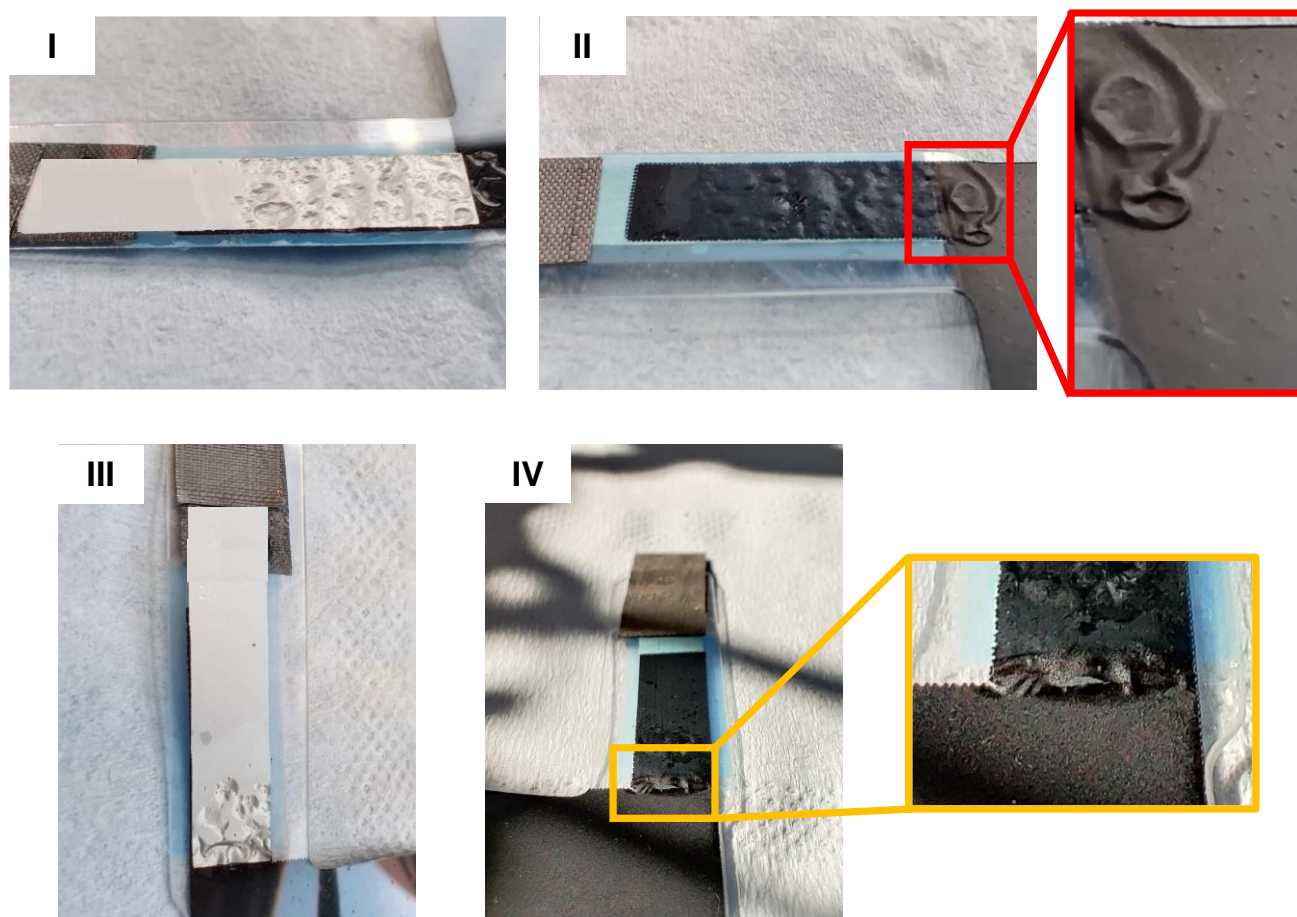
Figure V-28 – Damaged printed GDL electrodes after being submitted to CA at -2.0 V (vs Ag/AgCl) in PBS pH 7 at 60 (**I** and **II**) and 80 °C (**III** and **IV**).

A similar phenomenon was observed after testing a bare printed GDL electrode at 60 °C (Figure V-28 I and II). In the last case the connection was not destroyed, but only partially damaged. In both cases, a simple visual inspection of the printed GDL electrodes suggested that the damages were caused by the delamination of the printed films from the PET substrate. However, different factors may have affected the mechanical stability of the printed films at 60 and 80 °C. Hence, the damages may be explained as a result of different events that might have occurred simultaneously or in different stages of the electrochemical testing and contributed together. The suggested events were:

   1.   Thermal expansion of the substrate causes delamination between the printed films and the substrate. PET has its glass transition temperature (T_g) between 67 and 88 °C (depending on its crystallinity), however, because of its high melting point (255 °C), it is expected to retain its good mechanical properties until 175 °C. Previous studies reported that exposing PET to high temperatures such as 130 °C has an aging effect and decreases the T_g of PET. In our work, PET substrate was submitted to 130 °C and above several times during the fabrication of printed GDL electrodes.[31–33] Therefore, we considered the glass transition temperature of the PET substrate as a potential limiting factor in the stability of the printed GDL electrodes.

2.   Thermal expansion of printed films causes delamination between the printed films and the substrate. Depending on the binder that the commercial inks used contain in their formulation. Furthermore, this event may lead to an increase in the electrodes' surface area.

In both scenarios the thermal expansion of the layers may promote the wettability of the electrode, *i.e.*, the reactant can reach parts of the electrode that were previously not reached, increasing the number of reactional sites for the HER. The arrival of reactant to the substrate-printed film interface may lead to the production of H_2 at this interface. The gas produced in this region may not have a path to escape through the printed film. Finally, an overpressure in this region due to accumulated H_2 promotes further delamination of the printed GDL electrode from the substrate and/or the collapsing of the film.

In conclusion, it was observed that higher temperature favors the activity of the printed GDL electrodes but may limit their lifetime. The thermal properties, such as the glass transition temperature, of the supporting substrate and the printed films may affect the stability of the printed GDL electrode. The maximum working temperature for the printed GDL electrode on PET, in this work, is 40 °C. Further studies are required to extend the stability of the electrodes to a higher temperature. However, these electrodes were found to meet the requirements for the eSCALED Project prototype, since their stability at room temperature ($\approx 23°C$) was proven to be satisfactory.

V.2.5. ACTIVE LAYER AGEING

The electrodes' morphology was analyzed by scanning electron microscopy (SEM) in top view before and after potentials cycles applied from 0 to -2.1 V at different scan rates (5 – 100 mV/s) in PBS (pH 7) at 40 ºC in a total experimental duration of 2 h and 15 min. The SEM characterization of the printed GDL electrodes before and after electrochemical characterization is presented in Figure V-29 a) and b), respectively.
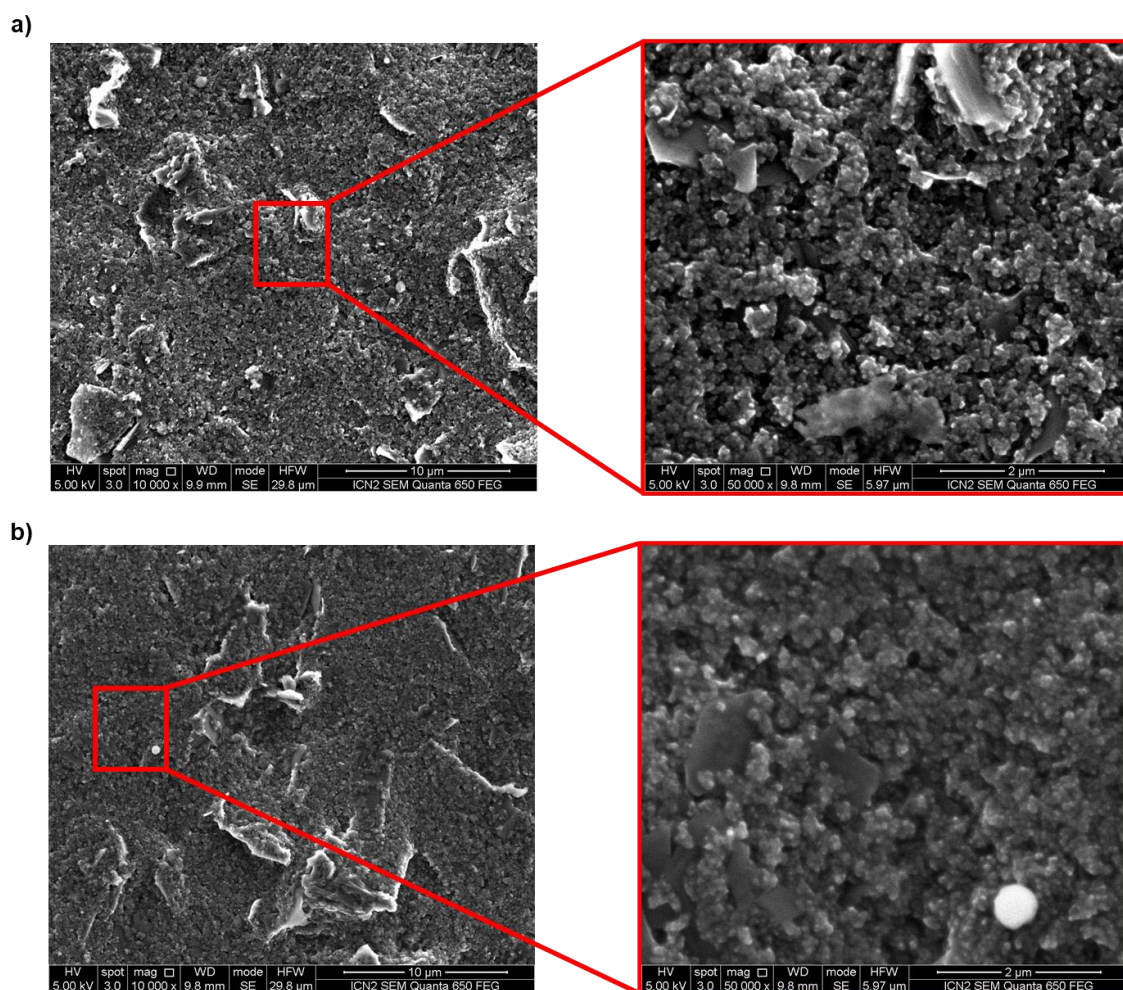
Figure V-29 - SEM images from the top view of bare printed GDL electrode **a)** before and **b)** after being submitted to electrochemical characterization (applied potentials between 0 and -2.1 V (vs Ag/AgCl) in PBS pH 7 at 40 ºC).

From the direct comparison of the images presented and respective insets at higher magnification, the analyzed electrodes present no significant differences that may be attributed to degradation caused by the electrochemical studies performed. The apparent surface roughness, as well as the apparent geometrical shape of the conductive filler of the ink used, are preserved, hence confirming the structural stability of the printed GDL electrodes to such experimental conditions.

Further studies are required to better understand the ageing mechanism and effects of the printed GDL electrodes. Techniques such as Time-of-Flight Secondary Ion Mass Spectrometry (ToF-SIMS), X-ray photoelectron spectroscopy (XPS), or SEM-EDS, provide information on the surface of the printed GDL electrodes may be insightful for this purpose.

V.3. ROLE OF GDL PATTERN DESIGN IN PRINTED GAS DIFFUSION ELECTRODES' PERFORMANCE

In this work, different designs were investigated for the printed electrodes. As presented in V.1 the GDL designs share the squared 2.0 x 2.0 cm^2 geometry but differ in their porosity. GDL with

design type B has no macropores and a total geometric working area of 4 cm^2. The printed GDL electrodes with GDL designs W and S present a total geometric working area of 3 cm^2. W and S designs differ in the shape of the macropores, squared windows, and rectangular slits, respectively. Within designs, W and S the number and size of pores vary, however, the sum of all pores' areas was set to be always equal to 1 cm^2.

As explained before, the open areas of the printed GDL were expected to facilitate the escape of the gaseous products from the electrode surface when integrated inside a flow cell.[34] Before this integration step, it was mandatory to investigate if the differences in the designs would be translated into significant losses in the electrochemical performance of the electrodes. In this study, the produced current density was used as the key parameter to evaluate the effect of the designs. The designs selected for this study are presented in Figure V-30. GDL designs W4; W6 and W7 were not the objects of this study due to the complexity of the pore opening process through laser cutting which frequently led to the loss of the electrode.
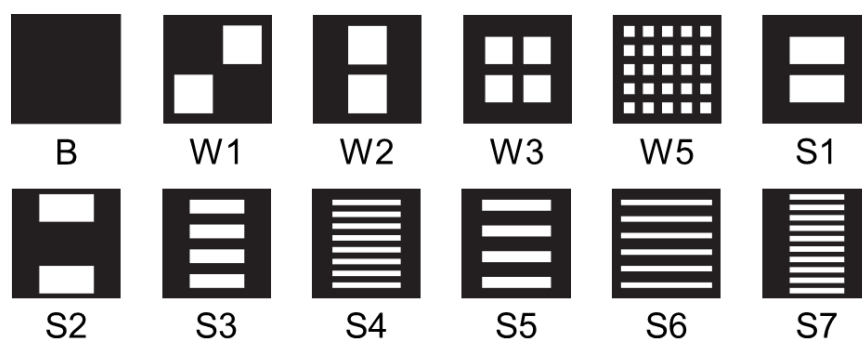
Figure V-30 – Selected printed GDL designs to study GDL's design influence on the electrochemical performance of the printed GDL electrodes.

The electrochemical study consisted of submitting the bare printed GDL electrode with different GDL designs to a polarization curve with applied potentials between -1 and -2.1 v (vs Ag/AgCl) followed by 30 min CA at -2.0 V (vs Ag/AgCl) applied. The studies were performed in PBS (pH 7) at room temperature (23 °C). The result of the CA measurements and displayed in Figure V-31.
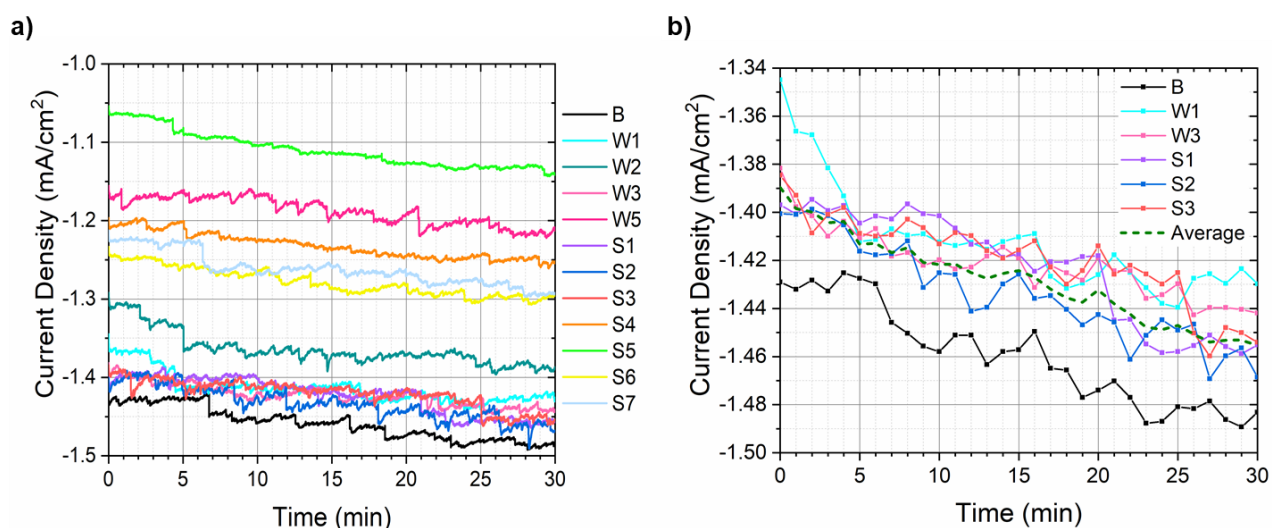
Figure V-31 – CA at -2.0 V (vs Ag/AgCl) performed on printed gas diffusion electrodes with different GDL designs. **a)** comparison of all the designs studied. **b)** simplified CA plot of designs B; W1; W3; S1; S3 and the calculated average current density.

A first analysis of the CA results in Figure V-31 a) suggests that the GDL designs S4; S5; S6; S7; W2 and W5 are strongly affected by their respective designs since these presented poorer performances, *i.e.*, less negative current densities produced when compared to B; W1; W3; S1; S2 and S3. In Figure V-31 b) it is observed that the GDL designs W1; W3; S1; S2 and S3 may follow a trend and give similar performances. The best performance was registered for design B; hence, one may conclude that the pores do not play the expected role of facilitating the escape of the gaseous products generated. However, these tests were performed in static reactant conditions, *i.e.*, there was no reactant flow induced by flow pumps or magnetic stirring. Given the previous observations, the designs S4; S5; S6; S7; W2, and W5 were abandoned here and were not integrated into a flow cell. The integration of GDL designs B; W1; W3; S1; S2 and S3 into such electrochemical devices are developed and discussed in section V.4.

GDL designs S4; S6; S7 and W5 have a high number of pores when compared to W1; W3; S1; S2 and S3. This simple comparison could suggest that the determining factor of the printed GDL electrodes' electrochemical performance is the number of macropores on the GDL (see Table V-6).

Table V-6 – Number of pores in the SPE design, initial (t=0 min) and final (t=30 min) current density (J) measured for each design tested.

Design	Number of pores	$J_{t=0\ min}$ (mA/cm^2)	$J_{t=30\ min}$ (mA/cm^2)
B	0	-1.43	-1.48
W1	2	-1.38	-1.43
W2	2	-1.29	-1.39
W3	4	-1.41	-1.44
W5	25	-1.16	-1.21
S1	2	-1.40	-1.46
S2	2	-1.40	-1.47
S3	4	-1.40	-1.45
S4	8	-1.20	-1.24

Design	Number of pores	$J_{t=0\,min}$ (mA/cm^2)	$J_{t=30\,min}$ (mA/cm^2)
S5	4	-1.05	-1.14
S6	6	-1.23	-1.30
S7	10	-1.21	-1.29

However, this argument immediately falls since design S5 was also discarded due to presenting the poorest performance of all. One may then conclude that the number of pores on the GDL may not be the determining factor of the printed gas diffusion electrode performance. Other parameters such as the distance between pores, the distance between pores and the edges of the electrode, the distance between the pores and the connector of the electrode, or the distribution of the pores along the electrode may influence its performance. These parameters may affect the resistance, charge distribution, and electric field at the surface of the electrode improving or reducing the performance of the SPE. Although this study may bring a deep understanding of how the mechanisms and parameters influence the SPE's behavior, the present work did not cover and explore these suggestions.

Given their higher electrochemical performance, GDL designs B, W1, W3, S1, S2, and S3 will be integrated into flow-cell and MEA devices in the following section for electrochemical characterization in PBS pH 7 at room temperature.

V.4. INTEGRATION OF PRINTED GAS DIFFUSION ELECTRODES INTO H$^+$ REDUCTION ELECTROCHEMICAL DEVICES

Previous reports in the literature stated the importance to analyze and study the catalysts for hydrogen evolution reaction (HER) in conventional three-electrode cell and electrolyzer cell setups, since the same material may perform differently depending on the testing configuration. Hence, it is possible to compare the performance in different configurations and understand if the object of study is a good candidate for further up-scaling and commercialization.[11,35–38] Accordingly, printed GDL electrodes were integrated into the H$^+$ reduction electrochemical devices, namely, H-cell (three-electrode cell), flow-cell (two-electrode electrolyzer cell), and membrane electrode assembly (MEA) (two-electrode electrolyzer cell) configurations.

V.4.1. THREE-ELECTRODE CONFIGURATION: H-CELL

Most of the studies in the literature are performed in three-electrode cells, such as the H-cell configuration, which is usually performed at room temperature, with a glassy carbon electrode as a working electrode and in potentiostatic mode.[35] This configuration is composed of two compartments, an anode, and a cathode, separated by an ion-exchange membrane which prevents the crossover of products from the HER and allows the use of different reactants in the anode and

cathode. Its simple configuration, assembly, and operation make this cell type the first choice for mechanistic studies. A porous fine ceramic frit may also be used to replace the membrane. The current density achieved is usually low and limited, but high product selectivity can be achieved, *i.e.,* high Faradaic efficiency.[39,40] Moreover, increasing the pressure in the H-cell electrolyzer may also increase the performance of the device.[11,41]

In this work, the activity of one bare and one Pt-loaded printed GDL electrode with B design was evaluated. A scheme of the electrochemical cell setup is presented in Figure V-32.
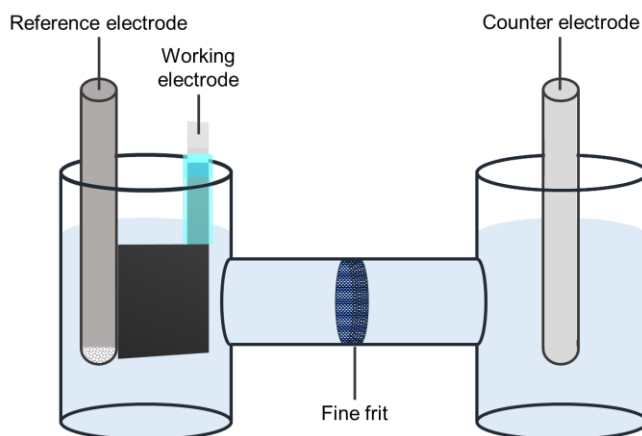
Figure V-32 – H-cell electrochemical setup including a printed gas diffusion electrode as the working electrode.

This study was performed to quantify the H_2 produced by the screen-printed electrode, bare and Pt-coated, in a controlled and steady-state environment, without the interference of other components that could affect the stability of the overall system, hence, adulterating the evaluation of the printed GDL electrodes.

The chronoamperometry experiments performed at -1.6 V (vs Ag/AgCl) are presented in Figure V-33 a).
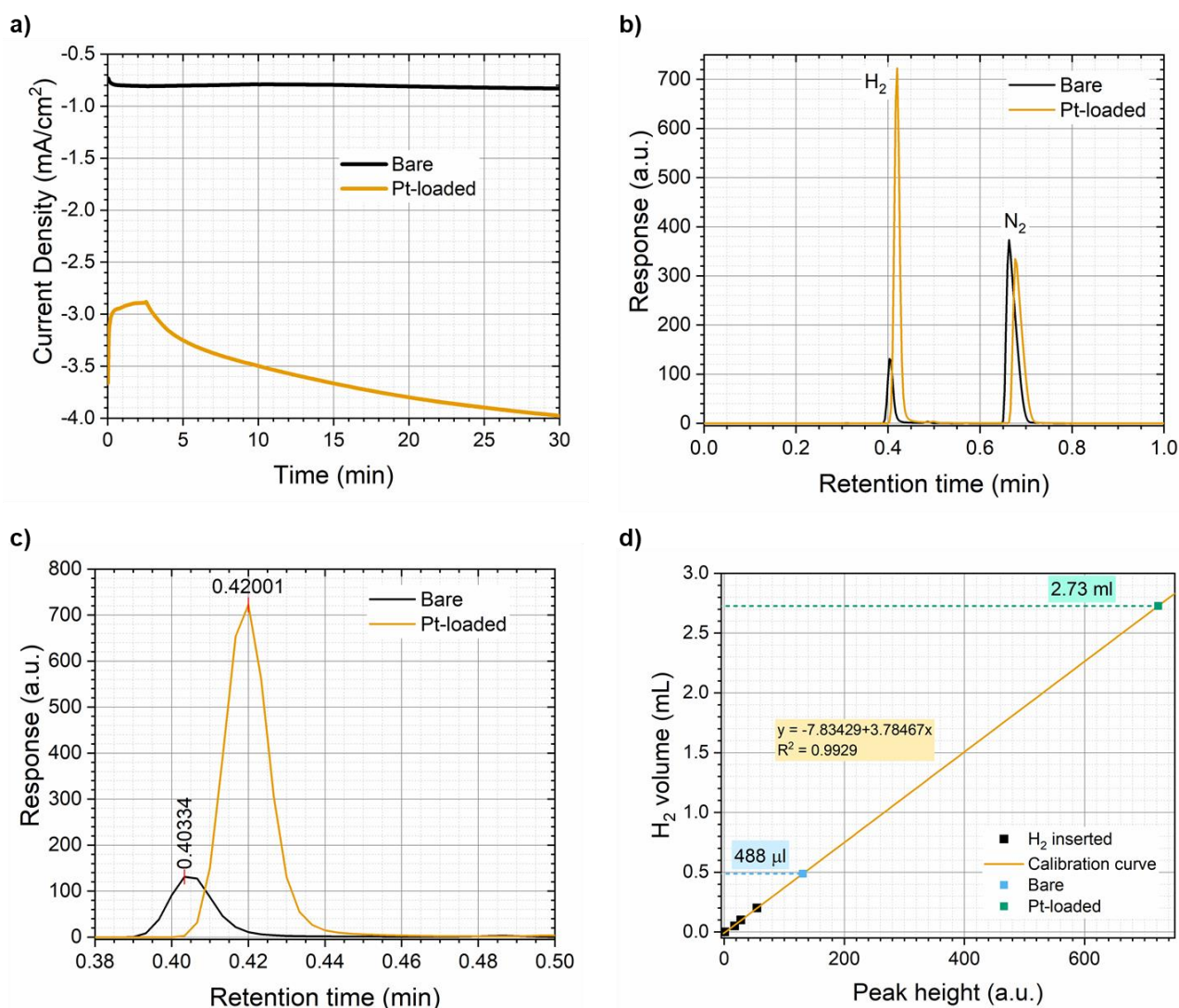
Figure V-33 – Electrochemical characterization of two printed GDL electrodes, one bare and on Pt loaded (0.24 mg/cm2) integrated and tested in H-cell configuration. **a)** CA experiments performed at -1.6 V (vs Ag/AgCl) in PBS (pH 7). **b)** and **c)** present the full and H_2 peaks in detail, respectively, gas chromatographs obtained for 50 µL gas samples extracted from the working electrode compartment of the H-cell after CA. **d)** presents the linear fit of the H_2 volume vs gas chromatogram peak height calibration performed and H_2 produced by the bare and Pt-loaded printed GDL electrodes.

As expected, the 0.24 mg/cm² Pt-loaded printed GDL electrode produced a higher current density, -3.98 mA/cm², while the bare SPE registered a maximum of -0.83 mA/cm². The chromatograms obtained for the gaseous samples collected after the CA of both electrodes are presented in Figure V-33 b). For both printed GDL electrodes, as demonstrated by Figure V-33 b), only two peaks were observed, *i.e.*, only two gaseous species were detected. The first peak was attributed to H_2 and the second to N_2, a product of the HER and the inert gas used to purge the H-cell compartments before the CA. The peaks attributed to H_2 are presented in detail in Figure V-33 c) where the intensity of the Pt-loaded printed GDL electrode signal is observed to be approximately six times higher than the signal obtained from the bare printed GDL electrode. Figure V-33 d) presents the calibration curve performed for the electrochemical setup studied and used to determine the volume of H_2 produced from applying -1.6 V (vs Ag/AgCl) for 30 min. As expected,

the Pt-loaded catalyst produced a higher volume of H_2, 2.73 mL, while the catalyst-free electrode, *i.e.*, the bare printed GDL electrode produced only 488 µL. The Faradaic efficiency (FE) of H_2 formation from the bare and Pt-loaded printed GDL electrodes was calculated from the total amount of charged, Q (C) passed through the cell during the CA and the total amount of H_2 produced $n(H_2)$ (mol). Since the proton reduction is a two electrons process, *i.e.*, two electrons are required to reduce two protons to produce one H_2 molecule, thus, Equation V-13 can be used to calculate the Faradaic Efficiency:

$$\text{Faradaic Eficciency} = \text{FE} = \frac{n(H_2)}{\left(\frac{Q}{2F}\right)} \qquad \textbf{Equation V-13}$$

where F is Faraday's constant[18]. The Q and $n(H_2)$ used to calculate FE for each electrode are presented in Table V-7.

Table V-7 – Total amount of charge (Q) passed through the cell during the 30 min CA (-1.6 V vs Ag/AgCl applied) experiments performed with bare and Pt-loaded printed GDL electrodes in H-cell configuration, amount (n) and volume (v) of H_2 produced as calculated from gas chromatography and respective Faradaic Efficiency.

Printed GDL electrode	Q (C)	$n(H_2)$ (mol)	$v(H_2)$ (mL)	Faradaic efficiency (%)
Bare	2.99	2.18×10^{-5}	0.488	141
Pt-loaded	14.32	1.22×10^{-4}	2.73	164

The bare and Pt-loaded printed GDL electrodes demonstrated a FE for H_2 formation of 141 and 164 %, respectively. However, the calibration curve may not be accurate since it led to a calculated FE above 100 %. Moreover, problems related to the manipulation; technique; sealing or syringe may have also contributed to inaccurate calibration. Given the lack of available time to perform this experiment, the calibration protocol was not repeated.

Printed GDL electrodes can be integrated into H-cell setups. Bare and Pt-loaded electrodes presented distinct performances in agreement with the results demonstrated in the preliminary studies performed in section V.2. Therefore, printed GDL electrodes are suitable catalyst support to characterize catalysts in H-cell configuration.

V.4.2. TWO ELECTRODE CONFIGURATIONS: FLOW-CELL AND MEA

The electrode designs selected to be used inside an electrolyzer cell through the studies described in section V.3 are presented in Figure V-34.

Figure V-34 – GDL designs integrated into flow-cell and MEA configurations.

Printed electrodes with GDLs B, W1, W3, S1, S2, and S3 were integrated into a 3D-printed electrolyzer cell as presented in the schemes in Figure V-35.
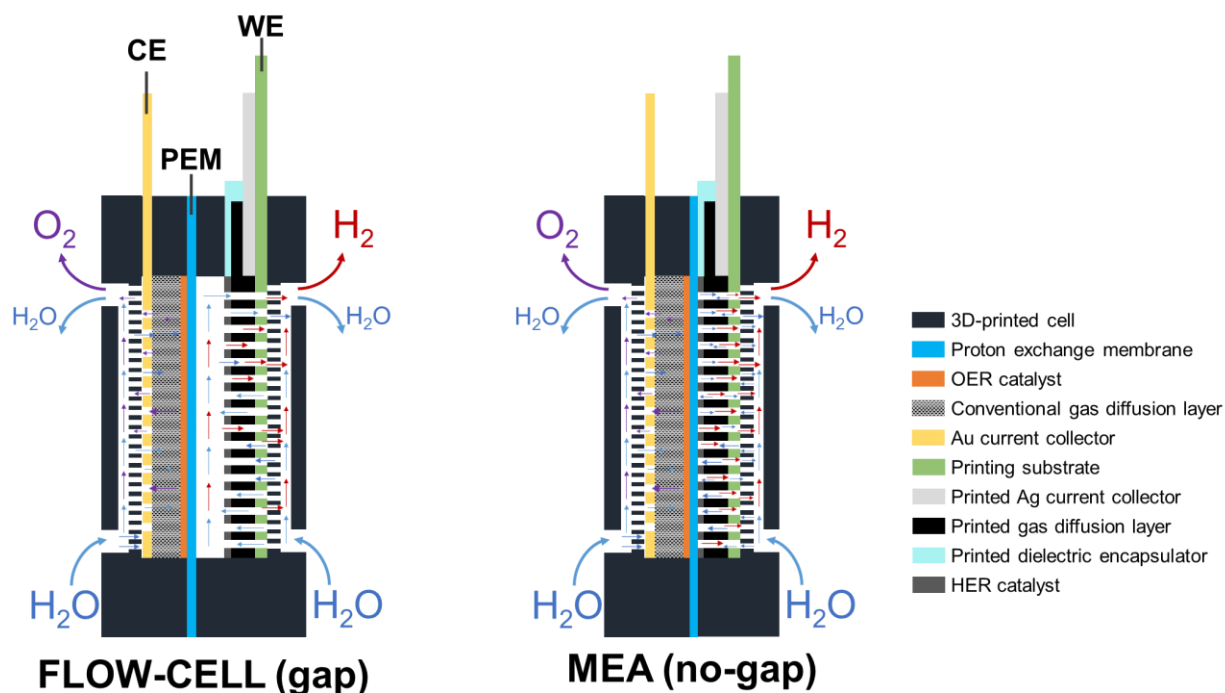
Figure V-35 – Cross-sectional schematic view of the flow-cell (gap) and membrane electrode assembly (MEA, no-gap) configurations with an integrated screen-printed electrode to host the HER studied inside a 3D-printed electrolyzer cell.

The difference between the two configurations, flow-cell and membrane electrode assembly (MEA) was that, on the latter, the Pt-loaded printed GDL electrode was thermally laminated by hot-press onto the proton exchange membrane (PEM), eliminating the gap between the HER catalyst layer and PEM. Furthermore, the "no gap" assembly of MEAs reduces the ohmic losses, hence decreasing the overall cell resistance which could then be translated to higher current density achieved.[42]

The acidic environment of PEMs favors the HER. However, the cathode flooding due to the accumulation of water may cause gradual degradation of the electrolyzer. This effect may be mitigated by increasing the hydrophobicity of the cathode using PTFE as a binder in the cathode catalyst layer.[43] Anion exchange membranes (AEMs) may also be used, replacing the PEM and allowing the transport of OH⁻ from the cathode to the anode but they usually present lower ionic conductivity than PEMs. This can be improved by supplying liquid reactants such as $KHCO_3$ or KOH to the anode. In this case, the higher the pH of the anolyte the lower the resistance of the cell, which favors the kinetics of the OER at the anode and results in lower cell potential and, thus, higher energy efficiency. However, alkaline reactants may threaten the mechanical stability of the solid polymer electrolyte membrane.[11] To overcome the membrane stability challenges due to a strongly alkaline environment at the anode and/or strong acidity at the cathode, bipolar solid polymer electrolyte membranes have been proposed.[44,45]

Due to the complexity of the experimental setup and lack of time to create such experimental conditions, the products of these experiments were not characterized by gas chromatography due so that the H_2 produced could be quantified. Nonetheless, the volume of H_2 produced was estimated using Faraday's law for electrolysis. According to this law, the weight of the products formed (m) at the electrode during the electrolysis experiment is proportional to the current (I) and is given by Equation V-14:

$$m = \frac{I \times t \times M}{n \times F} \qquad \textbf{Equation V-14}$$

where M is the molar mass of the produced compound, n is the number of electrons involved in the reaction (n=2 for HER), t is the time and, finally, F is the Faraday's constant.[46,47]

V.4.2.1. FLOW-CELL – GAP CONFIGURATION

The results obtained from the chronoamperometry experiments (-2.0 V vs Ag/AgCl potential applied) performed with the printed GDL electrodes integrated into the 3D-printed electrolyzer cell are
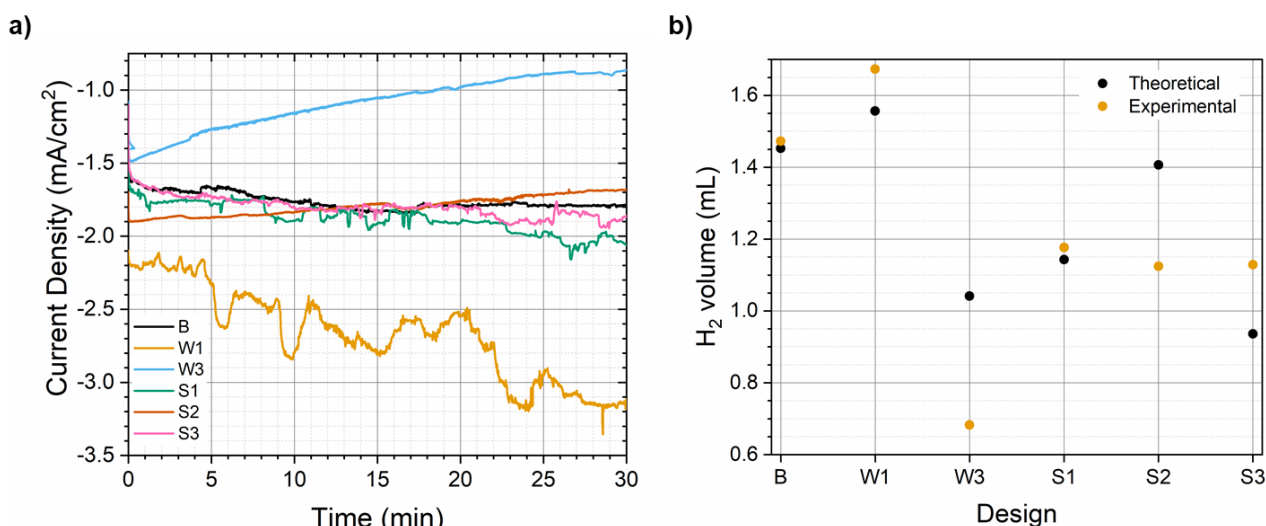
Figure V-36 – Electrochemical characterization of Pt-loaded printed GDL electrodes with different GDL designs (B, W1, W3, S1, S2, and S3) integrated into 3D-printed electrolyzer cell in flow-cell configuration. **a)** 30 min CA measurement with -2.0 V (vs Ag/AgCl) applied potential with PBS pH 7 at 25 °C. **b)** Theoretical (calculated from polarization curve current measured at -2.0 V vs Ag/AgCl) and experimental (calculated from CA experiment) volume of produced H_2 compared for each GDL design tested.

presented in Figure V-36 a). GDL design W1 stood out by achieving the highest current density registered in the present configuration, starting at -2.10 mA/cm^2 and increasing until -3.15 mA/cm^2 after 30 min. The detected drops in the measured current density along the experiment were attributed to the nucleation of H_2 nanobubbles blocking the electrode surface.[48] Contrarily, the worst performance was given by design W3, which presented the lowest initial (t=0 min) and final (t=30 min) current densities, -1.08 and -0.86 mA/cm^2. GDL designs B, S1, S2, and S3 did not present outstanding performances, having their respective current density at t=0 min and t=30 min narrowed

to -1.10−-1.70 and -1.69−-2.06 mA/cm^2 as shown in Table V-8. The calculated theoretical and experimental volume of H_2 produced by each design are compared in Figure V-36 b) and details are given in Table V-8. As expected, due to the proportionality between the current and the weight of the produced substance in Equation V-14, the highest production of H_2 was achieved by printed GDL electrode with GDL design W1 which produced 1.67 mL (V_{exp}). Surprisingly, the second highest $V_{exp}(H_2)$ was given by GDL design B, 1.47 mL. This result suggested that in this flow-cell configuration, the presence of the macro-pores did not always improve the production of H_2 by introducing turbulence in the reactant flow, subsequently, promoting the removal of H_2 from the surface of the electrode and recreating the solid-liquid interface between the electrode's surface and reactant, respectively, needed for the HER to take place.

Table V-8 – Current density (J) at t=0 min and t=30 min (t represents the elapsed time), theoretical (V_{th}), and experimental (V_{exp}) volume of H_2 produced for each GDL design tested in flow-cell configuration.

Design	$J_{t=0\ min}$ (mA/cm^2)	$J_{t=30\ min}$ (mA/cm^2)	$V_{th}(H_2)$ (mL)	$V_{exp}(H_2)$ (mL)
B	-1.52	-1.79	1.45	1.47
W1	-2.10	-3.15	1.56	1.67
W3	-1.08	-0.86	1.04	0.68
S1	-1.40	-2.06	1.14	1.18
S2	-1.70	-1.69	1.41	1.12
S3	-1.10	-1.86	0.94	1.13

Despite the poor performance of GDL designs W3, S1, S2, and S3, it was important to understand and justify the outstanding performance of design W1. In this case, it was observed that when integrated into the 3D-printed cell, the position of the macro-pores from the W1 design matched the position of the reactant inlet and the outlet for reactant and gaseous products of the cell as presented in Figure V-37.

3D-PRINTED CELL   W1 GDL overlapped
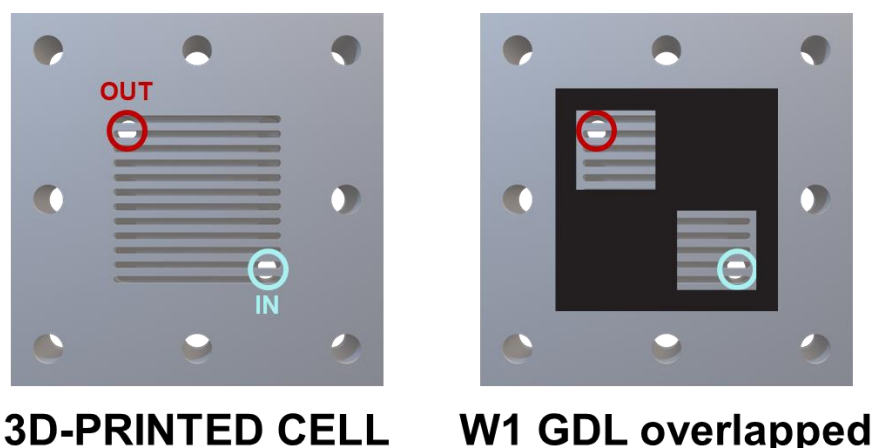
Figure V-37 – Perspective of the inner surface of the 3D-printed cell, the position of the reactant inlet (cyan) and reactant + products outlet (red), and overlapping of a printed GDL electrode with GDL design W1.

This was proposed to be one possible explanation for the superior performance demonstrated by GDL design W1, since the mentioned matching could facilitate the reactant circulation through the

printed GDL electrode and in front of the printed GDL electrode, *i.e.*, between its surface and the PEM, creating a unidirectional flow. However, more detailed, and fundamental studies would be needed to properly clarify the factors determining the performance of each design.[49]

V.4.2.2. MEMBRANE ELECTRODE ASSEMBLY – NO-GAP CONFIGURATION

The current density recorded in the chronoamperometry experiments performed with -2.0 V (vs Ag/AgCl) for the different printed GDL electrodes is presented in Figure V-38 a).
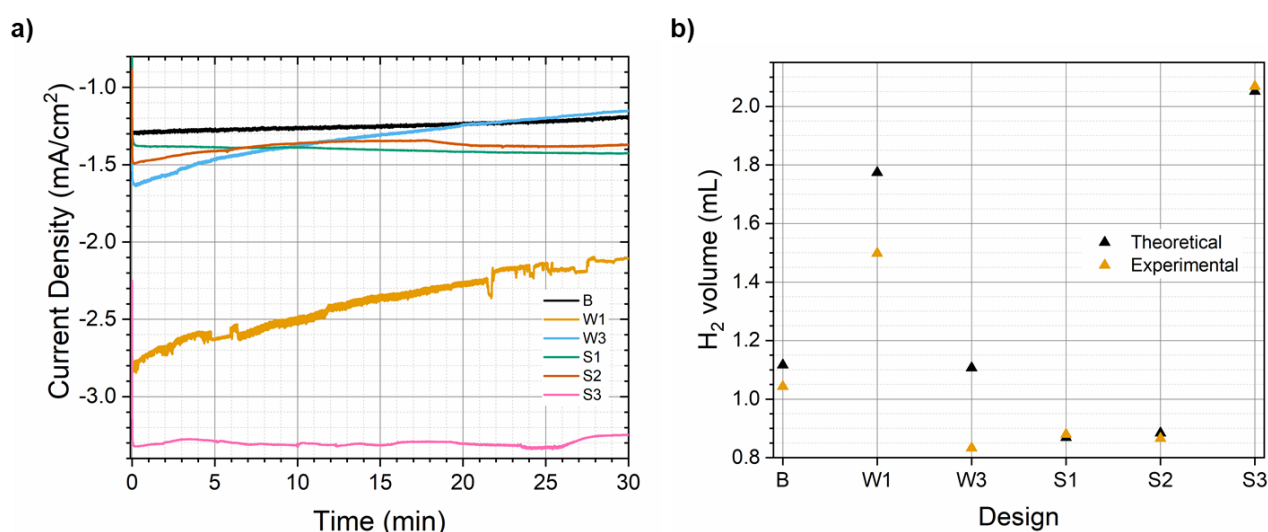
Figure V-38 – Electrochemical characterization of Pt-loaded printed GDL electrodes with different GDL designs (B, W1, W3, S1, S2, and S3) integrated into 3D-printed electrolyzer cell in MEA configuration. **a)** 30 min CA measurement with -2.0 V (vs Ag/AgCl) applied potential with PBS pH 7 at 25 °C. **b)** Theoretical and experimental produced H_2 volume values compared for each design tested.

As reported in the previous flow-cell configuration, design W1 presented the highest initial (t=0 min) current density, -2.62 mA/cm^2. However, after 30 min the current density decayed to -2.10 mA/cm^2. Yet, W1 did not present the highest current density registered in this MEA configuration. This time, the best performance was attributed to design W3 which presented an initial current density of -2.25 mA/cm^2 and increased to -3.25 mA/cm^2 after 30 min. From a visual analysis of Figure V-38 a) it is possible to observe that design W3, despite an increase in current density in the first minute of CA, presented a stable behavior having a short variation of current density between -3.2 and -3.4 mA/cm^2. The remainder of GDL designs, *i.e.*, designs B, W3, S1, and S2 presented lower current densities ranging from -0.79−-1.40 mA/cm^2 (t=0 min) to -1.15−-1.43 mA/cm^2.

Table V-9 presents the theoretical and experimental volumes of H_2 produced, calculated through Equation V-14, which were plotted together for each GDL design studied and are presented in Figure V-38 b). The highest V_{exp} was obtained for design W3, producing 2.07 mL of H_2, followed by W1 with only 1.50 mL of H_2. Furthermore, the electrodes with designs B, S1, and S3 registered an experimental volume of produced H_2 of 1.04, 0.88, and 0.87 mL, respectively.

Table V-9 – Current density (J) at t=0 min and t=30 min (t represents the elapsed time), theoretical (V_{th}), and experimental (V_{exp}) volume of H_2 produced for each GDL design tested in MEA configuration.

GDL Design	$J_{t=0\ min}$ (mA/cm^2)	$J_{t=30\ min}$ (mA/cm^2)	$V_{th}(H_2)$ (mL)	$V_{exp}(H_2)$ (mL)
B	-1.24	-1.20	1.12	1.04
W1	-2.62	-2.10	1.77	1.50
W3	-1.40	-1.15	1.11	0.83
S1	-0.79	-1.43	0.87	0.88
S2	-0.88	-1.37	0.89	0.87
S3	-2.25	-3.25	2.05	2.07

Interestingly, not all the designs had their performance improved in MEA configuration as would be expected since the overall resistance of the cell is reduced by the elimination of the gap between the Pt-loaded printed GDL electrodes' surface and the PEM. Table V-10 compares the volume of H_2 produced by each design on both configurations.

Table V-10 – Comparison of the calculated experiment value of H_2 produced for each GDL design in flow-cell and MEA configuration.

GDL Design	Flow-cell (mL)	MEA (mL)
B	1.47	1.04
W1	1.67	1.50
W3	0.68	0.83
S1	1.18	0.88
S2	1.12	0.87
S3	1.13	2.07

Curiously, the only GDL designs that revealed better performance when integrated into MEA configuration were W3 and S3. In contrast, GDL designs B, W1, S1, and S3 had their best performance in flow-cell configuration. However, the worst performance attribution was

shared between both configurations, *i.e.*, the design which presented the lowest volume of H_2 produced, in both configurations was W3.

When comparing the performance of the printed GDL electrodes in flow-cell and MEA configurations it is mandatory to consider the possibility of *operando* degradation mechanisms of the latter. Figure V-39 presents a cross-section scheme of the interface between the Pt-loaded SPE and the PEM. Under working conditions, three different degradation mechanisms may occur at this interface and may explain the loss of performance, *i.e.*, a decrease in current density, during its operation. Moreover, the three proposed interface damaging events may also justify the loss of performance of most of the electrodes when integrated into the MEA configuration. The first mechanism consists of the delamination of the membrane from the surface of the Pt-loaded printed GDL electrodes originated by poor adhesion between both or by the formation of H_2 at the interface and thus creating a solid-gas-solid interface. The presence of the H_2 bubble interrupts the protons' path to the Pt catalyst, decreasing the amount of active catalytic sites where the HER may take

place.[48,50] The second mechanism proposes the deactivation of catalytic sites by the separation of the electron-conducting network. A possible scenario would be the delamination of the spray-coated catalyst layer from the printed GDL electrodes' surface or the physical degradation of the printed GDL. Finally, the third mechanism predicts the leaching of the Pt particles from the carbon support (as graphitized carbon) and consequently migrating within the MEA or leaving the cell. In the case of the flow-cell configuration, the second and third mechanisms may also occur.[51]
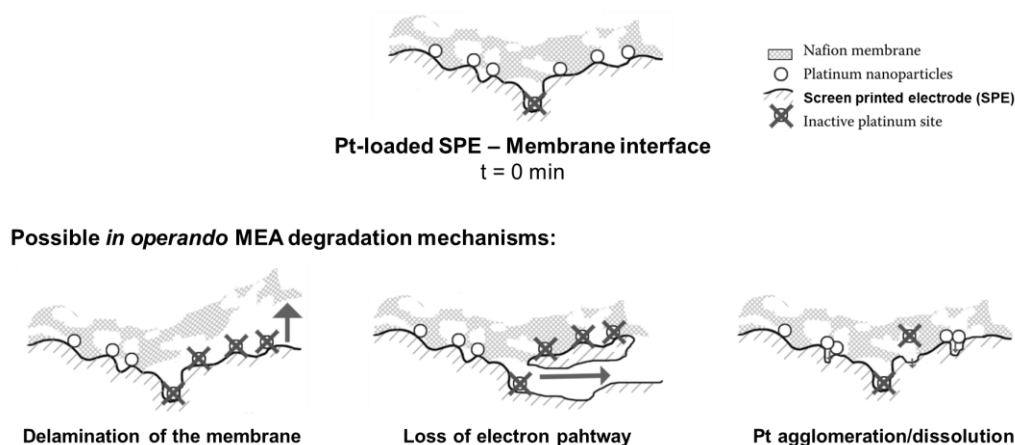
Figure V-39 – Cross-sectional perspective of the Pt-loaded printed GDL – membrane interface in MEA configuration and possible *in operando* degradation of mechanisms of the MEA. Adapted from [51].

In conclusion, the majority of the printed GDL electrodes demonstrated better performance in flow-cell configuration. These studies indicated that it may not be possible to indicate a single GDL design as the best design of printed GDL electrodes for HER. Moreover, each configuration, as observed with flow-cell and MEA configurations, may have a preferred electrode design. In this case, the application of printed GDL electrodes in such electrochemical devices was not only validated but also their versatility and possibility for design variation were proved to be an important advantage and possible pathway to improve the performance of the electrolyzer cell.

V.5. INTEGRATION OF eSCALED MATERIALS

The application of screen-printed electrodes in electrochemical devices for the H^+ reduction was validated with commercial materials and proved to be advantageous. However, when using commercially available materials one may not fully understand the whole electrochemical system or be aware of all the possible intervenient in the composition of each commercial material. The unknown participants may affect the performance of the device and the user may not be able to fully explain the mechanisms contributing to the device's performance. Thus, it is important to propose new materials to replace the commercial ones, giving the user full control of the system, and allowing him to tune the composition and, consequently, the properties of each component according to the *in-operando* conditions and achieve the best performance possible. Moreover, as proposed by

eSCALED, the overall cost of the electrochemical device may be reduced by using earth-abundant raw materials and tailor-made organic compounds as binders, membranes, and/or catalysts.

This part of the study addressed the integration of such materials, *i.e.*, alternative materials to the commercially available options proposed by eSCALED and from now on denoted as "eSCALED materials". Alternative conducting pastes suitable for screen-printing, substrates for the printed electrodes, electrode configurations as an alternative to conventional GDLs, and molecular catalysts were tested. The results and discussion of such experiments will be described in this section.

V.5.1. SCREEN-PRINTING CONDUCTING PASTES FROM COMMERCIAL POLYMER BINDERS

Commercial screen-printing conducting pastes present the advantage of convenience regarding the easy manipulation, good quality of the printed films, and high conductivity achieved. However, for intellectual property reasons, the full formulation of such inks is not always available to the consumer, and it becomes challenging to predict the properties and performance of the printed films in different working conditions. The preparation of "homemade" ink formulations gives the user full control over the properties of the printed film, being able to tune its electrical, mechanical, and surface properties with simultaneous optimization of the processability of the ink. The work described in this chapter did not focus on the optimization of the proposed ink's formulation, since this study was previously reported, but on the application of such ink in larger-scale production of screen-printed electrodes.

The present study follows preliminary works performed during the stay at UPPA (see section V.11.1). Herein, we replaced the reported mesitylene and o-xylene solvents with propylene glycol 1-monomethyl ether 2-acetate (PGMEA) since the latter is non-toxic and suitable for paint and coatings.[4,52] The morphology and electrical properties, and electrochemical performance of the produced electrodes were characterized.

Two lab-prepared carbon-based inks sharing the same formulation (described in V.9.1) and named "Graphite eSCALED" were prepared, however, they differed in the polymer binder used. The binders studied were poly(methyl methacrylate-butyl acrylate-methyl methacrylate) (MBM) and poly(styrene-butadiene-styrene) (SBS), both commercially available triblock copolymers.

Both Graphite eSCALED (MBM) and Graphite eSCALED (SBS) revealed problems of fast solvent evaporation during the printing process, which led to clogging of the screen and low reproducibility between the printed layers and electrodes. None of the commercial inks raised similar process difficulties. The surface roughness and homogeneity and thickness of the electrodes were evaluated by optical microscopy and profilometry. Figure V-40 a) and b) present the optical microscopy images from the printed GDL electrodes produced with SBS and MBM as the binder, respectively. Graphite eSCALED (SBS) revealed a highly heterogeneous porous surface.
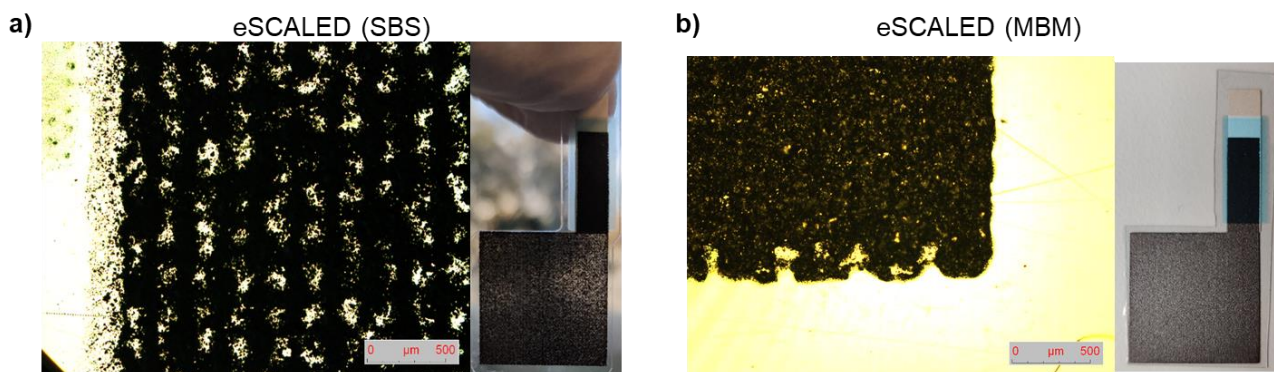
Figure V-40 – Micrographs and pictures from the screen- printed GDL electrodes from **a)** Graphite eSCALED (SBS).and **b)** Graphite eSCALED (MBM).

The images presented for eSCALED inks result from the printing of two wet on wet layers, *i.e.*, two layers were printed without drying and/or curing step in between the layers. Although the same fabrication process and ink formulation were applied, the electrodes were visually different with eSCALED (SBS) showing poor surface homogeneity.

The measured thicknesses of the electrodes characterized by profilometry are presented in Table V-16 (see section V.11 Appendixes). The eSCALED inks produced electrodes with average thicknesses of 23.0 ± 1.7 µm with MBM binder and 19.0 ± 2.3 µm with SBS binder. These values are within the range expected for the screen-printing technique.[6,53]. The thicknesses observed with these inks were higher than those obtained with commercial inks (see section V.2.2) which may be attributed to the large particle size of the graphite powder used in eSCALED ink's formulation.
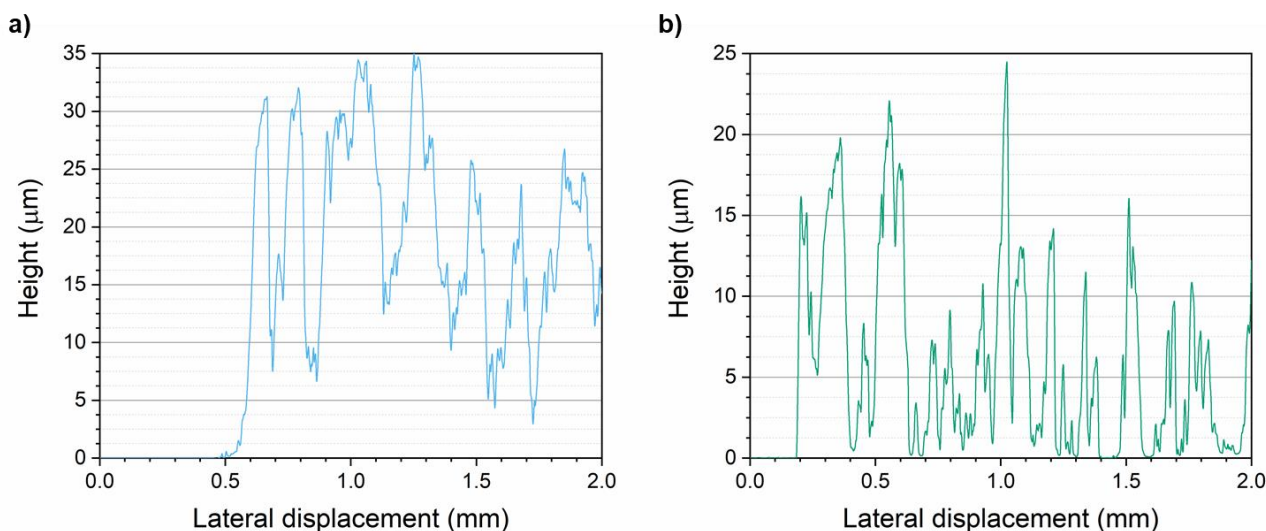
Figure V-41 – Height profiles of the screen-printed GDLs from **a)** Graphite eSCALED (MBM) and **b)** Graphite eSCALED (SBS) (three wet on wet layers).

Figure V-41 presents the height profiles of the electrodes produced from the previous two inks. As expected, from the optical microscopy imaging, eSCALED inks originated with rougher surface electrodes when compared with both commercial inks presented in V.2.2. In the case of eSCALED (SBS), the profilometry technique proved that some sites of the electrode had no film deposited,

which may be explained by the clogging of the screen's mesh due to fast solvent evaporation, large graphite particle size, and low viscosity of the ink.[54]

HIGH VISCOSITY INK   **LOW VISCOSITY INK**
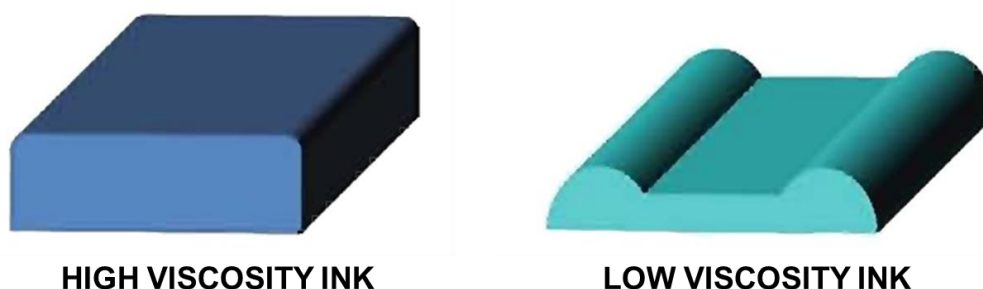
Figure V-42 – Typical cross-section pattern from printed inks with high and low viscosity. Adapted from.[54]

In Figure V-43 the measured electrode's conductivity – thickness relation is demonstrated. It was observed that the increase in thickness led to an increase in conductivity. The highest conductivity, 3.71 S cm^{-1} (three wet on wet printed layers, 22.7 µm film) was registered for eSCALED (MBM), while eSCALED (SBS) ink had its highest conductivity at 2.40 S cm^{-1} for a 21.3 µm film (three wet on wet printed layers). In the case of eSCALED (MBM), the conductivity was improved with increasing the number of printed layers due to improved electron percolation through graphite particles.[4] The measured conductivities of the eSCALED inks were lower than what was reported in V.2 for the commercial inks. The conductivity of the films obtained from the eSCALED inks could be increased by printing more layers during the screen-printing process, increasing the content of conducting filler in the ink formulation, or mixing other conducting particles, preferentially smaller than the graphite used, such as carbon black. The addition of carbon black dispersed between the graphite domains would improve the percolation between conducting particles and, thus, increase the conductivity.[55]
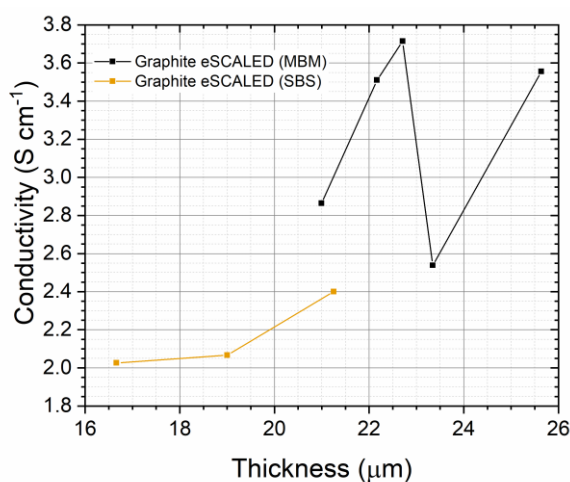
Figure V-43 – Measured conductivity and respective thickness of screen-printed GDLs produced from eSCALED (MBM) and eSCALED (SBS) inks.

The ECSA of the eSCALED (SBS) and eSCALED (MBM) printed GDL electrodes were assessed as described before for the printed GDL electrodes obtained from commercial inks. Figure V-44 presents the CVs obtained from the SRS for the studied eSCALED (MBM) and eSCALED (SBS), respectively.

a)

b)
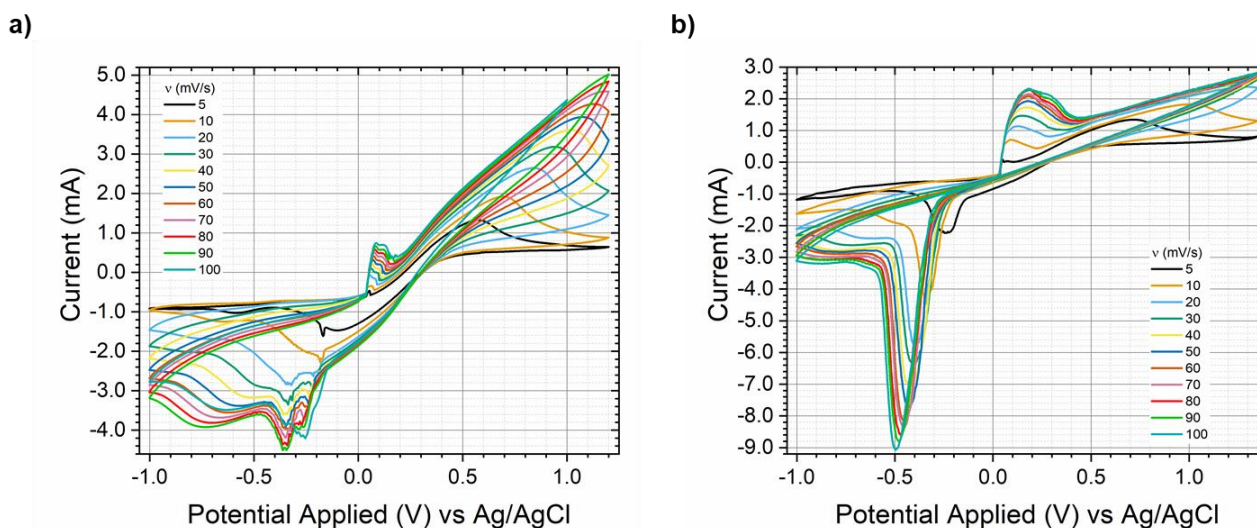
Figure V-44 – SRS (the second cycle from the CV obtained from each scan rate studied) of **a)** eSCALED (MBM) and **b)** eSCALED (SBS) (A_{geo} = 4 cm^2) printed GDL electrode.

In both cases, the obtained CVs did not present one anodic and one cathodic peak only, as seen before with the glassy carbon electrode and the Sunchemical-printed GDL electrode. In Figure V-44 a) (eSCALED (MBM) printed GDL electrode) the presence of the ferrocyanide-ferricyanide redox system was attributed to the anodic peak at +0.58 V and the cathodic peak at -0.59 V (v = 5 mV/s). Other oxidation and reduction peaks were observed between 0 and +0.20 V and -0.50 and 0 V, respectively which indicated that another redox system could be occurring at the electrode or in the solution. Since these groups of peaks were not observed before in experiments with a glassy carbon electrode, these new redox mechanisms could not have their origin in any other component of the experimental setup, except the working electrode, *i.e.*, one of the electroactive printed layers of the eSCALED (MBM) printed GDL electrode. Given the heterogeneity of the graphite layer in the electrode, it was suspected that the silver current collector under it was exposed to the electrolyte, being the source of the extra oxidation and reduction peaks detected. Equation V-15 and Equation V-16 describe the possible reversible oxidation-reduction processes happening at the Ag current collector sites exposed to the electrolyte.[1,56]

$$Ag_2O + 2OH^- \rightleftarrows 2AgO + H_2O + 2e^- \quad \textbf{Equation V-15}$$

$$2Ag + 2OH^- \rightleftarrows Ag_2O + H_2O^- + 2e^- \quad \textbf{Equation V-16}$$
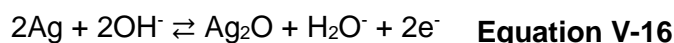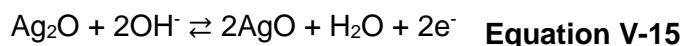
The electrode prepared from eSCALED (SBS) ink presented a similar CV response as presented in Figure V-44 b). In this case, for v = 5 mV/s the ferrocyanide-ferricyanide system was observed by the anodic peak at +0.78 V, but the respective cathodic peak could not be distinguished.

However, for v = 10 mV/s this peak, *i.e.*, the reduction of $Fe^{III}(CN)_6^{3-}$ to $Fe^{II}(CN)_6^{4-}$, was detected at -0.58 V. It was then considered that at v = 5 mV/s this cathodic peak was hindered by the cathodic peak with higher intensity observed between -0.04 and -0.44 V, attributed to the reductions processes involving the Ag current collector. The respective Ag oxidation processes were detected between 0 and +0.50 V. Comparing the intensity of the peaks attributed to the Ag oxidation and reduction processes, it was observed that the eSCALED (SBS) printed GDL electrode presented a higher current than the electrode from eSCALED (MBM). As observed in Figure V-41, the eSCALED (SBS) electrode presents poor surface homogeneity when compared to the electrodes obtained from eSCALED (MBM). Consequently, a larger area of the Ag current collector may have been exposed to the electrolyte in the case of the eSCALED (SBS) printed GDL electrode and, hence, more Ag sites participated in the electrochemical experiment. After the experiment, the result of the Ag oxidation could be visually observed, as seen in Figure V-45, by the appearance of dark grey spots in the current collector, which was not observed in the case of the Sunchemical-printed GDL electrode.

Finally, the ECSA for eSCALED (SBS) and eSCALED (MBM) electrodes was not calculated. It was considered that the oxidation of the silver current collector could affect the detection of the $(Fe^{II}(CN)_6^{4-})$-$(Fe^{III}(CN)_6^{3-})$ probe, leading to the estimation of a false ECSA. The ECSA could be properly calculated by removing the silver current collector from the system or improving the homogeneity of the graphite layer by printing more layers or reformulating the ink so that there would be no silver exposed to the electrolyte. However, due to the limitation of experimental time, none of these approaches was attempted.

Ag not oxidized   **Ag oxidized**

Sunchemical   **eSCALED (SBS)**
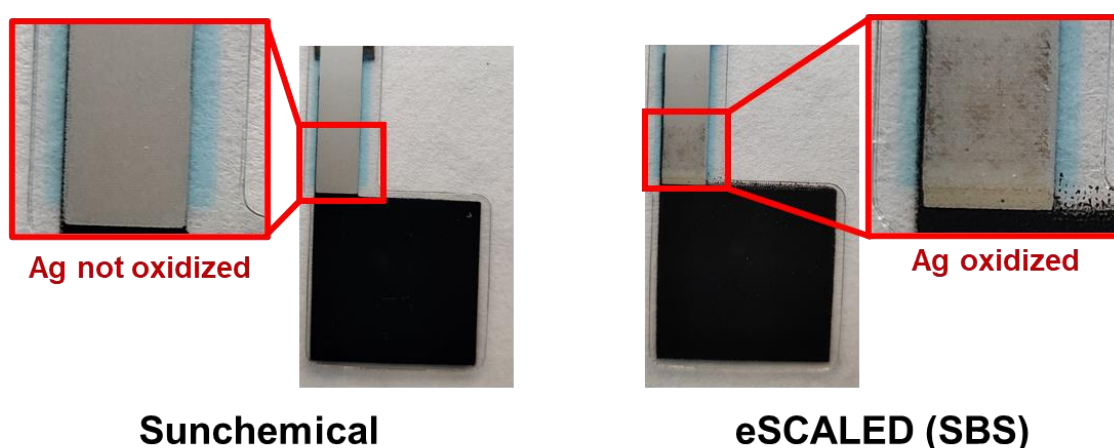
Figure V-45 – Pictures of Sunchemical and eSCALED (SBS) printed GDL electrodes after being submitted to the SRS experiments to assess the ECSA of each electrode. The oxidized Ag is observed by the appearance of dark grey spots at the current collectors.

Table V-11 compares the position of the anodic and cathodic peaks of the $(Fe^{II}(CN)_6^{4-})$-$(Fe^{III}(CN)_6^{3-})$ probe as detected by the glassy carbon electrode and printed GDL electrode from Sunchemical, eSCALED (MBM), and eSCALED (SBS) inks. As expected, it was observed that ΔE_{pp} increased with the decrease in conductivity of the electrodes.

190

Table V-11 – Position of the oxidation and reduction peaks (v = 10 mV/s) attributed to the ferrocyanide-ferricyanide system for the eSCALED (MBM), eSCALED (SBS), and Sunchemical screen-printed GDL electrodes and glassy carbon electrode.

Electrode	$Fe^{II}(CN)_6^{4-} \rightarrow Fe^{III}(CN)_6^{3-}$	$Fe^{III}(CN)_6^{3-} \rightarrow Fe^{II}(CN)_6^{4-}$	ΔE_{pp}
Glassy carbon	+0.28 V	+0.21 V	75.4 mV
Sunchemical	+0.62 V	-0.14 V	775 mV
eSCALED (MBM)	+0.69 V	-0.65 V	1.35 V
eSCALED (SBS)	+1.00 V	-0.58 V	1.58 V

(Conductivity — indicated by upward arrow alongside the table)

V.5.2. SCREEN-PRINTING CONDUCTING PASTES FROM eSCALED POLYMERIC BINDERS

The preparation of screen-printed GDL electrodes containing polymeric binders synthesized within the eSCALED framework was approached in collaboration with Ludovico Riccardi who synthesized statistical copolymers with hydrophilic properties. The copolymer used as a binder was poly(methyl methacrylate-*stat*-styrene-*stat*-hydroxyethyl methacrylate) (P(MMA-*stat*-S-*stat*-HEMA)). The ink was prepared with the formulation. The printed GDLs prepared with such binder achieved a maximum conductivity of 5.30 S cm^{-1} for 72.8 μm thick (four repetitions of two wet on wet layers). In this case, the conductivity tendency to decrease with increasing thickness was not observed (see Table V-17 in section V.11 Appendixes).

The printed GDL electrodes prepared with P(MMA-*stat*-S-stat-HEMA) are still being studied by Ludovico. The studies aim toward the integration of molecular catalysts and hierarchical porous carbon supports.

The use of in-lab prepared conducting inks presents several advantages such as full control of the ink elements and formulation. The proposed eSCALED inks studied need further optimization in terms of ink formulation to promote higher conductivity and better surface homogeneity.

V.6. POROUS SUPPORTING SUBSTRATE

After studying non-porous substrates as supporting substrates to prepare printed GDL electrodes with gas flow controlled only by geometrical design apertures, it was investigated the same printed GDL electrode design on a paper substrate, the same substrate used in large area printed batteries.[1] This substrate has clear technological and environmental advantages, being mechanically stable, biodegradable, renewable, recyclable, sustainable, and low-cost material, and could serve to exploit the microporosity of electrodes through the porous substrate.[57]

Over recent years, the application of paper in electronics, energy storage devices, or disposable devices in point-of-care devices has been studied. Its high surface area and porosity are given by its fibrous composition and its strong adhesion to different materials and mechanical

properties making this material a good candidate for printing technology-based processes such as screen printing, inkjet, or spray coating.[58–62]

The printed GDL electrode on porous supporting substrate configuration consists of sandwiching a catalyst layer containing an HER catalyst, such as Pt/C, adhered by a proton conductive binder, such as Nafion, between paper, such as office paper, and a printed electrode. Figure V-46 presents a cross-section representation of this configuration.
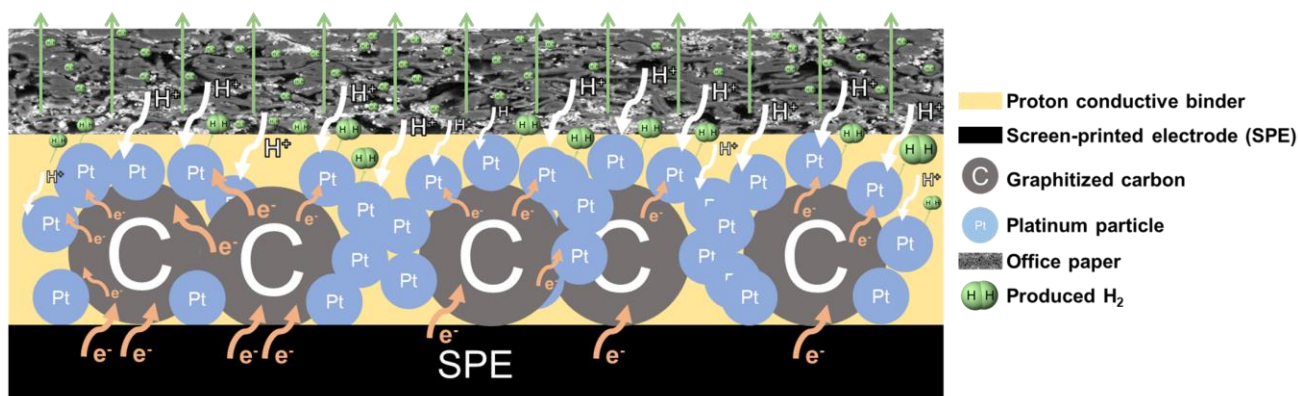
Figure V-46 – Cross-section of the printed GDL electrode on a porous supporting electrode. The produced H_2 is expected to diffuse through the porous supporting substrate.

It was expected that the paper layer could avoid the leaching of the catalyst from the screen-printed electrode surface. Moreover, it was also expected that the H_2 produced could diffuse through the intrinsic porosity of paper and be released. Two versions of the Pt-loaded (0.34 mg/cm^2) printed GDL electrode on porous supporting substrate configuration containing a printed GDL with type B design were tested; non-laminated and laminated.

The first version, the non-laminated printed GDL electrode on a porous supporting substrate, was submitted to a SRS study. The result of this experiment is presented in Figure V-47 a) where the catalytic activity is observed from -1.2 to -2.1 V (vs Ag/AgCl).

a)

b)

0 V APPLIED   **-2.0 V APPLIED**
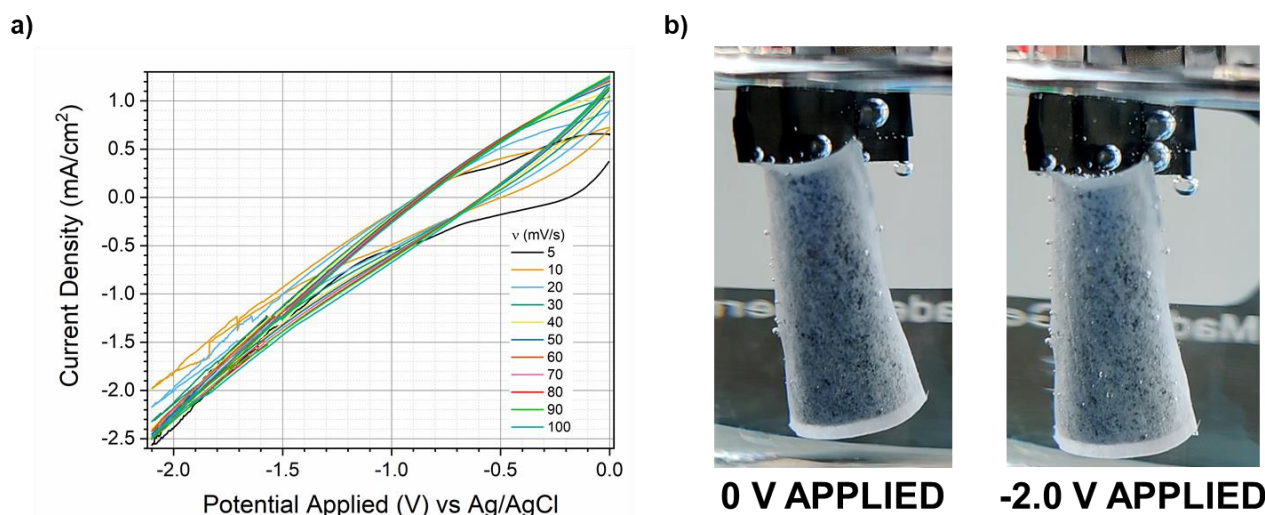
Figure V-47 – a) SRS performed in PBS (pH 7) between 0 and -2.1 V (vs Ag/AgCl) with the Pt-loaded (0.34 mg/cm^2) non-laminated printed GDL electrode on a porous supporting substrate having the screen-printed carbon-based layer facing the counter electrode. **b)** Pictures of the deformed non-laminated printed GDL electrode on porous supporting substrate electrode during the SRS experiment at 0 V and -2.0 V (vs Ag/AgCl) applied potential.

A maximum of -2.5 mA/cm^2 was achieved by this electrode test. As expected, the printed GDL electrode on the porous supporting substrate that had its GDL layer initially facing the counter electrode deformed when immersed in the electrolyte solution. Figure V-47 b) presents pictures of the deformed non-laminated printed GDL electrode on the porous supporting substrate. It was observed that, as predicted, the produced H$_2$ diffused through the paper and was released as it is presented in Figure V-47 b) "-2.0 V applied". However, it was considered that such deformation of the electrode could endanger the stability and performance of the printed GDL electrode on the porous supporting substrate. For this reason, it was found that to avoid such deformation mechanical support would be required. Therefore, the electrode was thermally laminated between two plastic pouches, keeping the 2.0 x 2.0 cm^2 working area open to be reached by the electrolyte.

The laminated printed GDL electrode on the porous supporting substrate was tested by chronoamperometry with -2.0 V (vs Ag/AgCl) applied potential in two different positions: first, having, the GDL facing the counter electrode and then, exposing the catalyst-paper interface directly to the counter electrode. The result of the CA performed in the first position is presented in Figure V-48 a).
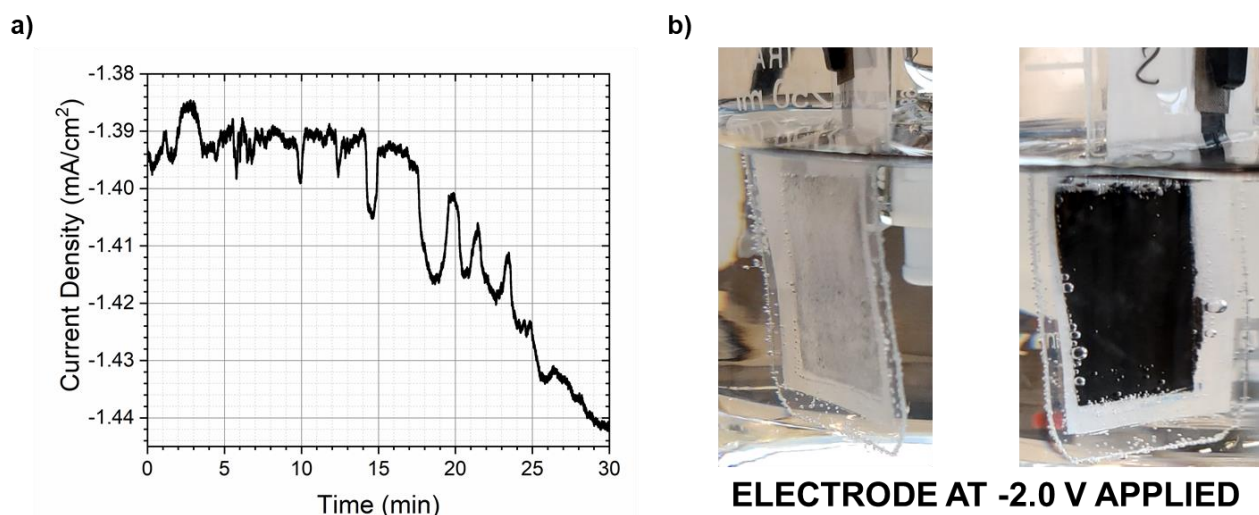
Figure V-48 – a) Chronoamperometry performed in PBS (pH 7) with -2.0 V (vs Ag/AgCl) potential applied with the Pt-loaded (0.34 mg/cm^2) laminated-printed GDL electrode on a porous supporting substrate having the screen-printed GDL facing the counter electrode. **b)** Pictures of the laminated-printed GDL electrode on a porous supporting substrate during the CA experiment.

During this experiment, the electrode achieved a maximum of -1.442 mA/cm^2 after 30 min of the experiment, which presents an increase of, approximately, 5 mA/cm^2 since the beginning of the experiment. The CA presented some perturbations in the signal which were attributed to the release of the H$_2$ produced. The produced H$_2$ was released through the SPE surface as shown in the pictures presented in Figure V-48 b). Contrarily, to what was observed in the non-laminated printed GDL electrode on a porous supporting substrate, no H$_2$ was perceived to be diffused and consequently released through the paper side. Moreover, it was observed that the electrode did not deform during the experiment, *i.e.*, its flat and planar shape was preserved by the supporting laminated pouches, as expected.

When the catalyst-paper interface was exposed to the counter electrode, a new CA experiment was recorded at the same applied potential. However, since the previous experiment revealed the increase of current density after 30 min, in this case, the experimental duration was increased from 30 min to 5 h to evaluate how the current density would evolve with time. The CA is presented in Figure V-49 a).

a)

b)

ELECTRODE AFTER CHRONOAMPEROMETRY

Figure V-49 – a) Chronoamperometry performed in PBS (pH 7) with -2.0 V (vs Ag/AgCl) potential applied with the laminated- printed GDL elec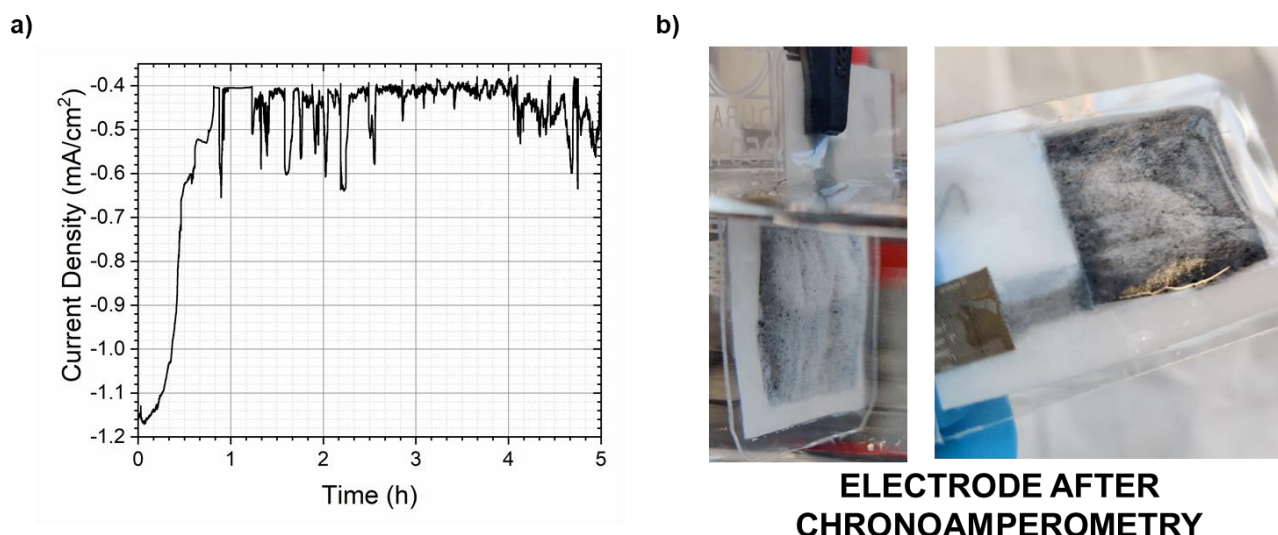trode on the porous supporting substrate having the catalyst-paper interface facing the counter electrode. **b)** Pictures of the laminated-printed GDL electrode on a porous supporting substrate after the 5 h CA containing the H_2 produced trapped inside.

The printed GDL electrode on paper achieved its maximum current density. -1.17 mA/cm^2, after 4 min, and then decreased during the first hour, reaching a minimum of -0.4a mA/cm^2. During the next 4 hours, it was observed that the current density varied between -0.64 and -0.40 mA/cm^2. Figure V-49 b) presents two pictures of the printed GDL electrode on the porous supporting substrate after the 5 h experiment. Interestingly, a bubble of H_2 was found trapped between the catalyst layer and the paper. This phenomenon was the source of the loss of current density observed since that, with time, the catalyst layer-liquid interface needed for the HER was blocked by H_2 gas bubbles and a catalyst layer-H_2 interface was created, decreasing the catalyst utilization.[48,50,63,64]

The diffusion of H_2 through paper was not spotted in the laminated printed GDL electrode on a porous supporting substrate, as would be expected after the observations with the non-laminated printed GDL electrode on a porous supporting substrate. It was surprising that paper acted as an H_2 barrier in the case of the laminated printed GDL electrode on a porous supporting substrate. It was then suggested that the deformation of the paper played a crucial role to allow the diffusion of H_2 through the paper. When the paper deformed in the electrolyte its cellulosic fibers were submitted to mechanical stress that, in some sites, cause the collapse of the fibers. Once the fibers collapsed, the diffusion paths were created to allow the escape of H_2 from the catalyst layer-paper interface.

The results obtained open doors to explore paper as a gas-permeable or impermeable layer, but more studies are required to understand its behavior.

V.7. ARTIFICIAL PHOTOSYNTHESIS DEVICE – e⁻LEAF PROTOTYPE

An ultra-light, flexible and cost-effective cell design that can be used as a water electrolysis cell and fuel cell as a portable power source for flexible electronics was developed based on the previously reported fully printed MEA. To achieve such flexibility and ultra-lightness, the MEA was encapsulated in a polymer envelope using a lamination technique, previously developed in previous works (Garcia *et al*, *ACS Omega* **4**, 16781–16788 (2019)).[1] These lamination polymer sheets play the role of the thick and heavy cathode/anode endplate in conventional cell design. The water electrolysis single cell prepared with this novel design presents an area of 3 cm^2, a thickness of only 3 mm weight of only 10 g, and 20-30 times lighter than a conventional commercial cell of the same active area. This innovative flexible cell design is a proof-of-concept for disruptive flexible proton exchange membrane water electrolysis (PEMWE) cells, and/or fuel cells, to achieve specific power density with small size, small volume, low weight, and low cost for *niche* applications when compared to current designs.

The e⁻LEAF design respects the principle of a single-cell design for water electrolysis application, with a proton exchange membrane in the middle of the cell, an anode for oxygen evolution reaction (OER), and a cathode for hydrogen evolution reaction (HER) (Figure V-50).

Figure V-50 – Schematic representation of the e⁻LEAF concept: a fully printed MEA in a flexible lightweight cell.

Two innovative points can be highlighted in our novel design:

1.   The MEA is fully printed with screen-printed carbon electrodes as a gas diffusion layer and screen-printed metal current collector. This replaces the conventional commercial carbon GDL and the metal current collector plate.

2.   The thick and heavy endplates are replaced by laminated flexible polymer foil using lamination.

Both changes bring the advantage of significantly reducing the thickness, weight, and cost of cell fabrication. Figure V-51 presents a picture of the e⁻LEAF prototype side-by-side with a conventional commercially available electrolyzer cell.
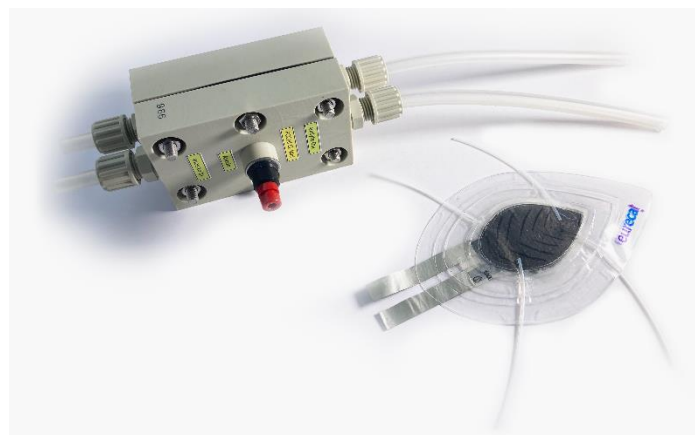
Figure V-51 – Picture of commercially available electrolyser cell and e⁻LEAF.

The e⁻LEAF prototype presented in Figure V-51 was submitted to the OE-A Competition 2022 promoted by the Organic and Printed Electronics Association (OE-A) occurring at LOPEC 2022, the world's leading International Exhibition and Conference for the Printed Electronics Industry. The prototype competed in the "Freestyle Demonstrator" category. A demo video of the functional prototype is available at the following link: https://youtu.be/B9J1mMWfuH4.

The e⁻LEAF was integrated with a tandem triple junction perovskite solar cell from Bruno Branco (Eindhoven University of Technology) to make the eSCALED artificial photosynthesis device as displayed in Figure V-52.
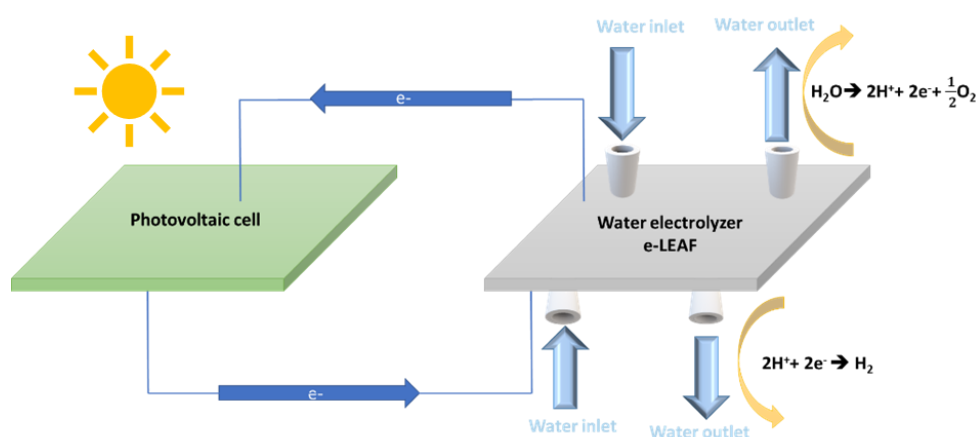
Figure V-52 – Schematic representation of a water electrolyzer cell with an integrated photovoltaic cell.

V.7.1. PRINTED GDL ELECTRODES FOR INTEGRATION AS CONVENTIONAL GDL SUBSTITUTES

Figure V-53 presents the printed GDL design used for the prototype.

W5
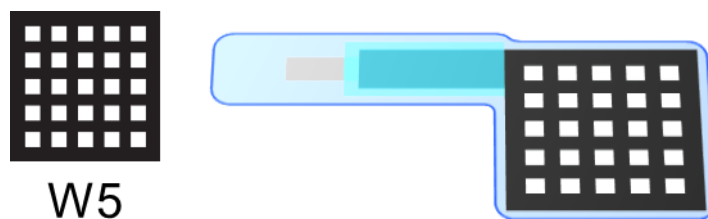
Figure V-53 – Printed GDL (left) and example of the fully fabricated printed GDL electrode (right).

The screen-printed GDL electrodes consist of a silver current collector, a printed graphite-based GDL, and a dielectric ink defining the working area (3 cm^2) (see Figure V-54). For this purpose, a 125 μm thick poly(ethylene terephthalate) (PET) substrate was used. The electrodes' openings are laser cut.

a)   b)
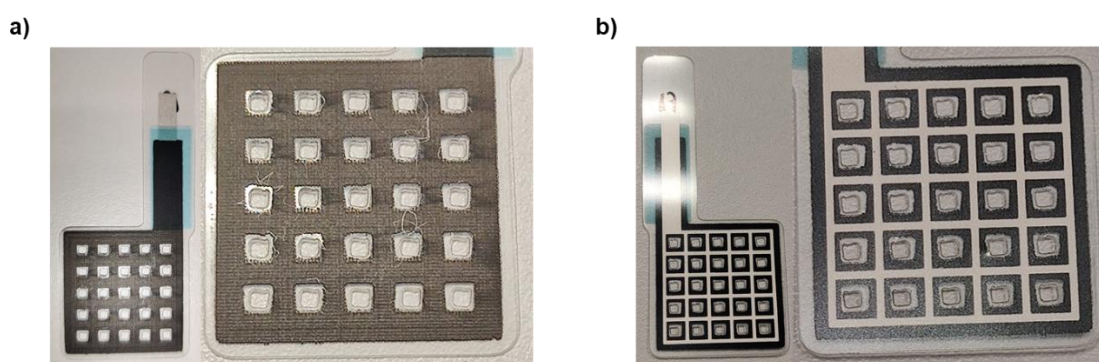
Figure V-54 – Pictures of the printed GDL electrode: a) graphite-based GDL and b) silver current collector printed between the substrate and the graphite GDL.

V.7.2. MEA WITH SUPPORTED PRINTED GDLS

The anode and cathode catalyst are directly deposited onto the PEM by ultrasonic spray-coating as described before. The platinum (Pt) loading of the cathode has been targeted to be 0.20 mg/cm^2 and the RuO$_2$ loading of the anode has been adjusted to 2.20 mg/cm^2. Figure V-55 below illustrates the catalyst-coated membrane (CCM) method employed.

Catalyst coated membrane (CCM):

| Pre-treated membrane | First catalyst coated on membrane | Catalyst coated membrane |
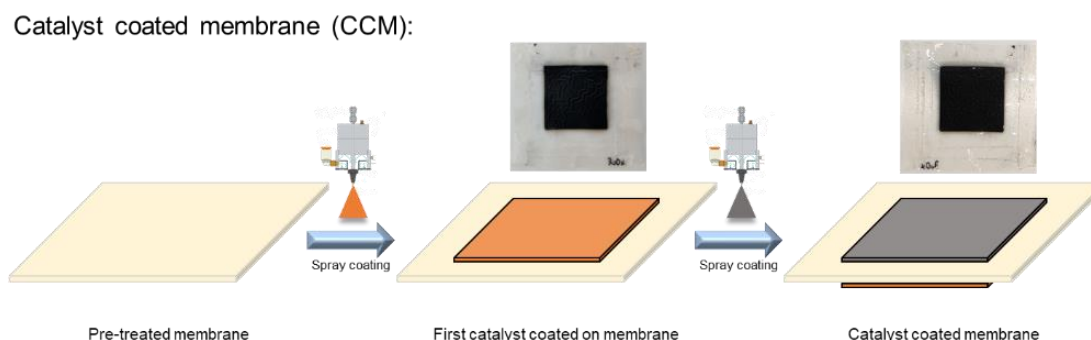
Figure V-55 – Conventional CCM method employed.

The MEA was prepared by hot-press using printed GDL electrodes as cathode and anode and a catalyst-coated paper-based PEM. Figure V-56 presents a scheme and pictures of the prepared membrane electrode assembly (MEA).
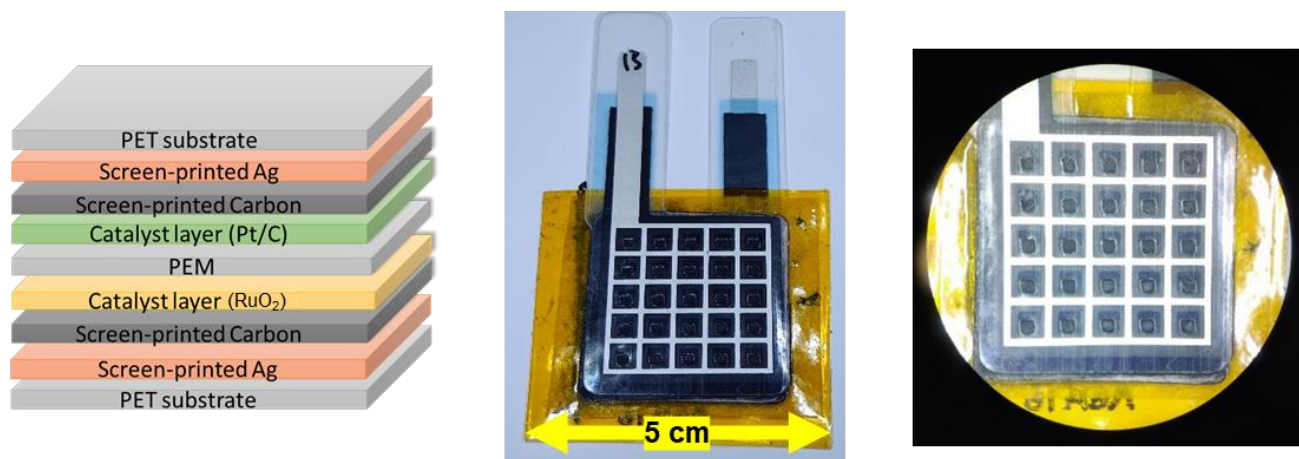
Figure V-56 – Cross-sectional scheme of the MEA assembled with the printed GDL electrodes (left), a picture of the assembled MEA (middle), and an enlarged picture of the MEA working area where the openings of the printed GDL electrodes can be seen (right).

V.7.3. ASSEMBLY OF e⁻LEAF

The MEA is encapsulated with transparent adhesive laminating pouches and Teflon tubes are used as inlets and outlets. Figure V-57 presents a picture of the e⁻LEAF water electrolyzer.
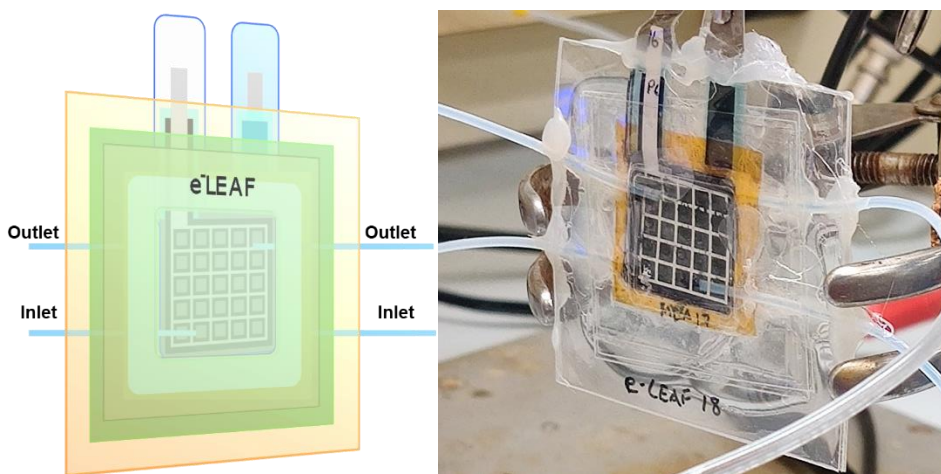
Figure V-57 – Design (left) and picture (right) of the assembled e⁻LEAF water electrolyser.

A complete description of the e⁻LEAF assembly procedure is given in section V.9.7.

V.7.4. INTEGRATED SOLAR TO HYDROGEN PROTOTYPE

Figure V-58 displays the I–V characteristics of both tandem solar cells and e⁻LEAF electrolyser before and after the electrolysis experiment.
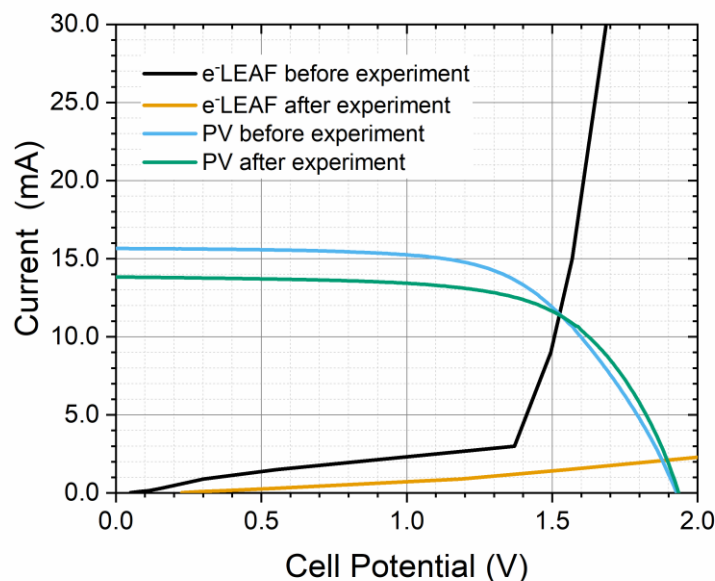
Figure V-58 – Photovoltaic (PV) cell and e-LEAF electrolyser performance at the beginning and end of the experiment.

The blue and green curves are the solar cell I–V curves under 1-sun equivalent light intensity before and after the electrolysis experiment, respectively. The black and yellow are the I–V curves of the e⁻LEAF before and after the experiment, respectively. The intersection between the polarization curve of the e⁻LEAF and the I – V curve of the tandem solar cell indicates the operating voltage (V_{OP} = 1.51 V) and operating current (I_{OP} = 11.85 mA) for the described system. These conditions correspond to a solar-to-hydrogen (STH) efficiency of 14.6 % as calculated from Equation V-17:

$$\text{STH (\%)} = \frac{1.23 I_{op} \eta_{far}}{A_{sc} P_{in}} \times 100 \qquad \textbf{Equation V-17}$$

where n_{far} is the faradaic efficiency (n_{far} = 1), A_{sc} is the solar cell area (A_{sc} = 1 cm²) and P_{in} is the light intensity (P_{in} = 100 mW cm⁻²). The faradaic efficiency was assumed to be 1 as the used catalysts are highly active for their respective reactions without side products. Subsequently, the two systems were connected via external wiring and operated for 4 h 45 min with continuous illumination (Figure V-59).
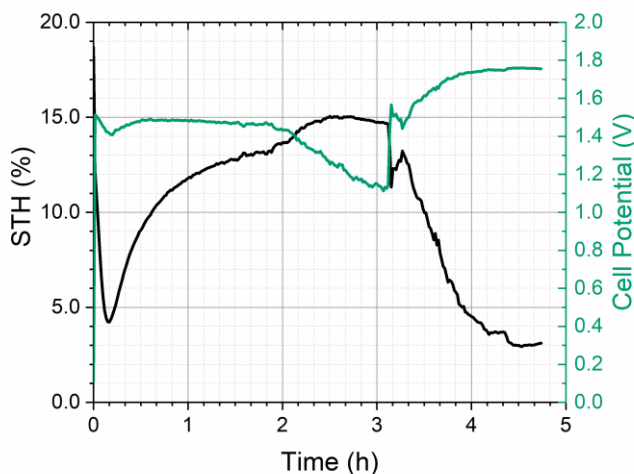
Figure V-59 – STH efficiency and e⁻LEAF voltage during operation.

The PV-EC experiment was stopped after 4 h 45 min as the STH had dropped remarkably, down to 3%. This can be explained by the performance loss of e⁻LEAF as seen in Figure V-59. At the end of the test, the Ag current collector of the e⁻LEAF electrode on the anode side presented visible oxidation. The solar cell had dropped its efficiency as well at the end of the test.

Even though STH drops in at the beginning and the end of the experiment, it maintains relatively stable at the range of 14-15 % during 1h, from t=2 h to t=3 h. This is a promising result as it is relatively comparable with previous research where commercial solar cells or commercial /stack water electrolyser cells are involved. In 2016, J.Schüttauf *et al* published their work where an STH of 14.2% was obtained and demonstrated by interconnecting state-of-the-art Si PV modules to an external proton exchange membrane electrolyzer stack[66].

The decrease in STH after 4h h of operation is mainly due to an increase of V_{OP} over the maximum power point primarily caused by a decrease in the performance of the electrolysers over time. Therefore, a stability study on e-LEAF performance deserves further investigation.

Figure V-60 presents pictures of the anode and cathode of e⁻LEAF during the experiment where the release of gas bubbles can be observed.
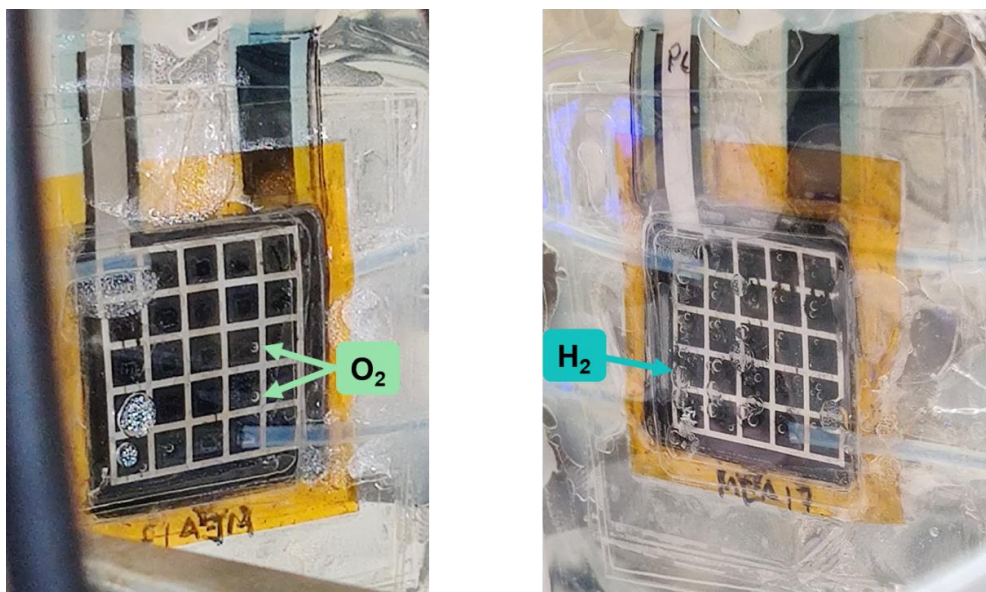
Figure V-60 – Pictures of the anode (left) and cathode (right) of e⁻LEAF in operation demonstrating the production of O_2 and H_2 by electrolysis powered by the photovoltaic cell.

The prototype built demonstrated a STH efficiency of 15 % which is above the 8 % initially targeted by the eSCALED Project.

V.8. CONCLUSION AND PERSPECTIVES

In this work, the design rules to prepare printed cathodes for green hydrogen generation were investigated. For this purpose, membrane electrode assemblies (MEAs) electrode elements were studied and converted into printed versions with a particular interest in substituting the gas diffusion layer and current collector. Using printed electronics technology, twenty-one designs of printed gas diffusion layers were proposed, and the fabrication protocol was established. The fabrication consisted of printing silver ink, followed by carbon ink, and finally, a dielectric ink to set the working area and encapsulate and protect the connection to the external power source from the reactants. The inks were deposited by screen-printing with several thermal and UV curing steps. The printing process was preceded by the thermal treatment of the substrate chosen, a 125 μm thick PET. Finally, macro-pores were created on the printed electrodes by laser cut.

To understand the role of materials used in the printed electrode device, two commercially available carbon-based inks were compared in terms of morphology and conductivity, of which the one provided by Sunchemical registered the highest conductivity and was chosen to perform the following studies. Then the electrochemical characterization of the Sunchemical SPEs was performed in three electrodes configuration using a commercial Ag/AgCl reference electrode and a Pt foil as the counter electrode. The ECSA determination experiments demonstrate that only 50 % of the geometric area of the electrode is active.

Then, to investigate the influence of interferent parameters, known to affect reaction yield, the performance of the printed GDL electrodes for HER was evaluated against different pH levels and temperatures of the reactant (PBS). The electrodes were tested bare and coated with Pt/C catalyst for HER at -1.6 and -2.0 V (vs Ag/AgCl). As expected, the printed GDL electrodes demonstrate better performance in terms of current density at lower pH, which is known to favor the HER. Moreover, the electrodes demonstrated excellent stability (30 min experiment) under such conditions without significant performance losses. However, when tested at 60 and 80 °C the electrodes presented delamination and significant loss of current density during the experiment. Several reasons were suggested as an explanation for the poor performance of the electrodes at these temperatures. At 40 °C, both electrodes, bare and Pt-loaded, performed with higher current density when compared with the tests at room temperature.

The influence of the catalyst load in the printed cathode device was also investigated. Printed GDL electrodes were coated with different Pt loads (0.06 – 0.68 mg/cm^2). The increase of catalyst load on Pt-coated printed GDL electrodes did not translate into a significant increase in the produced current density. However, it was possible to observe a trend leading to higher current density production with a higher Pt load. The hindering of Pt catalytic sites by the ionomer binder used was suggested to be the reason why no significant differences were observed between the lowest and

the highest catalyst loads. Further studies are required to optimize the Nafion content in the catalyst layer, promoting the best possible performance of the electrode.

The designs to be tested in flow-cell and MEA devices were selected through chronoamperometry experiments at -2.0 V (vs Ag/AgCl). Designs B; W1; W3; S1; S2 and S3 presented higher current density and were therefore integrated into flow cells and MEAs. Design B was also tested in the H-cell device so that its products could then be quantified by gas chromatography. In this configuration in a 30 min chronoamperometry at -1.6 V (vs Ag/AgCl), the bare and the Pt-loaded printed GDL electrodes produced 488 µL and 2.73 mL of H_2, respectively. However, the calculated Faradaic efficiencies above 100 % raised some doubts about the experimental procedure and the H_2 may have been overestimated. In flow cell configuration GDL design W1 presented outstanding performance, probably due to the match of its macro-pores position with the reactant inlet and outlets of the 3D-printed cell. However, in MEA configuration, GDL design W1 was the second-best performance, preceded by GDL design S3. It was demonstrated that the different designs tested presented a different performance in flow-cell and MEA configurations. Except for design S3, all the designs presented a lower performance in the MEA configuration.

Two in-lab prepared graphite-based inks, sharing the same formulation, were compared. The ink prepared with MBM as a binder produced screen-printed electrodes with better surface homogeneity and higher conductivity than the ink with SBS as the binder. However, none of the inks demonstrated higher conductivity than the commercial inks tested before. Furthermore, the high surface roughness produced by both inks (compared to commercial inks) was attributed to the low viscosity of the inks used, fast solvent (PGMEA) evaporation, and large graphite particle size, and clogging of the screen during the printing process. During the ECSA determination experiments the silver in the current collector intervened in the overall electrochemical experiment. Moreover, it was considered that the results obtained were adulterated and not suitable to calculate ECSA. Further studies are required to validate the application of such inks for HER.

An unprecedented printed GDL electrode on paper as a porous supporting substrate configuration was proposed in this work. In this configuration, the catalyst is encapsulated between the office paper substrate and the printed electrode. Interestingly, it was observed that depending on the mechanical deformation of the office paper used, it may perform as a gas diffusion or gas barrier layer. These observations are of great interest and should be further explored not only for electrolyzers but also for fuel cells, for instance, as reinforcement of the membrane and electrode support.

In this work, the applicability of screen-printed electrodes in water electrolysis was demonstrated and validated. This work opens opportunities to further explore printing technologies for electrolysis devices. The results obtained are promising and present an alternative for the high-cost commercial material such as GDLs, electrodes manufactured through printing techniques would

lead to a cost decrease for the overall device. Moreover, electrodes could be prepared in different substrates, and designs, with or without macro-pores, leading to fine-tuning of the electrode properties for each specific device towards the best performance. Although the performance may not be as high as conventional materials, fully printed devices may be an alternative for short-term usage or smaller applications where high performance is not required. However, further studies on the development of large-area electrodes for water electrolysis should be performed. Printed electrodes also promote the modularity of the device, *i.e.*, the integration and testing of different catalysts are facilitated, as well as the maintenance and replacement of electrodes, for instance in flow-cell configuration.

A new ultra-light, flexible and cost-effective cell design for water electrolysis was created: e-LEAF. A proof-of-concept experiment of an artificial photosynthesis prototype was performed by integrating a triple junction tandem perovskite solar cell with e-LEAF, and a STH efficiency of 15 % was demonstrated, exceeding the eSCALED Project ambitions of achieving at least STH≈8 %.

V.9. EXPERIMENTAL PROCEDURES

Table V-12 presents the list of materials used in the following experimental procedures described.

<p align="center">Table V-12 – List of materials used.</p>

Material, grade	Provider
125 μm PET substrate, Melinex® 506	HiFi
2-propanol	Fluka Analytical
40 wt% Pt on graphitized carbon	Merck
5 wt% Nafion solution	Aldrich Chemistry
Carbon ink	Creative 122-49
Dielectric ink	Sunchemical Suntronic 681
GDL Freudenberg H23C2	Fuel Cell Store
Graphite ink	Sunchemical C2030519P4
Graphite powder (<20 μm)	Sigma-Aldrich
H_2O_2, 30 wt% in H_2O	Sigma-Aldrich
H_2SO_4 95.0-98.0 %	Sigma-Aldrich
$K_3Fe(CN)_6$, ACS reagent ≥99.0 %	Sigma-Aldrich
$K_4[Fe(CN)_6] \cdot 3H_2O$, ACS reagent, 98.5-102.0%	Sigma-Aldrich
LAIRD tape	LairdTech
MBM LA-2550	Kurarity™
$Na_2HPO_4 \cdot H_2O$ BioUltra >99.0 %	Sigma-Aldrich
Nafion 212 membrane	Sigma-Aldrich
NaH_2PO_4, BioXtra >99.0 %,	Sigma-Aldrich
80 g/m^2 Paper Office document DIN A3	REY
PGMEA	Sigma-Aldrich
Ruthenium (IV) oxide, anhydrous, 99,9% $RuO2$	ThermoFisher
SBS D1191 E	Kraton™
Silver ink	Dupont 5000
Tifoo gold electrolyte bath	Marawe
Tifoo nickel electrolyte	Marawe
Graphite anode for electroplating	Marawe
Nickel anode for electroplating	Marawe

V.9.1. PREPARATION OF HOMEMADE GRAPHITE INKS

Homemade graphite inks are prepared according to the following formulation: 67 wt% of solvent, 10 wt% polymer binder, and 23 wt % of graphite powder (<20 μm, synthetic, Sigma-Aldrich). Methyl methacrylate-butyl acrylate-methyl methacrylate (MBM, Kurarity™ LA-2550) and styrene-butadiene-styrene (SBS, Kraton™ D1191 E) block copolymers were used as polymer binders in this study and propylene glycol 1-monomethyl ether 2-acetate ($C_6H_{12}O_3$, PGMEA) as solvent.

V.9.2. DESIGN AND FABRICATION OF THE PRINTED GDL ELECTRODES

The design and patterns for the 2 x 2 cm^2 square-shaped-electrodes were created using Inkscape software and screen-printed with a medium-sized pneumatic flat screen printer from ATMA (model AT-60FA). The electrodes were printed on office paper and PET film (HiFi, film type 506, 125 μm thickness) as substrates. Commercial silver (Dupont 5000), carbon-graphite (Sunchemical C2030519P4), and dielectric (Sunchemical Suntronic 681) inks were screen-printed according to steps 1 to 4 of Figure V-10. Thermal and UV treatments were performed on the UN160 lab oven (Memmert) and UV lamp (model HOC-35/1-200/BE OBC from B.C.B.), respectively.

V.9.3. CATALYST DEPOSITION

Electrodes for H$^+$ reduction: Pt/C catalyst ink is prepared by mixing 62.5 mg of Pt on graphitized carbon (40 wt% loading, Merck), 1.50 g of distilled H$_2$O/2-propanol (LC-MS CHROMASOLV®, Fluka Analytical) 1:1 w/w as solvents with 1.563 g of 5 wt% Nafion® perfluorinated resin solution (Aldrich Chemistry) as the binder.

Electrodes for H$_2$O oxidation: 75 mg of RuO$_2$ (ThermoFisher) 1.80 g of distilled H$_2$O/2-propanol 1:1 w/w as solvents with 1.875 g of 5 wt% Nafion® perfluorinated resin solution as the binder.

The catalyst ink is deposited, after 15 min of sonication, by ultrasonic spray coating using Sonotek's ALIGN module equipped with a syringe pump and Accumist nozzle. The nozzle air pressure and power were set at 80 mbar and 2 W, respectively and it is mounted into a re-adapted 3D printer (RepRap BCN3D+). The nozzle motion (controlled by the 3D printer) at 45 mm height follows a pattern with 2 mm line spacing. The bed temperature is set to 50 °C during the whole deposition process and the flow rate (controlled by the syringe pump) is set to 300 μL/min. The electrode is let to dry at this temperature for 5 min between each layer sprayed and for 20 min after the last layer.

V.9.4. ELECTROCHEMICAL CHARACTERIZATION

Cyclic voltammetry (CV), scan-rate study (SRS), chronoamperometry (CA), and electrochemical impedance spectroscopy (EIS) measurements were carried out on AUTOLAB PGSTAT204 equipped with FRA-32M and BOOSTER 10A modules. The individual characterization of the electrodes is performed in a three-electrode configuration with Ag/AgCl (3 M KCl) reference electrode (RE) and a Pt sheet electrode as the counter electrode (CE). These studies are carried out on phosphate-buffered saline (PBS) solution prepared from a mixture of 0.1 M sodium phosphate monobasic (NaH$_2$PO$_4$, BioXtra >99.0 %, Sigma-Aldrich) and 0.1 M sodium phosphate dibasic dihydrate (Na$_2$HPO$_4$·H$_2$O, BioUltra >99.0 %, Sigma-Aldrich) solutions to achieve pH 7 and 9. To

prepare pH 4 PBS solution, 0.1 M H_2SO_4 was added to 0.1 M NaH_2PO_4 solution until the desired pH was achieved. The electrodes were connected to the potentiostat with LAIRD double-sided conductive adhesive tape.

V.9.4.1. ECSA DETERMINATION EXPERIMENTS

The experiments to determine the electrochemically active surface area are performed in the Fe^{2+}/Fe^{3+} electrolyte system. For this purpose 0.422 g potassium hexacyanoferrate(II) trihydrate ($K_4[Fe(CN)_6] \cdot 3H_2O$, ACS reagent, 98.5 - 102.0 %, Sigma-Aldrich) and 0.329 g potassium hexacyanoferrate(III) ($K_3Fe(CN)_6$), ACS reagent ≥99.0 %, Sigma-Aldrich) are solubilized in 100 mL 0.1 M PBS. The experiment consisted of performing three cyclic voltammograms at different scan rates (5-100 mV/s) with Ag/AgCl (3 M KCl) reference electrode (RE) and Pt sheet electrode as the counter electrode (CE).

V.9.4.2. STUDIES WITH H-CELL CONFIGURATION

These studies were performed at the facilities of Antoni Llobet's research group at the Institut Català d'Investigació Química. The printed GDL electrodes were connected to a CH Instruments 7300E potentiostat, using a Pt mesh counter electrode, Ag/AgCl (3 M KCl) reference electrode, and 0.1M pH7 PBS as reactant purged with nitrogen after sealing the cell and before the electrochemical experiments. The experiments were performed at room temperature and a sample of the gas inside the working electrode chamber was collected after the 30 min chronoamperometry at -1.6 V (vs Ag/AgCl). After the experiments, a calibration curve was done through gas chromatography by adding a known amount of pure hydrogen into the cell using a gas-tight Hamilton syringe. An Agilent 6890N gas chromatograph coupled to a mass selective detector with an electronic impact ionization source and an Agilent 6890N with FID and TCD detectors was used in the experiments performed

V.9.4.3. STUDIES WITH FLOW-CELL AND MEA CONFIGURATIONS

These studies were performed using a 1.04 mg/cm^2 RuOx-coated gas diffusion layer (GDL) from GDL Freudenberg H23C2. The GDL was coated by automatized ultrasonic spray coating as described in V.9.3.

V.9.4.4. PREPARATION OF GOLD CURRENT COLLECTORS

The gold current collectors used in the flow-cell and MEA configurations were prepared as follows: first, the copper (Cu) plates are polished to remove impurities and debris. Then, a nickel (Ni) layer is electrodeposited. A Cu plate is connected to the potentiostat as a working electrode, while a nickel plate is used as the counter electrode. A Tifoo nickel electrolyte from Marawe is used electrolyte and the electrodeposition takes place at -1.3 V for 90 min. After this time, the Ni-coated

plate is thoroughly rinsed with distilled water to remove any residues of the nickel electrolyte and carefully dried with precision tissue wipes to avoid abrasion of the Ni surface. Finally, the Ni-coated plate is connected to the potentiostat as a working electrode, together with a graphite plate as a counter electrode and Tifoo gold electrolyte bath from Marawe. The electrodeposition occurs at -3.1 V for 90 min. After this period, the Au and Ni-coated plate is washed with distilled water to remove any residues of the electrolyte and carefully dried with precision tissue wipes to avoid abrasion of the surface.

V.9.4.5. PRE-TREATMENT OF NAFION MEMBRANE

Nafion 212 membrane (Sigma-Aldrich) is pre-treated by immersion in 3 wt% H_2O_2 solutions at 80 °C for 1 h. After this period, the membrane is removed from the previous bath, thoroughly washed with distilled H_2O, and then immersed in a bath of distilled H_2O at 80 °C for 1 h. The membrane is then immersed in 0.5 M H_2SO_4 solution at 80 °C for another hour. Finally, the membrane is carefully washed with distilled H_2O and stored in a humid environment.

V.9.4.6. MEMBRANE ELECTRODE ASSEMBLY

To assemble RuOx-coated GDL and pre-treated Nafion 212 membrane these are laminated together by hot-press at 130 °C and 0.5 ton for 10 min with a CARVER Model 4386 Bench Top Laboratory Manual Press with Electrically Heated Platens. This assembly is used as a membrane anode for flow cell tests. Then a screen-printed electrode is laminated against the other face of the membrane by hot-press at 60 °C and 0.5 ton for 10 min (for electrodes on PET).

V.9.5. CHARACTERIZATION

Scanning electron microscopy (SEM) images were obtained with FEI Quanta 650 FEG Field Emission scanning electron microscope (ESEM).

A Dektak 150 Surface Profilometer was used to characterize the thickness of the printed carbon GDLs.

The electron conductivity of the printed electrodes was characterized with Ossila Four-Point Probe System and Ossila Sheet Resistance Software.

Optical microscopy images were obtained from a Nikon ECLIPSE LV100D microscope and Clara Vision Perfect Image software

V.9.6. POROUS SUPPORTING SUBSTRATE

In this configuration, the printed GDL electrodes were prepared using a paper substrate (80 g/m^2 Paper Office document DIN A3 from REY). The catalyst was deposited as described in V.9.3, followed by the screen printing of the carbon layer as described in V.9.2).

V.9.7. ASSEMBLY OF e⁻LEAF

The methodology developed for the assembly of e⁻LEAF is presented in Figure V-61.
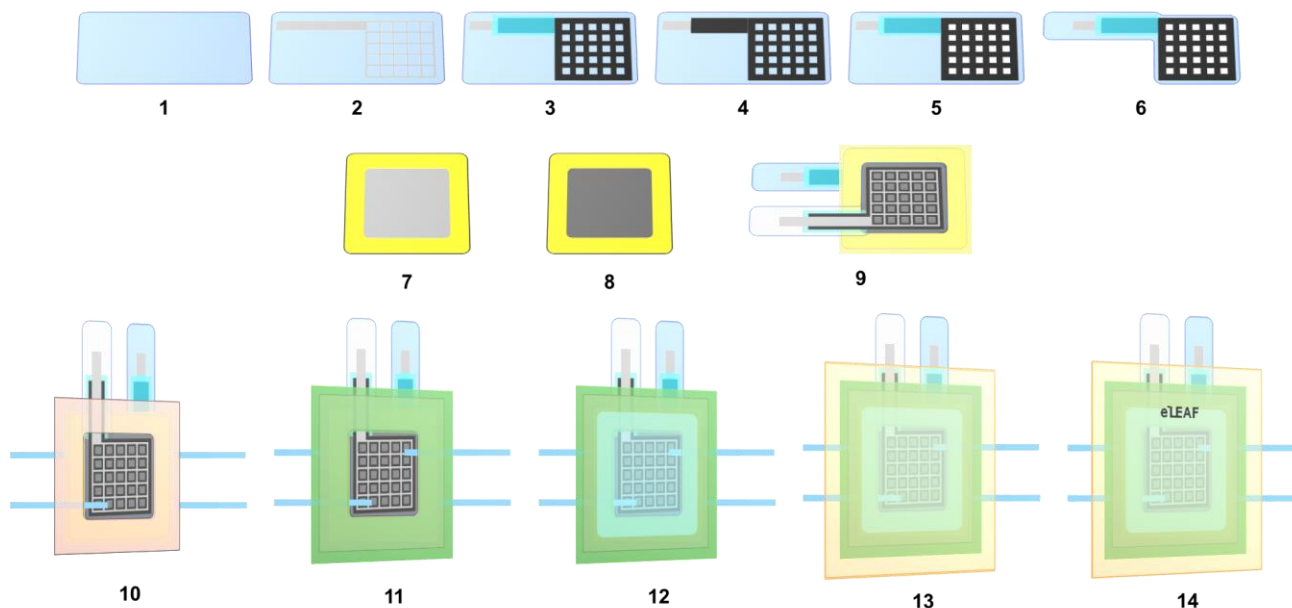
Figure V-61 – Methodology for the preparation of printed GDL electrodes (top row) and membrane electrode assembly for e⁻LEAF (middle row) and assembly of the e⁻LEAF cell.

Steps **1-5** are equivalent to the methodology described in section V.9.1. Step **6** is a laser cut procedure to create the necessary gas diffusion pathways and individualize the electrodes. Steps **7** and **8** are the catalyst deposition protocols performed as described in section V.9.3, while **9** is the fabrication of the membrane electrode assembly (MEA) following the method in V.9.4.6. Steps **10-14** represent the assembly of the e⁻LEAF cell. In step **10** the MEA is laminated together with the Teflon tubes used as inlets and outlets between two thermoplastic polyurethane (TPU) sheets using Fellowes Venus A3 laminating machine. The result of **10** is again laminated between a Fellowes 80 µm laminating pouch (**11**); two 125 µm PET squares and a Fellowes 120 µm laminating pouch to close and seal the half-cell compartments (**12** and **13**). **14** presents the final look of e⁻LEAF.

V.10. BIBLIOGRAPHY

[1]   D. M. E. Garcia, A. S. T. M. Pereira, A. C. Almeida, U. S. Roma, A. B. A. Soler, P. D. Lacharmoise, I. M. das Mercês Ferreira, C. C. D. Simão, *ACS Omega* **2019**, *4*, 16781.

[2]   B. M. Koraishy, J. P. Meyers, K. L. Wood, *J. Electrochem. Soc.* **2011**, *158*, B1459.

[3]   A. Mayyas, M. Mann, *Procedia Manuf.* **2019**, *33*, 508.

[4]   R. N. Dürr, S. Chasvised, M. Gil-Sepulcre, A. Howe, M. A. Hoque, V. N'Guyen, S. Sadeghi, S. Reynaud, C. Cugnet, L. Authier, C. Gimbert-Suriñach, A. Bousquet, A. Llobet, L. Billon, *ACS Appl. Energy Mater.* **2021**, *4*, 10534.

[5]   A. P. Manso, F. F. Marzo, J. Barranco, X. Garikano, M. Garmendia Mujika, *Int. J. Hydrogen Energy* **2012**, *37*, 15256.

[6]   H. Kipphan, *Handbook of Print Media*, **2001**.

[7]   F. Gaspari, in *Compr. Energy Syst.* (Ed.: I. Dincer), Elsevier Ltd., **2018**, pp. 88–116.

[8]   V. Airaksinen, in *Handb. Silicon Based MEMS Mater. Technol.* (Eds.: M. Tilli, T. Motooka, V.-M. Airaksinen, S. Franssila, M. Paulasto-Kröckel, V. Lindroos), Elsevier Inc., **2015**, pp. 381–390.

[9]   F. M. Smits, *Bell Syst. Tech. J.* **1957**, 711.

[10]   D. K. Schroder, Ed. , in *Semicond. Mater. Device Charact.*, WILEY-INTERSCIENCE, **2006**, pp. 1–59.

[11]   D. Gao, P. Wei, H. Li, L. Lin, G. Wang, X. Bao, *Acta Phys. Chim. Sin.* **2021**, *37*, 2009021.

[12]   J. G. Chen, C. W. Jones, S. Linic, V. R. Stamenkovic, *ACS Catal.* **2017**, *7*, 6392.

[13]   D. A. C. Brownson, C. E. Banks, in *Handb. Graphene Electrochem.* (Eds.: D.A.C. Brownson, C.E. Banks), Springer London, London, **2014**, pp. 23–77.

[14]   N. Aristov, A. Habekost, *World J. Chem. Educ. Vol. 3, 2015, Pages 115-119* **2015**, *3*, 115.

[15]   A. García-Miranda Ferrari, C. Foster, P. Kelly, D. Brownson, C. Banks, *Biosensors* **2018**, *8*, 53.

[16]   N. Elgrishi, K. J. Rountree, B. D. McCarthy, E. S. Rountree, T. T. Eisenhart, J. L. Dempsey, *J. Chem. Educ.* **2018**, *95*, 197.

[17]   F. Marken, A. Neudeck, A. M. Bond, in *Electroanal. Methods Guid. to Exp. Appl.* (Ed.: F. Scholz), Springer, **2010**, pp. 57–102.

[18]   A. C. C. L. Mccrory, S. Jung, I. M. Ferrer, S. M. Chatman, C. Jonas, T. F. Jaramillo, *J. Am. Chem. Soc.* **2015**, *137*, 4347.

[19]   V. Fragkou, Y. Ge, G. Steiner, D. Freeman, N. Bartetzko, A. P. F. Turner, *Int. J. Electrochem. Sci.* **2012**, *7*, 6214.

[20]   J. N. Hansen, H. Prats, K. K. Toudahl, N. Mørch Secher, K. Chan, J. Kibsgaard, I. Chorkendorff, *ACS Energy Lett.* **2021**, *6*, 1175.

[21]   T. J. Smith, K. J. S. The, in *Handb. Electrochem.* (Ed.: C.G. Zoski), Elsevier, **2007**, pp. 73–110.

[22]   V. S. Bagotsky, Ed. , in *Fundam. Electrochem.*, John Wiley & Sons, Inc., Hoboken, NJ, USA, **2005**, pp. 33–50.

[23]   L. Wang, C.-Y. Lee, P. Schmuki, *J. Mater. Chem. A* **2013**, *1*, 212.

[24]   J. Lopata, Z. Kang, J. Young, G. Bender, J. W. Weidner, S. Shimpalee, *J. Electrochem. Soc.* **2020**, *167*, 064507.

[25]   T. Lagarteira, F. Han, T. Morawietz, R. Hiesgen, D. Garcia Sanchez, A. Mendes, A. Gago, R. Costa, *Int. J. Hydrogen Energy* **2018**, *43*, 16824.

[26]   S. Erkan, I. Eroglu, in *Prog. Clean Energy, Vol. 2* (Eds.: I. Dincer, C.O. Colpan, O. Kizilkan, M.A. Ezan), Springer International Publishing, Cham, **2015**.

[27]   M. Carmo, D. L. Fritz, *Int. J. Hydrogen Energy* **2013**, *38*, 4901.

[28]   K. Wuttikid, S. Shimpalee, J. W. Weidner, K. Punyawudho, *Fuel Cells* **2017**, *17*, 643.

[29]   W. Xu, K. Scott, *Int. J. Hydrogen Energy* **2010**, *35*, 12029.

[30]   S. Shiva Kumar, V. Himabindu, *Mater. Sci. Energy Technol.* **2019**, *2*, 442.

[31]   J. P. Jog, *J. Macromol. Sci. Part C* **1995**, *35*, 531.

[32]   Y. Wang, W. Wang, Z. Zhang, L. Xu, P. Li, *Eur. Polym. J.* **2016**, *75*, 36.

[33]   R. Panowicz, M. Konarzewski, T. Durejko, M. Szala, M. Łazinska, M. Czerwinska, P. Prasuła, *Materials (Basel).* **2021**, *14*.

[34]   S. C. Perry, C. Ponce de León, F. C. Walsh, *J. Electrochem. Soc.* **2020**, *167*, 155525.

[35]   M. P. Browne, J. Dodwell, F. Novotny, P. R. Shearing, V. Nicolosi, D. J. L. Brett, M. Pumera, *J. Mater. Chem. A* **2021**, *9*, 9113.

[36]   D. Xu, M. B. Stevens, M. R. Cosby, S. Z. Oener, A. M. Smith, L. J. Enman, K. E. Ayers, C. B. Capuano, J. N. Renner, N. Danilovic, Y. Li, H. Wang, Q. Zhang, S. W. Boettcher, *ACS Catal.* **2019**, *9*, 7.

[37]   M. Inaba, A. W. Jensen, G. W. Sievers, M. Escudero-Escribano, A. Zana, M. Arenz, *Energy Environ. Sci.* **2018**, *11*, 988.

[38]   H. Nolan, M. P. Browne, *Curr. Opin. Electrochem.* **2020**, *21*, 55.

[39]   Y. Hori, K. Kikuchi, S. Suzuki, *Chem. Lett.* **1985**, *14*, 1695.

[40]   Y. Hori, K. Kikuchi, A. Murata, S. Suzuki, *Chem. Lett.* **1986**, *15*, 897.

[41]   J. Li, Y. Kuang, Y. Meng, X. Tian, W. Hung, X. Zhang, A. Li, M. Xu, W. Zhou, C. Ku, C. Chiang, G. Zhu, J. Guo, X. Sun, H. Dai, *J. Am. Chem. Soc.* **2020**, *142*, 7276.

[42]   Y. Yang, F. Li, *Curr. Opin. Green Sustain. Chem.* **2021**, *27*, DOI 10.1016/j.cogsc.2020.100419.

[43]   A. Reyes, R. P. Jansonius, B. A. W. Mowbray, Y. Cao, D. G. Wheeler, J. Chau, D. J. Dvorak, C. P. Berlinguette, *ACS Energy Lett.* **2020**, *5*, 1612.

[44]   A. Patru, T. Binninger, B. Pribyl, T. J. Schmidt, *J. Electrochem. Soc.* **2019**, *166*, F34.

[45]   Y. C. Li, Z. Yan, J. Hitt, R. Wycisk, P. N. Pintauro, T. E. Mallouk, *Adv. Sustain. Syst.* **2018**, *2*, DOI 10.1002/adsu.201700187.

[46]   M. Carmo, D. Stolten, in *Sci. Eng. Hydrog. Energy Technol.* (Ed.: P.E.V. de Miranda), Elsevier, **2019**, pp. 165–199.

[47]   C. Hartnig, L. Jorisse, J. Kerres, W. Lehnert, J. Scholta, in *Mater. Fuel Cells* (Ed.: M. Gasik), Woodhead Publishing Limited, **2008**, pp. 101–184.

[48]   R. Ranaweera, L. Luo, *Curr. Opin. Electrochem.* **2020**, *22*, 102.

[49]   S. Shukla, K. Domican, M. Secanell, *ECS Trans.* **2014**, *64*, 341.

[50]   A. R. Zeradjanin, *ChemSusChem* **2018**, *11*, 1278.

[51]   Z. Chen, R. Hsu, in *PEM Fuel Cell Fail. Mode Anal.* (Eds.: H. Wang, H. Li, X.-Z. Yuan), CRC Press, **2011**, pp. 33–72.

[52]   M. Ash, I. Ash, Eds. , in *Handb. Green Chem.*, Synapse Information Resources Inc., **2008**, pp. 1372–2165.

[53]   R. R. Søndergaard, M. Hosel, F. C. Krebs, *J. Polym. Sci. Part B Polym. Phys.* **2013**, *51*, 16.

[54]   M. Pavlovic, B. Balint, *Introduction to Printed Electronics*, Springer, **2014**.

[55]   C. Phillips, A. Al-Ahmadi, S.-J. Potts, T. Claypole, D. Deganello, *J. Mater. Sci.* **2017**, *52*, 9520.

[56]   A. P. Karpinski, in *Linden's Handb. Batter.* (Eds.: D. Linden, T.B. Reddy), McGraw-Hill Book Co., **2012**, pp. 763–792.

[57]   C. Dinh, T. Burdyny, M. G. Kibria, A. Seifitokaldani, C. M. Gabardo, F. P. García de Arquer, A. Kiani, J. P. Edwards, P. De Luna, O. S. Bushuyev, C. Zou, R. Quintero-Bermudez, Y. Pang, D. Sinton, E. H. Sargent, *Science (80-.).* **2018**, *360*, 783.

[58]   T. H. Nguyen, A. Fraiwan, S. Choi, *Biosens. Bioelectron.* **2014**, *54*, 640.

[59]   F. Sharifi, S. Ghobadian, F. R. Cavalcanti, N. Hashemi, *Renew. Sustain. Energy Rev.* **2015**, *52*, 1453.

[60]   Q. Cheng, Z. Song, T. Ma, B. B. Smith, R. Tang, H. Yu, H. Jiang, C. K. Chan, *Nano Lett.* **2013**, *13*, 4969.

[61]   A. Fraiwan, S. Mukherjee, S. Sundermier, H. S. Lee, S. Choi, *Biosens. Bioelectron.* **2013**, *49*, 410.

[62]   J. P. Rolland, D. A. Mourey, *MRS Bull.* **2013**, *38*, 299.

[63]   D. S. Falcão, A. M. F. R. Pinto, *J. Clean. Prod.* **2020**, *261*, 121184.

[64]   A. R. Zeradjanin, P. Narangoda, I. Spanos, J. Masa, R. Schlögl, *Curr. Opin. Electrochem.* **2021**, *30*, 100797.

[65]   J. Jia, L. C. Seitz, J. D. Benck, Y. Huo, Y. Chen, J. W. D. Ng, T. Bilir, J. S. Harris, T. F. Jaramillo, *Nat. Commun.* **2016**, *7*, 1.

[66]   J.-W. Schüttauf, M. A. Modestino, E. Chinello, D. Lambelet, A. Delfino, D. Dominé, A. Faes, M. Despeisse, J. Bailat, D. Psaltis, C. Moser, C. Ballif, *J. Electrochem. Soc.* **2016**, *163*,

F1177.

[67]   O. Zaouak, L. Authier, C. Cugnet, A. Castetbon, M. Potin-Gautier, *Electroanalysis* **2010**, *22*, 1151.

[68]   O. Zaouak, L. Authier, C. Cugnet, A. Castetbon, M. Potin-Gautier, *Electroanalysis* **2009**, *21*, 689.

[69]   C. Parat, S. Betelu, L. Authier, M. Potin-Gautier, *Anal. Chim. Acta* **2006**, *573–574*, 14.

[70]   O. Bagel, B. Limoges, B. Schöllhorn, C. Degrand, *Anal. Chem.* **1997**, *69*, 4688.

[71]   E. Sowade, K. Y. Mitra, E. Ramon, C. Martinez-Domingo, F. Villani, F. Loffredo, H. L. Gomes, R. R. Baumann, *Org. Electron.* **2016**, *30*, 237.

[72]   S. H. Ko, J. Chung, Y. Choi, C. P. Grigoropoulos, D. Poulikakos, in *ASME Int. Mech. Eng. Congr. Expo.*, **2005**.

[73]   S. Conti, C. Martínez-Domingo, M. Lay, L. Terés, F. Vilaseca, E. Ramon, *Adv. Mater. Technol.* **2020**, *1900773*, 1900773.

[74]   T. T. T. Can, T. C. Nguyen, W. S. Choi, *Sci. Rep.* **2019**, *9*, 1.

V.11. APPENDIXES

Table V-13 – Design parameters of the printed GDLs building blocks.

Design name	N^{open}	a	b	c	d	e	f	g
B	0	N.A.	N.A.	N.A.	N.A.	N.A.	N.A.	N.A:
Windows (a=b)								
W1	2	7.07	7.07	2.00	10.9	1.86	1.93	10.9
W2	2	7.07	7.07	6.36	1,99	0	1.86	N.A.
Open mesh (a=b AND c=d AND e=f)								
W3	4	5.00	5.00	3.99	3.99	2.00	2.00	N.A.
W4	4	5.00	5.00	1.00	1.00	8.00	8.00	N.A.
W5	25	2.00	2.00	2.00	2.00	1.50	1.50	N.A.
W6	25	2.00	2.00	1.00	1.00	2.00	2.00	N.A.
W7	100	1.00	1.00	1.00	1.00	0.89	0.89	N.A.
Slits (a>b)								
S1	2	10.0	5.00	5.00	4.00	0	2.00	N.A.
S2	2	10.0	5.00	5.00	1.00	0	8.00	N.A.
S3	4	10.0	2.50	5.00	2.00	0	2.00	N.A.
S4	8	12.5	1.00	3.74	2.00	0	1.14	N.A.
S5	4	12.5	2.00	3.74	2.00	0	2.66	N.A.
S6	6	16.7	1.00	1.66	2.00	0	2.00	N.A.
S7	10	10.0	1.00	5.00	1.00	0	0.89	N.A.

Note: "a to g" parameters (in mm) and the number of openings (N^{open}) of the designed electrodes.

N.A. – not applicable.

Table V-14 – Thickness and conductivity measured by profilometry and four-probe analysis, respectively, for Carbon Creative 122-49 and Graphite Sunchemical C2030519P4.

Sample number	Thickness (µm)	Conductivity (S cm^{-1})	Number of layers*
Carbon Creative 122-49			
1	10.1	15.3 ± 0.005	3
2	10.9	13.3 ± 0.003	1
3	11.3	14.0 ± 0.003	1
4	11.8	12.2 ± 0.003	3
5	12.3	11.5 ± 1.72	2
6	12.3	12.0 ± 0.002	2
7	12.5	11.7 ± 0.002	3
8	13.4	11.4 ± 0.002	1
9	14.0	10.5 ± 0.003	2
Graphite Sunchemical C2030519P4			
10	7.04	15.3 ± 0.007	2
11	7.10	14.7 ± 0.003	2
12	7.78	16.5 ± 0.002	3
13	8.17	12.7 ± 0.007	2
14	8.23	17.1 ± 0.003	2

Sample number	Thickness (μm)	Conductivity (S cm⁻¹)	Number of layers*
15	8.26	16.8 ± 0.003	1
16	8.41	17.8 ± 0.006	2
17	8.98	15.3 ± 0.004	2
18	9.60	14.1 ± 0.003	2
19	10.0	14.2 ± 0.003	2
20	10.2	12.3 ± 0.003	2
21	10.4	13.8 ± 0.003	2
22	11.6	12.2 ± 0.006	2
23	17.3	6.84 ± 0.002	2
24	18.2	7.13 ± 0.001	2
25	18.2	7.78 ± 0.002	2

*wet on wet layers

Table V-15 – Current density variation in CA measurements for different pH and reactants at room temperature (RT ≈ 23 °C). J symbolizes the current density and ΔJ is the variation of J between t=0 min and t=30 min (t represents the elapsed time).

Electrode	Reactant	pH	Potential applied (V vs Ag/AgCl)	$J_{t=0\ min}$ (mA/cm²)	$J_{t=30\ min}$ (mA/cm²)	ΔJ (mA/cm²)	ΔJ (%)
Bare	$PBS+H_2SO_4$	2	-1.6	-1.79	-2.04	-0.25	+14.0
Pt	$PBS+H_2SO_4$	2	-1.6	-3.35	-3.56	-0.21	+6.27
Bare	$PBS+H_2SO_4$	2	-2.0	-3.08	-3.21	-0.13	+4.22
Pt	$PBS+H_2SO_4$	2	-2.0	-4.81	-4.75	+0.06	-1.25
Bare	$PBS+H_2SO_4$	4	-1.6	-0.74	-0.85	-0.09	+14.9
Pt	$PBS+H_2SO_4$	4	-1.6	-1.78	-1.85	-0.07	+3.93
Bare	$PBS+H_2SO_4$	4	-2.0	-1.73	-1.77	-0.04	+2.31
Pt	$PBS+H_2SO_4$	4	-2.0	-2.81	-2.81	0	0.00
Bare	PBS	7	-1.6	-0.01	-0.02	-0.01	+100
Pt	PBS	7	-1.6	-2.55	-2.62	-0.07	+2.75
Bare	PBS	7	-2.0	-1.54	-1.65	-0.11	+7.14
Pt	PBS	7	-2.0	-2.99	-2.98	+0.01	-0.33
Bare	PBS	9	-1.6	-0.24	-0.21	+0.03	-12.5
Bare	PBS	9	-2.0	-0.98	-0.90	+0.08	-8.16
Bare	Dist. H_2O	7	-1.6	-0.01	-0.01	0	0.00
Bare	Dist. H_2O	7	-2.0	-0.01	-0.01	0	0.00

Table V-16 – Thickness and conductivity measured by profilometry and four-probe analysis, respectively, for the eSCALED conductive pastes containing commercial polymeric binders tested.

Thickness (μm)	Conductivity (S cm⁻¹)	Number of layers*
Graphite eSCALED (MBM)		
21.0	2.86 ± 0.0004	2
22.2	3.51 ± 0.0005	3
22.7	3.71 ± 0.0019	3
23.4	2.54 ± 0.0004	1
25.6	3.56 ± 0.0007	3

Thickness (µm)	Conductivity (S cm^{-1})	Number of layers*
Graphite eSCALED (SBS)		
16.7	2.03 ± 0.0011	3
19.0	2.07 ± 0.0012	3
21.3	2.40 ± 0.0008	3

*wet on wet layers

Table V-17 – Thickness and conductivity measured by profilometry and four-probe analysis, respectively, for the eSCALED conductive pastes containing P(MMA-*stat*-S-*stat*-PHEMA) as the binder.

| Thickness (µm)	Conductivity (S cm^{-1})	Number of layers*
eSCALED P(MMA-*stat*-S-*stat*-PHEMA)		
18.5	1.73	2
18.5	3.01	1
21.4	2.42	2
21.5	1.94	1
22.7	4.70	2x2$^+$
24.9	1.68	2
28.2	1.49	1
58.4	3.65	4x2$^+$
61.7	4.48	4x2$^+$
63.4	3.56	4x2$^+$
69.9	3.78	4x2$^+$
70.8	3.61	4x2$^+$
72.8	5.30	4x2$^+$
77.9	4.16	4x2$^+$
79.3	3.52	4x2$^+$
83.6	4.72	4x2$^+$

*wet on wet layers

$^+$number of repetitions x wet on wet layers per repetition

V.11.1. PRELIMINARY STUDIES PERFORMED AT UPPA

V.11.1.1. SCREENS' SELECTION AND DESIGN

Three different screens were designed to screen-print DuPont 5000 Ag (77 threads/cm) ink, carbon-based (77 threads/cm) pastes and insulating or conducting polymers (120 threads/cm) pastes with inspiration from[65]. The mesh size for each screen was selected according to the provider's recommendations and considering the solid particle size. Since in insulating and conducting polymer no solid particles are expected to be present the screen does not require large mesh sizes.

The screens are designed to allow the user to produce electrodes with three different architectures presented in Figure V-62 by the cross-section illustration of the three architectures.
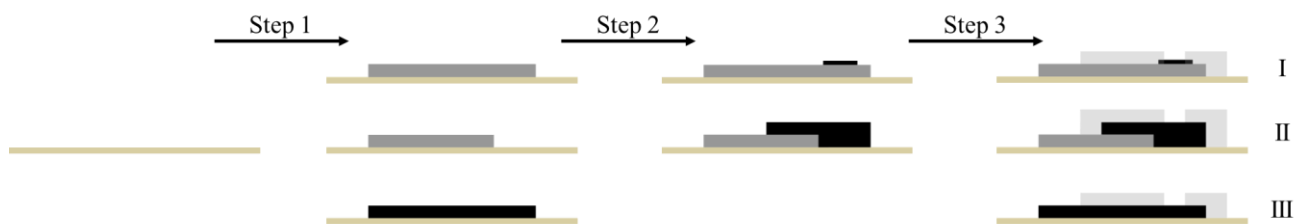
Figure V-62 – Proposed screen-printing process to produce three different architectures.

Architecture **I** consists of printing a conducting layer, as a current collector (dark grey), of a commercially available or well-developed conducting paste, such as silver, while the paste to be studied (black) should be deposited only at the working area of the electrode, to save homemade paste and increasing the number of possible tests. Architecture **II** and **III** allow the progressive development of a single-layer electrode with the optimized conducting paste. All three screens allow the user to print 1 cm^2 square electrodes to control the quality of the printing, thickness, and electrical conductivity.

The electrodes were designed adapting the electrodes previously reported by Zaouak *et al* and are presented in Figure V-63.
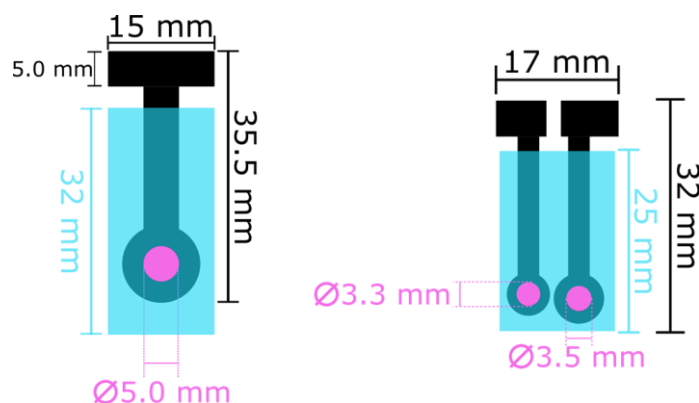
Figure V-63 – Screen-printed electrode designs. Black and blue colors represent the carbon and insulating layers, respectively. The pink color represents the working area of the electrodes. Adapted from [65].

An insulating layer is printed on top to control the size of the electrode's working area and to define the area for external connection. The screen designed to print the insulating layer allows the user to control the working area diameter from 3 to 10 mm, allowing studying the influence of this parameter on the electrode performance. An insulating layer is printed on top to control the size of the electrode's working area and to define the area for external connection. The screen designed to print the insulating layer allows the user to control the working area diameter from 3 to 10 mm, allowing studying the influence of this parameter on the electrode performance.[65–68]

V.11.1.2. SCREEN-PRINTED CARBON-BASED ELECTRODES

Polystyrene (PS), high impact polystyrene (HIPS), and styrene-butadiene-methyl methacrylate (SBM) triblock copolymer were initially used as the binders to prepare manually screen-printed carbon-based electrodes. These three binders have in common a styrene block, which is

expected to be compatible with the PS-based copolymer functionalized with tetra-aniline (TANI) prepared in this work. SBM is expected to offer great advantages with its cross-linkable methyl methacrylate (MMA) block and the low T_g of its butadiene block, -70 ºC, offering better processability, adhesion to the substrate, and flexibility. Graphite powder is used as the conducting solid carbon-based filler and 1.6 mL of mesitylene as the solvent, following the work previously reported by Zaouak *et al.*[65][65] The prepared inks were printed on two different substrates, HIPS, and polyvinyl chloride (PVC) sheets. No thermal curing was performed after printing any of the layers, the solvent evaporated at room temperature.

Not all the printing results of pastes with 42.0 wt% solid content were satisfactory (see Table V-18).

Table V-18 – Summary of the tested mesitylene-based pastes for electrode printing. ✓and ✖ symbols qualify the printing results as good and bad, respectively.

Binder	Solid content wt%	Substrate	
		HIPS	PVC
SBM	42.0	✓	✖
	47.5	✓	✓
PS	42.0	✖	✓
HIPS	42.0	✓	✓

PS could not be printed on HIPS but the results on PVC were satisfactory, while the inverse was observed for SBM paste. HIPS paste showed good printing results on both substrates. Since SBM was of greater interest for the reasons previously mentioned, a new paste with higher solid content (47.5 wt%) was prepared. It was expected that by increasing the solid content the paste's viscosity would also increase and facilitate the printing process and adhesion to PVC. Figure V-64 compares the printed SBM electrodes and it is possible to confirm that the paste with higher solid content resulted in better and more defined and continuous electrodes on PVC.
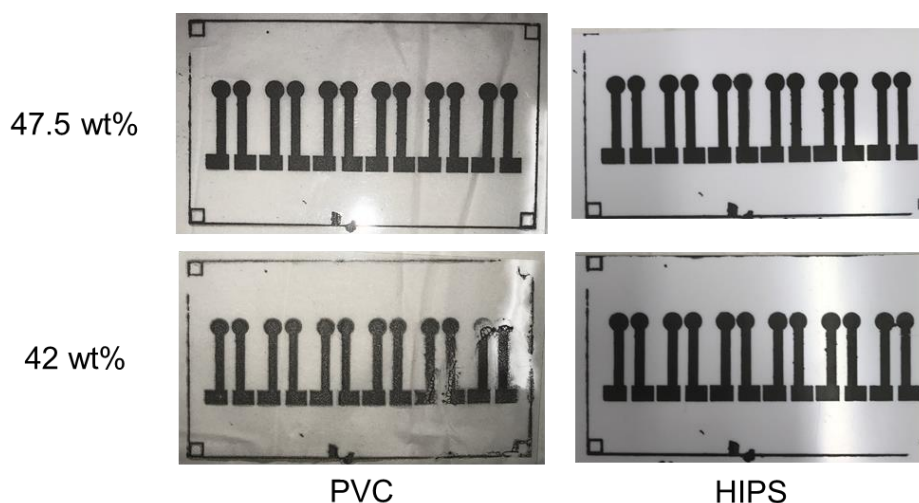
Figure V-64 – Electrodes printed with SBM conducting pastes with different solid content wt% on PVC and HIPS.

The electrodes were characterized by cyclic voltammetry (CV) measurements in two different electrolytes: pH 7 phosphate buffer saline (PBS) using (ferrocenylmethyl)trimethylammonium hexafluorophosphate, a derivative compound ($[FcCH_2NMe_3FcCH_2Nme_3]^+$) of ferrocene (FCN), as internal standard.[65] The setup used two of the printed electrodes as a working counter. It was not possible to bring a lot of conclusions from the electrochemical performance of the electrodes due to low reproducibility during the printing process and poor control of experimental parameters such as the distance from the reference electrode. The use of a homemade printed counter electrode could also lead to false conclusions and under or overestimate the performance of the different pastes for electrode production. Considering this, it is not possible to compare the results and conclude which paste is the best to produce electrodes. With this being said, this study only answers the question: "is it possible to print an electrode that is conducting enough to detect the FCN compound in the electrolyte?". Yes, all the different electrodes were able to detect the FCN compound during the cyclic voltammetry experiment. Figure V-65 a) presents the CVs registered of the electrodes with HIPS and SBM as binders printed on HIPS substrate, HIPS@HIPS, and SBM@HIPS, respectively. In Figure V-65 b) the CVs of the electrodes with HIPS and PS binders printed on PVC substrate are presented. In all cases, the obtained CVs presented one anodic and cathodic peak, *i.e.*, the oxidation of ferrocene compound (Fe^{II}) to ferrocenium (Fe^{III}) at the forward scan and the following reduction of Fe^{III} to Fe^{II}, respectively.

a)

b)
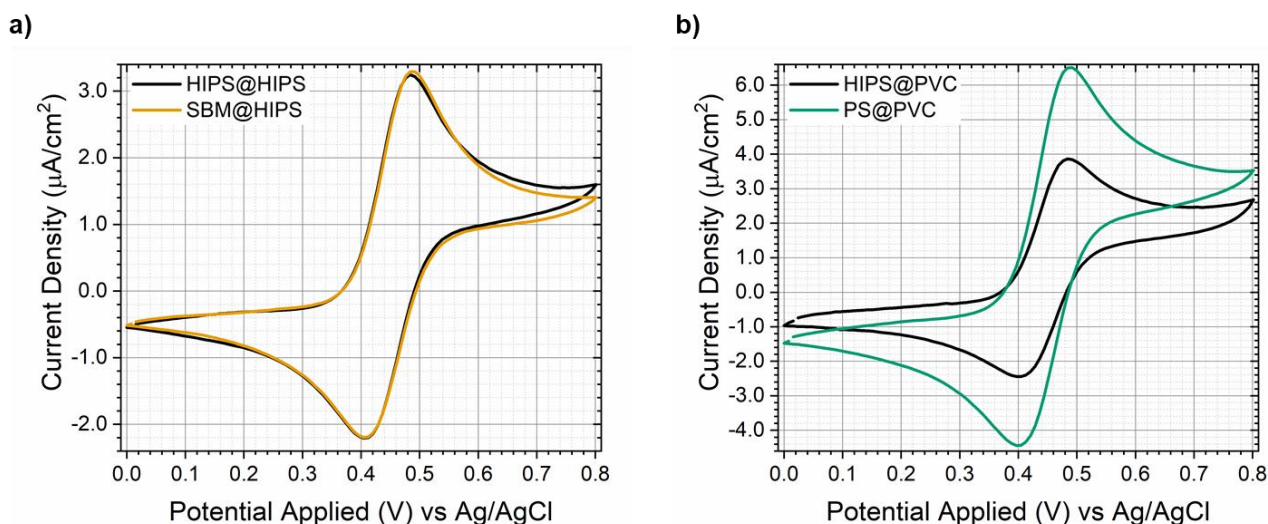
Figure V-65 – CV of screen-printed carbon-based electrodes with a working electrode radius of 1.65 mm in PBS (pH 7 at room temperature) in the presence of a derivative compound of ferrocene ($[FcCH_2Nme_3]^+$): **a)** HIPS and **b)** PVC as substrates.

Table V-19 compares the peak centers (E_p), anodic and cathodic, of the ferrocenium/ferrocene (III/II) redox couple for each type of electrode tested. The distance between anodic and cathodic peaks (ΔE_{pp}) was calculated by Equation V-18:

$$\Delta E_{pp} = |E_p(anodic) -– E_p(cathodic)|$$ **Equation V-18**

The tested electrodes demonstrated moderate peak-to-peak separation (79 – 86 mV). The electrodes prepared with HIPS as the binder, in both substrates, showed the lowest ΔE_{pp}, 79 mV, which indicates that these electrodes presented higher electron mobility, *i.e.*, their electron conductivity was higher than the electrodes obtained from SBM and PS beads.[13][13] The electrodes produced with HIPS were tested by a colinear four-point probe technique, and a conductivity of 1.2 S cm^{-1} was registered.

Table V-19 – Position (center and height) of the oxidation and reduction peaks (v = 100 mV/s) and peak-to-peak separation (ΔE_{pp}) attributed to the ferrocene/ferrocenium redox couple for the screen-printed electrodes tested.

Substrate	Binder	$Fe^{II} \rightarrow Fe^{III}$		$Fe^{III} \rightarrow Fe^{II}$		ΔE_{pp} (mV)
		Center (V)	Height ($\mu A/cm^2$)	Center (V)	Height ($\mu A/cm^2$)	
HIPS	HIPS	+0.484	+3.29	+0.405	-2.20	79
	SBM	+0.492	+3.25	+0.405	-2.21	87
PVC	HIPS	+0.476	+3.80	+0.397	-2.44	79
	PS	+0.491	+6.51	+0.405	-4.43	86

The analysis of Table V-19 together with Figure V-65 revealed that the electrodes printed on PVC exhibited higher current density a the ferrocenium/ferrocene peaks. Given that the same concentration of (ferrocenylmethyl)trimethylammonium hexafluorophosphate was present in the electrolyte the increase in current was attributed to the higher surface area of the electrodes. This could be explained by higher surface tension, thus, higher contact angle, thus, poor wetting of PVC

compared to HIPS as substrate. However, other parameters should be considered such as the fact that the printing process was manual and the human hand variability associated, namely, the speed of printing and pressure applied on the squeegee during the printing. Furthermore, mesitylene is used as a solvent to prepare the inks, therefore, it was expected that better wetting, adhesion, and, consequently, smoother films with a lower surface area would be achieved when using HIPS as substrate. Further characterization such as profilometry and the determination of the electrochemically active surface area is needed to better fundament the arguments given.

Printing mesitylene-based pastes was a difficult process due to the fast evaporation of mesitylene, forcing the user to wash frequently the screen with toluene to avoid clogging the screen and bad printing quality. Although this formulation of carbon-mesitylene ink was previously described as advantageous due to room temperature fast drying, this property can strongly affect the printing process and become a disadvantage.[65,68] Moreover, the toxicity of both mesitylene and toluene solvents involved in this process presents a harmful threat to the user. Hence, the substitution of mesitylene with another solvent that offers easier processability and a less toxicological threat from manipulation becomes relevant. Propylene glycol 1-monomethyl ether 2-acetate ($C_6H_{12}O_3$, PGMEA) has been described in the literature as a green and clean solvent of great interest for electronics and printing inks for ink-jet.[52,69–72]

GENERAL

CONCLUSION AND

PERSPECTIVES

GENERAL CONCLUSION AND PERSPECTIVES

The works developed in this thesis aimed to contribute to the cathode of an artificial photosynthesis device for the eSCALED project in an innovative multi-disciplinary approach. The results of the works performed successfully achieved the objectives defined.

In our block copolymer strategy, we successfully synthesized, by controlled radical polymerization (ATRP), polystyrene (PS), and P(S-*stat*-Butylacrylate) as precursory blocks for a conducting block copolymer where oligomer of polyaniline, *i.e.* tetra-aniline (TANI) was the organic conducting block. The size, size distribution, and end-chain functionality have been controlled. The presence of the Butylacrylate (BuA) unit proved to be crucial for the optimization of the mechanical properties of the conducting block copolymer. Porous structured films of PS-*b*-TANI and P(S-*stat*-BuA)-*b*-TANI were prepared into different supporting substrates by breath figure methodology and their electroactivity was electrochemically proved. Interestingly, the porous structuration not only turned the film color from dark to white without altering the electroactive properties but also enhanced the electrochemical activity of the films. **Objective 1** of this thesis was therefore successfully achieved: develop structured electroactive polymer films as a catalyst supporting layer. The results of this work open new perspectives for the use of P(S-*stat*-BuA)-*b*-TANI films in different fields of applications, hence further studies are required to explore and understand its properties. For instance, the microporous P(S-*stat*-BuA)-*b*-TANI films may be suitable redox mediators in second-generation glucose sensors, taking advantage of the micropores to immobilize enzymes and the redox mechanism of TANI.

Objective 2 was also successfully achieved: to investigate strategies to immobilize the catalyst on the catalyst-supporting layer developed by two approaches.

First, in our approach to the synthesis of TANI-functionalized molecular catalyst, promising results in the strategy using HATU (as for 1-[Bis(dimethylamino)methylene]-1H-1,2,3-triazolo[4,5-b]pyridinium 3-Oxide Hexafluorophosphate) for the coupling of TANI with a bipyridine were obtained. However, because of a lack of time, the strategy was not completely developed, and more studies should be performed to optimize the synthesis pathway. Furthermore, we suggest studying TANI-functionalized molecular catalysts for hydrogen evolution reaction (HER). As the electron conductivity of TANI is promoted in an acidic environment, also known as a relevant experimental medium for HER, the influence of having a TANI group in a molecular catalyst for this reaction should be studied.

After the organic material approach, we developed for the first time a novel hierarchically porous structure for ZnO and studied its application for the photocatalytic degradation of organic pollutants in water. The ZIF-8-derived ZnO obtained by calcination with porous tetrakaidecahedron

morphology presented a pure wurtzite phase of ZnO. Well-structured materials have been obtained and further studies are needed to fully understand the influence of the pore size of the ZnO structures when employing this material as a photocatalyst.

At last, this work ends with the use of screen-printed electrodes for hydrogen evolution, replacing the conventionally used gas diffusion layer electrodes and bipolar plates used as current collectors. We proposed and studied different designs for the printed electrodes and demonstrated that different cell configurations may require specific electrode designs to achieve higher performances. With the right choice of substrate, the printed electrodes are stable in acidic conditions. PET substrate was found to limit the maximum operating temperature of the electrode up to 40 ºC. Printed electrodes also promote easy integration and testing of different catalysts in water electrolyzers. This work should be seen as the first step in the implementation of printed electrodes in water electrolysis devices. Screen-printing inks may be used to produce electrodes and the use of porous supporting substrates, such as paper or non-woven fabrics, for the printed electrodes, may represent an interesting perspective to promote gas diffusion. The study and definition of a methodology based on printed electronics to achieve novel functional cathodes for artificial photosynthesis was successfully performed, meeting the ambitions of **Objective 3**.

Going beyond the goal of this thesis an innovative prototype of an electrolyzer cell was developed: e⁻LEAF. This unprecedented flexible cell was built following printed electronics methodologies converging with the requirements of a functional single-cell water electrolyzer. When integrated with a tandem triple junction perovskite solar cell, e-LEAF demonstrated STH≈15 %. Having transparent endplates, e⁻LEAF allows the integration of photoactive materials, such as the porous hierarchically porous ZnO. Moreover, the structured electroactive polymeric films based on P(S-*stat*-BuA)-*b*-TANI developed could also be integrated into e⁻LEAF being cast on top of the printed GDL electrodes. Ideally, a TANI-based molecular catalyst would be employed as a selective catalyst for H^+ or CO_2 reduction reactions.

The work developed in this thesis is a strong contribution to the development of water electrolysis technology in general, but also the specific academic community of each of the domains covered. We forecast that several research opportunities and new topics arise from the studies presented herein.

PUBLICATIONS AND

PATENTS

PUBLICATIONS

1. "Synthesis of new tetra-aniline capped poly(Styrene-*statistical*-Butyl Acrylate) block copolymer for bio-inspired structured electrodes" (currently under development).

2. "Fully printed membrane electrode assembly (MEA) for H_2 production" (currently under development).

PATENTS

1. V. Nguyen, D. Garcia, M. Berenguel, P. Lacharmoise, C. Simão, *Fabrication method of a membrane electrode assembly (MEA), MEA, cell and uses thereof*. Fundació Eurecat. App. Nr. EP21383086.2, **2021**, Spain.